Training and Research on Probabilistic Hydro-Thermo-Mechanical Modeling of Carbon Dioxide Geological Sequestration in Fractured Porous Rocks

Type of report:	FINAL TECHNICAL REPORT
Reporting period start:	December 1, 2009
Reporting period end:	May 31, 2013
Principal author:	Dr. Marte Gutierrez
Date report was issued:	September 25, 2013
DOE award number:	DE-FE0002058
Name and address of submitting organization:	Colorado School of Mines 1500 Illinois St. Golden, CO 80401-1887

TABLE OF CONTENTS

DISCLAIMER

ABSTRACT

Colorado School of Mines conducted research and training in the development and validation of an advanced CO_2 GS (Geological Sequestration) probabilistic simulation and risk assessment model. CO_2 GS simulation and risk assessment is used to develop advanced numerical simulation models of the subsurface to forecast CO_2 behavior and transport; optimize site operational practices; ensure site safety; and refine site monitoring, verification, and accounting efforts. As simulation models are refined with new data, the uncertainty surrounding the identified risks decrease, thereby providing more accurate risk assessment. The models considered the full coupling of multiple physical processes (geomechanical and fluid flow) and describe the effects of stochastic hydro-mechanical (H-M) parameters on the modeling of CO_2 flow and transport in fractured porous rocks. Graduate students were involved in the development and validation of the model that can be used to predict the fate, movement, and storage of CO_2 in subsurface formations, and to evaluate the risk of potential leakage to the atmosphere and underground aquifers. The main major contributions from the project include the development of: 1) an improved procedure to rigorously couple the simulations of hydro-thermo-mechanical (H-M) processes involved in CO_2 GS; 2) models for the hydro-mechanical behavior of fractured porous rocks with random fracture patterns; and 3) probabilistic methods to account for the effects of stochastic fluid flow and geomechanical properties on flow, transport, storage and leakage associated with CO_2 GS. The research project provided the means to educate and train graduate students in the science and technology of CO_2 GS, with a focus on geologic storage. Specifically, the training included the investigation of an advanced CO_2 GS simulation and risk assessment model that can be used to predict the fate, movement, and storage of CO_2 in underground formations, and the evaluation of the risk of potential CO_2 leakage to the atmosphere and underground aquifers.

1. BACKGROUND AND MOTIVATION

1.1 Introduction

With the increasing emission of greenhouse gases in the atmosphere, their reduction has become of paramount importance. Carbon capture and sequestration in appropriate geologic formations (saline aquifers, coal seams, and oil and gas reservoirs) are one of the promising methods to reduce the release of greenhouse gases in the atmosphere. However, there is still much work needed to be done to better account for the processes involved of CO_2 geological sequestration. Chief among these is the need to understand and predict the fate, movement, transport, storativity and potential leakage of CO_2 injected in sequestration reservoirs. Numerical models can help improve this understanding and can play significant roles in planning, design and management of CO_2 geological sequestration projects.

The development and use of numerical models to CO_2 geological sequestration have many challenges. Chief among these is that CO_2 geological sequestration involved multi-physical processes including hydrological, mechanical and geochemical. Moreover, processes involved are interacting and coupled in that one process affects the other. The geochemical reactions related to CO_2 geological sequestration (i.e., solubility and mineral trapping) are long-term processes that typically occur in decades or hundreds of years. Hence the focus of the project is on short term processes related to the hydrodynamic trapping of CO_2. Another challenge is that geologic formations suitable for CO_2 sequestration are inherently inhomogeneous and non-uniform. As a result, there is a natural variability of the measured parameters that are required to simulate fluid flow and transport in geologic formations. The analysis of subsurface flow of CO_2 requires a stochastic analysis to account for the effects of variable parameters on saturation profiles, pressure drop and injected volumes.

Improved procedures for coupled modeling are needed due to the fact that the hydraulic and mechanical (H-M) response related to the hydrodynamic trapping of CO_2 in storage reservoirs are fully coupled process. For instance, pore pressure changes will cause deformations in the rock matrix and fractures. In turn, the mechanical deformations will alter the matrix and fracture permeabilities, thereby affecting the fluid flow and the pore pressure distributions. Models cannot be reliably used to forecast the long term response of CO_2 storage reservoirs without incorporating the fundamental coupled processes involved in CO_2 GS.

Models for hydro-thermo-mechanical behavior of fractured porous rocks are needed to account for the important effects of faults and fractures and other discontinuities on the fluid flow and mechanical response of CO_2 storage reservoirs. Fractures and their distribution, properties and response to fluid pressure and temperature changes affect the injectivity, migration and distribution of CO_2 in storage reservoirs. Conductive fractures in hydraulic seals or cap rocks are detrimental to long term storage as they can be pathways for leakage of CO_2. On the other hand, conductive fractures can facilitate the injection and lateral migration of CO_2 ensuring larger volumetric intake. The coupling between hydro-thermo-mechanical processes is particularly important for fractured rock masses.

Probabilistic models are needed to account for the randomness in fracture geometries and distributions, and the uncertainties in the geomechanical and fluid flow properties on the response of CO_2 storage reservoirs. Parameters used in simulations of the hydro-thermo-mechanical modeling of CO_2 GS are subject to different types and levels of uncertainties due to: 1) inherent random heterogeneities (or spatial variability) in geological formations, 2) measurement errors, 3) statistical errors (due to small sampling sizes), and 4) errors in model

parameters obtained from correlations with laboratory and in situ test data. These uncertainties have to be accounted for in determining the reliability of predictions of the fate and movement of CO_2 in storage reservoirs, and to assess potential risks such as leakage of CO_2.

1.2 Project Objectives

The specific objectives of the project are:

1) Formulate a rigorous procedure to couple the hydraulic, thermal, and mechanical modeling of CO_2 storage reservoirs using Biot's theory for fluid flow in deformable porous media.
2) Implement a model for hydro-mechanical behavior of fractured porous rocks with random fracture geometries based on Oda's crack tensor formulation.
3) Develop a Monte Carlo-based risk assessment procedure for assessing the effects of uncertainties in the predictions of the fate and movement of CO_2 in storage reservoirs and the risks associated with the leakage of CO_2 to the atmosphere and underground aquifers.
4) Test and validate models using available data and case histories of geological sequestration of CO_2.

1.3 Project Tasks

The objectives of the project were accomplished through the following tasks:

Task 1 Develop Rigorous Procedure for Coupled Hydro-Thermo-Mechanical (HTM) Modeling

Task 2 Implement a Hydro-Mechanical Model for Fractured Porous Rocks with Random Fracture Geometries

Task 3 Develop a Monte-Carlo-Based Risk Assessment Procedure

Task 4 Test and Validate the Models against Case Histories of Geological Sequestration of CO_2

2. METHODOLOGY

2.1 Coupled Hydro-Mechanical (H-M) of CO_2 Geological Sequestration

The rigorous hydro-mechanical (H-M) coupling procedure is be based on the staggered solution of Biot's coupled poro-elasticty equations for fluid flow in deformable porous media (Biot 1941a,b). Current coupling procedures used in existing codes are based on the loose or "modular" coupling strategy, and do not rigorously account for the poro-mechanical effects from the coupling of fluid flow and deformation in porous and fractured media (Gutierrez & Lee 2009). As discussed in Gutierrez et al. (2001), the coupling effects between geomechanics and fluid flow are due to three factors. All these factors are accounted for in the proposed procedure outlined. The first component of the coupling is due to the thermo-poro-elastic effective stress changes that need to be included in geomechanical calculations. These effective stress changes caused by the changes in fluid pressures and temperature from the non-isothermal multi-phase fluid flow. The effective stress changes induced by pore pressure and temperature changes are calculated using the Terzaghi-Biot effective stress law (Terzaghi 1943; Biot 1941a,b). The effective stress changes are then converted to and applied as nodal loads in geomechanics model. The second component of the coupling is the change in the porosity of the rock mass due to the volumetric strain resulting from the effective stress changes (Chin et al. 2002; Gutierrez & Lee 2009). The third component of the coupling is due to the dependency of permeability on porosity. For intact rocks, a particular form of porosity-dependent permeability is the widely used Carman-Kozeny equation.

Generally, the coupling methods of the H-M processes can be divided into four categories: full coupling, one-way coupling, iterative coupling (two-way) and loose coupling. The full coupling scheme solves the governing equations of flow and geomechanics simultaneously, and hence is unconditionally stable. However, this method is difficult to implement when multiphase processes are involved and can be computationally intensive. In one-way coupling, the equations for fluid flow and geomechanical processed are solved independently, then the output from one simulator is passed as input to the other at certain time intervals. The flow of the information is only in one direction. The one-way method is only suitable for certain problems, and fluid flow dominated problem is one kind. In iterative coupling, the information is passed usually in a sequential fashion in both directions, between two simulators. This method takes advantages of the well developed and validated simulators and can provide sufficient accuracy. The loose coupling method is similar to the iterative coupling except that the coupling between two simulators only occurs at an interval of certain number of time steps. Hence, this method is less accurate and is applicable to limited circumstances.

The project adopted the iterative coupling method by coupling TOUGH2-ECO2N (Pruess et al., 2005), a simulator that deals with multiphase, multi-component, non-isothermal thermodynamics, using integral finite difference method and FLAC (Itasca, 2005) a finite difference geomechanical simulator which has been extensively scrutinized, validated and applied in related areas. According to Rutqvist (2011), there are three levels of coupling schemes: 1) Jacobian, which is the highest level of iterative coupling scheme, where the geomechanical and flow parameters changes are accounted for in the Jacobian matrix calculation in every Newtonian iteration of every time step; 2) Iterative, where the geomechanical and flow parameters changes are not updated during each Newtonian iteration, but only updated at the end

of the Newtonian iteration process; and 3) time-steppping, which is the lowest level of iterative coupling in which geomechanical and flow parameters are only corrected once (usually at the end of the time step) every time step.

2.1.1 Multiphase Flow and Heat Flow Governing Equations

The multiphase fluid flow mass and heat balance equations share similar mathematical forms, and they can be expressed in the following equation:

$$\frac{d}{dt}\int_{V_n} M^{\kappa} dV_n = \int_{\Gamma_n} F^{\kappa} \cdot n\Gamma_n + \int_{V_n} q^{\kappa} dV_n \tag{2.1}$$

where, $\kappa = 1, ..., NK$ (total number of components) and subscript $n = 1, ..., NEL$ (total number of gridblocks). In Eq. (2.1), integration is performed over the element volume V_n bounded by a closed surface Γ_n. n is the normal vector pointing towards the inside of the volume V_n. The general form of the mass accumulation term is all fluid phases, β, is,

$$M^{\kappa} = \phi \sum_{\beta} S_{\beta} \rho_{\beta} X_{\beta}^{\kappa} \tag{2.2}$$

in which the total mass of component κ can be calculated by the summation of concentrations of component κ in fluid phase β. ϕ is the porosity of the formation, S_β is saturation of phase β, or in other words, fraction of pore space that is occupied by phase β. ρ_β is density of phase β, and X_β^κ is mass fraction of component κ in phase β.

Depending on the physical process involved in the sequestration process, the mass flux term F^κ may include advective and diffusive-dispersive components (will be discussed below), each of which is a sum of individual phase flux of component κ across the boundary surface Γ_n. The advective mass flux term is:

$$F^{\kappa}\Big|_{adv} = \sum_{\beta} X_{\beta}^{\kappa} F_{\beta} \tag{2.3}$$

where the mass flux F^κ of phase β is given by a multiphase version of Darcy's law using density and Darcy's velocity of each phase:

$$F_{\beta} = \rho_{\beta} \bar{u}_{\beta} = -k \frac{k_{r\beta}\rho_{\beta}}{\mu_{\beta}} \left(\nabla P_{\beta} - \rho_{\beta} g \right) \tag{2.4}$$

The diffusive fluxes can be evaluated using the following equation:

$$J_{\beta}^{\kappa} = -\phi \tau_{\beta} \rho_{\beta} d_{\beta}^{\kappa} \nabla X_{\beta}^{\kappa} \tag{2.5}$$

where, d_β^κ is the molecular diffusion coefficient for component κ in phase β, τ_β is the tortuosity as a function of rock property and phase saturation.

The heat accumulation term is given in the equation follows, which accounts for contributions from the rock matrix, gaseous and fluid phases.

$$M^{\kappa} = (1-\phi)\rho_R C_R T + \phi \sum_{\beta} S_{\beta} \rho_{\beta} u_{\beta} \tag{2.6}$$

where, $\kappa = NK+1$ (the heat "component" term); ρ_R and C_R are grain density and specific heat of the rock, respectively; T is temperature, and u_β is specific internal energy in phase β.

The heat conduction, advection and radiation heat transfer can be accounted for by the heat flux term as follows:

$$F^{\kappa} = -\left[(1-\phi) K_R + \phi \sum_{\beta=1,2,3} S_{\beta} K_{\beta} \right] \nabla T + f_{\sigma} \sigma_0 \nabla T^4 + \sum_{\beta=1,2} h_{\beta} F_{\beta} \tag{2.7}$$

in which, similarly $\kappa = NK+1$, K_R is thermal conductivity of the rock, K_β is thermal conductivity of phase β, f_ϕ is radiant emittance factor, σ_0 is the Stefan-Bolzmann constant, h_β is specific enthalpy of phase β, and F_β is heat flux of phase β.

2.1.2 Poroelastic Theory of Deformable Porous Media

The three basic principles of poroelastic theory are stress equilibrium, strain-displacement compatibility relation and stress-strain constitutive relation. They are combined with Terzaghi's effective stress principle in this study, as well as parallel with the mass and heat balance, Darcy's Law and equation of state of multiphase flow. The mathematical forms expressing Terzaghi's effective stress and poroelasticity theory in deformable media are shown as follows:

1) Terzaghi's effective stress law (six equations):

$$\sigma_{ij}' = \sigma_{ij} - \delta_{ij} p,\ \sigma_{ij} = \sigma_{ji} \tag{2.8}$$

2) Stress equilibrium (six equations):

$$\sum_{j=1}^{3} \frac{\partial \sigma_{ij}}{\partial x_j} = 0;\ \sigma_{ij} = \sigma_{ji} \tag{2.9}$$

3) Strain-displacement compatibility relation (six equations):

$$\varepsilon_{ij} = \frac{1}{2}\left(\frac{\partial u_i}{\partial x_j} + \frac{\partial u_j}{\partial x_i} \right) \tag{2.10}$$

4) Stress-strain constitutive relation (six equations):

$$\varepsilon_{ii} = \frac{1}{E}\left[\sigma_{ii}' - \nu\left(\sigma_{jj}' + \sigma_{kk}' \right) \right] + \frac{1}{3K_s}\Delta p + a_L \Delta T\,, \tag{2.11}$$

$$\varepsilon_{ij} = \sigma_{ij}' / (2G),\ (i \neq j) \tag{2.12}$$

In Eqs. (2.7) to (2.12), $\varepsilon_{ij}, \sigma_{ij}$ and σ_{ij}' are the components of bulk strain tensor and total stress tensor, effective stress tensor, respectively; u_i is the component of solid/rock displacement vector $\vec{u} = (u_x, u_y, u_z)$; E, G ($G = E/[2(1+\nu)]$), and ν are Young's modulus, shear modulus, and Poisson's ratio for the solid phase/rock under drained conditions, respectively; $K_s = 1/c_s$, with c_s being solid/grain compressibility, is grain compressive modulus; p is pore pressure; T is temperature and a_L is the linear coefficient of thermal expansion, which can be obtained from the volumetric expansion coefficient.

Considering the 3D Cartesian coordinate system, Eq. (2.12) can turn into the following equation in terms of stresses:

$$\sigma_l = \lambda \varepsilon_v + 2G\varepsilon_l + \alpha \Delta p + \frac{E a_L}{(1-2\nu)\Delta T},\ l = x, y, z \tag{2.13}$$

where λ is the Lame's constant which can be calculated by shear modulus G and bulk K, $\lambda = K\text{-}2G/3$; α is Biot's poroelastic constant; ε_v is the volumetric strain and can be calculated using the following equation:

$$\begin{aligned} \varepsilon_v &= \varepsilon_x + \varepsilon_y + \varepsilon_z \\ &= \frac{3(1-2\nu)}{E}(\sigma_m - \sigma_m^0) - \frac{1}{H}(p - p^0) + a_{dr}(T - T^0) \end{aligned} \tag{2.14}$$

where $H = 1/(c_b\text{-}c_s)$, with c_b and c_s being drain bulk compressibility and solid/grain compressibility, respectively; a_{dr} is the volumetric heat expansion coefficient; σ_m is the mean normal total stress and $\sigma_m = \left(\sigma_x + \sigma_y + \sigma_z\right)/3$. Quantities with superscript of 0 denote initial values.

Given the governing equations discussed above, the coupling of TOUGH2 and FLAC can be linked directly through the pore volume change, or indirectly, through the stress dependent hydraulic properties, such as porosity $\phi = \phi(\sigma', \varepsilon)$, permeability change $k = k(\sigma', \varepsilon)$, and capillary pressure scaling. The coupling schemes will be elaborated in the later section.

2.1.3 Coupling Procedure

According to Settari and Mourits (1998), and Rutqvist (2011), the pore volume change (direct) coupling requires the coupling scheme on a full Jacobian scheme, meaning that the fluid mass and heat balances need to be rigorously preserved, while in the case of hydraulic properties changes coupling (indirect), the iterative or time-step coupling schemes can provide enough accuracy. Because of the massive computational effort that Monte Carlo simulation requires, this study will adopt the iterative or time-step coupling schemes, which are dominated by the hydraulic properties changes. The hydraulic properties changes include porosity $\phi = \phi(\sigma', \varepsilon)$, permeability change $k = k(\sigma', \varepsilon)$, and capillary pressure scaling.

In the fluid flow simulator alone (e.g., TOUGH2), the porosity change can be accounted for using the following equation:

$$\phi = \phi_0 \cdot \left[1 + c_r (P - P_0)\right] \tag{2.15}$$

in which ϕ_0 is the initial porosity at initial pore pressure P_0, the rock pore compressibility c_r is usually a constant. In the coupling scheme, the porosity will be calculated by the stress/strain solution because the volumetric strain-induced porosity change is based on a more complex material constitute model of the formation and hence is more accurate. The porosity change due to the volumetric strain resulting from the effective stress changes can be expressed as follows (Chin et al., 2002; Gutierrez and Lee, 2009):

$$\phi = \phi_0 + \exp(\varepsilon_v) - 1 \tag{2.16}$$

where $\varepsilon_v = tr(\varepsilon)$ is the volumetric strain.

For intact rock formation, the relationship between intrinsic permeability and porosity can be accounted for with the commonly used Carman-Kozeny equation:

$$k = c_0 \frac{\phi^3}{M_s^2 (1-\phi)^2} \tag{2.17}$$

where, k is intrinsic permeability; ϕ is porosity; c_0 is a numerical parameter called Kozeny's coefficient and varies according to the geometrical form of the individual channels in the bundle of capillary tubes (Bear, 1988); M_s is the specific surface per unit volume of solid material. It should be mentioned that the Carman-Kozeny coefficient of the rock formation $c = \sqrt{c_0} / M_s$ can have different values for different region of the formation.

After the new intrinsic permeability and porosity are obtained, the capillary pressure can be scaled using the Leverett *J*-function (Leverett, 1940):

$$P_c = P_{c0} \left(\frac{\sqrt{k_0 / \phi_0}}{\sqrt{k / \phi}} \right) \tag{2.18}$$

where, k_0 is reference/original/initial permeability , ϕ_0 is reference/original/initial porosity, P_c is capillary pressure and P_{c0} is capillary pressure at reference/original/initial permeability and porosity.

A flowchart in Fig. 2.1 presents a brief illustration of the numerical calculation procedure using iterative coupling scheme.

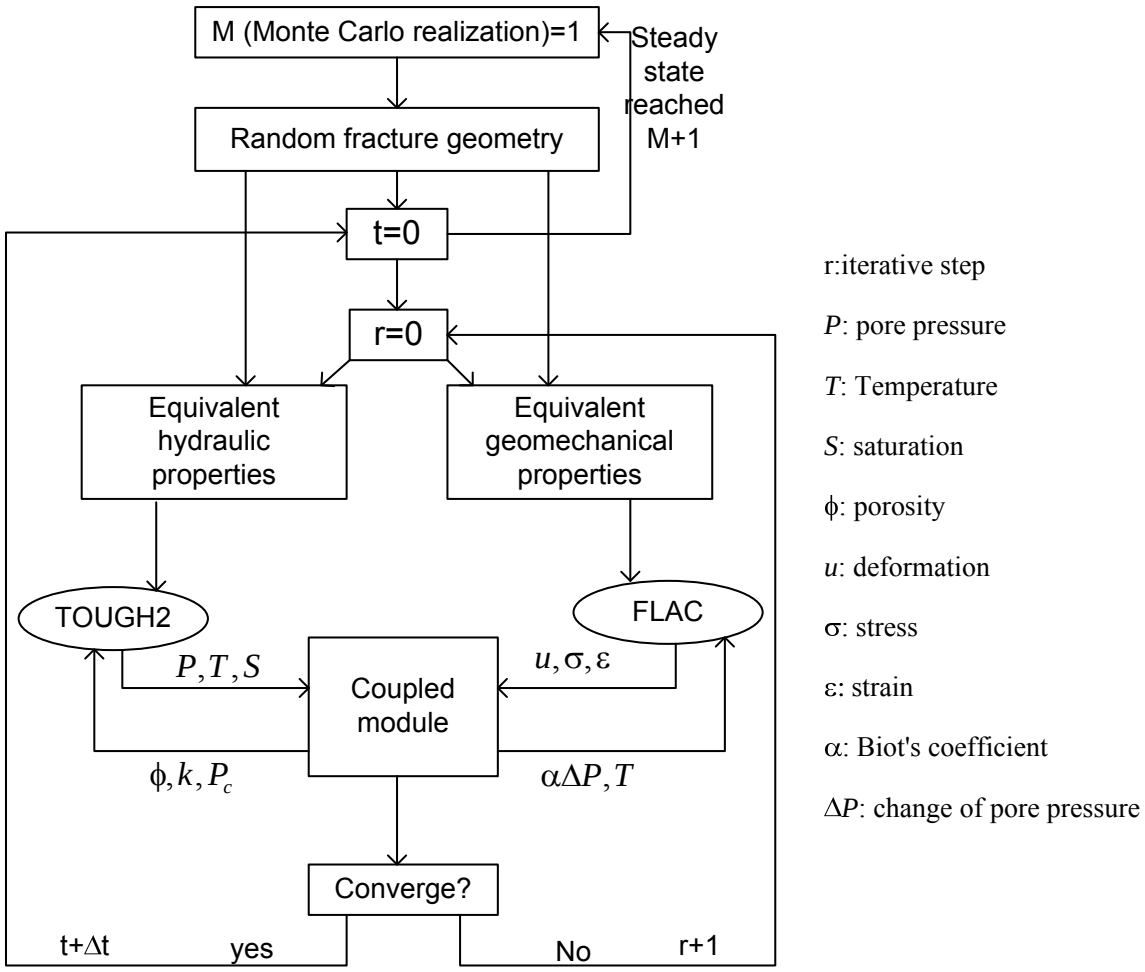

Fig. 2.1 - Flowchart of the iterative stochastic HTM coupling.

2.2 Hydro-Mechanical Model for Fractured Porous Rocks with Random Fracture Geometries

The model for the hydro-mechanical behavior of fractured porous rock is based on the use of Oda's crack tensor (Oda 1984, 1985; Oda et al. 1986) in the formulation of an equivalent anisotropic constitutive matrix and a stress-dependent permeability tensor for fractured porous rock masses. There are several distinct advantages of using an equivalent continuum formulation over methods such as the double porosity formulation. Realistic fracture patterns from geostatistical modeling are used in the equivalent continuum models. In the equivalent continuum technique, it is assumed that the size of a sampled volume exceeds a Representative Elementary Volume REV of the fractured rock mass. The REV of a fractured rock mass is defined as the smallest volume of the rock mass which is large enough relative to the characteristic scale of the fractures in the volume, but small relative to the characteristic scale of interest. The volume is homogeneously cut by fractures whose centers are randomly distributed. The fracture pattern is characterized by a probability density function (PDF). To obtain an equivalent continuum stress-strain or compliance relation for the fractured rock mass, the principle of superposition is used. The matrix stress-strain response and the fracture stress-displacement response are related by separate compliance matrices. The model for fracture behavior is based on the Barton-Bandis joint model (Bandis et al. 1993). Fracture permeability is modeled using the parallel plate model.

2.2.1 Permeability Tensor for Fractured Rocks

Several approaches are now available in modeling of the permeability of fractured rock masses. The three most common general classes of modeling techniques for fractured rock mass permeability are: (1) the Distinct Fracture Network (DFN) approach where individual fractures in a rock mass are modeled explicitly as distinct features assuming fluid flow in a fracture follows the parallel plate flow model (Gale 1982; Priest 1993; Ouenes and Hartley 2000; Min et al. 2004); (2) the dual-continuum model (DCM) which includes the double-porosity, dual-permeability and multiple interacting continua (MINC) models (e.g. Warren and Root 1963; Kazemi 1969; Narasimhan and Pruess 1988); and 3) the Equivalent Continuum Model (ECM) where the fractured rock mass anisotropic permeability tensor is obtained by averaging the permeability contributions from all the fractures over a Representative Element Volume (REV) of a rock mass (Long et al. 1982; Oda 1985; Neuman 1987; Lee et al. 1995). All three modeling techniques have found wide use in different applications and have been implemented in different computational models for fluid flow in fractured rock masses.

Due to its wide use, the project used the Equivalent Continuum Model for fractured rock mass permeability. The study used a particular technique in deriving fractured rock mass permeability which was developed by Oda (1985) based on the crack tensor (Oda, 1982). The symmetric crack tensor is generated based only on the geometrical properties of the fractures consisting of the fracture lengths, apertures and orientations. Using Darcy's law and parallel plate fracture flow law, a homogenized or averaged anisotropic permeability tensor for fractured rock masses is derived. The fabric tensor can be easily established from data on fracture geometry obtained from core samples or rock exposures. It has been shown that the first and second invariants of the crack tensor can be correlated to rock mass quality and rock mass anisotropy, respectively (Kulatilake et al. 1996). Also, the principal directions of the permeability tensor were shown to be coaxial with the principal directions of the crack tensor

(Oda 1985). Oda's permeability tensor has been widely adopted in different applications (e.g. Brown and Bruhn 1998; Dershowitz et al. 2000).

In the derivation of the equivalent permeability tensor for the fractured rock mass, it is assumed that the equivalent fractured rock permeability obeys Darcy's law. Also, to simplify the derivation and analysis, it is assumed that the rock matrix is impermeable, and permeability comes only from flow along the fracture system. However, the intact rock mass permeability, as in the case of porous and non-crystalline rocks, can be easily superimposed on the fracture network permeability. Based on the aforementioned assumptions, Oda (1985) developed the following analytical permeability tensor equation in two-dimensions:

$$k_{ij} = \lambda\left(1-\alpha\right)\left(P_{kk}\delta_{ij} - P_{ij}\right) \tag{2.19}$$

where $i, j = x, y$, P_{ij} = crack tensor, λ = connectivity fracture connectivity parameter, α = conversion coefficient, and δ_{ij} = Kronecker delta. The conversion coefficient α varies from zero to one, and prevents yielding a non-zero permeability when P_{ij} is close to zero. The summation form of the crack tensor P_{ij} is given as (Oda, 1982):

$$P_{ij} = \frac{1}{V}\sum_{k=1}^{m^{(v)}} Tr_k \left(t_k\right)^3 n_i n_j \tag{2.20}$$

where V = sample volume, $m^{(v)}$ = total number of fractures, T = thickness of the rock mass, r_k = trace length of the k^{th} fracture, t_k = aperture of the k^{th} fracture, and n_i and n_j = the direction cosines of the normal and tangent to the fracture orientation.

In this research, the connectivity parameter λ is assumed to be equal to a value of 1/12, which is derived from parallel plate law (Snow 1969) and implies full connectivity and continuous flow along the fracture network. Long et al. (1982) have studied the influence of λ on the equivalent permeability tensor of fractured rock masses. They have showed that the upper bound permeability of fractured rock masses is obtained when λ=1/12. However, they have also suggested that the typical value of λ should depend on the fracture geometry and may be different from 1/12.

Using Mohr's circle, the permeability components along the *x*, *y*, and *xy* directions are converted to the major and minor principal permeability values k_1 and k_3.

$$k_1,\ k_3 = \frac{k_{xx}+k_{yy}}{2} \pm \sqrt{\left(\frac{k_{xx}+k_{yy}}{2}\right)^2 + k_{xy}^2} \tag{2.21}$$

To provide a consistent assessment of the results, the permeabilities from the different cases will be compared with each other using the computed principal permeability values.

2.2.2 Elastic Compliance Tensor for Fractured Rocks

Since the 1950s, several numerical procedures have been developed for analyzing the mechanical behavior of fractured rock masses and the effect of different fracture patterns. The most rigorous approach for modeling the mechanical behavior of fractured rock masses is the Distinct Fracture Network (DFN) model. In this model, individual fractures in a rock mass are modeled explicitly as distinct features that deform in the normal and shear directions. This method can be used to precisely determine the explicit behavior of fractured rock masses. In many cases, however, considering all the individual fractures by the DFN model is

computationally impossible and practically unachievable due to the lack of reliable data on fracture distribution and pattern. Thus, this simulation technique is typically used only for defining the mechanical behavior of major faults and fractures as individual features (Guvanasen and Chan, 2000; Rots, 1991).

An alternative approach to modeling discontinuities as distinct features is to average the mechanical contributions from all the fractures to obtain an equivalent continuum representation of the stress-strain behavior of the fractured rock mass. Equivalent continuum models (ECM) assume that a sufficiently large Representative Element Volume (REV) exists, and that this REV contains "a sufficient number of representative fractures in a rock mass over which the fracture stress-strain behavior can be averaged." Since the initial concept of ECM was first developed by Eshelby (1957), many different numerical approaches that are based on ECMs have been introduced. The three most general ECMs for the mechanical analysis of fractured rock masses are the smeared crack model, multilaminate model, and anisotropic constitutive models. In the smeared crack model, fractures are considered to be mechanically initiated by applying the relation for orthotropic elasticity instead of the isotropic stress-strain relation (Borst et al. 2004; Rashid, 1968). In the multilaminate model developed by Zienkiewicz and Pande (1977), the fractured rock's mechanical behavior is measured along various planes that are randomly oriented. Although this model is useful for determining the effect of rotating the principal stress axes, the local stress calculation along the weak plane needs to be transformed along global axes in each time step. Thus, the method is generally adopted for relatively simple configurations of fracture orientation. In the anisotropic constitutive models, the strength and deformability of fractured rock masses are expressed as stiffness tensors. Cai and Horii (1992), Oda (1988), and Yoshida and Horii (1998) have proposed anisotropic constitutive models that can simulate the effects of fracture geometries using an elastic compliance tensor of fractured rock masses. All three modeling techniques have found wide use in different applications.

Despite its simplicity, there are two important issues that have not been completely addressed in the use of ECMs. These issues are related to: (1) the sensitivity of the equivalent continuum compliance of fractured rock mass to fracture geometry and distribution, and (2) the dependency of the compliance values on the length scale and the volume of the rock mass. The sensitivity of the calculated compliance values to fracture geometry is an important issue, since fracture geometry and distributions are inherently uncertain and statistical in nature. The expected length scale dependency of ECMs stems from their formulation, which assumes the existence of an REV. The REV of a fractured rock mass is qualitatively defined as the smallest volume of the rock mass that is large enough relative to the characteristic scale of the fractures in the volume. However, there is currently no rigorous quantitative criterion for establishing the REV of a rock mass given the fracture geometry.

Oda's compliance tensor formulation (1988) suggests a way to express the geometry of complicated fracture systems in tensorial form and to deal with any fractured rock mass as a mechanically equivalent continuum. To apply Oda's compliance tensor formulation for fractured rock mass as an equivalent continuum, the following assumptions are made: (1) The position of a fracture corresponds to its centroid, and the centroids are evenly distributed in the entire rock sample (i.e., fracture locations are assumed to follow a Poisson distribution). (2) The fracture is assumed to have a planar shape. Thus, the surface area of a fracture and volume of fractured rock under plane strain conditions can be converted to length of fracture and cross sectional area of rock outcrop, respectively, due to the unity width of the sampling area. (3) The mechanical behavior of fractures is assumed to be elastic. Therefore, it is commonly assumed that a fracture

plane can be replaced by an elastically equivalent set of parallel plates connected by two elastic springs for normal and shear directions. The formulations of the stiffness of the two springs are discussed below.

On the basis of these assumptions, Oda (1988) has suggested the following equivalent continuum compliance tensor equation for fractured rock masses:

$$S_{ijkl}^{f} = \left(\frac{1}{k_n} - \frac{1}{k_s} \right) F_{ijkl} + \frac{1}{4k_s} \left(\delta_{ik} F_{jl} + \delta_{jk} F_{il} + \delta_{il} F_{jk} + \delta_{jl} F_{ik} \right) \tag{2.22}$$

where S_{ijkl}^{f} = compliance tensor of fractures; k_n and k_s = fracture normal and shear stiffnesses, respectively; δ_{ij} = Kronecker delta; and F_{ij} and F_{ijkl} = second- and fourth-rank crack tensors, respectively. The summation forms of the crack tensors F_{ij} and F_{ijkl} in Eq. (1) are given by Oda (1982) as:

$$F_{ij} = \frac{1}{V} \sum_{k=1}^{m(v)} A^{(k)} r^{(k)} n_i^{(k)} n_j^{(k)} \tag{2.23}$$

$$F_{ijkl} = \frac{1}{V} \sum_{k=1}^{m(v)} A^{(k)} r^{(k)} n_i^{(k)} n_j^{(k)} n_k^{(k)} n_l^{(k)} \tag{2.24}$$

with $i, j, k, l = 1, 2$; V = sample volume; $m(v)$ = total number of fractures; $A^{(k)}$ = surface area of the k-th fracture; $r^{(k)}$ = trace length of the k-th fracture; and $n_i^{(k)}$ = the direction cosines of the normal and tangent to the k-th fracture orientation.

The following empirical correlation developed by Barton and Choubey (1977) for the fracture shear stiffness is used in Eq. (1):

$$k_s = 100 \sigma_n \tan \left\{ JRC \log_{10} \left(\frac{JCS}{\sigma_n} \right) + \phi_r \right\} \tag{2.25}$$

where σ_n = normal stress on the fracture surface; JRC = joint roughness coefficient; JCS = joint compressive strength; and ϕ_r = residual friction angle. The estimated stiffness value is converted to the shear fracture stiffness parameter k_s by multiplying it with the length of fracture, following Oda et al. (1993). It should be noted that the converted fracture stiffness parameter has the units of force/length and is independent of the fracture length. Thus, the value can be substituted in Eq. (1) with non-dimensional crack tensors regardless of the effect of fracture length.

Fracture normal stiffness is assumed to be a constant ratio of the shear stiffness (1981):

$$k_n = R \cdot k_s \tag{2.26}$$

where R = stiffness ratio between normal and shear fracture stiffnesses. Bandis et al. (1981) have reported that the experimentally determined stiffness ratio R is a function of the normal stress on the fracture surface. According to their experimental results, the ratio decreases exponentially when the normal stress increases, and converges approximately to R =1.0 under extremely high normal stress. Although further research is required to estimate a reasonable magnitude of R for a wide normal stress variation, this research assumes that the normal stress is relatively high and that the stiffness ratio has a stable value of 10.

2.2.3 Elasto-plastic Model for Fractured Rocks

To account for nonlinear fracture behavior and fracture failure in the fractured rock mass behavior, the elastic model described is extended. This section demonstrates the calculation of

perfectly plastic fracture stress-strain relationship based on the Mohr-Coulomb failure criteria. Due to the weakness, the failure is assumed to occur only via fracture planes. To define the failure along the fracture plane, the global stresses must be converted to the local stresses along the fracture plane. To measure the oriented stress state, the following equations are applied with the fracture orientation.

$$\sigma_n = \sigma_x \sin^2\alpha - 2\tau_{xy}\sin\alpha\cdot\cos\alpha + \sigma_y\cos^2\alpha \tag{2.27}$$

$$\tau = -(\sigma_x - \sigma_y)\sin\alpha\cdot\cos\alpha + \tau_{xy}(\cos^2\alpha - \sin^2\alpha) \tag{2.28}$$

where the superscript *f* indicates the fracture, τ and σ_n are the shear and normal stress along the fracture plane respectively, and α is the fracture orientation, measured counterclockwise from the global *x*-axis.

The local stresses in Eqs. (2.27) and (2.28) are implemented into the failure criteria of the fracture plane as shown in Eq. (2.29). Fig. 2.2 illustrates the fracture failure criterion given as

$$f(\sigma_n, \tau) = \tau - \sigma_n \cdot \tan\phi - c \tag{2.29}$$

where c and ϕ are the cohesion and friction angle, respectively, of the fracture.

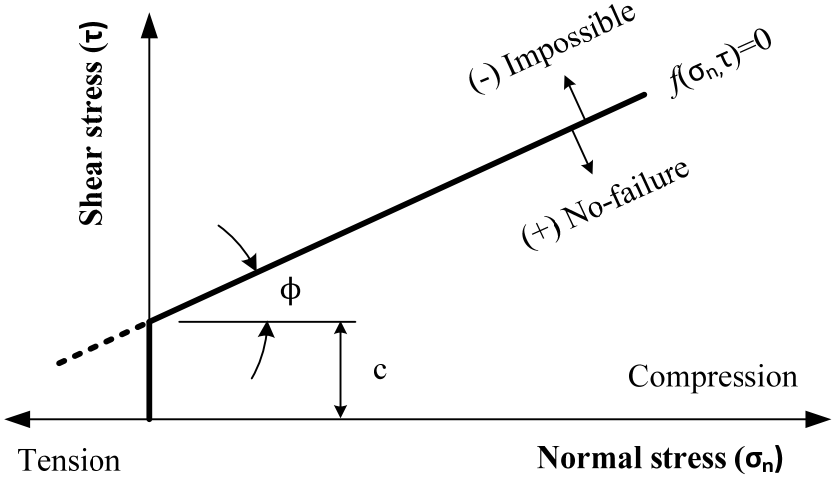

Fig. 2.2 – Mohr-Coulomb failure criterion of intact rock mass

The plastic potential function for the fracture plane follows a non-associated flow rule with the dilation angle different from the friction angle.

$$g(\sigma_n, \tau) = \tau - \sigma_n \cdot \tan\psi \tag{2.30}$$

where ψ is the dilation angle of fracture. Due to the fact that the analysis is applied for in-depth geologic formations, tensile failure of the rock mass and the fracture sets is not of concerned.

First, the plastic strain increment has the form as in Eq. (2.31).

$$\Delta e_i^p = \lambda \frac{\partial g}{\partial \sigma_i} \tag{2.31}$$

with i=1, 2, and 3; where λ is the plastic multiplier for shear failure that can be determined from the consistency condition. In terms of principal stresses, Eq. (2.31) can be written as:

$$\Delta e_1^p = \lambda \frac{\partial g}{\partial \sigma_1} = 0,\ \Delta e_2^p = \lambda \frac{\partial g}{\partial \sigma_2} = -\lambda \tan\psi$$
$$\Delta e_3^p = \lambda \frac{\partial g}{\partial \sigma_3} = 0,\ \Delta \gamma^p = \lambda \frac{\partial g}{\partial \tau} = -\lambda \tag{2.32}$$

where α is the orientation of a fracture set. Substituting Eq. (2.32) to elastic stress-strain relationship makes expanded equation for principal stress increments.

$$\begin{aligned}
\Delta\sigma_1 &= S_{11}\Delta\varepsilon_1 + S_{12}\Delta\varepsilon_2 + S_{13}\Delta\varepsilon_3 + S_{14}\Delta\gamma - S_{12}\lambda\tan\psi - S_{14}\lambda \\
\Delta\sigma_2 &= S_{21}\Delta\varepsilon_1 + S_{22}\Delta\varepsilon_2 + S_{23}\Delta\varepsilon_3 + S_{24}\Delta\gamma - S_{22}\lambda\tan\psi - S_{24}\lambda \\
\Delta\sigma_3 &= S_{31}\Delta\varepsilon_1 + S_{32}\Delta\varepsilon_2 + S_{33}\Delta\varepsilon_3 + S_{34}\Delta\gamma - S_{32}\lambda\tan\psi - S_{34}\lambda \\
\Delta\tau_{12} &= S_{41}\Delta\varepsilon_1 + S_{42}\Delta\varepsilon_2 + S_{43}\Delta\varepsilon_3 + S_{44}\Delta\gamma - S_{42}\lambda\tan\psi - S_{44}\lambda
\end{aligned} \tag{2.33}$$

The new and old stresses are represented by the superscripts *N* and *O*, respectively, thus:

$$\sigma_i^N = \sigma_i^O + \Delta\sigma_i \tag{2.34}$$

with i = 1, 2, and 3. Substituting Eq. (2.33) into Eq. (2.34) yields:

$$\begin{aligned}
\sigma_1^N &= \sigma_1^I - S_{12}\lambda\tan\psi - S_{14}\lambda \\
\sigma_2^N &= \sigma_2^I - S_{22}\lambda\tan\psi - S_{24}\lambda \\
\sigma_3^N &= \sigma_3^I - S_{32}\lambda\tan\psi - S_{34}\lambda \\
\tau_{12}^N &= \tau_{12}^I - S_{42}\lambda\tan\psi - S_{44}\lambda
\end{aligned} \tag{2.35}$$

where σ^I is the elastic guess which contains the old stress and elastic stress increments. The elastic guesses along the principal directions are presented by:

$$\begin{aligned}
\sigma_1^I &= \sigma_1^O + S_{11}\Delta\varepsilon_1 + S_{12}\Delta\varepsilon_2 + S_{13}\Delta\varepsilon_3 + S_{14}\Delta\gamma \\
\sigma_2^I &= \sigma_2^O + S_{21}\Delta\varepsilon_1 + S_{22}\Delta\varepsilon_2 + S_{23}\Delta\varepsilon_3 + S_{24}\Delta\gamma \\
\sigma_3^I &= \sigma_3^O + S_{31}\Delta\varepsilon_1 + S_{32}\Delta\varepsilon_2 + S_{33}\Delta\varepsilon_3 + S_{34}\Delta\gamma \\
\tau_{12}^I &= \tau_{12}^O + S_{41}\Delta\varepsilon_1 + S_{42}\Delta\varepsilon_2 + S_{43}\Delta\varepsilon_3 + S_{44}\Delta\gamma
\end{aligned} \tag{2.36}$$

Finally, substituting Eq. (2.18) into the failure function Eq. (2.11), and setting the value of the function zero. yield the following value of the plastic multiplier:

$$\lambda = \frac{f^{shear}\left(\sigma_2^I, \tau_{12}^I\right)}{(S_{42} - S_{22}\tan\phi)\tan\psi + S_{44} - S_{24}\tan\phi} \tag{2.37}$$

Using the old stress components and the stress increments computed with Oda's compliance tensor discussed in Section 3.2.2 above, an elastic guess can be assumed in the first step. The elastic guess for each loading stage will be adopted in the new stress calculations, and in the failure function. When the stress state violates the yielding function of fracture set, a plastic correction will be applied to the original elastic guess, and the new corrected stresses are then generated.

2.2.4 Fracture Probability Distribution Functions (*PDFs*)

As can be seen from Eqs. (2.20), (2.23) and (2.24), the main parameters required to derive the permeability and elastic compliance tensors are the fracture lengths, apertures and orientations. Fracture locations, although not directly can also affect rock mass permeability and deformability depending on the fracture locations relative to the sampling volume. Due to the

complexity and variability of natural fracture systems, there have been numerous studies analyzing and categorizing fracture field data, and different PDFs have been used to define the statistical distribution of fractures. Table 2.1 lists the most common PDFs that have been used to characterize the statistical variations of the length, aperture, orientation and location of fractures. The table also lists authors who have used and studied and applicability of the different PDFs for characterizing fracture distributions. The most widely used PDFs are normal, lognormal, exponential, power law, Fisher and Poisson.

Table 2.1 - Suitability and use of different PDFs to characterize the statistical variation of fracture geometrical parameters. ✓ = applicable, × = not applicable.

PDFs	Length	Aperture	Orientation	Location
Normal distribution	×	×	✓ (Long et al. 1982)	×
Lognormal distribution	✓ (Baecher and Lanney 1978; Long et al. 1982; Dershowitz and Einstein 1988)	✓ (Long et al. 1982; Dershowitz and Einstein 1988)	×	×
Exponential distribution	✓ (Baecher et al. 1977; Long et al. 1982; Dershowitz and Einstein 1988)	✓ (Dershowitz and Einstein 1988)	×	×
Power law distribution	✓ (Heffer and Bevan 1990; Bonnet et al. 2001; Park et al. 2001; De Dreuzy et al. 2002)	✓ (Barton and Zoback 1990; Bonnet et al. 2001; Gale 2004)	×	×
Fisher distribution	×	×	✓ (Fisher 1953; Priest 1993)	×
Poisson distribution	×	×	×	✓ (Long et al. 1982; Priest 1993; Min et al. 2004)

Table 2.1 is also helpful in understanding the statistical characteristics of each of the geometrical parameters. Table 2.1 suggests that fracture length and aperture are correlated because the same PDFs can be used to describe their distributions. In comparison, fracture orientation and location are independent of the other parameters. The PDFs for fracture length and aperture have their peak points at the relatively low values. This tendency reflects the characteristics of natural fracture distributions which has numerous small fractures and but much fewer major fractures. As a result, both fracture length and aperture can only be realistically represented by lognormal, exponential and power law. In comparison, fracture orientation is typically clustered around distinct directions and can be adequately represented by a normal distribution. Fracture locations in a single lithology and unconstrained rock layers appear to be completely random and can be described by a Poisson's distribution. Since various PDFs are

used to fit the distributions of the parameters listed in Table 2.1, adopting all the PDFs in a parametric study would result in an unrealistically huge number of realizations and analyses. Thus, only the most appropriate and widely used PDFS are selected for each of the parameters listed in Table 2.1.

For fracture length and aperture, the power law (PL) distribution is used because a large number of studies have supported the validity of this PDF. Field data on which this PDF is based cover a wide range of length scales, from mm to km, and various rock types, from igneous rocks to sedimentary rocks. Furthermore, a PL distribution implies self-similarity or fractal behavior that has been confirmed by physics-based models of fracturing in a wide range of materials. Several researchers, based on extensive studies, have confirmed that fracture lengths in different rock types follow a PL distribution (e.g. Heffer and Bevan 1990; Bonnet et al. 2001; Park et al. 2001; De Dreuzy et al. 2002). In this paper, the following truncated form of the PL distribution, as proposed by Min et al. (2004) is used:

$$r = \left\{ cut_{\min}^{-D} - F\left(cut_{\min}^{-D} - cut_{\max}^{-D} \right) \right\}^{-\frac{1}{D}} \tag{2.38}$$

where r = trace length of fracture, D = fractal dimension, cut = the minimum and maximum fracture lengths, and F = random number between 0 and 1.

Similar to fracture length, Barton and Zoback (1990), and Gale (2004) also found that PL distribution may be used to define the fracture aperture distribution. However, in the fracture geometry realization using MCS, separate and independent fracture length and aperture data generation may yield unrealistic results due to the correlation between these two fracture parameters. In general, field data indicate that fracture aperture increases with fracture length. Thus, to produce geologically realistic data, the aperture distribution is produced using a correlation function based on the fracture length distribution. Bonnet (2001) suggested the following correlation function between fracture aperture t and trace length r

$$t = \delta \cdot r^{n} \tag{2.39}$$

where δ = scale factor, and n = exponent of the correlation.

Fracture orientation data are represented by Fisher distribution, which is the most widely used PDF to quantify the orientation of fractures. The validity of using the Fisher PDF to represent fracture orientation has been demonstrated by Fisher (1953) and Priest (1993). The following inverse cumulative form of the Fisher distribution from Priest (1993) is used in the modeling:

$$\theta = \cos^{-1}\left[\frac{\ln\left\{ e^{K} - F\left(e^{K} - e^{-K} \right) \right\}}{K} \right] \tag{2.40}$$

where K = Fisher coefficient, and F = random number between 0 and 1.

Finally, the Poisson distribution is utilized to characterize the fracture locations in the realization of fracture geometry. The suitability of the Poisson PDF for characterizing fracture locations has been supported by Min et al. (2004), and Priest (1993). The Poisson distribution is used to stochastically generate the center points of the fractures. In some cases, some fractures can extend over the sample realization boundary, and the protruding parts of fractures lying outside of the sampling area are truncated and not included in the permeability calculations. However, based on an extensive study, fracture truncation does not significantly affect the calculations of the rock mass permeability.

Finally, as mentioned above, the Poisson distribution is employed to yield the fracture locations for the realization of fracture geometry. Fractures are located independently based on a uniform distribution. The validity of the Poisson distribution for characterizing fracture locations has been supported by Dershowitz and Einstein (1988), Min et al. (2004), and Priest (1993).

2.3 Stochastic Modeling

To recapitulate, the probabilistic coupled hydro-mechanical modeling used: 1) geostastical techniques to generate fracture patterns and fracture properties, and 2) the Monte-Carlo method to simulate the effects of stochastic fracture distributions, and geomechanical and fluid flow properties on the flow, transport, storage and leakage of CO_2 in geologic formations. A computer program transforms the fracture geometries from geostatistical data in combination with fracture hydro-mechanical properties to generate the equivalent continuum anisotropic constitutive and stress-dependent permeability matrices using Oda's crack tensor. The Monte Carlo method is used to simulate stochastic CO_2 flow, transport and storage and potential leakage in fractured geologic formations. Monte Carlo methods are a class of computational algorithms that rely on repeated random sampling to compute their results. Monte Carlo simulation methods are especially useful in studying systems with a large number of coupled degrees of freedom such as those encountered in CO_2 GS where there are significant uncertainties in input data. The steps involved in Monte Carlo simulations include: 1) Definition of the range of possible inputs; 2) Generate inputs randomly from the range; 3) Repeated deterministic computations using the inputs; and 4) Aggregation of the results of the individual computations into the final result. The Monte Carlo simulations will be used to: 1) investigate the effects of uncertainties in input data on predicted response of CO_2 GS through uncertainty propagation, 2) obtain probabilistic estimates of volumes of stored CO_2; and 3) calculate the risk of potential leakage of CO_2 to the atmosphere or to water aquifers through fractures in cap rocks. The Monte Carlo method requires definitions of uncertainties and distributions of model parameters, efficient producers to carry out the repeated simulations, and techniques to aggregate the results of multiple simulations.

2.3.1 Fracture Geometry Realization Using MCS

Rock fracture systems vary naturally and their characteristics are inherently stochastic. To ensure that the results from the study are valid not just for specific fracture patterns, a large number of simulations that cover a wide spectrum of fracture geometries and distributions are needed. Monte Carlo Simulation (MCS) is a general and straightforward technique to perform stochastic analysis by repeating the stochastic process a sufficient number of times with randomized input. This randomized input describes the variability of the input parameters. The random variables are represented as PDFs while deterministic variables are represented as constants. Two requirements are needed in order to perform the MCS: 1) a large number of simulations in order to provide a reliable conclusion; and 2) random number input which requires methods to generate random numbers or random fields. In this study, MCS is used to generate fracture patterns using the PDFs described above for the fractures parameters. Once a series of random numbers, varying from 0 to 1, is applied as F in the inverse cumulative PDFs, then random geometry distributions which follow the each PDFs is generated. Each fracture patterns or realizations are then used to calculate the equivalent continuum permeability tensor and the equivalent continuum compliance tensor using Oda's formulations.

2.3.2 Stochastic Multiphase Fluid Flow Modeling

Stochastic Modeling - A stochastic system refers to a system whose behavior is intrinsically non-deterministic, in a way that the system's subsequent state is determined by both the system's predictable actions and by random elements. In order to understand this kind of system, one needs to perform stochastic analysis, that are related to a process involving a randomly determined sequence of observations, each of which is considered as a sample of one element from a probability distribution. Monte Carlo simulation is a general and straightforward technique to perform stochastic analysis by repeating the stochastic process for a sufficient number of times with randomized input. This randomized input may follow a specific probabilistic distribution (or probability density function), which is a function that describes the probability of a random variable to take certain values. A large number of experiments based on field data were conducted to address the distribution of certain rock formation material properties. The related literature show that the probability density function for the absolute permeability k is log-normal (Law, 1944; Bulnes, 1946; Warren *et al.*, 1961), or in other words the log value of k is normally distributed. Freeze (1975) observed that porosity ϕ is normally distributed. There are two kinds of analysis when it comes to stochastic analysis on formation properties. One is single random variable approach, and the other is an approach that considers the spatial dependence among the properties at each location. Both of the approaches are aided by Monte Carlo Simulation (MCS).

Monte Carlo Simulation (MCS) - Monte Carlo Simulation is a procedure that simulates the stochastic process with randomized input parameters repeatedly. The Monte Carlo Simulation method is especially suitable for cases where there are many independent variables or strongly non-linear systems. For the non-linear system in this paper, MCS uses the same analysis method as conventional analysis does but iterates on each analysis many times. The random variables are represented as probability density functions (PDFs), while deterministic variables are represented as constants. Using a random number/field generator, MCS selects the value(s) of each random parameter(s) from the PDFs and perform the analysis. For instance, in the case of single random variable approach, the stochastic parameter is selected randomly from a given distribution during each realization. The selected parameter is constant over the whole domain. There requirements are to be needed in order to perform the MCS: 1) The MCS requires a large number of simulations in order to provide a reliable conclusion and hence computer program is essential; 2) The MCS relies on random numbers input, and thus requires methods to generate random numbers or random fields.

Spatial Variability of Geological Formations - The geological properties (porosity, permeability, grain density, etc.) of the formations almost always vary from point to point. Oftentimes this variability is ignored by using average material properties to model an entire formation domain of interest. In a more realistic case, the formation properties have random values from point to point, but with spatial dependence. In other words, the formation properties that are within close enough distance are not independent, moreover they are correlated. The spatial variability is a major source of the uncertainty in the risk assessment analysis and therefore needed to be accounted for. A statistical model called random field is used to describe the spatial variability of the geological formation and is discussed in the following section. There is a convenient method to measure the variability of the random field by introducing the parameter correlation length (scale of fluctuation) ρ , which measures the distance within which the formation properties show strong correlation. That is, two points separated by a distance

larger than ρ will be uncorrelated. The correlation length ρ can be mathematically defined as the area under the correlation function (Vanmarcke, 1983) as follows:

$$\rho = \int_{-\infty}^{\infty} \rho_k(\tau) d\tau = 2\int_{0}^{\infty} \rho_k(\tau) d\tau \tag{2.41}$$

Engineers are more interested in the correlation coefficient of the parameters from two different locations of the domain. Therefore in this study, the correlation coefficient between the material properties in two locations can be calculated using the following equation, which was obtained after conducting a field experiment at Borden research site (Sudicky, 1986).

$$\rho_k(\tau) = \exp(-\tau / \rho) \tag{2.42}$$

In the equation, τ is the absolute distance between two points, and ρ is the correlation length, which can be estimated for different formation properties though the analysis of spatial field experiment data. Eq. (2.42) indicates that the degree of correlation of two points is decaying exponentially as the distance between the two points increases. The vertical and horizontal correlation lengths should be analyzed when accounting for spatial variability. Correlation lengths are typically larger in the horizontal directions as compared to the vertical direction as a result of layering caused by geologic processes. For example, material properties are likely to be similar within a particular soil deposit at the same elevation over considerably distances. Whereas, the material properties at different elevations within a soil deposit will likely vary over shorter distances. Appropriate ρ values should be chosen to represent material variability in the vertical or horizontal directions.

Random Field Theory and 1-D Random Field Generation - As discussed before, the spatial variability of the geological formation can be represented by a statistical mathematical model called random field. A complete probabilistic description of this random field would be the infinite dimensional probability density function (PDF):

$$f_{x_1, x_2 \ldots}(x_1, x_2 \ldots) \tag{2.43}$$

Equation (2.43) is difficult to use in practice not only in the aspect of mathematical computational work but also in the aspect of real data estimation work as it is almost impossible to obtain infinite field data . Therefore, a simpler model under an appropriate assumption is needed. According to Griffiths and Fenton (2007), a simple assumption to describe the random field of the formation parameters with spatial dependence is that the random field is Guassian and stationary. Guassian means the joint PDF is a multivariate normally distributed random process, while stationary means that the joint PDF is independent of spatial position, and it depends just on relative positions of the points.

Under the above assumption, there are three things needed in order to "characterize the fields: 1) The field mean μ_x, 2) The field variance: σ_x^2, and 3) How rapidly the field varies in space" (Griffiths and Fenton, 2007), which is characterized by the second moment of the field's joint distribution. There are three functions that can be used to obtain the field's joint distribution: the covariance function; the spectral density function; or the variance function. These functions are used to obtain the correlation coefficient between every two locations and construct the correlation matrix for the random field that represents the spatially correlated material properties of the formation. The correlation length (ρ) of the material properties is also needed to construct the correlation matrix. More details are discussed in the book of Griffiths and Fenton (2007).

The generation of random parameter fields has been achieved in the past using several kinds of techniques. A number of the random field generators use the algorithms that are provided by the following common methods: 1) The Turning Bands Method (Mantoglou and Wilson, 1982; Cassiani and Christakos, 1998), 2) The Nearest Neighbor Method (Smith and Schwartz, 1980), 3) The Discrete Fourier Transform (DFT) Method (Robin *et al.*, 1993), 4) The Fast Fourier Transform (FFT) Method (Cooley and Tukey, 1965), and 5) The Local Average Subdivision (LAS) Method (Fenton and Vanmarcke,1990).

The turning bands method and the FFT method are the most commonly used methods. The nearest neighbor method is relatively easier to implement than other methods. The DFT method does not display any artificial distortions in the generated fields, but requires the first two moments of the target random field and tends to be computationally slow. The LAS method produces a field of local average cells whose statistics are consistent with the field resolutions, but is probably the most difficult to implement. In this paper, the random fields are generated using the open sourced FORTRAN subroutines based on LAS method (Fenton and Vanmarcke,1990; Griffiths and Fenton, 2007).

Previous research results in the literature (Essaid and Hess, 1993; Kaluarachchi and Abdin, 1995; Zhu and Sykes, 2000) indicate that the stochastic values of the parameters of Van Genuchten (1980) saturation vs. capillary function has some effect on the two-phase flow predicting than the other flow parameters. Therefore in this study, the influence of the shape of capillary pressure - water (gas) saturation was investigated. The major stochastic parameters will be the absolute permeability k , the formation porosity ϕ , the Van Genuchten parameters α and n .

In the paper of Essaid and Hess (1993), the Van Genuchten parameters α and n are under a proper assumption that they are related to permeability k . In each realization, the random absolute permeability field will be generated using the 1-D random field generator which uses the LAS method. The Van Genuchten parameters α and n will then be calculated using Eqs. (2.26) to (2.28) below:

$$\alpha_i = \bar{\alpha}\left[\frac{\ln(\bar{k})}{\ln(k_i)}\right]^3 \tag{2.44}$$

$$n_i = \bar{n}\left[\frac{\ln(k_i)}{\ln(\bar{k})}\right], \text{ for } \ln(k_i) \le \ln(\bar{k}) \tag{2.45}$$

$$n_i = \bar{n}, \qquad \text{for } \ln(k_i) > \ln(\bar{k}) \tag{2.46}$$

where $\bar{\alpha}$, $\bar{n}$ and $\bar{k}$ are the mean values for their corresponding distributions, and the α_i , n_i and k_i are the values for each block. Therefore in order to obtain the spatial variables of α_i and n_i , one needs to consider the spatial variability of absolute permeability. In this study, because the rock deformation is not calculated, the compressibility index would be considered deterministic.
Among the four stochastic parameters in the simulation, some of them maybe cross- correlated, meaning that between two random fields or two set of random values of the parameter, there are dependence. Several measures including Rank correlation (Kendall, 1948), Pearson product - moment correlation coefficient (Rodgers and Nicewander, 1988), Distance correlation (Székely *et al.*, 2007) and Brownian covariance (Székely and Rizzo, 2009) can be employed to define the dependence structure between two sets of random variables. The most familiar one is the Pearson product - moment correlation coefficient, which can be calculated using the following equation:

$$\rho_{X,Y} = \mathrm{corr}(X,Y) = \frac{\mathrm{COV}(X,Y)}{\sigma_X \cdot \sigma_Y} = \frac{E\left[\left(X-\mu_X\right)\left(Y-\mu_Y\right)\right]}{\sigma_X \cdot \sigma_Y} \tag{2.47}$$

where E is the expected value operator; COV is the coefficient of variance (X and Y are two set of random variables; μ_X and μ_Y are expected values; σ_X and σ_Y are standard deviations. In this paper, the porosity and absolute permeability are under two assumptions of cross-correlations with correlation coefficients of 0.0 and 1.0. In the case of correlation coefficient equals 0.0, the two set of random values of these parameters are actually not correlated.

Random Field Generation using HYDRO_GEN - The basic approach of HYDRO_GEN is based on the theory of space random functions which is used to handle spatial variability (Vanmarcke, 1983; Bras and Rodriguez-Iturbe, 1985; Dagan, 1989; Gelhar, 1993). This theory states that the spatially distributed attributes of a random field can be expressed by a Space Random Function (SRF), and are characterized through its spatial moments. When the SRF is correlated in space or over time, it should be defined by its multivariate distribution, and thereafter a complete representation of the random field is established. The SRF approach allows a simple treatment of the complicated phenomena of spatial variability and provides a quantitative evaluation on the effects of un-modeled heterogeneity and data uncertainty. Therefore this approach is appealing and usually coupled with Monte Carlo Simulation (MCS).

Consider a spatially distributed physical parameter $z(x)$ with x denoting the spatial coordinate. Assume the Space Random Function that models the spatial structure of $z(x)$ is $Z(x)$, which can be characterized statistically by its second moment, also known as the covariance function in Gaussian or log-Gaussian fields. In such fields, the expected value $E[Z(x)]$ is the mean value of Z at position x, $\mu(x)$:

$$E\left[Z(x)\right] = \mu(x) \tag{2.48}$$

and hence the spatial covariance between two coordinates x and x' is:

$$C_Z(x,x') = E\left[\left(Z(x)-\mu(x)\right)\left(Z(x')-\mu(x')\right)\right] = C_Z(r = x - x') \tag{2.49}$$

in which r is the distance between the two positions. For random fields like Gaussian or log-Gaussian, their distribution can be defined entirely by Eqs. (2.48) and (2.49). This study focuses on only Gaussian random fields, but for fields with spatial attribute following other than Gaussian or log-Gaussian, they can be transformed into such ones by using the methods discussed by Journel and Alabert (1989).

It should be noted that when $x = x'$, Eq. (2.39) becomes:

$$C_Z(x,x') = E\left[\left(Z(x)-\mu(x)\right)^2\right] = \sigma(x)^2 \tag{2.40}$$

with $\sigma(x)$ denoting the standard deviation and $\sigma(x)^2$ the variance. This indicates that the variance should be finite to ensure it is well defined. In cases of infinite variance, the space random function $Z(x)$ cannot be defined using the method of covariance function. Alternatively, a random field with infinite variance can be defined by its spatial structure of increments $Z'(x) = Z(x) - \mu(x)$, which is defined by a stationary mean:

$$E\left[Z(x)-\mu(x)\right] = 0 \tag{2.41}$$

and the semivariogram:

$$r(x,x') = \frac{1}{2}E\left[\left(Z'(x)-Z'(x')\right)^2\right] \tag{2.42}$$

The fields defined by Eqs. (2.48) and (2.49) usually have heterogeneity that is characterized by a finite integral scale. The semivariogram in Eq. (2.42) is used to characterize variability when the

scale of variability is evolving in an infinite sequence, and this type of variability represents self-similar or fractal fields.

The technique of HYDRO_GEN is based on the theory discussed above and the sufficiency of a small neighborhood results from the screening effect of measurement. The algorithm starts by choosing a starting point x_0, followed by generation of a realization of $z(x_0)$ using a standard random generator with the unconditional mean values $\mu(x)$ and variance $\sigma(x)^2$ considered as targeted statistics. $z(x_0)$ will be considered as a base datum and utilized to condition the nodal z values inside the search neighborhood of x_0. The procedure discussed above will be applied to every position/node in the computing geometry. The conditioning procedure follows the procedure developed by Mood *et al.* (1963). Details of the algorithm of HYDRO_GEN can be found in the paper written by Bellin and Rubin (1996).

2.4 Test and Validation of Models

The models developed in the project were tested and validated against theoretical predictions, prototype studies and actual field case histories of actual CO_2 GS projects. Theoretical predictions from poroelasticity including the so-called Mandel-Cryer and Nordbergum effects provide the bases for checking the correctness of the procedure to couple fluid flow and geomechanics. There are now several large-scale field tests of CO_2 GS in different parts of the world. The project used the Sleipner CO_2 Sequestration Project in Norway, and the In Salah fi CO2 Storage Project in Algeria. These projects were previously analyzed using coupled two-phase fluid flow and geomechanics models by Pruess et al. (2002), and Preisig and Prevost (2011), respectively. The coupled model developed in this project is used to predict the movement of CO_2 in the field, and the predictions are compared with other coupled modeling studies that have been previously carried out by other researchers.

3. RESULTS AND DISCUSSIONS

3.1 Fractured rock mass permeability

Oda's permeability tensor described in Section (2.2) and the MCS procedure described in Section (2.3.1) are to generate the fracture geometries and properties were programmed in Matlab. Random fracture geometries were generated by the prescribed PDFs for each fracture parameter. To obtain geologically realistic fracture distributions and geometries, data from various field studies were used to generate the required length data based on the truncated power law distribution. All data sets were based on the summary of 22 field data collected by Bonnet et al. (2001). The required data sets for the simulations consist of the number of fractures, the maximum and minimum fracture lengths, cumulative function exponent, and the total area of the sampling field. These parameters are listed in Table 3.1.

After the center point of each fracture is positioned following the Poisson distribution, stochastically generated fracture lengths and orientations are generated to yield the random fracture geometry. Fig. 3.1 shows examples of four fractured rock mass realizations using four of the different field data given in Table 3.1. Fracture apertures are calculated using the correlation given in Eq. (2.39).

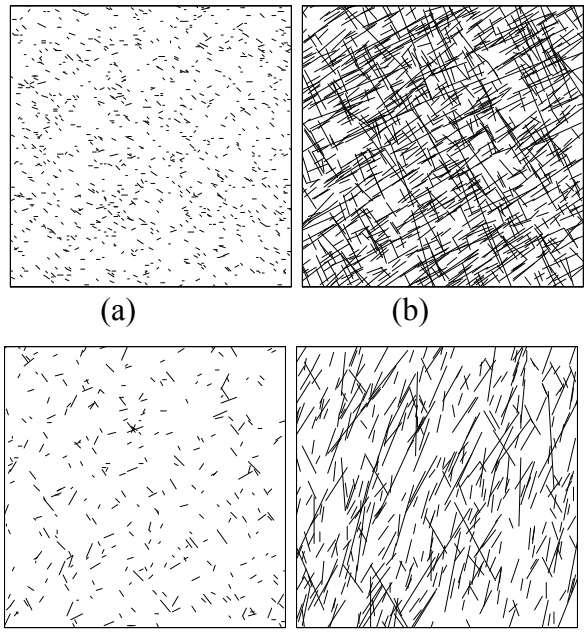

Fig. 3.1 - Fractured rock mass realizations based on field data from: (a) Ackermann and Schlische (1997), (b) Clark et al. (1999), (c) Gauthier and Lake (1993), and (d) Yielding et al. (1996).

Different fracture geometry realizations were stochastically generated to obtain the full distribution of the calculated permeability. Before studying the effects of the different random parameters, an analysis was first performed to determine the adequate number of Monte Carlo simulations needed to obtain a stable distribution of the permeability. To quantify the stability of

the calculated permeability values as function of number of realizations, the Relative Error *RE* defined below is used:

$$RE = 100 \cdot \sqrt{\left\{k_i^{(N)} - k_i^{REP}\right\}^2} \Big/ \sqrt{\left\{k_i^{REP}\right\}^2} \tag{3.1}$$

with i = 1, 3 and where $k_i^{(N)}$ = mean principal permeability from N realizations and k_i^{REP} = mean principal permeability from 10,000 realizations, which is a sufficiently stable permeability value.

Table 3.1 - Compilation of Power Law Exponents for Fracture Length Distributions (Bonnet et al. 2001).

Reference	$N_{Fracture}$	Length range, m	Exponent (D)	Area, m^2
Ackermann and Schlische (1997)	873	$4 \cdot 10^{-2}$-$15 \cdot 10^{-2}$	1.64	34
Krantz (1988)	50	150-1500	0.67	$29 \cdot 10^6$
Kakimi (1980)	180	1000-7000	0.97	$280 \cdot 10^6$
Scott and Castellanos (1984)	400	300-2000	1.21	$120 \cdot 10^6$
Blackstone (1988)	250	$10 \cdot 10^{-3}$-$60 \cdot 10^{-3}$	1.11	$250 \cdot 10^9$
Stewart (1980)	400	$15 \cdot 10^{-3}$-$50 \cdot 10^{-3}$	1.84	$290 \cdot 10^9$
Cladouhos and Marrett (1996)	70	$7 \cdot 10^{-3}$-$25 \cdot 10^{-3}$	1.67	$3600 \cdot 10^6$
	150	$7 \cdot 10^{-3}$-$25 \cdot 10^{-3}$	1.66	$5100 \cdot 10^6$
	200	$7 \cdot 10^{-3}$-$25 \cdot 10^{-3}$	2.07	$6200 \cdot 10^6$
Clark et al. (1999)	1034	360-4500	1.51	$87 \cdot 10^6$
Fossen and Hesthammer (1997)	40	1-20	0.60	$2 \cdot 10^4$
Gauthier and Lake (1993)	318	150-800	1.42	$169 \cdot 10^6$
	291	150-800	1.69	$169 \cdot 10^6$
	78	100-700	1.10	$169 \cdot 10^6$
Knott et al. (1996)	218	0.31-0.93	1.02	1
Odling et al. (1999)	470	2-20	0.80	$11.7 \cdot 10^3$
Pickering et al. (1997)	417	200-1000	1.18	$60 \cdot 10^6$
Schlische et al. (1996)	201	$3 \cdot 10^{-3}$-$10 \cdot 10^{-3}$	1.40	0.30
Villemin and Sunwoo (1987)	100	$4 \cdot 10^3$-$30 \cdot 10^3$	1.40	$6 \cdot 10^8$
Watterson et al. (1996)	1034	200-5000	1.36	$87 \cdot 10^6$
Yielding et al. (1996)	450	500-6000	1.18	$220 \cdot 10^6$
	350	$4 \cdot 10^3$-$50 \cdot 10^3$	1.75	$1.5 \cdot 10^9$

Fig. 3.2 shows the variation of *RE* from the data sets in Table 3.1, which shows *RE* rapidly reduces to small values as the number of simulation increases. Although it is recommended to use a small *RE* as possible, it assumed that *RE* = 5% gives an acceptable level of error in the MCS. Therefore, it was confirmed that discretizing the PDFs of the input variables into 2,000 discrete data, corresponding to an *RE* = 5%, is sufficient to investigate the effects of stochastic parameters on the permeability values.

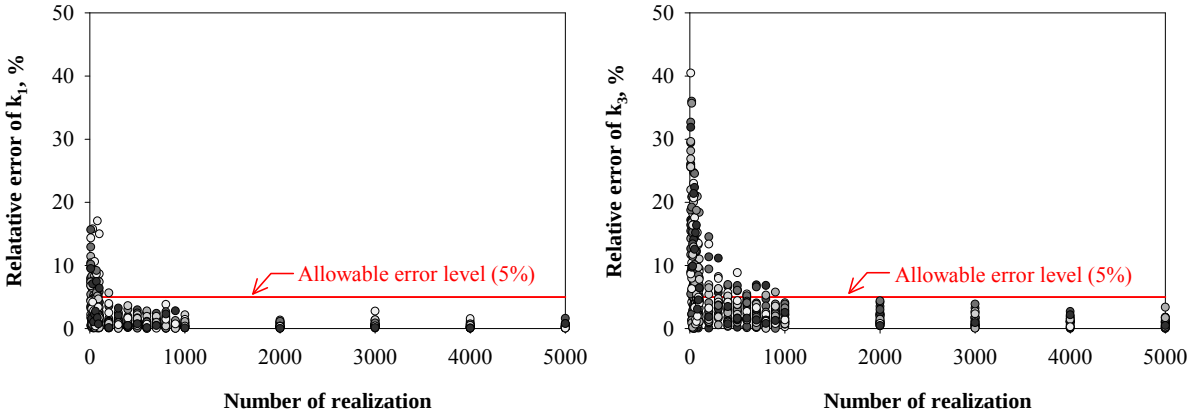

Fig. 3.2 - Relative error *RE* of the principal permeability values from MCS as function of number of realizations. (Left: major principal permeability, Right: minor principal permeability).

To study the effects of each fracture parameter, parametric studies were conducted where a range of values for the particular parameter was generated while the other parameters were kept constant. First, random values are developed to define fracture length distribution using different fractal dimensions D. Since the typical range of the exponent is between 0.70-1.75 (Bonnet et al. 2001), three different values were chosen. For the second series of analyses, three different aperture distributions are used assuming the same fracture length geometrical distribution for the three fracture aperture scenarios. The random fracture aperture sets are produced with the different exponents of the correlation within the usual range of the exponent varies between 0.5 and 2.0 in Eq. (2.39) based on the data from Bonnet et al. (2001). In addition, to evaluate the influence of fracture orientations, the effects of the number of fracture sets on the permeability is investigated. A total 400 fractures are divided into several fracture sets, each with a random mean orientation. Each fracture group has its own variation in orientation based on the characteristics of different Fisher distributions. Fisher coefficient for each distribution is also selected randomly in the typical range, summarized by Post (2001). The shape factors for the PDF generation in each case are summarized in the Table 3.2.

3.1.1 Effects of the PDF on Permeability

Typical results of the calculation of the equivalent anisotropic permeability tensor using Oda's formulation and the stochastically-generated fracture geometries are shown in a polar plot in Fig. 3.3. The polar plot shows the directional magnitudes of permeability, and hence the resulting fluid flow, as function of flow direction. The maximum permeability value corresponds to the major principal value k_1 of the permeability tensor, and the minimum value corresponds to the minimum principal value k_3. The polar plots also illustrate the corresponding directions of the maximum and minimum permeability.

The first part of the parametric study is to evaluate the effects of fracture length distribution while keeping the same apertures and three fracture sets. The fracture length distributions are shown in Fig. 3.4 for three values of the fractal dimension *D*. The resulting directional permeability values are shown in a polar plot in Fig. 3.3. As shown in Fig. 3.4, lower fractal dimension results in a lower number of major fractures. In turn, a higher proportion of major fractures yields larger rock mass permeabilities as shown in Fig. 3.3. A high fractal

dimension, which produces more long fractures than shorter ones compared to a low fractal dimension, provides higher permeabilities.

Table 3.2 - Summary of PDF parameters for the random number generation.

Fracture parameter	Length	Aperture	Orientation
Variation	Fractal dimension (D) in Eq. (2.38)	Correlation exponent (n) in Eq. (2.39)	Number of fracture sets (N_{FS})
Fractal dimension (D)	0.70, 1.21, 1.75	1.21	1.21
Correlation exponent (n)	1.25	1.15, 1.25, 1.35	1.25
Fisher constant (K)	Random in a range (20-100)	Random in a range (20-100)	Random in a range (20-100)
Mean orientation	Random in a range (0-360°)	Random in a range (0-360°)	Random in a range (0-360°)
Number of fracture sets (N_{FS})	3	3	1, 2, 3, …, 100

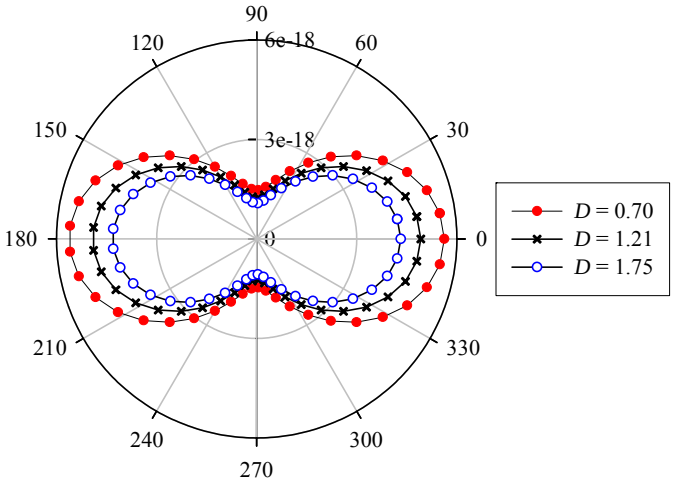

Fig. 3.3 - Polar plot of the permeability distribution (in m^2) obtained from Oda's permeability tensor as function of the fractal dimension D.

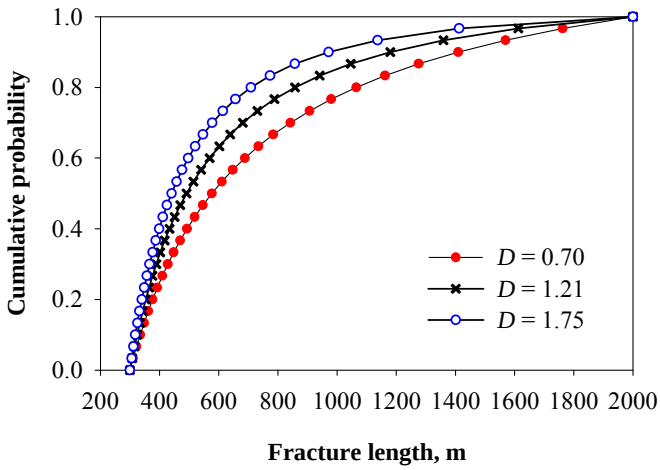

Fig. 3.4 - Fracture length distributions for three values of fractal dimension *D*.

The second part of the parametric study is to evaluate the effect of the different aperture distributions when the same fracture length distribution is used. The exponent *n* in Eq. (2.39) is varied in the parametric study and its influence on the magnitudes of the fracture apertures is shown in Fig. 3.5. As expected, a large value of the exponent *n* results in higher fracture apertures, and correspondingly in higher values of rock mass permeability as shown in the polar plots in Fig. 3.6. Note that the radial axis in Fig. 3.6 is in logarithmic scale reflecting a wide range of permeability values and strong sensitivity to the permeability exponent *n*. Compared with the permeability values in Fig. 3.5, the effects of the variability of the fracture apertures is much significant than the effects of the variability in fracture lengths. Even with only small variations of the parameter *n* in Eq. (2.39), permeability varied significantly. The strong effect of the changes in fracture aperture comes from the characteristics of the analytical permeability equation, which has a cubic aperture law while the permeability is only linearly dependent on fracture length.

The third series of parametric study involves the effects of fracture orientations and number of fracture sets. In this series, the total number of fractures in a realization is divided into several fracture sets, with fracture orientation in each set following the Fisher distribution. Figure 3.7 shows how the directional permeability deviates from an isotropic distribution due to the number of fracture sets N_{FS}. More fracture sets give larger variation of the fracture orientations. In turn, larger variation in fracture orientations leads to more isotropic permeability distribution. This can be clearly seen in Fig. 3.8 which shows the ratio of the maximum and minimum permeabilities k_1/k_3 as function of the fracture set N_{FS}. The k_1/k_3 ratio decreases exponentially when N_{FS} is relatively small, but as N_{FS} becomes large, the ratio tends towards a value of 1.0 or isotropic permeability.

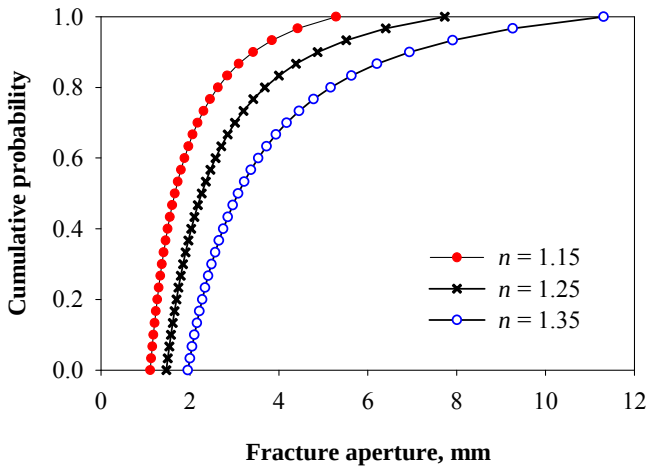

Fig. 3.5 - Fracture aperture distribution.

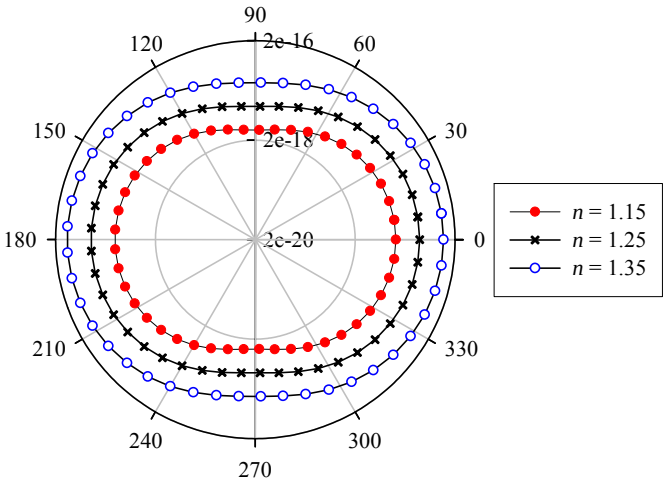

Fig.3.6 - Permeability distribution (in m^2) with variation of the exponent (n).

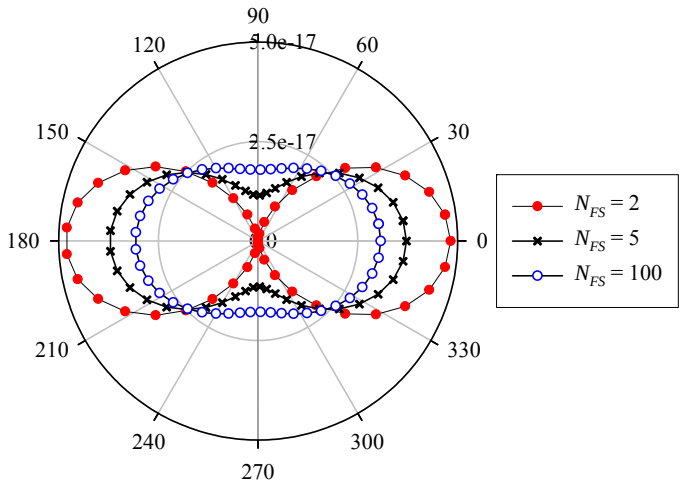

Fig. 3.7 Permeability distribution (in m^2) for three values of N_{FS}.

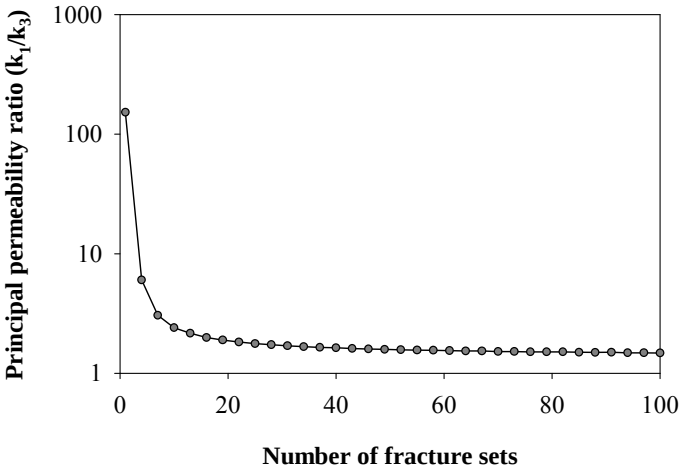

Fig. 3.8 Principal permeability ratio from different numbers of fracture sets.

3.1.2 Scale Effects on Fractured Rock Mass Permeability

To investigate the effects of the size of the sampling box used to generate the equivalent fracture permeability and the validity of the use of an REV, two parameters are introduced to characterize the sampling volume and the degree of fracturing in a rock mass. The first parameter is the relative measure of the sampling volume, which is specified by a parameter called the Side Length Ratio *SLR*. This parameter is equal to the length of the side of the square sampling area divided by the length of the region of interest, also assumed to be square:

$$SLR = \frac{\text{Length of the side of sampling area}}{\text{Length of the side of total area}} \tag{3.2}$$

Figure 3.9 shows an example which illustrates the variation of the mean values of the major and minor principal permeabilities k_1 and k_3 as function of *SLR* using the data collected by Blackstone (1988). When *SLR* is relatively large, the mean values remain relatively constant and independent of the size of the sampling box. However, for *SLR* less than a certain threshold value, the mean permeability values start to oscillate and drastically decrease. Therefore,

permeability variation with sampling volume can be predicted only when the sampling volume is greater than the threshold value, which is indicated by the inflection point in the Fig. 3.9. This inflection point effectively corresponds with that of an REV in that sampling volumes less than this point will not provide consistent permeability values. Above this value, any sampling volume would produce consistent permeability values that are relatively independent of the sampling volume. Similar results were obtained for the equivalent continuum permeability values calculated using the field data given in Table 3.2.

The second parameter used to investigate the effects of length scale on the equivalent continuum permeability of fractured rock mass and the validity of the use of an REV is the fracture intensity *FIT* parameter. This parameter, which quantifies the degree of fracturing in a rock mass, is defined as the sum of all the fracture lengths over the total volume of the region of interest:

$$FIT = \frac{1}{V}\sum_{k=1}^{m^{(v)}} r^{(k)} \tag{3.3}$$

Table 3.3 lists the *FIT* values for the different sets of in situ fracture data given in Table 3.2. As can be seen, most field sites have *FIT* magnitudes in the range of 10^{-4} and 10^{-3} /m, and only two sites have values above 1.0 /m.

The parametric study also investigated whether the fracture intensity *FIT* can be related with the *SLR*, and the results are shown in Fig. 3.10. Above a certain *SLR* threshold value, *FIT* is almost constant and independent of *SLR*. Below this threshold value, the *FIT* values start to oscillate and can no longer be directly related with *SLR*. This behavior of *FIT* as function of *SLR* provides an explanation for the trend in the values of permeability as function of the sampling volume. As permeability is a function of the intensity of fracturing as quantified by the *FIT* parameter, the tendency of the permeability value to oscillate below a threshold value should be reflected by similar oscillation in the *FIT* parameter. An important observation that can be obtained from Figs. 3.9 and 3.10 is that the *SLR* values at the inflection points for both the permeability and *FIT* values are identical. This observation shows that the REV can also be determined by plotting *FIT* values against the sampling box size and observing at what point the *FIT* value start to oscillate. This procedure provides a faster way to determine the REV than calculating the permeability.

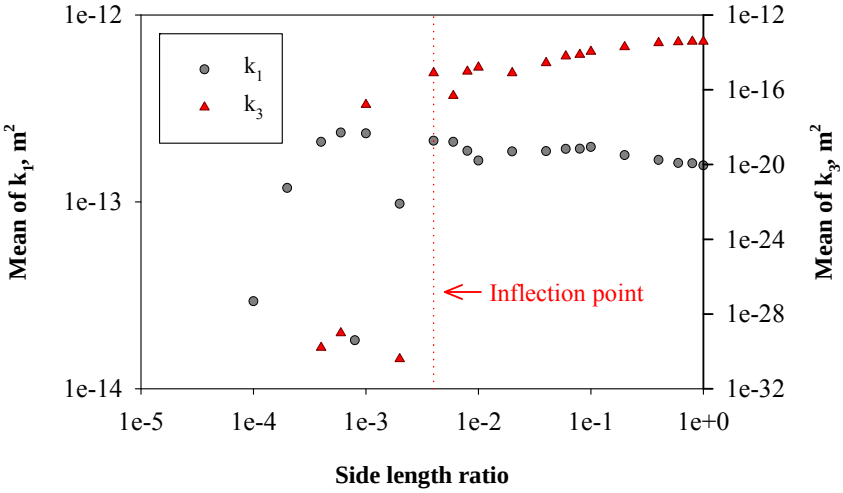

Fig. 3.9 - Permeability distribution as function of *SLR* from the field data by Blackstone (1988).

Table 3.3 - Compilation of *FIT* and fracture length data from different sites.

Reference	Length range, m	Sum of length, m	Area, m^2	*FIT*, m^{-1}
Ackermann and Schlische (1997)	$4 \cdot 10^{-2}$-$15 \cdot 10^{-2}$	$5.75 \cdot 10$	34	1.69
Krantz (1988)	150-1500	$2.12 \cdot 10^{4}$	$29 \cdot 10^{6}$	$7.32 \cdot 10^{-4}$
Kakimi (1980)	1000-7000	$3.88 \cdot 10^{5}$	$280 \cdot 10^{6}$	$1.39 \cdot 10^{-3}$
Scott and Castellanos (1984)	300-2000	$2.46 \cdot 10^{5}$	$120 \cdot 10^{6}$	$2.05 \cdot 10^{-3}$
Blackstone (1988)	$10 \cdot 10^{-3}$-$60 \cdot 10^{-3}$	$5.13 \cdot 10^{6}$	$250 \cdot 10^{9}$	$2.05 \cdot 10^{-5}$
Stewart (1980)	$15 \cdot 10^{-3}$-$50 \cdot 10^{-3}$	$9.24 \cdot 10^{6}$	$290 \cdot 10^{9}$	$3.18 \cdot 10^{-5}$
	$7 \cdot 10^{-3}$-$25 \cdot 10^{-3}$	$7.40 \cdot 10^{5}$	$3600 \cdot 10^{6}$	$2.06 \cdot 10^{-4}$
Cladouhos and Marrett (1996)	$7 \cdot 10^{-3}$-$25 \cdot 10^{-3}$	$1.61 \cdot 10^{6}$	$5100 \cdot 10^{6}$	$3.16 \cdot 10^{-4}$
	$7 \cdot 10^{-3}$-$25 \cdot 10^{-3}$	$1.97 \cdot 10^{6}$	$6200 \cdot 10^{6}$	$3.18 \cdot 10^{-4}$
Clark et al. (1999)	360-4500	$7.82 \cdot 10^{5}$	$87 \cdot 10^{6}$	$8.99 \cdot 10^{-3}$
Fossen and Hesthammer (1997)	1-20	$1.63 \cdot 10^{2}$	$2 \cdot 10^{4}$	$8.17 \cdot 10^{-3}$
	150-800	$8.89 \cdot 10^{4}$	$169 \cdot 10^{6}$	$5.26 \cdot 10^{-4}$
Gauthier and Lake (1993)	150-800	$7.73 \cdot 10^{4}$	$169 \cdot 10^{6}$	$4.57 \cdot 10^{-4}$
	100-700	$1.71 \cdot 10^{4}$	$169 \cdot 10^{6}$	$1.01 \cdot 10^{-4}$
Knott et al. (1996)	0.31-0.93	$9.22 \cdot 10$	1	$9.22 \cdot 10$
Odling et al. (1999)	2-20	$2.55 \cdot 10^{3}$	$11.7 \cdot 10^{3}$	$2.18 \cdot 10^{-1}$
Pickering et al. (1997)	200-1000	$1.59 \cdot 10^{5}$	$60 \cdot 10^{6}$	$2.64 \cdot 10^{-3}$
Schlische et al. (1996)	$3 \cdot 10^{-3}$-$10 \cdot 10^{-3}$	$9.87 \cdot 10^{-1}$	0.30	3.29
Villemin and Sunwoo (1987)	$4 \cdot 10^{3}$-$30 \cdot 10^{3}$	$7.10 \cdot 10^{5}$	$6 \cdot 10^{8}$	$1.18 \cdot 10^{-3}$
Watterson et al. (1996)	200-5000	$5.22 \cdot 10^{5}$	$87 \cdot 10^{6}$	$6.00 \cdot 10^{-3}$
Yielding et al. (1996)	500-6000	$5.37 \cdot 10^{5}$	$220 \cdot 10^{6}$	$2.44 \cdot 10^{-3}$
	$4 \cdot 10^{3}$-$50 \cdot 10^{3}$	$2.53 \cdot 10^{6}$	$1.5 \cdot 10^{9}$	$1.69 \cdot 10^{-3}$

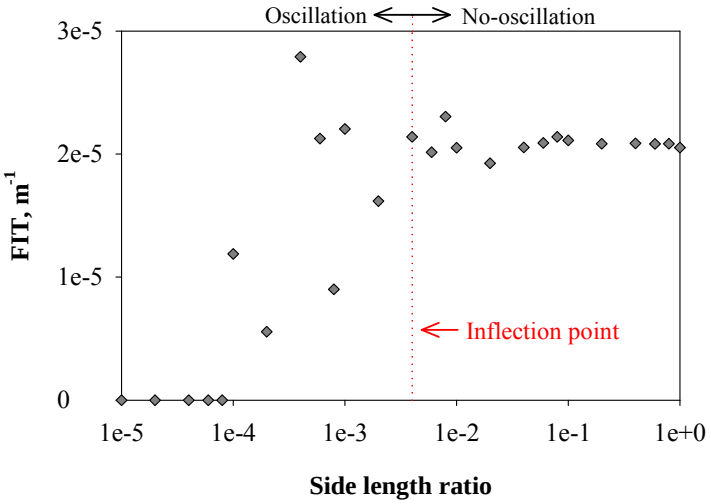

Fig. 3.10 - Permeability distribution as function of *SLR* from the field data by Blackstone (1988).

To recapitulate, the results from an extensive stochastic simulation of the permeability of fractured rock masses indicated that the REV can be formally defined as the *SLR* below which both the mean permeability and *FIT* values start to oscillate. Above this *SLR* value, the mean permeability and *FIT* remain relatively constant and independent of the size of the sampling volume. This REV value can be equally determined either by plotting *SLR* against the mean permeability values or the *FIT*. Using this definition of the REV, REV values were determined for all the different cases used in the stochastic simulations and plotted against *FIT* in Fig. 3.11. The plot shows that a linear relationship exists between the logarithmic values of the *SLR* and the REV. This relationship appears to be valid for both the major and principal permeability values. More importantly, the plot applies for a wide range of *FIT* values ranging from 10^{-5} to 10^{2} m^{-1}, and REVs from 10^{-7} to 10^{6} m.

The best-fit linear relationship between the logarithmic values of the *SLR* and the REV shown in Fig. 3.11 is given as:

$$REV = 3 \cdot 10^{4} \left(FIT \right)^{-2.01} \tag{3.4}$$

where *FIT* is in m^{-1} and REV is in m. The R^2 value for Eq. (3.4) is 0.96. If the *FIT* value can be calculated, for example from a rock outcrop, then REV can be easily calculated using Eq. (3.4). For guidance in the determination of *FIT*, typical values are given in Table 3.4 for different sites. The REV from Eq. (3.4) can be employed to decide on the size of elements relative to the degree of fracturing that can be used in Finite Element or Finite Difference simulations of fluid flow in fractured rock masses.

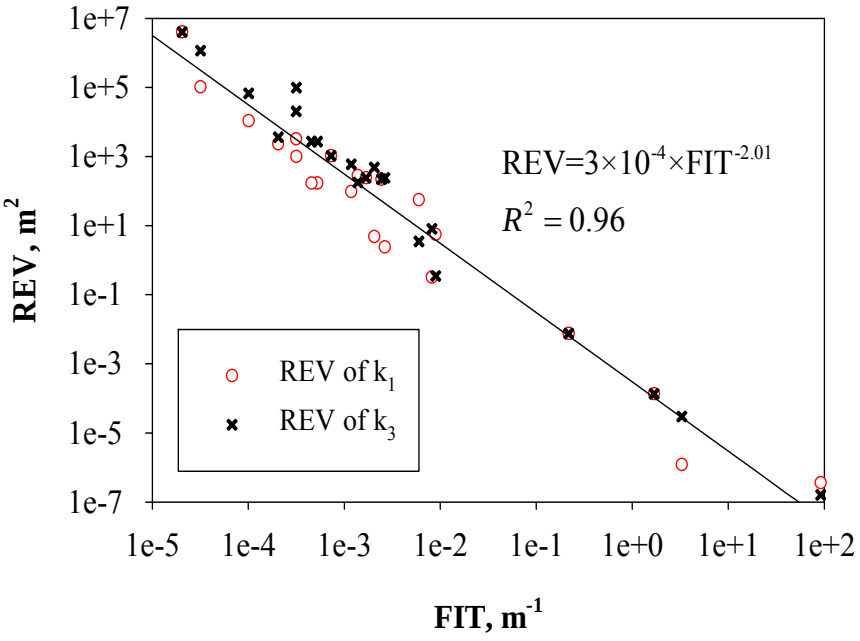

Fig. 3.11 - REV as function of *FIT*.

Table 3.4 - Compilation of power law exponents for fracture length distributions (Bonnet et al. 2001).

Reference	$N_{Fracture}$	Length range, m	Fractal dimension (D)	Area, m^2
Ackermann and Schlische [30]	873	$4 \cdot 10^{-2}$–$15 \cdot 10^{-2}$	2.64	34
Bahat [31]	107	0.7–2.5	1.74	24
	121	0.6–2.3	2.11	25
Blackstone [32]	250	$10 \cdot 10^{3}$–$60 \cdot 10^{3}$	2.11	$250 \cdot 10^{9}$
Cladouhos and Marrett [33]	70	$7 \cdot 10^{3}$–$25 \cdot 10^{3}$	2.67	$3600 \cdot 10^{6}$
	150	$7 \cdot 10^{3}$–$25 \cdot 10^{3}$	2.66	$5100 \cdot 10^{6}$
	200	$7 \cdot 10^{3}$–$20 \cdot 10^{3}$	3.07	$6200 \cdot 10^{6}$
Clark et al. [34]	1034	360–4500	2.51	$87 \cdot 10^{6}$
Fossen and Hesthammer [35]	40	1–20	1.6	$2 \cdot 10^{4}$
Gauthier and Lake [36]	318	150–800	2.42	$169 \cdot 10^{6}$
	291	150–800	2.69	$169 \cdot 10^{6}$
	78	100–700	2.1	$169 \cdot 10^{6}$
Gudmundsson [37]	120	600–5750	0.9	$8.25 \cdot 10^{7}$
Gudmundsson [38]	101	1000–7700	1	$2.62 \cdot 10^{7}$
Kakimi [39]	180	1000–7000	1.97	$280 \cdot 10^{6}$
Knott et al. [40]	218	0.31–0.93	2.02	1
Krantz [41]	50	150–1500	1.67	$29 \cdot 10^{6}$
Odling et al. [42]	470	2–20	1.8	$11.7 \cdot 10^{3}$
Ouillon et al. [43]	380	3–30	1.9	3433
	350	700–7000	2.1	$1.26 \cdot 10^{8}$
	1000	$2.2 \cdot 10^{3}$–$15 \cdot 10^{3}$	3.2	$1.60 \cdot 10^{9}$
	1000	$3.5 \cdot 10^{3}$–$11 \cdot 10^{3}$	2.1	$1.65 \cdot 10^{10}$
Pickering et al. [44]	417	200–1000	2.18	$60 \cdot 10^{6}$
Reches [45]	800	0.14–2.63	2.2	25
Schlische et al. [46]	201	$3 \cdot 10^{-3}$–$10 \cdot 10^{-3}$	2.4	0.3
Scholz [47]	1700	$3 \cdot 10^{3}$–$30 \cdot 10^{3}$	2.02	$1.00 \cdot 10^{10}$
Scott and Castellanos [48]	400	300–2000	2.21	$120 \cdot 10^{6}$
Segall and Pollard [49]	260	3–16	1.3	8750
	100	15–50	1.8	2100
Stewart [50]	400	$15 \cdot 10^{3}$–$50 \cdot 10^{3}$	2.84	$290 \cdot 10^{9}$
Villemin and Sunwoo [51]	100	$4 \cdot 10^{3}$–$30 \cdot 10^{3}$	2.4	$6 \cdot 10^{8}$
Watterson et al. [52]	1034	200–5000	2.36	$87 \cdot 10^{6}$
Yielding et al. [53]	450	500–6000	2.18	$220 \cdot 10^{6}$
	350	$4 \cdot 10^{3}$–$50 \cdot 10^{3}$	2.75	$1.5 \cdot 10^{9}$

3.2 Elastic Compliance of Fractured Rock Masses

Oda's compliance tensor formulation and the MCS procedure to produce random fracture geometries and properties were programmed in Matlab. Random fracture geometries were generated following the prescribed PDFs for each fracture parameter. To obtain geologically realistic fracture distributions and geometries, data from various field studies were used to generate the required length data based on the truncated power law distribution. All parameters required to stochastically generate the ECM compliance values were based on the summary of 34 field data sets collected by Bonnet et al. (2001). Their data cover a wide range of rock types and field geological history. The required data sets for the simulations consist of the number of fractures, the maximum and minimum fracture lengths, fractal dimension, and the total area of the sampling field. These parameters are summarized in Table 3.5.

Once the centroids of the fractures have been located, randomly generated fractured rock samples are assembled by applying stochastically produced fracture length and orientation data at the points. Figure 3.1 shows examples of fractured rock sample realizations from four different in situ data sets given in Table 3.5. After the process, if some fracture segments lie outside the sampling boundary, the program automatically truncates the extra part of the fracture and excludes that part from the compliance tensor calculations. Based on extensive studies, fracture truncations at the boundaries do not significantly change the original fracture length distribution or the magnitude of the fracture compliance tensor.

Table 3.5 - Summary of PDF parameters for fracture pattern realizations.

Fracture parameter	**Length**	**Stiffness**	**Orientation**
	Fractal dimension (D) in Eq. (2.38)	Normal stress (σ_n) in Eq. (2.39)	Number of fracture sets (N_{FS})
Fractal dimension (D)	0.90, 2.05, 3.20	Fractal dimension in each data in Table 3.4	Fractal dimension in each data in Table 3.4
Normal stress (σ_n)	10	20, 40, 80 MPa	10
Fracture stiffness ratio (R)	10	10	10
Fisher constant (K)	Random in a range (20–100)	Random in a range (20–100)	Random in a range (20–100)
Mean orientation	0°	0°	Random in a range (0–360°)
Number of fracture sets (N_{FS})	1	1	1, 2, 3, …, 100
Fracture surface values ($JRC/JCS/\phi_r$)	8.9/92 MPa/27.5°	8.9/92 MPa/27.5°	8.9/92 MPa/27.5°

After the random fractured rock geometry generation is completed, a stochastically generated fracture compliance tensor is superimposed on the homogeneous intact rock compliance:

$$S_{ijkl}^{c} = S_{ijkl}^{f} + S_{ijkl}^{r} \tag{3.5}$$

where S_{ijkl} = fourth rank compliance tensor. The superscripts *c*, *f*, and *r* indicate a combination of fracture and rock, fracture only, and rock mass only, respectively. The elastic compliance tensor for the intact rock can be written as

$$S_{ijkl}^{r} = \frac{1}{E}\left\{(1+\upsilon)\delta_{ik}\delta_{jl} - \upsilon\delta_{ij}\delta_{kl}\right\} \tag{3.6}$$

where E = Young's modulus for intact rock and υ = Poisson's ratio for intact rock. Typical elastic parameters for sandstone, i.e., E = 20 GPa and υ = 0.3, are used in this paper. The equivalent continuum fractured rock compliance is measured as an expanded tensorial calculation as shown in Eq. (10):

$$S_{ijkl}^{c} = \frac{1}{E}\begin{bmatrix} 1 & -\upsilon & 0 \\ -\upsilon & 1 & 0 \\ 0 & 0 & 2(1+\upsilon) \end{bmatrix} + \left(\frac{1}{K_n} - \frac{1}{K_s}\right)\begin{bmatrix} F_{1111} & F_{1122} & 2F_{1112} \\ F_{2211} & F_{2222} & 2F_{2212} \\ 2F_{1211} & 2F_{1222} & 4F_{1212} \end{bmatrix} + \frac{1}{K_s}\begin{bmatrix} F_{11} & 0 & F_{12} \\ 0 & F_{22} & F_{21} \\ F_{21} & F_{12} & F_{11}+F_{22} \end{bmatrix} \tag{3.7}$$

As can be gleaned from Eqs. (2.23) and (2.24), since the crack tensors F_{ij} and F_{ijkl} are symmetric, the elastic compliance tensor (Eq. 3.6) should be symmetric as well. The simplest case of material symmetry is obtained when the fractures are orthogonal and are parallel to the reference axes. In this case, the compliance tensor is orthotropic requiring only three parameters. In general in case of random fracture orientations, Eq. (3.6) yields a fully anisotropic elastic stress-strain relation requiring a total of six components to describe the two-dimensional rock mass elastic compliance tensor. Presenting all these compliance components will be intractable. Instead, the effects of fracture distribution and length scale will be analyzed and presented using two elastic parameters, which are the equivalent continuum Young's modulus $\overline{E} = \sigma_{11}/\varepsilon_{11}$ and the equivalent Poisson's ratio $\overline{\upsilon} = -\varepsilon_{22}/\varepsilon_{11}$. These parameters can be obtained from Eq. (3.6) as follows:

$$S_{1111}^{c} = \frac{1}{\overline{E}},\ S_{1122}^{c} = \frac{-\overline{\upsilon}}{\overline{E}} \tag{3.8}$$

$$\overline{E} = \left\{\frac{1}{E} + \left(\frac{1}{k_n} - \frac{1}{k_s}\right)F_{1111} + \frac{F_{11}}{k_s}\right\}^{-1} \tag{3.9}$$

$$\overline{\upsilon} = -\left\{\frac{-\upsilon}{E} + \left(\frac{1}{k_n} - \frac{1}{k_s}\right)F_{1122}\right\}\left\{\frac{1}{E} + \left(\frac{1}{k_n} - \frac{1}{k_s}\right)F_{1111} + \frac{F_{11}}{k_s}\right\}^{-1} \tag{3.10}$$

It is expected that the dependency of the other equivalent continuum elastic parameters on fracture distribution and length scale will follow that of $\overline{E}$ and $\overline{\upsilon}$. The direction dependency of the elastic parameters of fractured rock masses is discussed below.

To study the effects of variation in each fracture parameter, parametric studies were conducted where a range of values for the particular parameter was generated while the other parameters were kept constant. First, random values were developed to define a fracture length

distribution using different fractal dimensions D. Since the range of the fractal dimension in Table 3.5 is between 0.90 and 3.20 (Bonnet et al. 2001), three different values (lowest, intermediate, highest) were chosen from the range. In addition, to evaluate the influence of fracture stiffness, different normal stresses to vary the shear stiffness parameter, and the stiffness ratio R between the fracture normal and shear stiffnesses, were investigated. Finally, to evaluate the influence of fracture orientation, the effects of the number of fracture sets on the compliance was investigated. The total number of fractures was divided into several fracture sets, each with a random mean orientation. Each fracture group has its own variation in orientation based on the characteristics of different Fisher distributions. The Fisher coefficient for each distribution was also selected randomly from a typical range, from 20 to 100, collected by Post (2001). In addition, fracture surface values to measure the fracture stiffness parameters in Eqs. (2.25) and (2.26) were selected from the average values of empirical data reported by Barton and Choubey (1977). The shape factors for the PDF generation and the stiffness parameters in each case are summarized in Table 3.6. In representing the fracture orientation by the Fisher distribution, the mean orientation of all fractures is set to 0° to facilitate analysis of the direction-dependent elastic response of the fractured rock mass.

3.2.1 Minimum Number of Required Monte Carlo Simulations

Before studying the effects of the different fractured parameters, an analysis was first performed to determine the number of MCS needed to obtain a stable distribution of the compliance parameters. To quantify the stability of the calculated elasticity parameters as a function of number of random realizations, the Relative Errors (*RE*) defined below are used:

$$RE_{E_x}^{N} = 100 \cdot \sqrt{\left(\overline{E}_x^{N} - \overline{E}_x^{REP}\right)^2} \Big/ \sqrt{\left(\overline{E}_x^{REP}\right)^2} \tag{3.11}$$

$$RE_{\upsilon_{xy}}^{N} = 100 \cdot \sqrt{\left(\overline{\upsilon}_{xy}^{N} - \overline{\upsilon}_{xy}^{REP}\right)^2} \Big/ \sqrt{\left(\overline{\upsilon}_{xy}^{REP}\right)^2} \tag{3.12}$$

where $\overline{E}_x$ and $\overline{\upsilon}_{xy}$ = refer to Young's modulus and Poisson's ratio, and the superscripts N and REP indicate that the elastic parameters are measured from N realizations and from 10,000 realizations, which can produce sufficiently stable compliance parameters.

Fig. 3.12 shows the variation in *RE* from the data sets in Table 3.5, revealing that *RE* rapidly reduces to small values as the number of simulations increases. Although it is recommended to use as small an *RE* as possible, it assumed that *RE* = 5% gives an acceptable level of error in the MCS. Therefore, it was confirmed that discretizing the PDFs of the input variables into 2,000 discrete data points, corresponding to an *RE* = 5%, is sufficient to investigate the effects of stochastic parameters on the compliance values.

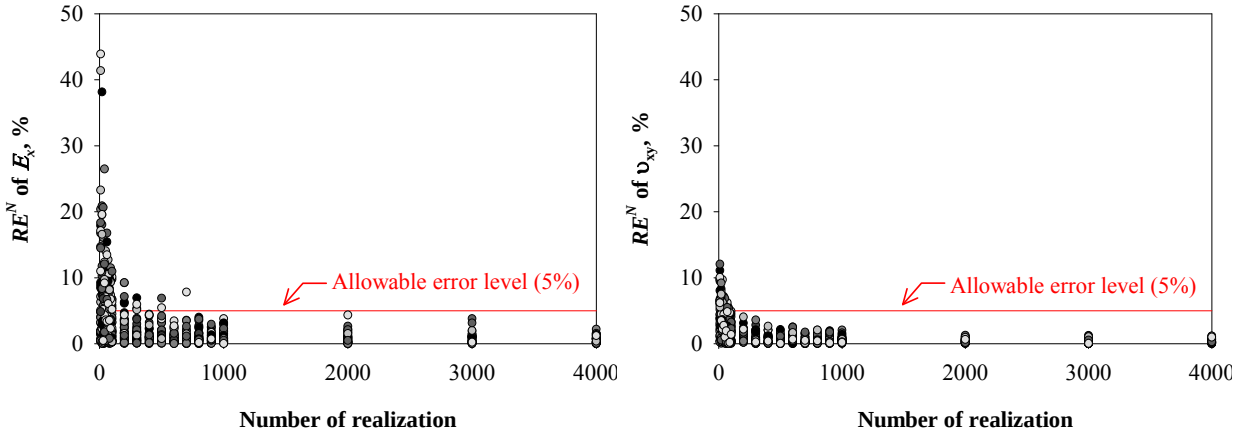

Fig. 3.12 - Relative error *RE*s of the equivalent continuum elastic parameters from MCS as function of number of realizations (left: Young's modulus; right: Poisson's ratio).

3.2.2 Effect of Fracture PDF on Elastic Compliance

As mentioned above, depending on the fracture orientations, Oda's compliance tensor (Eq. 1) generally yields a fully anisotropic elastic stress-strain relation. Owing to anisotropy, both the Young's modulus and Poisson's ratio are dependent on the direction of loading. To show this directional dependency, the variation in the elastic parameters corresponding to rotation of the local axis or sample orientation is also measured in this parametric study. The rotated elastic compliance tensor can be calculated by using a transformation matrix T as shown below:

$$\overline{S}^{\theta}_{ijkl} = T^{T} \cdot \overline{S}_{ijkl} \cdot T^{-1} \tag{3.13}$$

where

$$T = \begin{bmatrix} \cos^2\theta & \sin^2\theta & 2\sin\theta\cos\theta \\ \sin^2\theta & \cos^2\theta & -2\sin\theta\cos\theta \\ -\sin\theta\cos\theta & \sin\theta\cos\theta & \cos^2\theta - \sin^2\theta \end{bmatrix} \tag{3.14}$$

$\overline{S}^{\theta}_{ijkl}$ = equivalent continuum fractured rock compliance tensor oriented at angle θ counter clockwise from the positive *x*-axis. Once the oriented compliance tensor is measured, the elastic parameters along different directions can be measured by applying Eqs. (3.13) and (3.14).

The results of the calculation of the equivalent anisotropic compliance tensor are shown using polar plots in Figs. 3.13 to 3.16. Due to the symmetry of the elastic compliance tensor (Eq. 10), only the upper half of the polar plot needs to be shown. The first part of the parametric study evaluates the effects of fracture length distribution while keeping the same fracture stiffness and number of fracture set. The directional elastic parameters are shown in polar plots in Fig. 3.13. Since the power law distribution has a negative exponent, a higher fractal dimension results in a greater number of minor fractures and fewer longer fracture. The fracture length distribution from a higher fractal dimension yields greater equivalent fractured rock stiffness, as shown in Fig. 3.13. In addition, the deviations of the elastic parameters are linearly related to the magnitude of the fractal dimension.

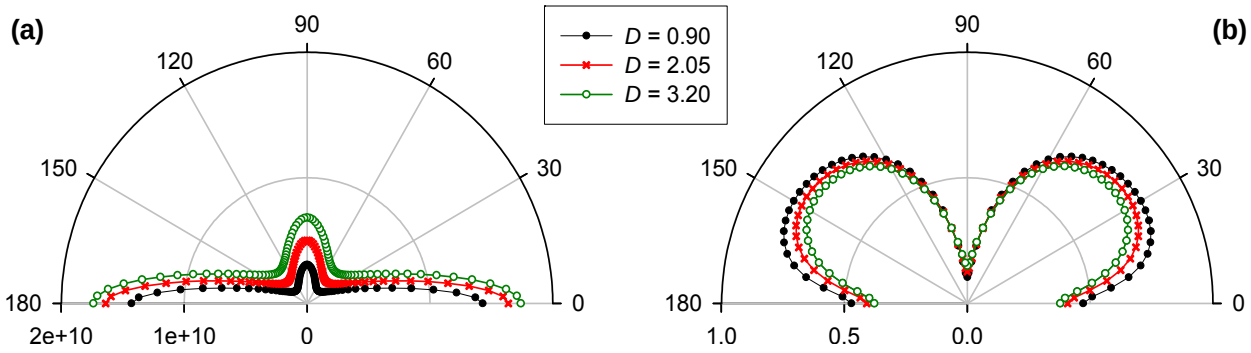

Fig. 3.13 - Polar plots of elastic parameters for three values of fractal dimension *D*, (a) Young's modulus in Pa, and (b) Poisson's ratio.

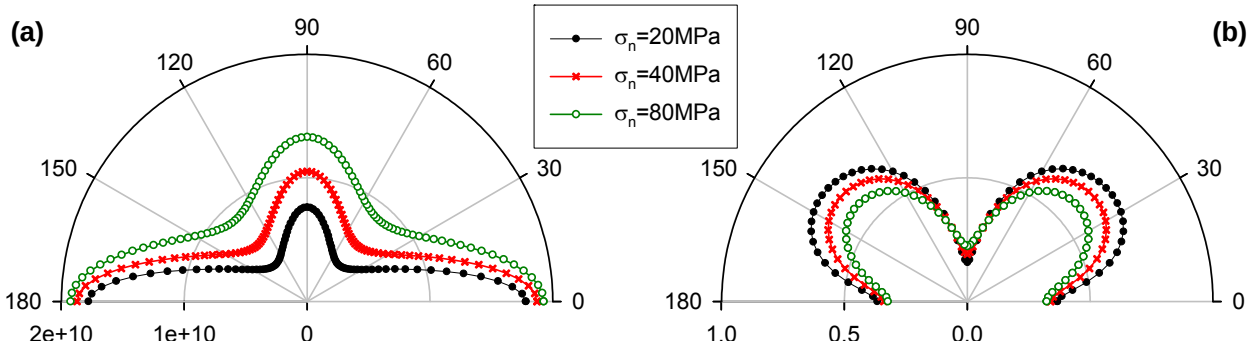

Fig. 3.14 - Polar plots of elastic parameters for three values of fracture normal stress σ_n, (a) Young's modulus in Pa, (b) Poisson's ratio.

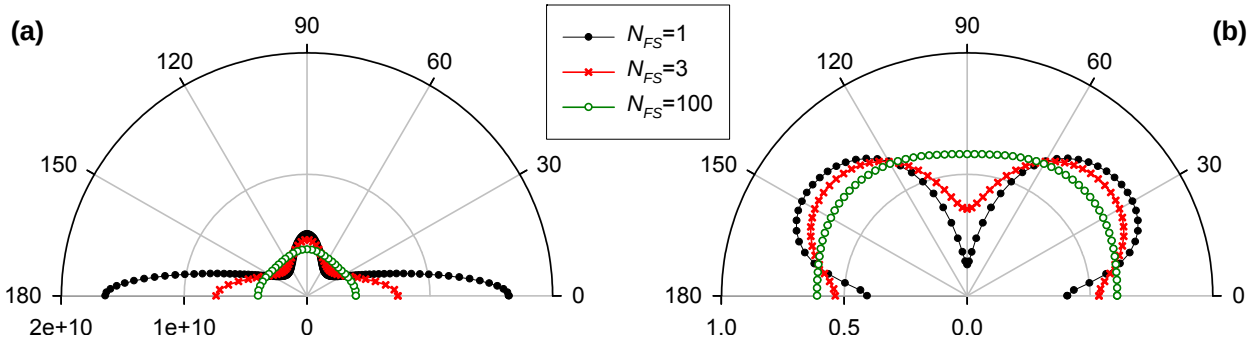

Fig. 3.15 - Polar plots of elastic parameters for three different numbers of fracture sets N_{FS}, (a) Young's modulus in Pa, (b) Poisson's ratio.

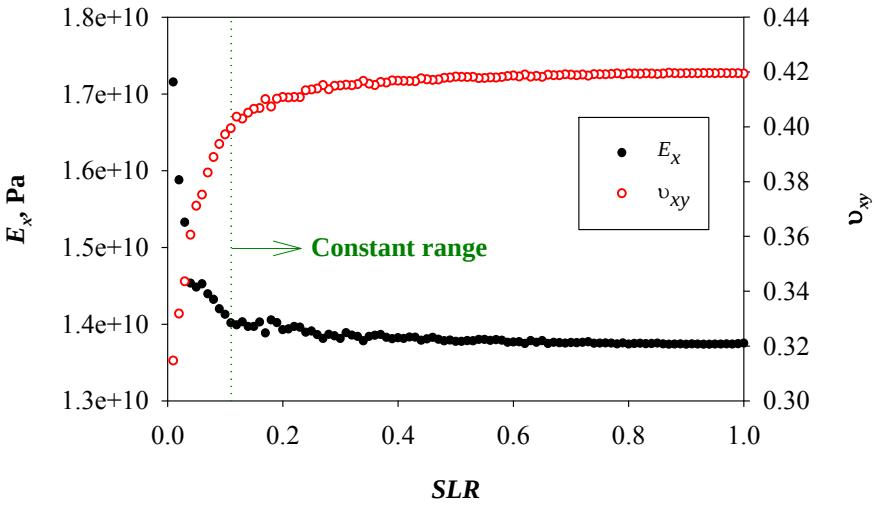

Fig.3.16 -Young's modulus and Poisson's ratio as a function of Side Length Ratio *SLR* from field data collected by Gauthier and Lake (1993).

The second part of the parametric study evaluates the effect of different fracture stiffness variations when the same fracture length and orientation distributions are used. The magnitude of stiffness is controlled via variation of fracture normal stress in Eq. (2.26), ranging from 20 MPa to 80 MPa, which is relatively making the stiffness ratio value *R* stable (Barton and Choubey, 1977). If a greater fracture normal stress is applied in the fracture stiffness calculation, the fracture stiffness parameters increase due to more friction and reduced aperture space. The increased fracture normal stress then results in relatively larger equivalent elasticity of fractured rock masses, corresponding to larger Young's modulus and smaller Poisson's ratio. In addition, it must be noted that there are directional sensitivities for both Young's modulus and Poisson's ratio. A lower normal stress yields strong directional variations and results in a more obvious orthotropic distribution of the elastic parameter distributions.

Although the normal stress range in this parametric study is limited to produce a stable fracture stiffness ratio *R* and reasonable fracture surface values such as *JRC* or *JCS* in the equivalent compliance calculation, it is expected that the mechanical effect of the fracture system can be ignored when the normal stress is extremely high, because it may result in a low fracture stiffness ratio and high fracture stiffness, which ultimately yield isotropic and homogeneous mechanical behavior.

The third series of parametric studies involves the effects of fracture orientations and number of fracture sets. In this series, the total number of fractures in a realization is divided into several fracture sets, with fracture orientation in each set following the Fisher distribution. Fig. 3.15 shows how the directional stiffness parameters deviate from an isotropic distribution due to the number of fracture sets N_{FS}. More fracture sets produce a larger variation of the fracture orientations. In turn, a larger variation in fracture orientation leads to increasingly isotropic elastic parameter distributions. The convergence rate decreases exponentially upon increasing the number of fracture sets and the mean orientation. When N_{FS} becomes large, the ratio between the major and minor principal stiffness parameters tends towards a value of 1.0, which indicates isotropic material parameters.

3.2.3 Scale Effects on Fractured Rock mass Elastic Compliance

To investigate the length scale effect of the equivalent continuum elasticity of fractured rock mass and the validity of the existence of an REV, two parameters are introduced to characterize the sampling volume and the degree of fracturing in a rock mass. The first parameter is a relative measure of the sampling volume, which is specified by a parameter called the Side Length Ratio, *SLR*. This parameter is equal to the length of a side of the square sampling area divided by the length of the region of interest, also assumed to be square.

$$SLR = \frac{\text{Side length of sampling area}}{\text{Side length of total area}} \tag{3.15}$$

The mean values of Young's modulus and Poisson's ratio are measured for different sampling box sizes, then the sampling box size is gradually decreased in each step. Fig. 3.16 shows an example that illustrates the variation of the mean values of the equivalent continuum Young's modulus and Poisson's ratio as a function of *SLR* using the data collected by Gauthier and Lake (1993). When *SLR* is relatively large, the mean values remain relatively constant and behaves as a continuum independent of the size of the sampling box. This observation is consistent with the formal definition of the REV as the "volumetric dimensions of the scale in which the continuum approach can be used." For *SLR* less than a certain threshold value, the mean elastic parameter values start to oscillate and drastically increase, finally reaching the host rock's properties, because the volume scale is too small to contain the proper fracture length. The REV can now be simply defined as the value of the *SLR* where the equivalent continuum elastic parameters start to significantly deviate from their asymptotic constant values. Similar results were obtained for all the simulations using the different field data sets listed in

In order to quantify the variation of the equivalent continuum elastic parameters from their asymptotically constant values, additional analyses were performed. The deviations of the values of the equivalent continuum elastic parameters from their asymptotic values are quantified by the following Relative Error *RE* values:

$$RE_{E_x}^{SLR} = 100 \cdot \sqrt{\left(\bar{E}_x^{SLR} - \bar{E}_x^{ORG}\right)^2} \Big/ \sqrt{\left(\bar{E}_x^{ORG}\right)^2} \tag{3.16}$$

$$RE_{\upsilon_{xy}}^{SLR} = 100 \cdot \sqrt{\left(\bar{\upsilon}_{xy}^{SLR} - \bar{\upsilon}_{xy}^{ORG}\right)^2} \Big/ \sqrt{\left(\bar{\upsilon}_{xy}^{ORG}\right)^2} \tag{3.17}$$

where $\bar{E}_x$ and $\bar{\upsilon}_{xy}$ = mean Young's modulus and Poisson's ratio, respectively, and superscripts *SLR* and *ORG* indicate that the elastic parameters are measured when the side length ratio is less than 1 and is equal to 1, respectively. By using these additional data processing calculations, it is possible to standardize the threshold to determine the data oscillation. As an example, Fig. 3.17 shows *RE* values as a function of *SLR* for both the equivalent continuum Young's modulus and Poisson's ratio. It is assumed that the variation of the elastic parameter values is no longer constant when the error level is higher than 5% relative to the stable value from the original volume of fractured rock, which is indicated by the blue line in Fig. 3.17. Thus, the lowest *SLR* in the constant *RE* range can be used to calculate the REV of the sample as:

$$\text{REV} = Area \cdot SLR_{\min}^2 \tag{3.18}$$

where *Area* = original rock outcrop area in Table 3.4.

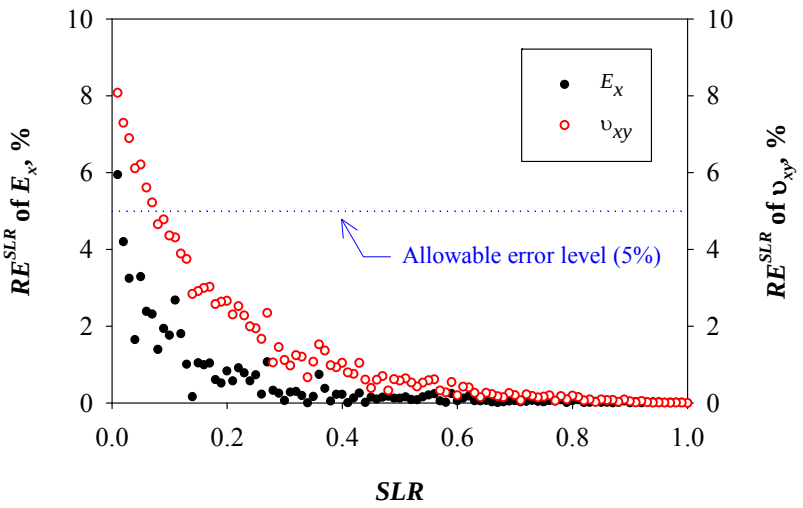

Fig. 3.17 -Relative Error for Young's modulus and Poisson's ratio as a function of *SLR* from field data collected by Fossen and Hesthammer (1997).

The second parameter used to investigate the effects of length scale on the equivalent continuum compliance of the fractured rock mass and the validity of the use of an REV is the fracture length scale parameter *MOV*. This parameter is defined as the maximum length of fracture over the total volume of the region of interest:

$$MOV = r_{\max} / Area \tag{3.19}$$

Table 3.6 lists the *MOV* values for the different sets of in situ fracture data given in Table 3.4. As can be seen, most field sites have *MOV* magnitudes in the range of 10^{-7} to 1.0 /m.

To summarize, the results from an extensive stochastic simulation of the compliance of fractured rock masses indicated that the REV can be formally defined as the value of the *SLR* below which the *RE* of the mean Young's modulus or Poisson's ratio starts to exceed the threshold value. Using this definition, REV values were determined for all the different cases used in the stochastic simulations and plotted against *MOV* in Fig. 3.18. The plot shows that a linear relationship exists between the logarithmic values of *MOV* and the REV. More importantly, the plot applies for a wide range of *MOV* values ranging from 10^{-7} to 1.0 m^{-1}, and REVs from 10^{-3} to 10^{12} m. If the *MOV* value can be calculated from a rock outcrop, then REV can be easily calculated using Fig.3.18.

The best-fit linear relationship between the logarithmic values of the *SLR* and the REV shown in Fig.3.18 is given as:

$$REV = 0.06 \cdot (MOV)^{-1.79} \tag{3.20}$$

where *MOV* is expressed in m^{-1} and REV, is m^2. The R^2 value for Eq. (3.20) is 0.81. For guidance in determining *MOV*, the typical values are given in Table 3.6 for different sites. The REV from Eq. (3.20) can be employed to decide on the size of elements, relative to the fracture length scale, that can be used in finite element or finite difference mechanical simulations for fractured rock masses.

Table 3.6 - Compilation of *MOV* and fracture length data.

Reference	Maximum length, m	Area, m^2	*MOV*, m^{-1}
Ackermann and Schlische [30]	$15 \cdot 10^{-2}$	34	$4.41 \cdot 10^{-3}$
Bahat [31]	2.5	1.74	1.04
	2.3	2.11	$0.92 \cdot 10^{-1}$
Blackstone [32]	$60 \cdot 10^{3}$	$250 \cdot 10^{9}$	$2.40 \cdot 10^{-7}$
Cladouhos and Marrett [33]	$25 \cdot 10^{3}$	$3600 \cdot 10^{6}$	$6.94 \cdot 10^{-6}$
	$25 \cdot 10^{3}$	$5100 \cdot 10^{6}$	$4.90 \cdot 10^{-6}$
	$20 \cdot 10^{3}$	$6200 \cdot 10^{6}$	$3.85 \cdot 10^{-6}$
Clark et al. [34]	4500	$87 \cdot 10^{6}$	$5.71 \cdot 10^{-5}$
Fossen and Hesthammer [35]	20	$2 \cdot 10^{4}$	$1.00 \cdot 10^{-3}$
Gauthier and Lake [36]	800	$169 \cdot 10^{6}$	$4.73 \cdot 10^{-6}$
	800	$169 \cdot 10^{6}$	$4.73 \cdot 10^{-6}$
	700	$169 \cdot 10^{6}$	$4.14 \cdot 10^{-6}$
Gudmundsson [37]	5750	0.9	$6.97 \cdot 10^{-5}$
Gudmundsson [38]	7700	1	$2.94 \cdot 10^{-4}$
Kakimi [39]	7000	$280 \cdot 10^{6}$	$2.50 \cdot 10^{-5}$
Knott et al. [40]	0.93	1	$9.30 \cdot 10^{-1}$
Krantz [41]	1500	$29 \cdot 10^{6}$	$5.17 \cdot 10^{-5}$
Odling et al. [42]	20	$11.7 \cdot 10^{3}$	$1.71 \cdot 10^{-3}$
Ouillon et al. [43]	30	1.9	$8.74 \cdot 10^{-3}$
	7000	2.1	$5.56 \cdot 10^{-5}$
	$15 \cdot 10^{3}$	3.2	$9.38 \cdot 10^{-6}$
	$11 \cdot 10^{3}$	2.1	$6.67 \cdot 10^{-7}$
Pickering et al. [44]	1000	$60 \cdot 10^{6}$	$1.67 \cdot 10^{-5}$
Reches [45]	2.63	2.2	$1.05 \cdot 10^{-1}$
Schlische et al. [46]	$10 \cdot 10^{-3}$	0.3	$3.33 \cdot 10^{-2}$
Scholz [47]	$30 \cdot 10^{3}$	2.02	$3.00 \cdot 10^{-6}$
Scott and Castellanos [48]	2000	$120 \cdot 10^{6}$	$1.67 \cdot 10^{-5}$
Segall and Pollard [49]	16	1.3	$1.83 \cdot 10^{-3}$
	50	1.8	$2.38 \cdot 10^{-2}$
Stewart [50]	$50 \cdot 10^{3}$	$290 \cdot 10^{9}$	$1.72 \cdot 10^{-7}$
Villemin and Sunwoo [51]	$30 \cdot 10^{3}$	$6 \cdot 10^{8}$	$5.00 \cdot 10^{-5}$
Watterson et al. [52]	5000	$87 \cdot 10^{6}$	$5.75 \cdot 10^{-5}$
Yielding et al. [53]	6000	$220 \cdot 10^{6}$	$2.73 \cdot 10^{-5}$
	$50 \cdot 10^{3}$	$1.5 \cdot 10^{9}$	$3.33 \cdot 10^{-5}$

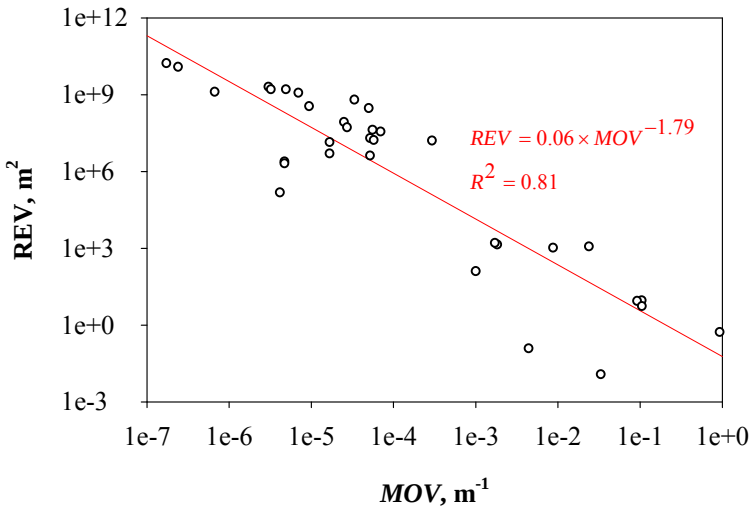

Fig. 3.18 -REV as function of *MOV*.

3.3 Elasto-plastic Behavior of Fractured Rock Masses

Figure 3.19 shows an example of the predicted behavior of a fractured rock mass using the elasto-plastic model described in Section (2.2.3) and implemented in FLAC. A sample of a rock containing a single set of fractures inclined 60° from the horizontal is subjected to biaxial loading with a constant horizontal stress σ_3 and increasing vertical strain ε_1. The results given at the bottom show the displacements of the sample and the principal stresses at failure. As can be seen, the rock deformed mainly by sliding along the fracture planes as shown by the directions of the displacement vectors. The principal stresses deviate slightly from the vertical and horizontal stresses as applied in the boundaries due to the sliding along the fracture planes. The elasto-plastic fractured rock model produced an additional displacements than the elastic model due to sliding along the fracture plane. Figure 3.19 also presents the rock mass stress-strain curve predicted by the model. Although elastic model gives linear relationship for the values, the elasto-plastic fractured rock model generated additional plastic strains and exhibited perfectly plastic behavior at an axial stress of about 4 MPa. After yielding, perfect plastic behavior is obtained, which is exhibited by a constant axial stress at increasing axial strain. The yield stress is also confirmed with the closed-form solution of the Mohr-Coulomb failure criterion with identical material properties. The results shown in Fig. 3.19 show that the fractured rock mass model is capable of predicting the stress-strain behavior of fractured rock masses.

Fractured rock masses typically have various failure modes, and its mechanical calculation is considerably complex. This is due to the fact that there are interactions between the intact rock and the fracture sets, and the effect of the geometrical system of fracture, for example orientation and frequency, can change the overall behavior of the fractured rock masses. To understand and analyze the intricate behavior of fractured rock masses and to show the validity of the elasto-plastic fractured rock mass model, a series of parametric studies are performed, and the results are compared with published data.

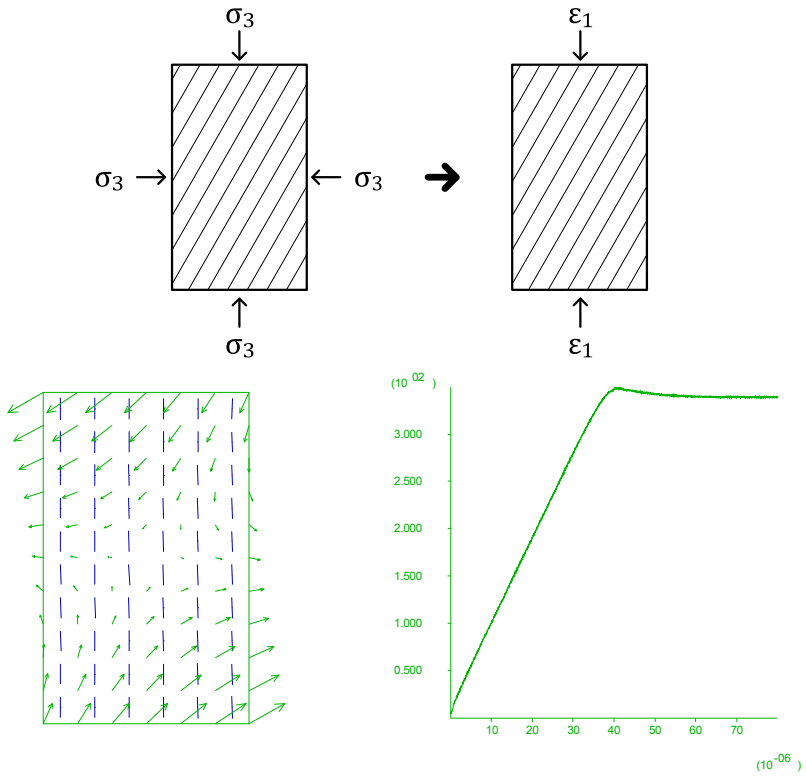

Fig. 3.19 – Predicted elasto-plastic behavior of a fractured rock mass containing a set of fractures oriented 60° from the horizontal. (Bottom left: principal stresses and displacements, Bottom right: stress-strain curve).

In the first set of parametric study, the analytical model for the ideal uniaxial strength of fractured rock sample predicted by Attewell and Sandford (1974) is compared to the predictions from the elasto-plastic rock mass model implemented in FLAC. The analytical solution is for rock sample with single fracture oriented 0° to 180°, measured from the *x*-axis in counterclock wise direction. In this case, the confining stress is zero, and the vertical direction velocity is added on the upper and bottom boundary of the model. In order to standardize the strength parameter, the failure stress along vertical axis is divided by the cohesion of the fracture. As seen in the Fig. 3.20a, the failure mode of the fractured rock sample can be divided by the different orientations of the fracture. The concave shape of the curve and lower unconfined compressive strength indicate that the failure occurred along the fracture plane. The higher values around 0°, 90°, and 180° mean that failure occurred in the intact rock mass. When the fracture orientation is about 60°, the strength of the fractured rock mass has the minimum value. Although there are some small variations, overall values and tendencies from the model of Attewell and Sandford (1974) are fitted well by the elasto-plastic rock mass model.

In the second parametric study, the experimental results collected by Priest (1993) are compared to the model predictions. Both results are come from the triaxial test conditions with the different confining stress. In this case, the effect of orientation for different confining stresses is also measured. As can be seen in Fig. 3.20b, the fractured rock strength has same tendency in the different confining stress variation. However, the higher confining stresses increase the normal stress along the fracture plane, and finally the failure stress get greater value. Although

the different confining stresses make different failure stress, the range of the fracture orientation in terms of the failure mode remains as almost same. When the results from the simulation and the experiment are compared, both data have similar tendency in the fracture orientation range from 50° to 90°. However for the smaller range of the fracture orientation from 0° to 40°, the differences between the simulation and experiment increases. Since the horizontal part in the simulation results originally mean the yielding in the intact rock mass, the experimental result in the range from 10° to 40° indicates the actual failure in the experiment is occurred in the fracture plane. In the experiment, however, it should be noted that it is very difficult to maintain the boundary condition of the fractured rock sample in the lab experiment. Priest (1993) has analyzed the data gap as the weakening effect along the fracture plane.

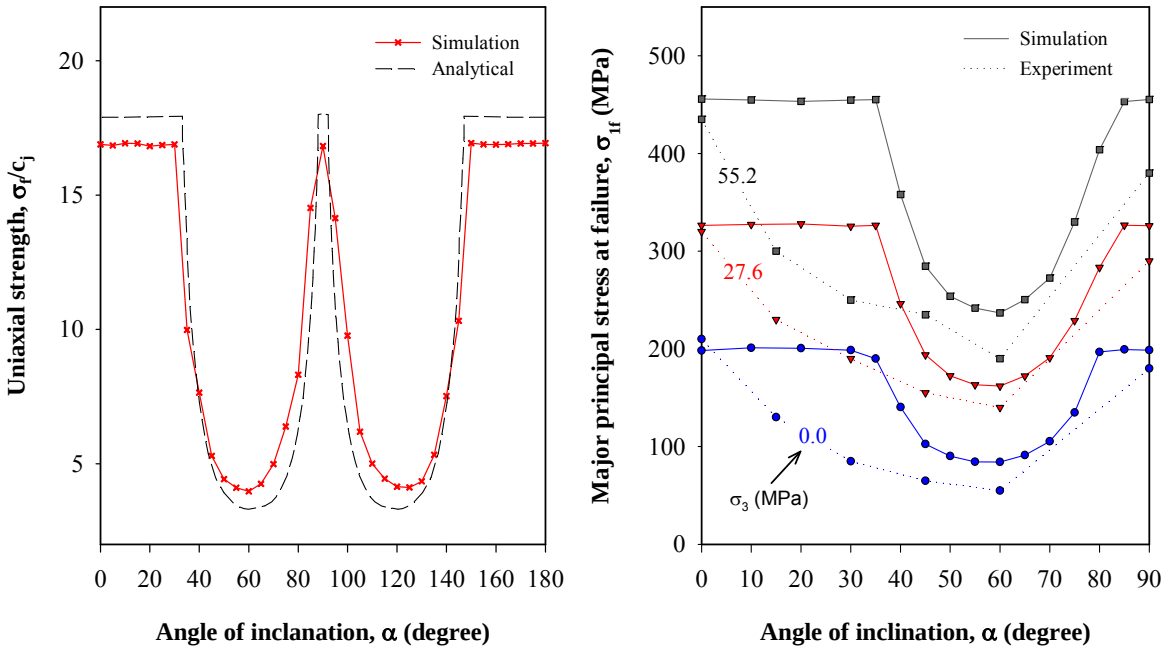

(c) Analytical model from Attewell and Sandford (1974)

(a) Experimental data from Priest (1993)

Fig. 3.20 - Strength comparisons of fractured rock. a) simulation vs. analytical solution, and b) simulation vs. experimental data).

Yoshinaka and Yamabe (1986) conducted biaxial loading experiments for fractured rock samples with two fracture sets. Figure 3.21 shows the details of their fractured rock sample. They made different samples using various fracture orientation combinations and the different mechanical parameters of the fractures. The first fracture orientation is varied from 0° to 45° counterclockwise from the *x*-axis, and the second fracture set is arranged along perpendicular direction from the first fracture set. After the initial confining stress is applied to all surrounding surface, the deviatoric stresses are added on the upper and bottom boundary until the sample get failed. The FLAC simulations identically followed all the conditions and material properties for the comparison. The material properties used in the simulation is summarized in the below Table 3.7. In addition, fracture stiffness parameters are assumed based on the values of the Young's modulus of the intact rock, and the fracture smoothness.

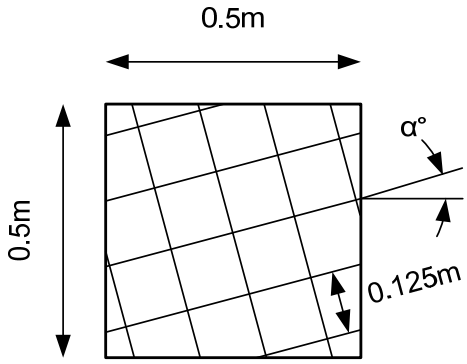

Fig. 3.21 - Details of the fractured rock specimen

Table 3.7 - Material property of intact rock and fracture planes.

Fracture surface	**Young's modulus of intact rock**	**Poisson's ratio of intact rock**	**Cohesion of fracture**	**Internal friction angle of fracture**
Smooth fracture	2.45 GPa	0.2	74.6 kPa	37°
Rough fracture	2.45 GPa	0.2	22.6 kPa	33°

Stress-stain curves from the different fracture orientation are obtained from the elasto-plastic rock mass model, and then compared to the experimental results collected by Yoshinaka and Yamabe (1986). By changing of the smoothness and orientation of fracture, different stress-strain curve are yielded and are summarized as in below Fig. 3.22. As seen in the figures, different fracture smoothness and orientation make variation of the stress-strain curves. The model predictions generally agree with the experimental data.

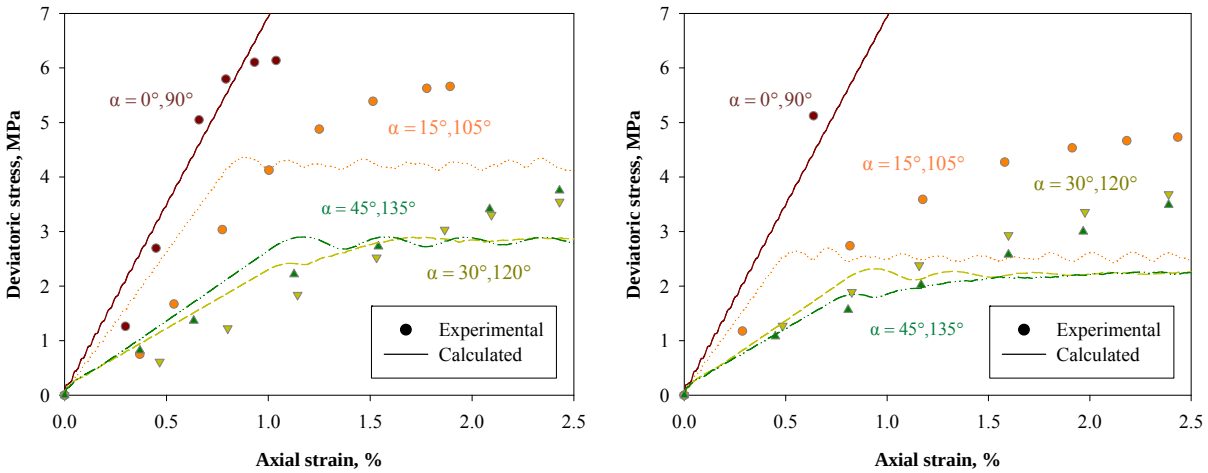

Fig. 3.22 - Stress-stain curves of fractured rock mass from experimental and numerical studies (left: smooth fracture surface, right: rough fracture surface)

Contrary to the experimental results, the simulation results show more obvious perfect plasticity tendency after the yielding stress. If the fracture orientations are 0° and 90°, the failure of the fractured rock is depend on the surrounding rock's strength. In the simulation, thus the stress-strain curves for the case show only linear elastic behavior. As the orientation is increased, however, the fracture sets take the main role of the failure, and the stress-strain curve are converged when the fracture orientations are 30° and 120°. Although there are small variations between the experiment and simulation, overall results are matched very well. From the two different parametric studies, it is possible to confirm that the simulation for the fractured rock mass including two fracture sets can generate reasonable outputs.

3.4 Stochastic Modeling of CO_2 Injection

The stochastic modeling procedures described above are illustrated using idealized two-dimensional geometries of CO_2 geological sequestration. The two-dimensional stochastic analysis of CO_2 sequestration is divided into two parts: CO_2 injection and CO_2 plume migration, due to the reason that the two parts follow two different dominant physical processes. During the injection process of CO_2, the dominant physical flow is advection flow, meaning that the CO_2 is transported by the fluid motion. While during CO_2 plume migration, the transport mechanism of CO_2 is diffusion-dispersion, which describes the molecular movement of particles/ molecules from regions of higher concentration to regions with lower concentration. Because of the different driving mechanisms of the processes during CO_2 sequestration, two kinds of simulations will be performed to investigate the uncertainty of the two processes respectively.
The random fields were generated using HYDRO_GEN first. The data representing random fields of formation properties, intrinsic permeability and porosity, is then stored in a text file. The information of random fields from the text file is imported into the input file of TOUGH2, by several stand-alone FORTRAN and MATLAB programs, before each realization of Monte Carlo simulation. The desired results from each realization are extracted by the FORTRAN and MATLAB programs at the end of TOUGH2 run for this realization, for the purpose of data analysis and visualization.

3.4.1 Results for the Injection Phase

A Monte Carlo simulation of 200 realizations with random input of intrinsic permeability and porosity was performed with a simulated injection time of 10 years. The computer on which the simulation was performed is HP Pavilion P6000 series with a processor of AMD Phenom(tm) II X4 830 2.8 GHz and 6 GB RAM, and computer running time was about 17 hours. Fig. 3.23 shows the locations of the observation spots, with the purpose of obtaining a direct and better understanding of the simulation process and results. As shown in Fig. 3.23, the size of the each element/block is 100 m (in *y* direction) × 10 m (in *z* direction) per unit width (1 m) in *x* direction. The definition of correlation length was discussed above, and correlation lengths in y direction and z direction are 200 m and 15 m, respectively.

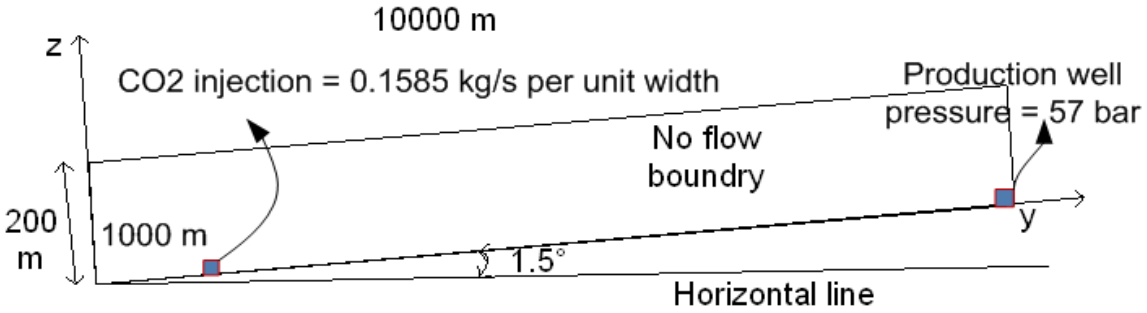

Fig. 3.23 - Schematic representation of the injection simulation domain.

Figs. 3.24 and 3.25 show CO_2 saturation profiles at different time for a single realization and CO_2 saturation profiles at injection time = 10 years for 5 realizations, respectively. It can be seen that in CO_2 is aggregating around the injecting well as injecting time elapsed (Fig. 3.25), and significantly difference shape of saturation profiles over the whole domain can be observed in Fig. 3.25. This significant uncertainty needs to be quantitatively evaluated by observations of other quantities. Figs. 3.26, 3.29, 3.32 and 3.35 show observation quantities at specific locations evolving with time for each realization. These observation quantities are: pore pressure at the middle point (5000 m); liquid flow rate at left interface of middle block (5000 m); total low rate at production well and CO2 saturation at the surface of the domain. Figs. 3.26 and 3.29 both exhibit very wide range of the curve distribution, indicating that the corresponding quantities, well pressure and middle point interface liquid CO_2 flow rate have more variations, especially the latter one. Figs. 3.27 and 3.28, Figs. 3.30, 3.31, 3.33 and 4.34 as well as Figs. 3.26 and 3.27 are their respective normal probability plot and histogram plot at the end of simulation time (time = 10 years). Most of them are self-explanatory. It should be noted that a normal probability plot can assess whether the data is coming from a normal distribution. If the data is normally distributed, the data points (blue cursors) will be located on or close to the red line. Therefore if the data is from other distributions, the data points will curve away from the red line.

A quantile-quantile plot can be used to find out if two sets of data are following the same distribution, as shown in Fig. 3.38. The four observation quantities are paired up with one another to generate quantile-quantile plots, and the good linearity of each plot suggests that they are all from the same distribution. Combining with the previous normal probability plots, it is safe to reach the conclusion that they are normally distributed. The upper and lower bounds of normal distribution estimations with 95% confidence level, of the statistical parameters of the observation quantities, are shown in Table 3.8, along with the statistical properties of the randomized input parameters. The covariance of variations (COV) is an attribute to compare the variation of several data sets when they have different magnitudes of values, and COV is simply calculated by dividing mean value by standard deviation of the data set. It can be seen that most of the COVs are smaller than or equal the COVs of the parameter porosity and intrinsic permeability, except for the interface liquid CO_2 flow rate. Thus it can be concluded that the interface liquid CO_2 flow rate is by comparison more sensitive to heterogeneity.

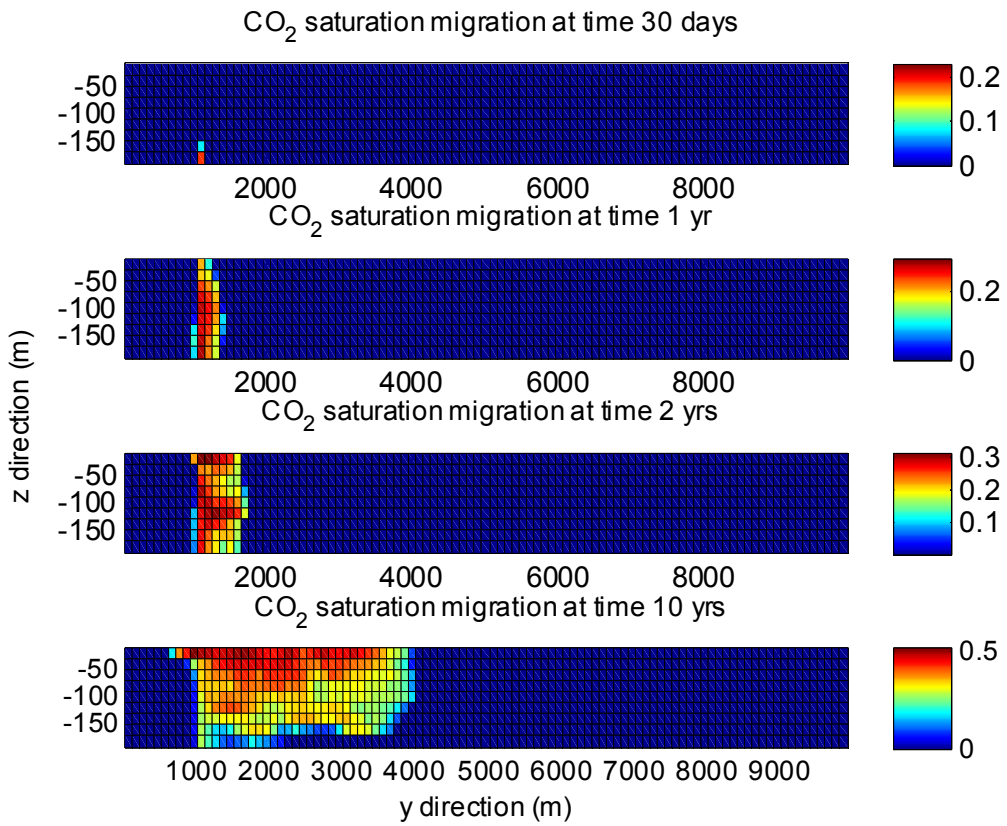

ig. 3.24 - CO_2 saturation profiles at different time, for single realization.

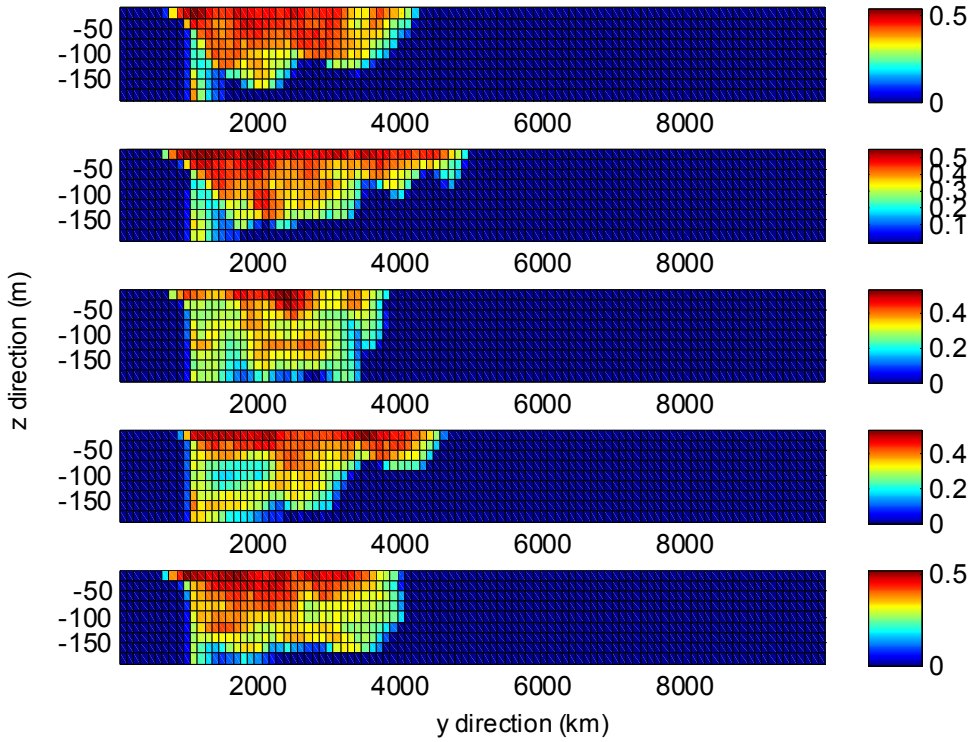

Fig. 3.25 - CO_2 saturation profiles at injection time = 10 years, for 5 realizations.

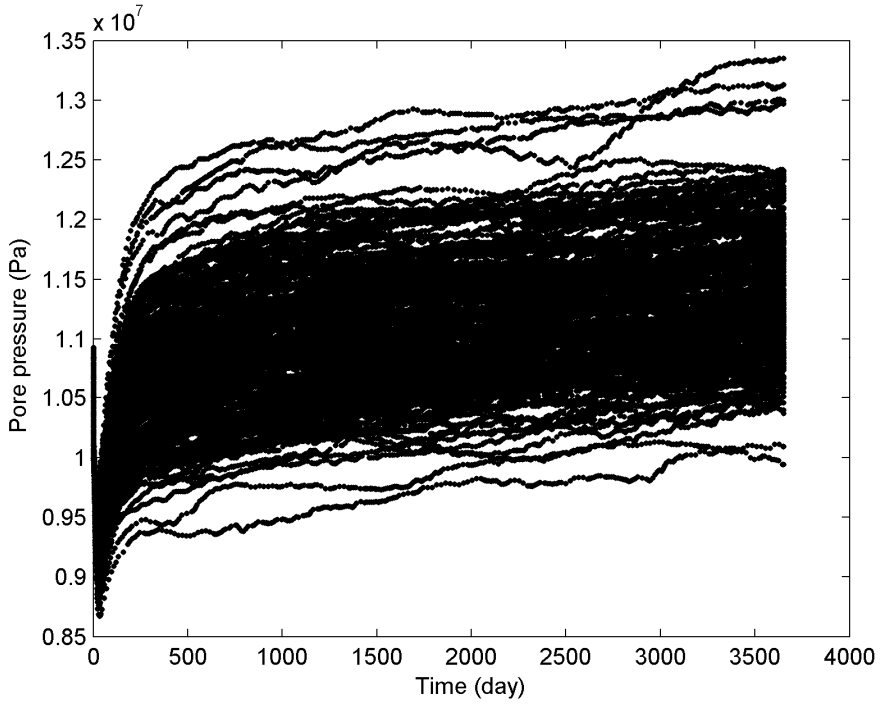

Fig. 3.26 - Pore pressure at the middle point (5000 m) for all realizations.

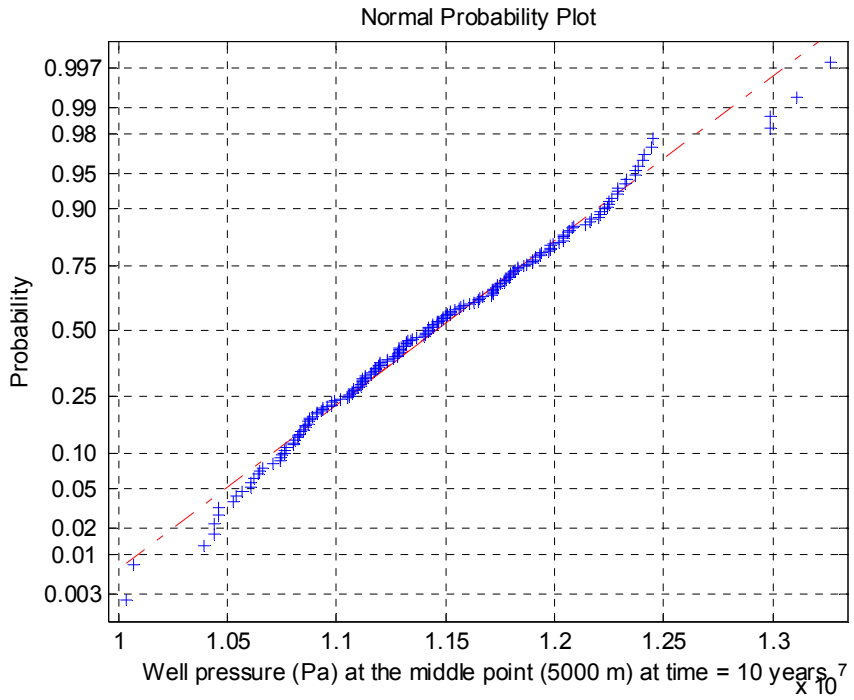

Fig. 3.27 - Normal probability plot for data from well pressure at middle point (5000 m), at time = 10 years for all realizations.

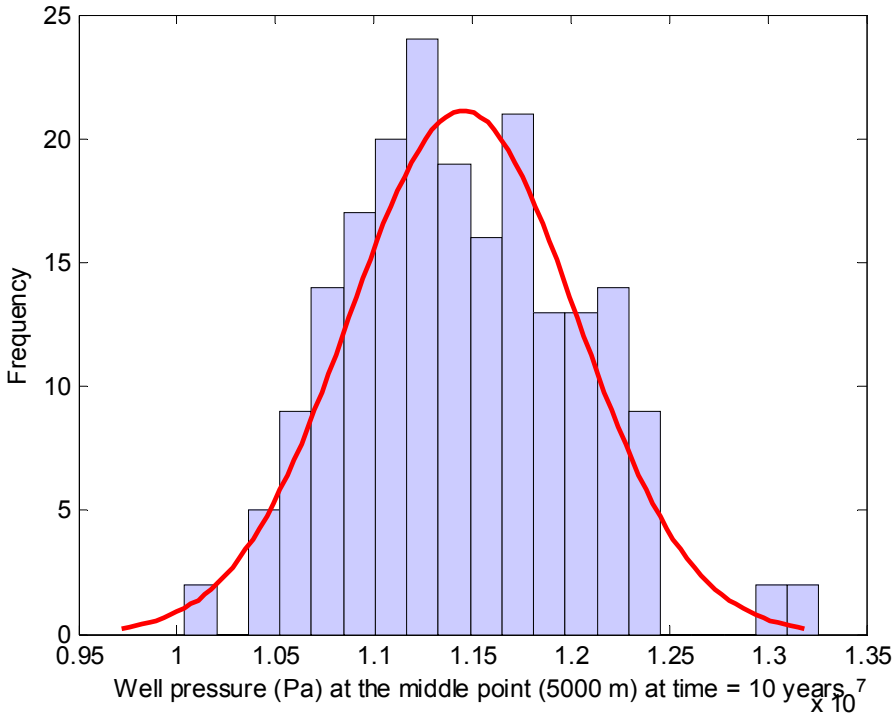

Fig. 3.28 - Histogram for well pressure at the middle point of the simulated domain for all realizations at time = 10 years.

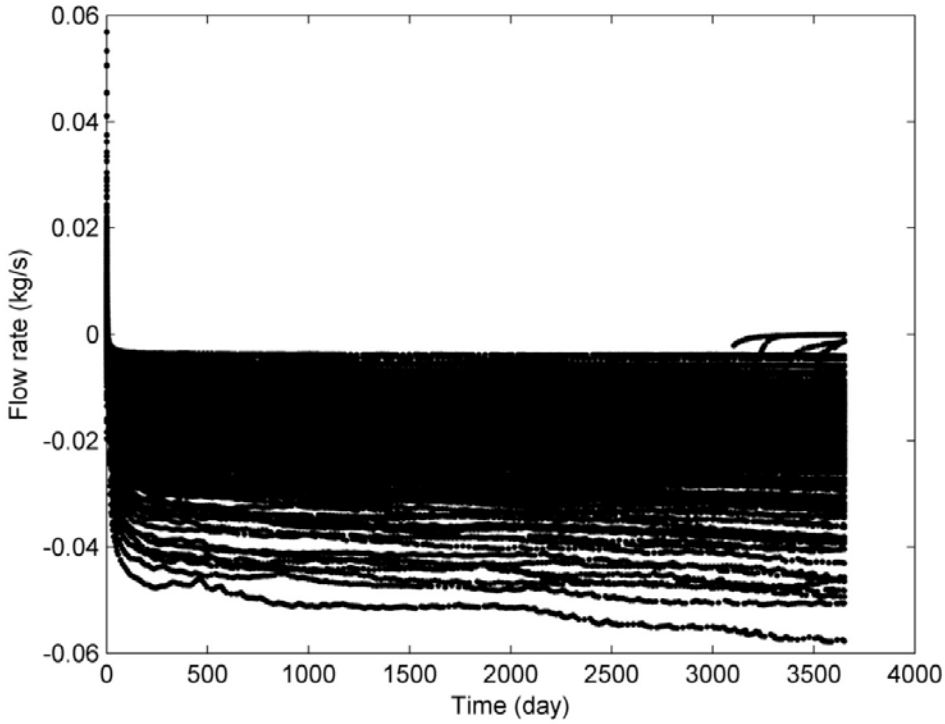

Fig. 3.29 - Liquid flow rate at left interface of middle block (5000 m) for all realizations.

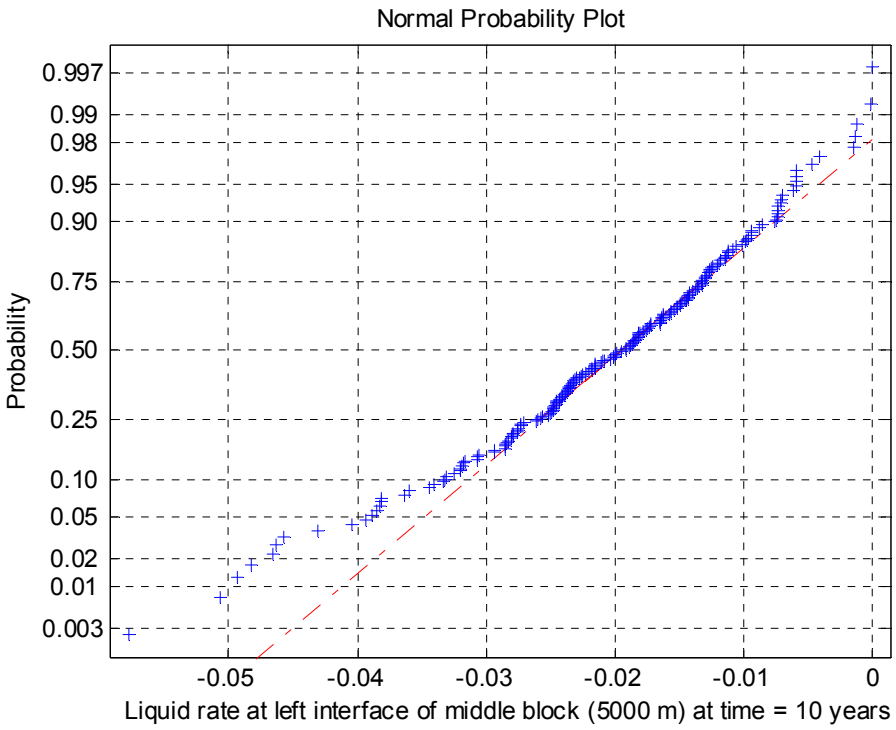

Fig. 3.30 - Normal probability plot for data from liquid flow rate at left interface of middle point (5000 m), at time = 10 years for all realizations.

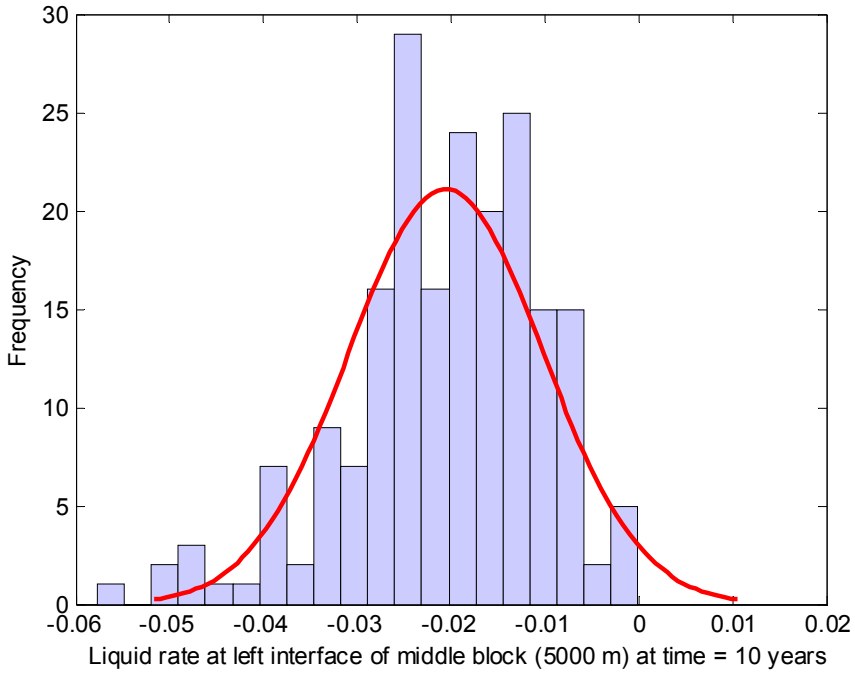

Fig. 3.31 - Histogram for flowing liquid rate at the middle point of the simulated domain, for all realizations at time = 10 years.

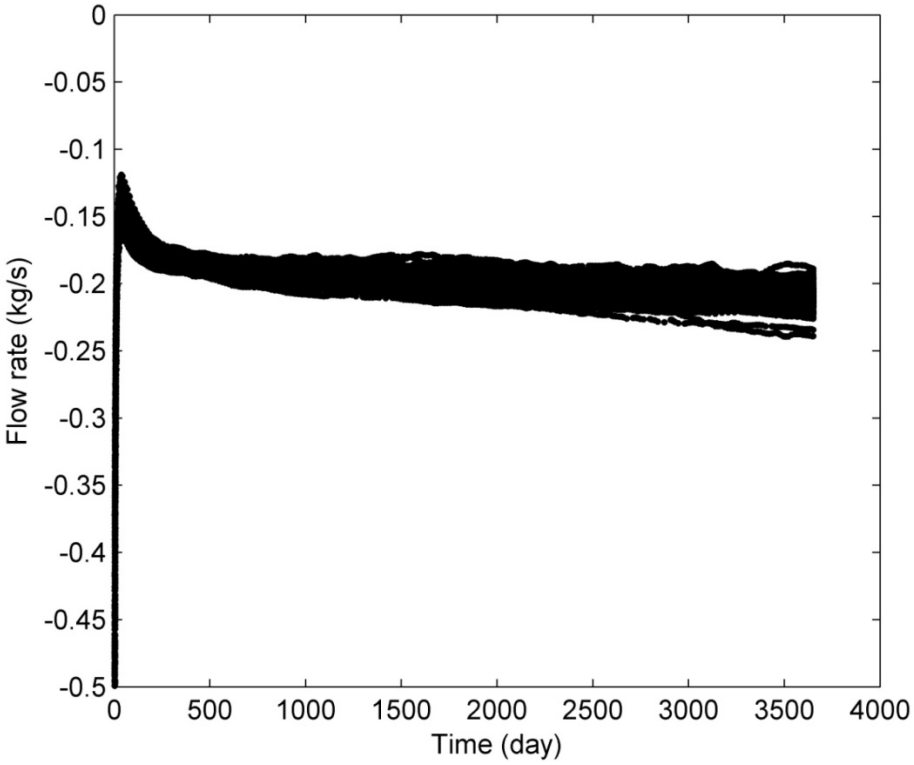

Fig. 3.32 - Total flow rate at production well (kg/s) for all realizations.

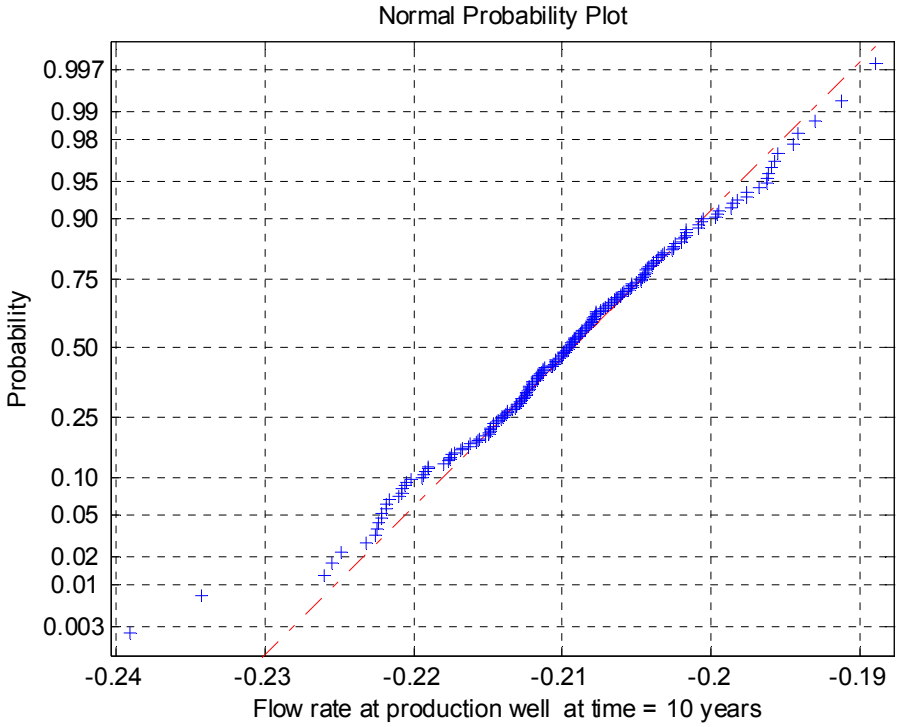

Fig. 3.33 - Normal probability plot for data from total flow rate at production well, at time = 10 years for all realizations.

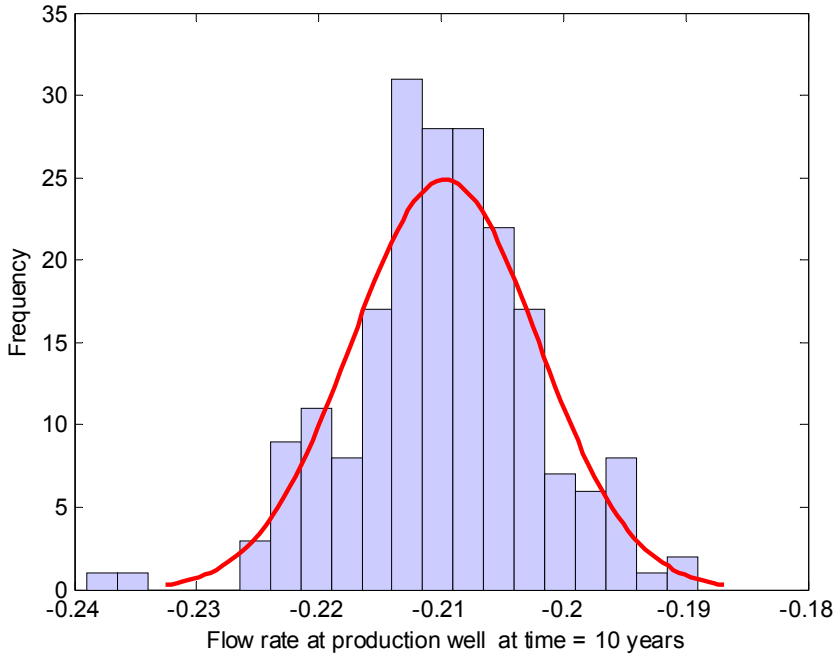

Fig. 3.34 - Histogram for flow rate at production well for all realizations at time = 10 years.

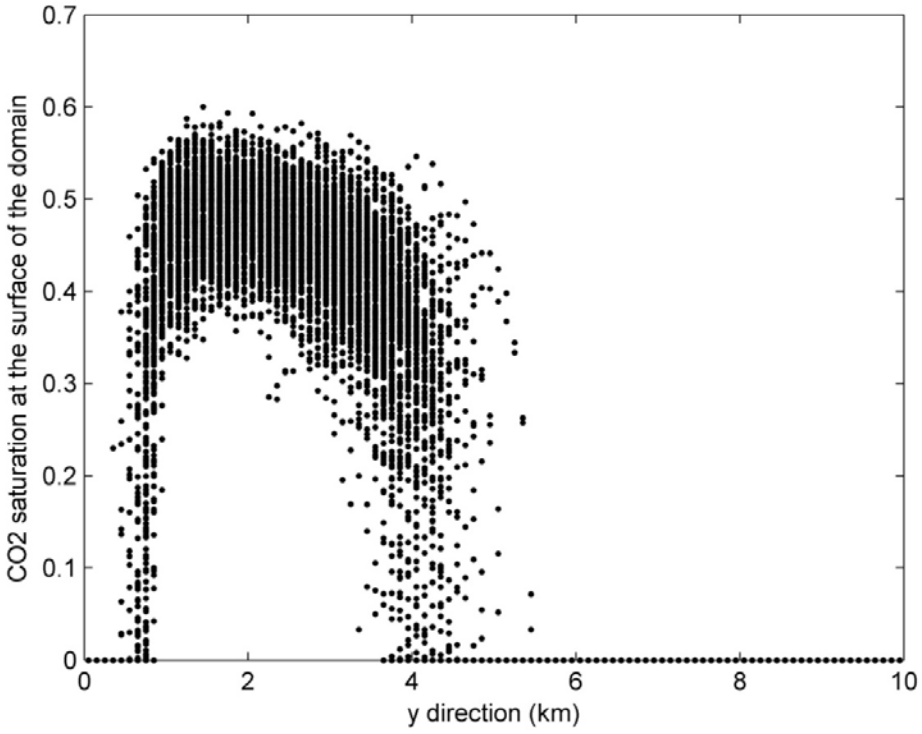

Fig. 3.35 - CO2 saturation at the surface of the domain for all realizations.

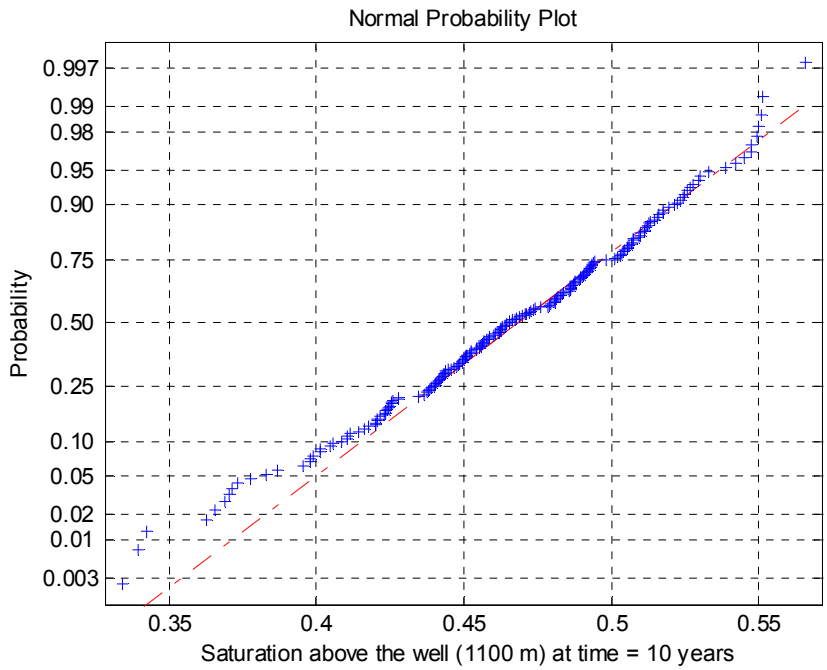

Fig. 3.36 - Normal probability plot for data from CO_2 saturation at 1100 m (above the well) for all realizations at time = 10 years.

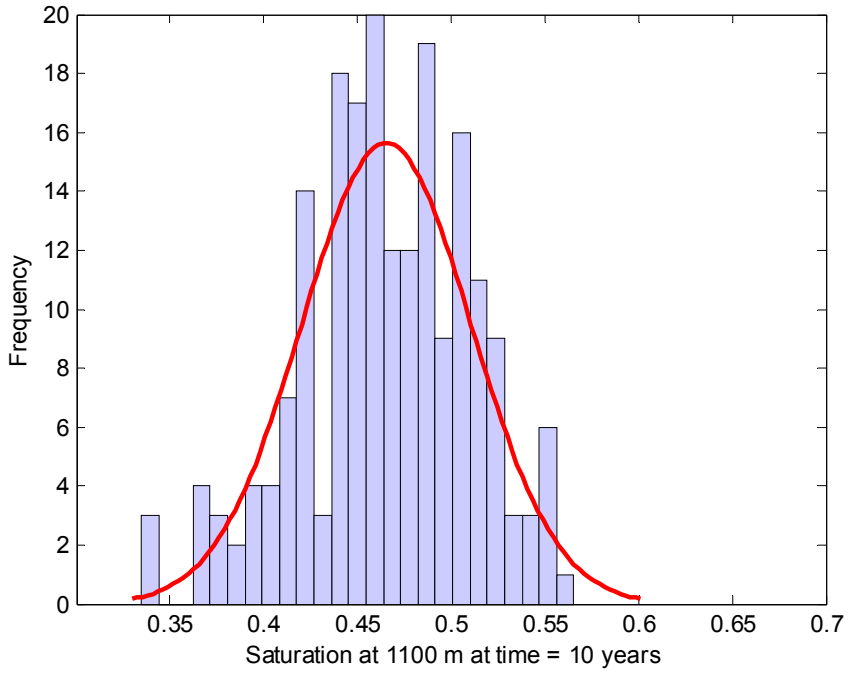

Fig. 3.37 - Histogram for CO_2 saturation at 1100 m (above the well) for all realizations at time = 10 years.

Note that the results were obtained using random input of both intrinsic permeability and porosity. In order to investigate the influence of the spatially correlated intrinsic permeability field and the spatially correlated porosity field on the results, two more simulations with random

input of each parameter were performed, and compared to the previous simulation. The statistical description of the three types of simulation is shown in Table 3.9. It can be observed in the column of COV values, that the COVs obtained from the results of random permeability input-only simulation is times larger than the ones obtained from the results of random porosity input-only simulation. In addition, the former COVs are close the ones obtained from simulation with both random permeability and porosity input. This observation indicates that most of the uncertainty is contributed by the variation of intrinsic permeability.

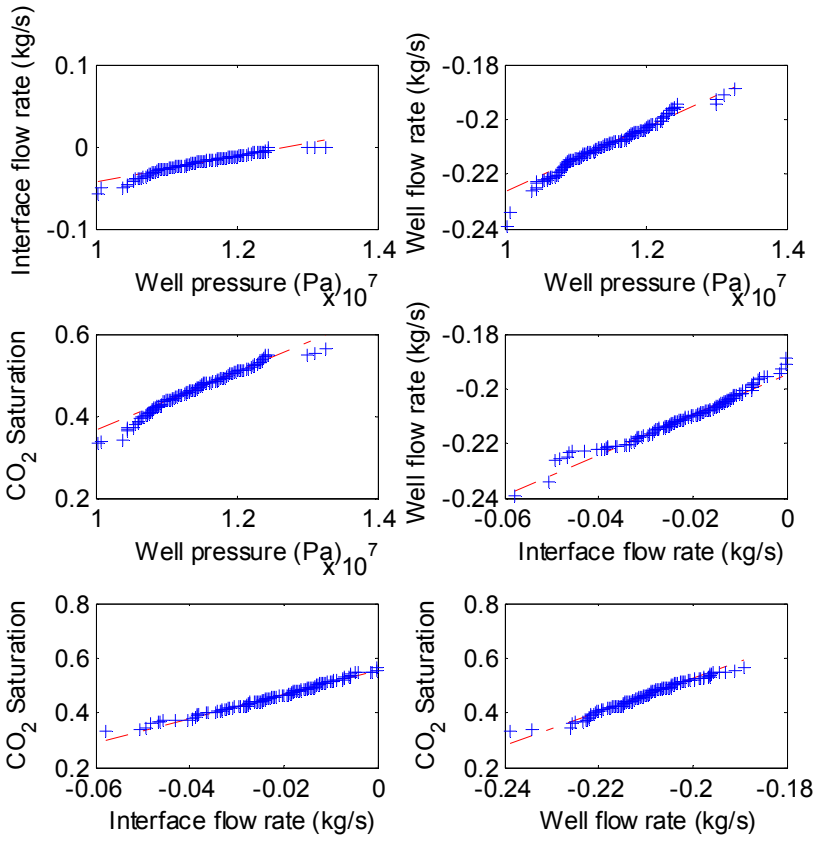

Fig. 3.38. Quantile-quantile plots from every pair of two quantities.

Table 3.8. Statistical description of results from injection simulation.

	Mean	Standard deviation (STD)	Coefficient of variance (COV)	Normal mean estimation with 95% confidence		Normal STD estimation with 95% confidence	
				Lower	Upper	Lower	Upper
Log(permeability) (mD)	6.21	0.6	0.097	N/A	N/A	N/A	N/A
Porosity	0.35	0.063	0.18	N/A	N/A	N/A	N/A
Pressure (bar)	114.53	5.78	0.051	113.73	115.34	5.26	6.41
Interface liquid flow rate (kg/s)	-0.0205	0.010	-0.504	-0.022	-0.019	0.009	0.011
Well flow rate (kg/s)	-0.210	0.0076	-0.036	-0.211	-0.209	0.0069	0.0085
CO_2 saturation above the well	0.465	0.045	0.097	0.459	0.471	0.041	0.050

Table 3.9. Comparisons of statistical description of results from injection simulation with different random input.

	Stochastic parameter	Mean	Standard deviation (STD)	Coefficient of variance (COV)	Normal mean estimation with 95% confidence		Normal STD estimation with 95% confidence	
					Lower	Upper	Lower	Upper
Pressure (bar) at 5000 m	K and ϕ	114.53	5.78	0.051	113.73	115.34	5.26	6.41
	ϕ	117.35	0.397	0.0034	117.30	117.41	0.361	0.440
	K	114.42	5.77	0.050	113.62	115.23	5.26	6.40
Interface liquid flow rate (kg/s)	K and ϕ	-0.0205	0.010	-0.504	-0.022	-0.019	0.009	0.011
	ϕ	-0.0209	1.33×10^{-4}	-0.006	-0.021	-0.021	1.12×10^{-4}	1.48×10^{-4}
	K	-0.0206	0.010	-0.496	-0.022	-0.019	0.009	0.011
Well flow rate (kg/s)	K and ϕ	-0.210	0.0076	-0.036	-0.211	-0.209	0.0069	0.0085
	ϕ	-0.209	0.0012	-0.0059	-0.209	-0.209	0.0011	0.0014
	K	-0.209	0.0073	-0.035	-0.210	-0.208	0.0067	0.0081
CO_2 saturation above the well	K and ϕ	0.465	0.045	0.097	0.459	0.471	0.041	0.050
	ϕ	0.477	0.013	0.026	0.475	0.478	0.011	0.014
	K	0.465	0.043	0.093	0.459	0.471	0.040	0.048

3.4.2 Results for the Migration Phase

As for the migration simulation, the realization number of Monte Carlo simulation is 200, and the computer running time is approximately 21 hours. The simulation time was set to 95.13 years and the simulation was performed with random input of intrinsic permeability and porosity too, only that the distribution of porosity is different from the one adopted in injection simulation. Compared to the test run of 100 realizations, the uncertainty from the 200 realization Monte Carlo simulation is slightly increasing. With the same purpose, a schematic plot showing the observation locations and wells are presented in Fig. 3.39, within which, there is a CO_2-rich region representing the in-place CO_2 after injection. The difference between Figs. 3.23 and 3.39 is that the domain for migration phase in twice longer than injected phase. As shown in Fig. 3.39, the size of the each element/block is 200 m (in y direction) × 20 m (in z direction) per unit width (1 m) in x direction. The correlation lengths in y direction and z direction are 400 m and 30 m, respectively. The same random intrinsic permeability field was adopted. However, a different random field of porosity with smaller mean and standard deviation values is more favorable for trapping the injected CO_2 in a realistic sense.

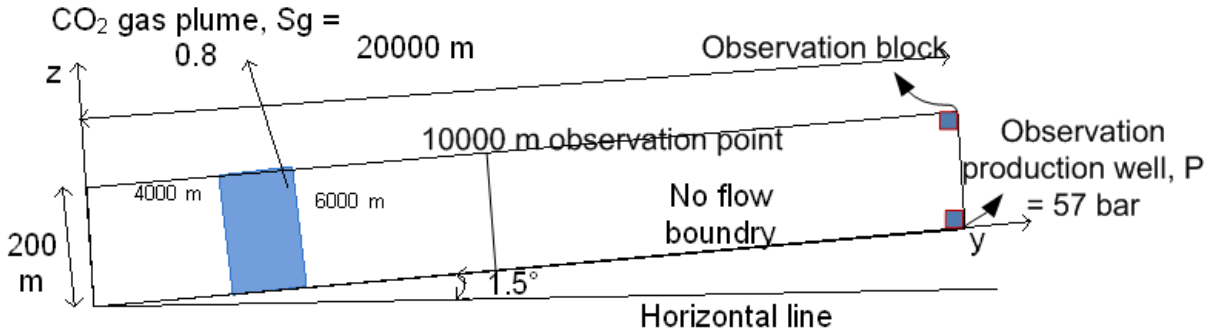

Fig. 3.39. Schematic representation of the migration simulation domain.

In Figs. 3.40, CO_2 saturation profiles at different time for a single realization show that the CO_2 is moving towards the highest elevation point. CO_2 saturation profiles at time = 31.71 years for 5 realizations are shown in Fig. 19, in which CO_2 gas plume has observable different shape in each realization.

As shown in Fig. 3.39, several observation spots are also set and some of the observation quantities are different from the injection simulation. The observation quantities are: CO_2 saturation at upper right hand corner; total CO_2 inflow rate at left interface of middle block (10000 m); flow rate at production well and CO_2 mass fraction at production well. Figs. 3.42 to 3.53 show the observation quantities evolving with time for each realization with their respective normal probability plot and histogram plot at the end of simulation time (time = 95.13 years).

Figure 3.25 shows CO_2 saturation at the surface of the simulation domain for all realizations, in which it can be observed that around 5000 meters, CO_2 saturation are higher than the rest part of the domain surface. According to the normal probability plot (Fig. 3.55), CO_2 saturation at the surface of the plume (5200 m) doesn't follow normal distribution. But according to the quantile-quantile plots in Fig. 3.56, CO_2 saturation at the upper corner of the domain is very likely to follow normal distribution, which would be naturally deductable, considering that the data sets show linearity in every plot for most part, and that the other three quantities are likely normally distributed. It can also be seen in Figs. 3.45 and 3.51 that, the block-to-block flow rate and CO_2 mass fraction are exhibiting more uncertainty than the other two observation quantities, which is reflected in their COVs in Table 3.10 discussed below.

Normal distribution estimations with 95% confidence level, of the statistical parameter of the observation quantities, are performed as well. The estimations bounds are shown in Table 2, with comparisons to the statistical properties of the random parameters. It can be seen that some of the COVs of the observation quantities are larger than the COV of the parameter porosity, but within the same scale of COVs obtained from the injection simulation. It can be observed though, that the CO_2 saturation profiles from the injection simulation are showing more differences than the ones from migration simulation. For example, the high saturation zones and the CO_2 fronts in Fig. 3.22 are very versatile. This may have something to do with the 10 times larger variance of porosity for the injected simulation even though the COVs of porosity for two simulations are not that different.

Table 3.10. Statistical description of results from migration simulation.

	Mean	Standard deviation (STD)	Coefficient of variance (COV)	Normal mean estimation with 95% confidence		Normal STD estimation with 95% confidence	
				Lower	Upper	Lower	Upper
Log(permeability) (mD)	6.21	0.6	0.097	N/A	N/A	N/A	N/A
Porosity	0.15	0.02	0.13	N/A	N/A	N/A	N/A
CO_2 saturation at the corner	0.711	0.016	0.023	0.709	0.713	0.015	0.018
Interface total flow rate (kg/s)	-0.0013	4.94×10^{-4}	-0.377	-0.0014	-0.0012	4.50×10^{-4}	5.48×10^{-4}
Well flow rate (kg/s)	-0.0044	9.79×10^{-4}	-0.223	-0.0045	-0.0042	0.0009	0.0011
CO_2 mass fraction	0.1827	0.08	0.44	0.1714	0.1939	0.0732	0.0891

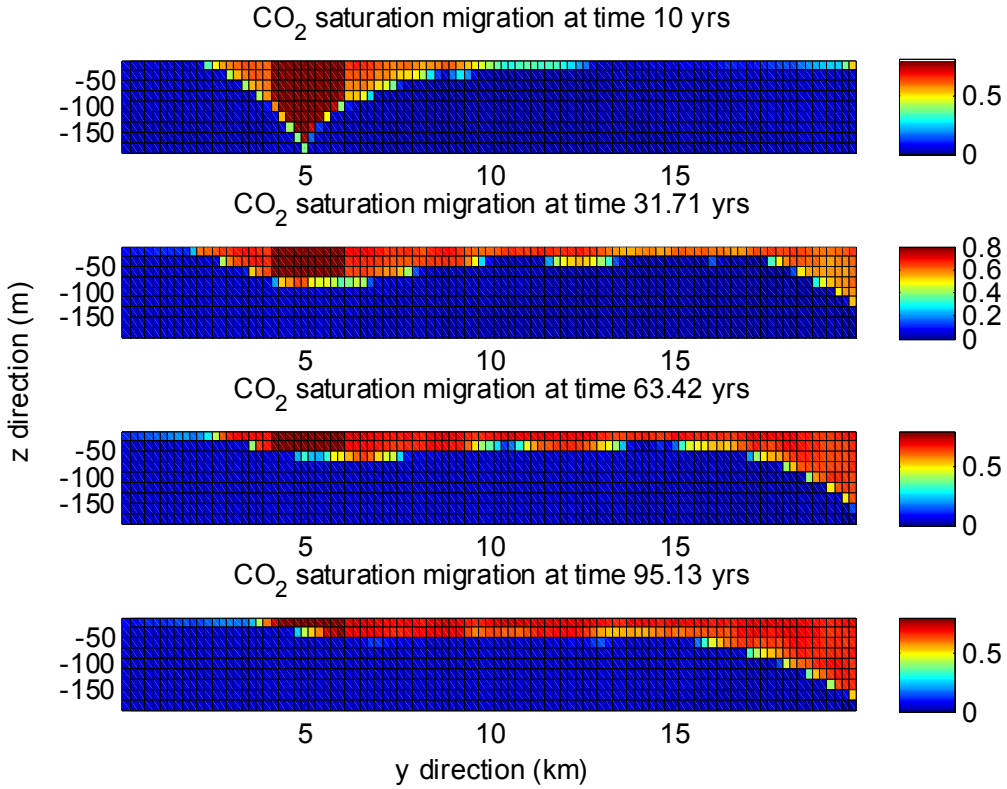

Fig. 3.40 - CO_2 saturation profiles at different time, for single realization

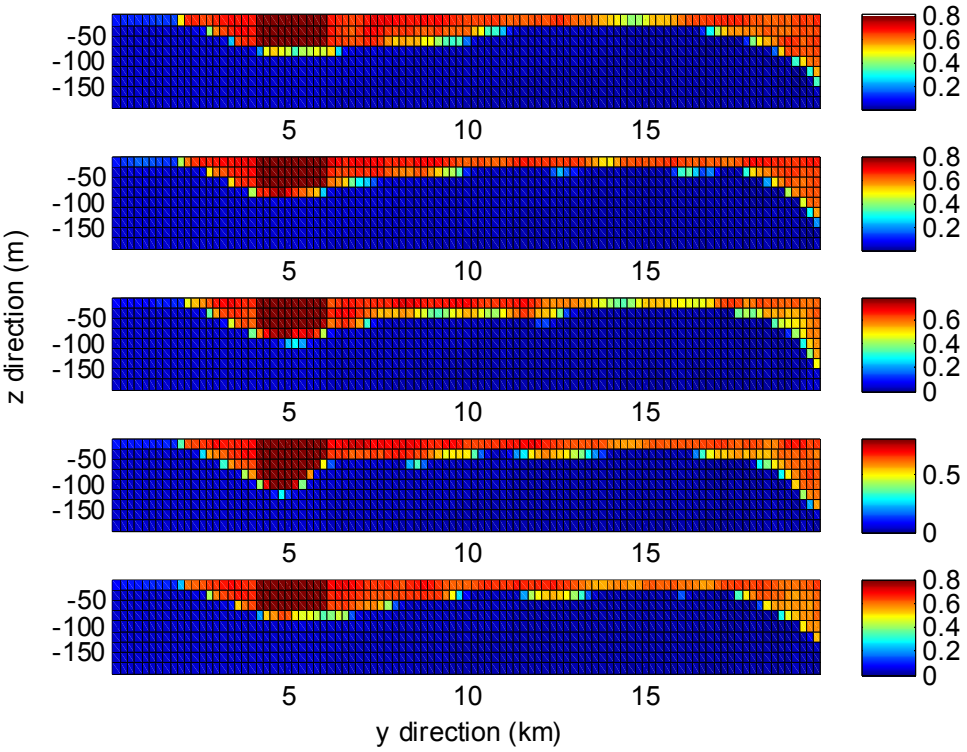

Fig. 3.41 - CO_2 saturations at time = 31.71 years, for 5 realizations.

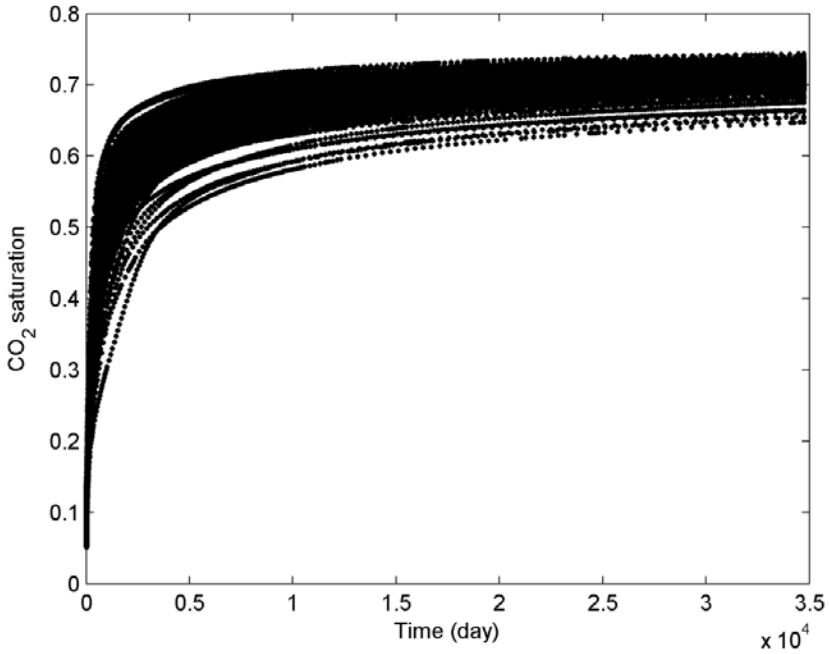

Fig. 3.42 - CO_2 saturation at upper right hand corner.

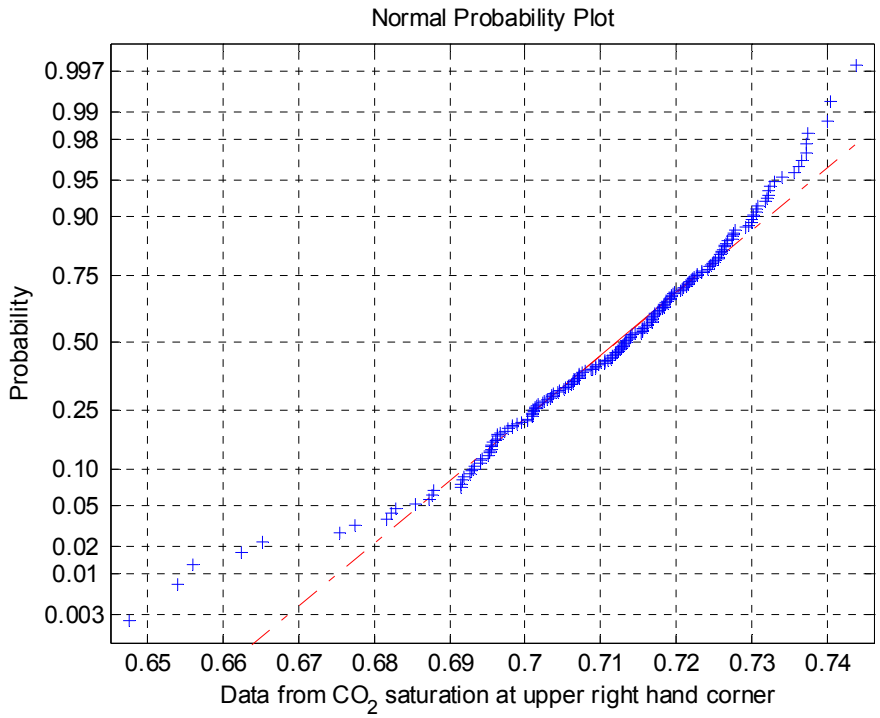

Fig. 3.43 - Normal probability plot for data from CO_2 saturation at upper right hand corner, at time = 95.13 years for all realizations.

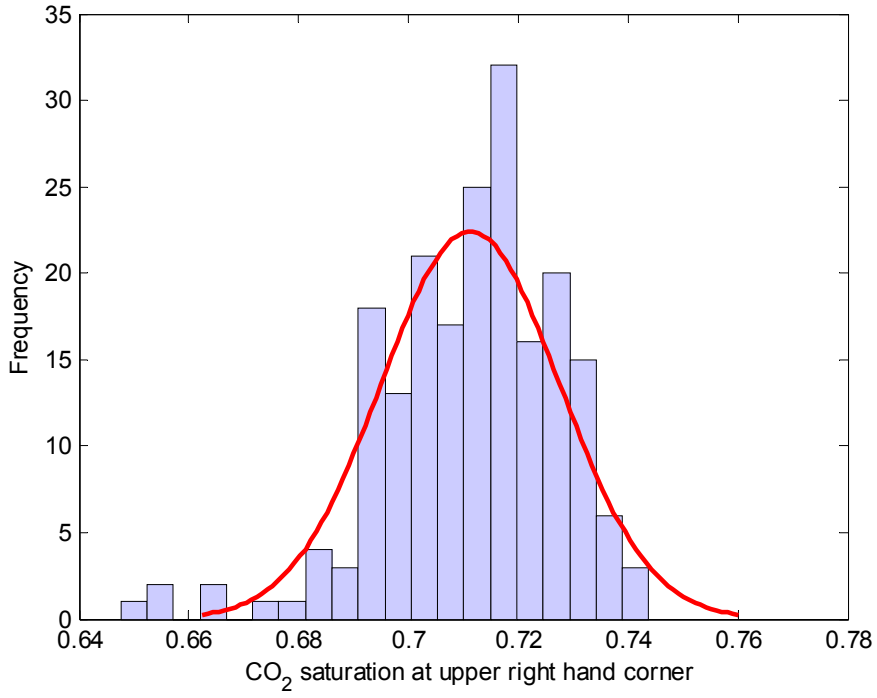

Fig. 3.44 - Histogram for CO_2 saturation at upper right hand corner, at tim e = 95.13 years for all realizations.

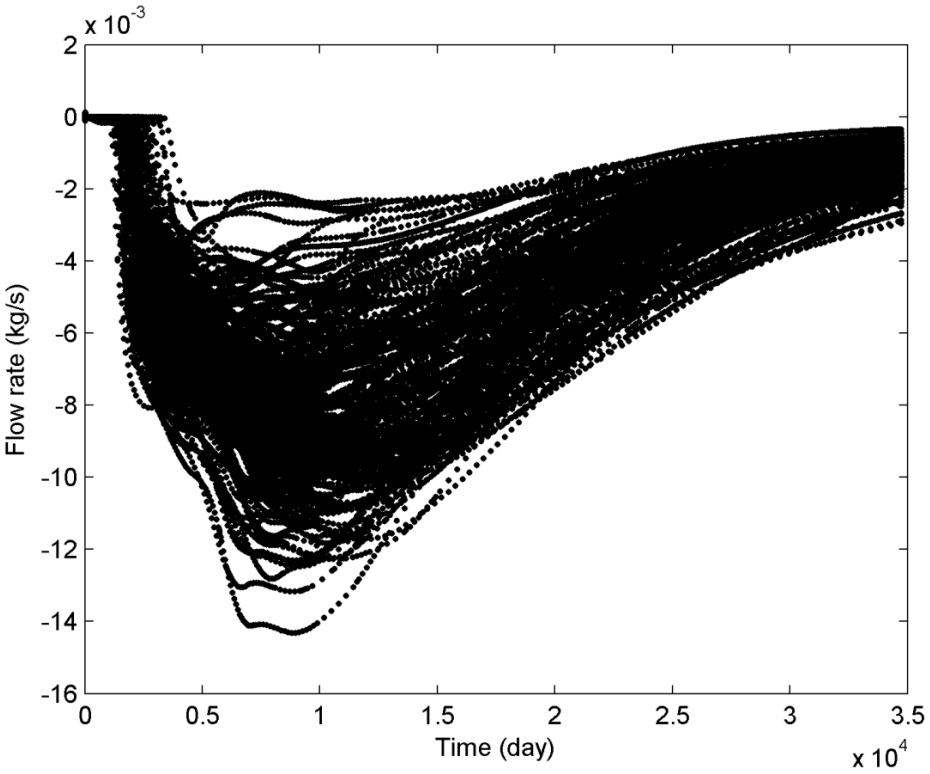

Fig. 3.45 - Total CO_2 inflow rate at left interface of middle block (10000 m).

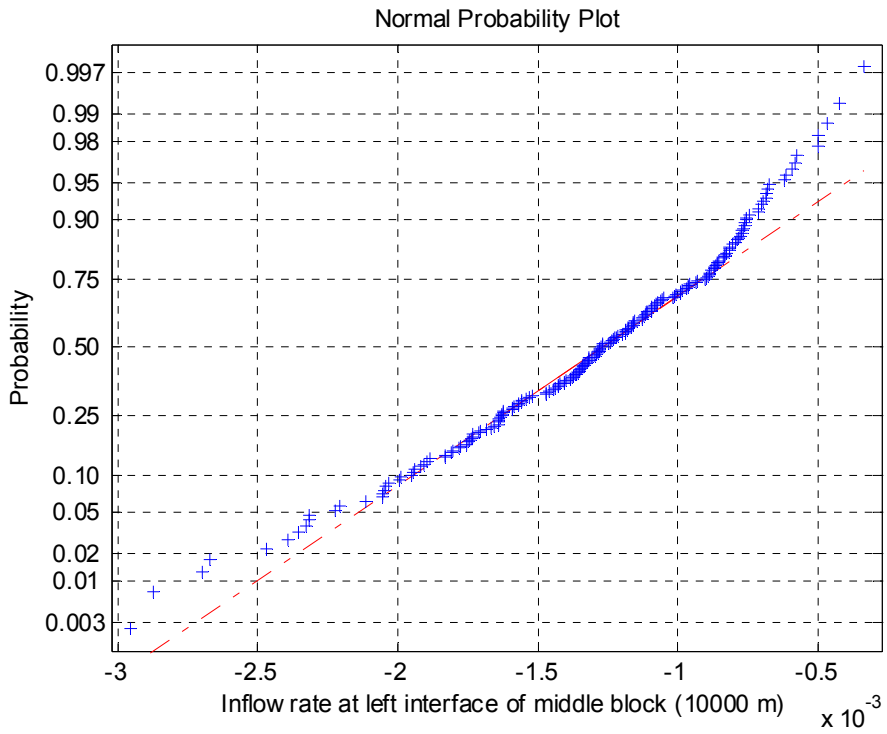

Fig. 3.46 - Normal probability plot for data from total CO_2 inflow rate at left interface of middle block (10000 m), at time = 95.13 years for all realizations.

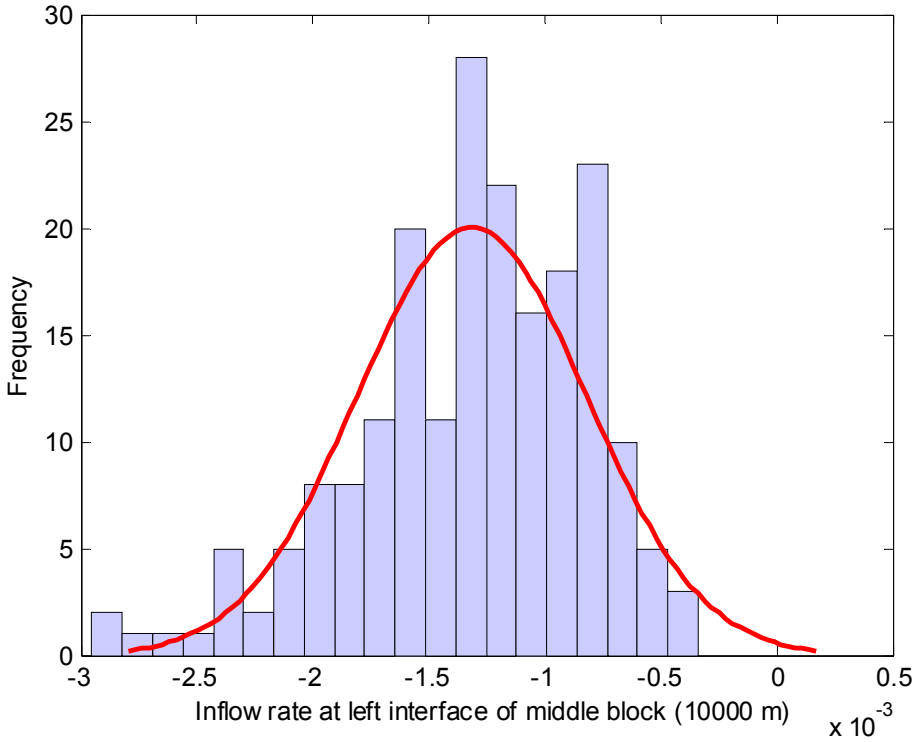

Fig. 3.47 - Histogram for total CO_2 inflow rate at left interface of middle block (10000 m), at time = 95.13 years for all realizations.

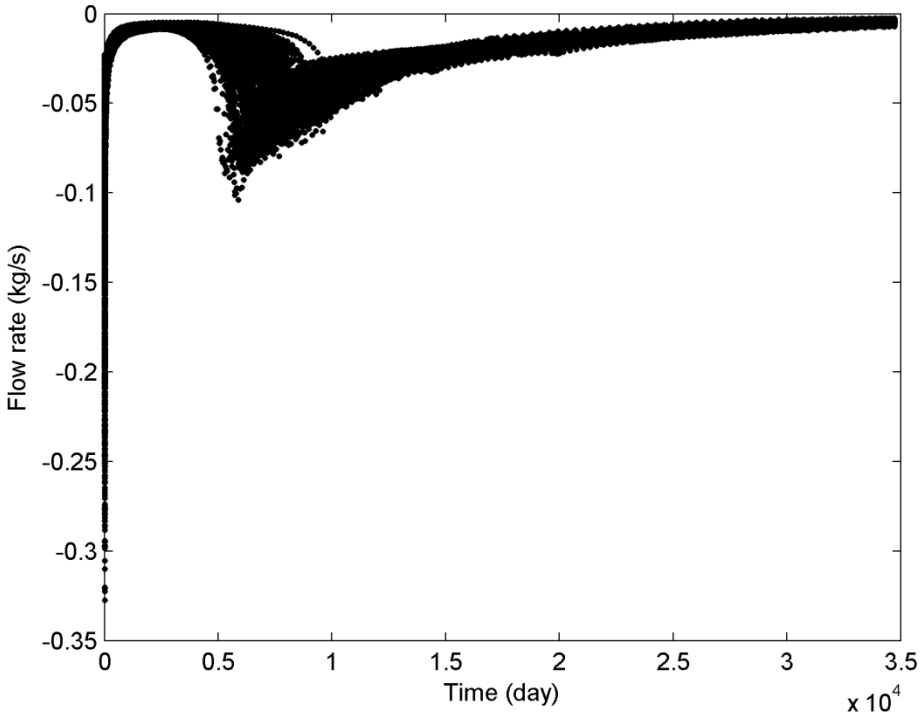

Fig. 3.48. Flow rate at production well (kg/s)

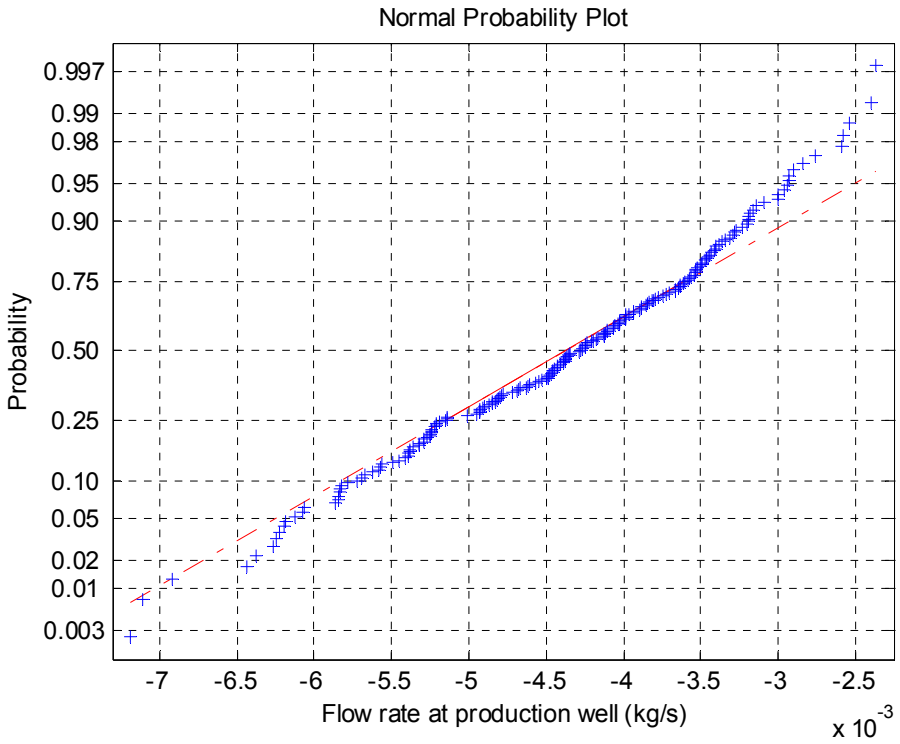

Fig. 3.49 - Normal probability plot for data from total flow rate at production well at time = 95.13 years for all realizations.

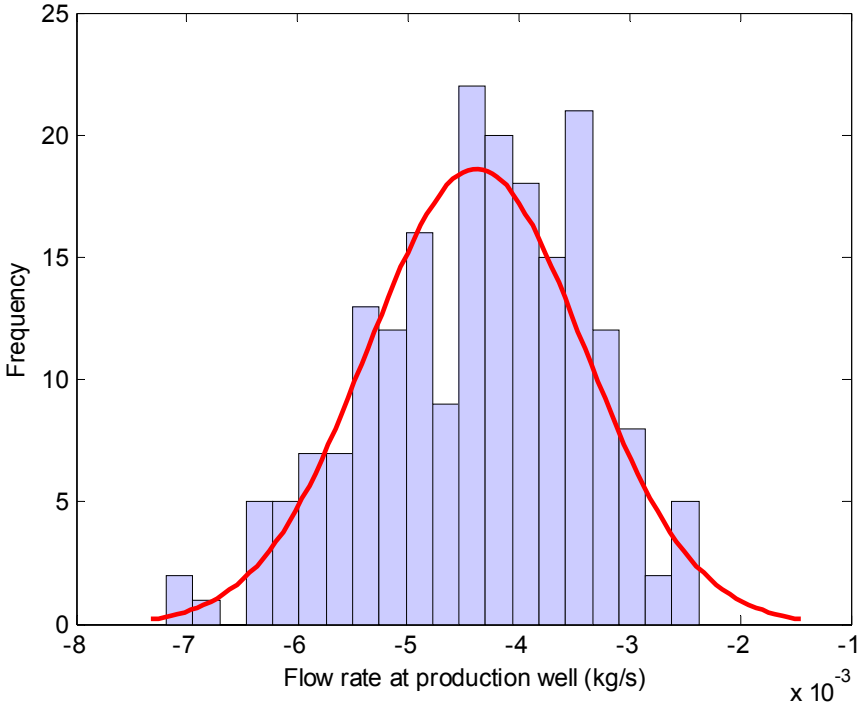

Fig. 3.50 - Histogram for total flow rate at production well at time = 95.13 years for all realizations.

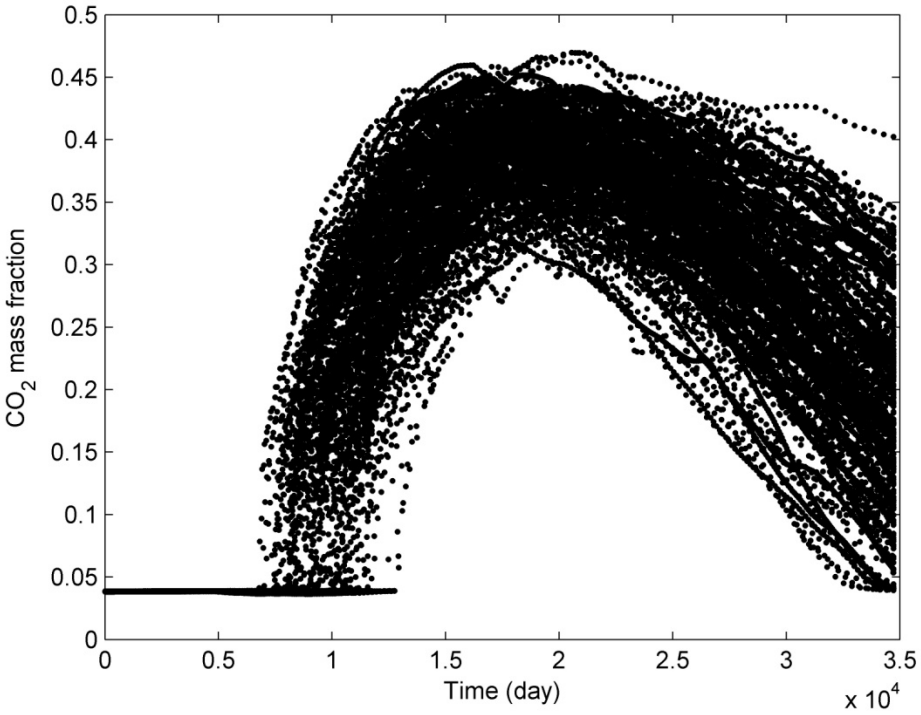

Fig. 3.51 - Flowing CO_2 mass fraction at production well.

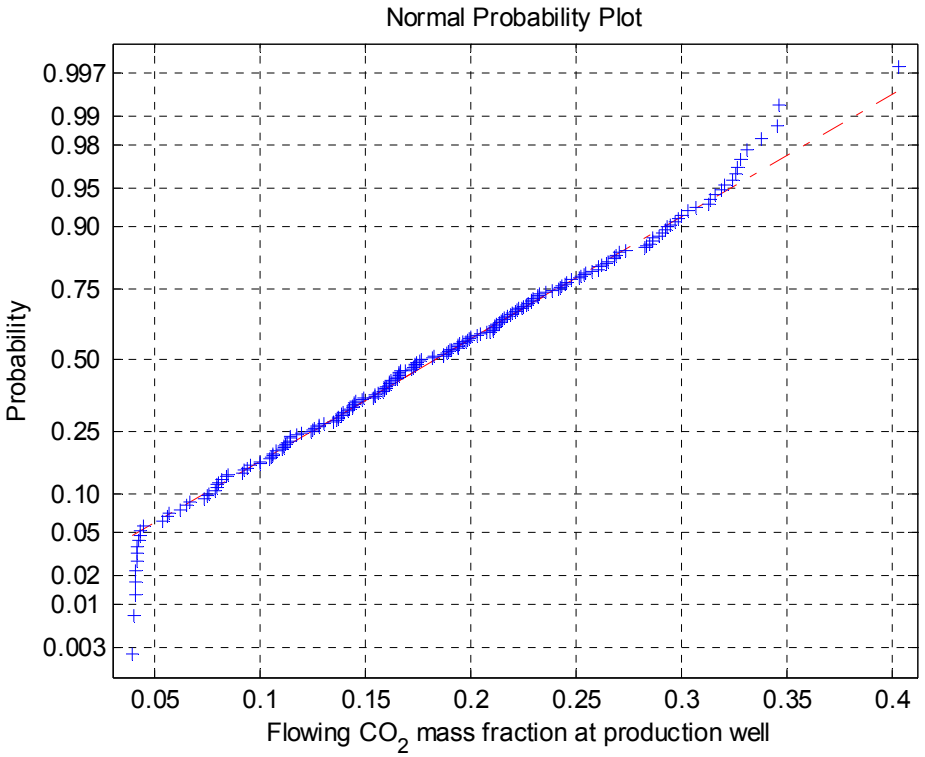

Fig. 3.52 - Normal probability plot for data from flowing CO_2 mass fraction at production well at time = 95.13 years for all realizations.

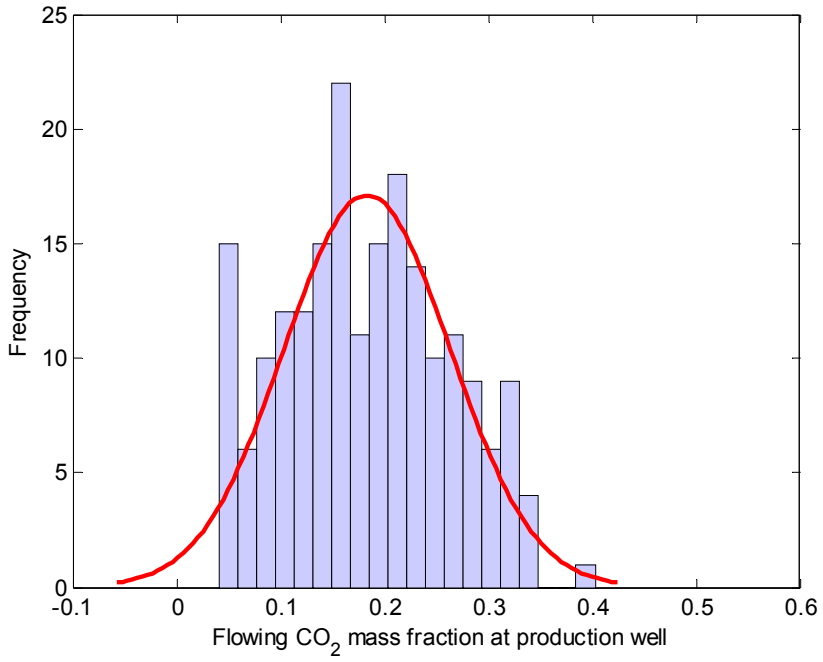

Fig. 3.53 - Histogram for flowing CO_2 mass fraction at production well at time = 95.13 years for all realizations.

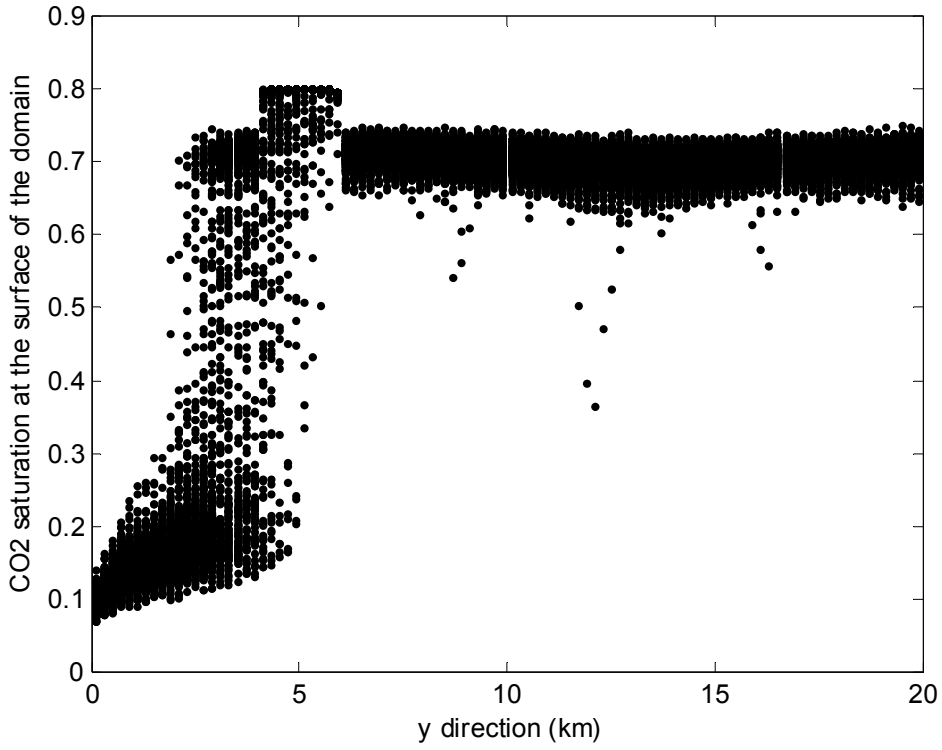

Fig. 3.54 - CO_2 saturation at the surface of the domain for all realizations.

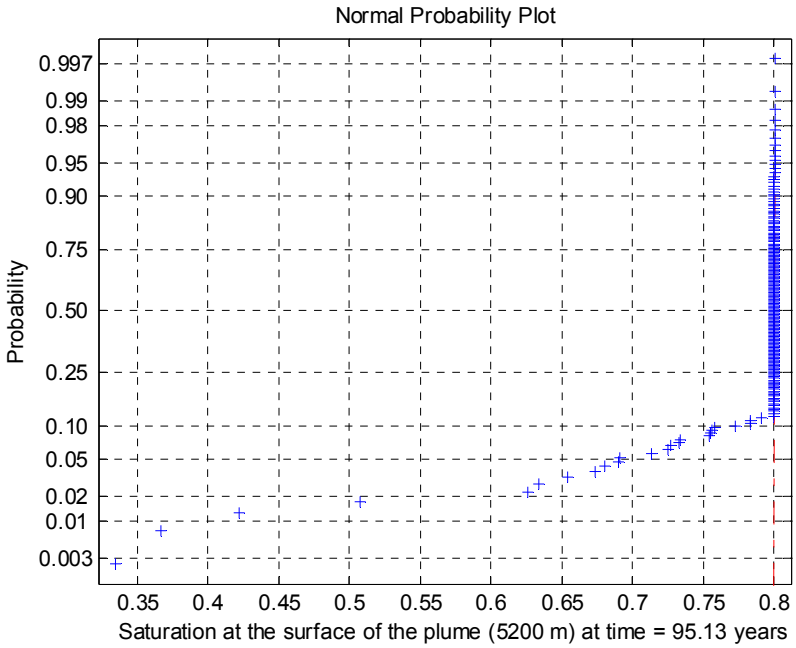

Fig. 3.55 - Normal probability plot for data from CO_2 saturation at the surface of the plume (5200 m), at time = 95.13 years for all realizations.

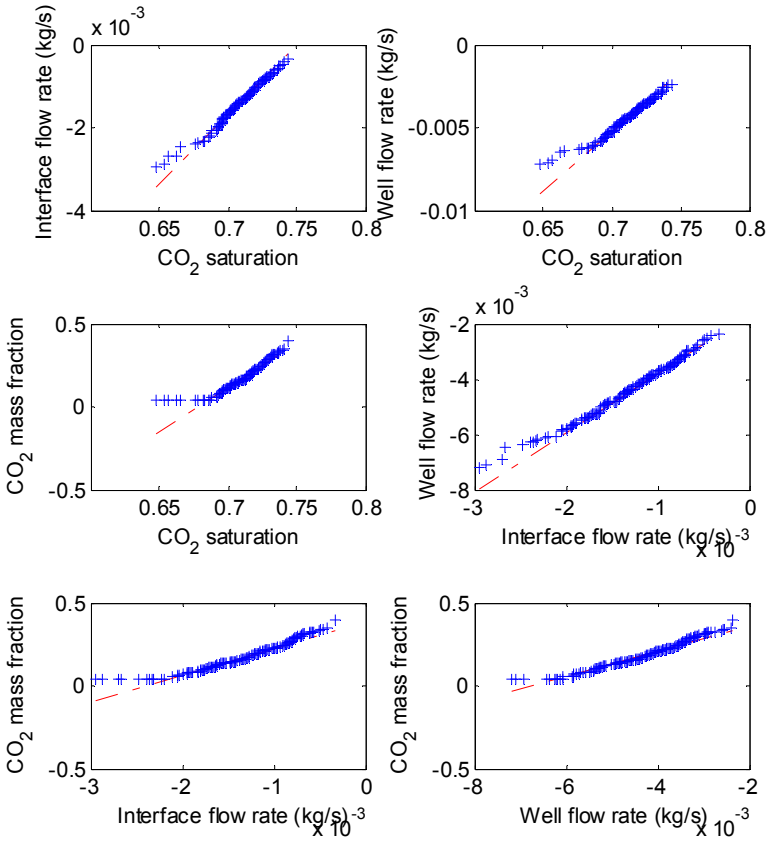

Fig. 3.56 - Quantile-quantile plots from every pair of two quantities.

Another two simulations with random input of intrinsic permeability only and porosity only were also performed. The comparisons of statistical description for the three simulations are shown in Table 3.11 From Table 3.11, it can be observed that COVs of the results from random permeability input-only simulation is close to the ones from simulation with both random permeability and porosity input. Meanwhile, the COVs obtained from the two simulations are times larger than the ones from random porosity input-only simulation. This observation is similar to the one from injection simulation. Therefore it can be concluded that, intrinsic permeability has significantly more influence on the CO_2 migration than porosity.

Table 3.11. Comparisons of statistical description of results from migration simulation with different random input.

	Stochastic parameter	Mean	Standard deviation (STD)	Coefficient of variance (COV)	Normal mean estimation with 95% confidence		Normal STD estimation with 95% confidence	
					Lower	Upper	Lower	Upper
CO_2 saturation at the corner	K and ϕ	0.711	0.016	0.023	0.709	0.713	0.015	0.018
	ϕ	0.712	0.003	0.004	0.712	0.713	0.0028	0.0034
	K	0.711	0.016	0.023	0.709	0.713	0.015	0.018
Interface total flow rate (kg/s)	K and ϕ	-0.0013	4.94×10^{-4}	-0.377	-0.0014	-0.0012	4.50×10^{-4}	5.48×10^{-4}
	ϕ	-0.0011	6.96×10^{-5}	-0.064	-0.0011	-0.0011	6.34×10^{-5}	7.72×10^{-5}
	K	-0.0013	4.97×10^{-4}	-0.378	-0.0014	-0.0012	4.52×10^{-4}	5.51×10^{-4}
Well flow rate (kg/s)	K and ϕ	-0.0044	9.79×10^{-4}	-0.223	-0.0045	-0.0042	9.00×10^{-4}	1.10×10^{-3}
	ϕ	-0.0041	2.98×10^{-4}	-0.073	-0.0041	-0.0041	2.71×10^{-4}	3.30×10^{-4}
	K	-0.0044	9.12×10^{-4}	-0.208	-0.0045	-0.0043	8.00×10^{-4}	1.00×10^{-3}
CO_2 mass fraction	K and ϕ	0.183	0.080	0.44	0.171	0.194	0.073	0.089
	ϕ	0.127	0.029	0.22	0.123	0.131	0.026	0.032
	K	0.183	0.077	0.42	0.172	0.194	0.070	0.085

3.4.3 Storage Capacity Factor

According to Doughty et al. (2001) and Doughty and Pruess (2004), a way to quantify the CO_2 sequestration is to use the storage capacity factor C, which is defined as the volume fraction of the volume in the subsurface that contains CO_2. The capacity factor can be divided into capacity factors in each phase in TOUGH2: $C = Cg+Cl$, with C_g being the fraction of the contained CO_2 in the specified volume in gas-like phase and Cl being the fraction of the contained CO_2 in the aqueous phase. Cg and Cl can be calculated with the following equations:

$$Cg = \frac{S_g \cdot \phi \cdot v}{V} \tag{3.21}$$

$$Cl = \frac{S_l \cdot \phi \cdot X_l^{CO_2} (\rho_l / \rho_g) \cdot v}{V} \tag{3.22}$$

in which, S_g and S_l are saturations for gas phase and liquid phase, respectively; ϕ is porosity; $X_l^{CO_2}$ is the mass fraction of CO_2 dissolved in the aqueous phase; ρ_g and ρ_l are gas- and liquid-phase densities, respectively; v is the volume of the specific element/block; V is the volume of the simulation model volume. The liquid/gas density ratio term ρ_l / ρ_g in Eq. (3.22) allows one to convert the volume occupied by CO_2 if it were to change from the status of dissolved in the liquid phase to gas-like phase. The density ratio term makes sure that the storage capacity for the

two-phase flow of gas-like CO_2 and aqueous phase is accounted for, regardless of the phase partitioning among the gas-like CO_2 phase. When CO_2 density equals zero, the density ratio term becomes singular, meaning that there is only one aqueous phase. In this case, *Cl* is calculated using the following equation:

$$Cl = \frac{S_l \cdot \phi \cdot X_l^{CO_2} \cdot v}{V} \tag{3.23}$$

It is very important to choose the domain on which the contained CO_2 is averaged over, because the selection of averaging domain can have impact on the calculated storage capacity values. An appropriate choice of averaging domain can ensure the comparison of different scenarios be meaningful. The averaging domains can be the a natural CO_2 trapping formation which consists of injection well/CO_2-rich region as inlet and a spill point or cap/impervious rock discontinuity at outlet, or a unit volume of a targeted geological sequestration formation.

The injection simulations were performed under the assumption of sandstone, and the hydrogeologic properties of the rock are shown in Table 3.12. The plots of *Cg* obtained from injection simulation with stochastic *K* and ϕ input with 200 MCS are shown in Fig. 3.57, in which, the fraction of subsurface containing CO_2 in gas-like phase in increasing with time almost linearly. This linearity comes from the constant injecting rate settings of the simulation experiment. This is also true in the one dimensional analysis (Chen and Gutierrez, 2011), where the injected volume ratio is the same as capacity factor *C*. Before the CO_2 reaches the outlet well in the lower right corner and start to spill out of the specified domain, the plots will remain almost linear. The statistical description of the ultimate *Cg*, *Cl* and *C* (time = 10 years) for injection simulation with different stochastic parameters is shown in Table 3.13. Percentile is a value such that certain percentage of the data set is smaller than this value. A 5% percentile means only 5% of the observed data value from the data set is smaller than the specified 5% value. The percentile values are not necessarily from the data set, and they can be also interpolated. The median value is also 50% percentile. Fig. 3.58 shows the plots of *Cg, Cl* and *C* obtained from injection simulation with stochastic *K* and ϕ input in a single realization. It can be observed in Fig. 3.58 that the fraction of subsurface containing CO_2 in liquid phase is much smaller than that the fraction in gas-like phase.

The migration simulations were performed using the same assumption of rocks with injection simulations. The plume migration scenario was represented by a formation that has a CO_2-rich region with high CO_2 saturation of 0.8, and the rest of the domain with zero CO_2 saturation. Note that the initial conditions do not necessarily provide the same initial CO_2 inventory for every realization. This migration scenario is similar to the previous migration simulations discussed in the previous sections, except that the rock formation has different characteristic curves (relative permeability and capillary pressure), and that the CO_2 saturation for the non-CO_2-rich region is 0.051 instead of zero. Figure 3.59 shows plots of *Cg* obtained from migration simulation with stochastic *K* and ϕ input with 200 MCS. As shown in Fig. 3.59, the plots show fair amount of uncertainty, and are almost linear before 60 years. The plots concave downward after 60 years and start to reach a quasi-steady state, which is caused by the spilling of CO_2 out of the specified domain though the outlet well. It should be noted that since the CO_2 saturation was pre-assigned into the simulation domain before simulation, the *Cg* plots in Fig. 3.59 don't start from zero as in Fig. 3.57. Figure 3.60 shows the plots of *Cg, Cl* and *C* obtained from injection simulation with stochastic *K* and ϕ input in a single realization. It can be seen in Fig. 3.60 that there is a rapid increase of speed of dissolved CO_2 in the aqueous phase after 30 years or so. On the other hand, CO_2 in gas-like phase tends to increase with a slower

speed starting from the same time. Table 3.14 shows the statistical description of the ultimate *Cg*, *Cl* and *C* (time = 95.13 years) for migration simulation, with different stochastic parameters. Fig. 3.60 and Table 3.14 show that, the fractions of subsurface containing CO_2 in liquid phase and gas-like phase don't differ a lot, although the former is still smaller than the latter one in a general sense. This results are different from the results of injection simulation, which indicates that CO_2 tends to dissolve in the liquid in the injection process significantly less than in the migration process. It is likely that this difference is rather caused by the trapping mechanism of the CO_2, than the heterogeneity of the formation, which means that the difference would still be the same with homogenous formation.

Table 3.12. Hydrogeologic description of the rocks.

Parameters	Values
Rock grain density (kg/m^3)	2600
Formation conductivity (W/m °C)	2.51
Rock grain specific heat (J/kg °C)	920
Rock compressibility (Pa^{-1})	4.5×10^{-10}
Relative permeability Liquid: Van Genuchten function (1980) $k_{rl} = \sqrt{S^*}\left\{1-\left(1-\left[S^*\right]^{1/\lambda}\right)^{\lambda}\right\}^2$	$S^* = (S_l - S_{lr})/(1-S_{lr})$
Irreducible water saturation	$S_{lr} = 0.20$
Exponent	$\lambda = 0.40$
Relative permeability Gas: Corey (1954) $k_{rg} = (1-\hat{S})^2(1-\hat{S}^2)$	$\hat{S} = (S_l - S_{lr})/(1-S_{lr}-S_{gr})$
Irreducible water saturation	$S_{lr} = 0.20$
Irreducible gas saturation	$S_{gr} = 0.05$
Capillary pressure Van Genuchten function (1980) $P_{cap} = -P_0\left(\left[S^*\right]^{-1/\lambda}-1\right)^{1-\lambda}$	$S^* = (S_l - S_{lr})/(1-S_{lr})$
Irreducible water saturation	$S_{lr} = 0.20$
Exponent	$\lambda = 0.40$
Strength coefficient	P_0 = 3.58 kPa

The cumulative frequency distribution (CFD) plots *C* from injection and migration simulations are shown in Figs. 3.61 and 3.62, respectively. A cumulative frequency distribution summarizes a data set and shows the frequency of values that are smaller than or equal a certain upper limit. If the slope of a CFD curve is gentle, then the representing data set has a large variance. On the contrary, a CFD curve with a steep slope will indicate small variance of the data set. As it is shown in Fig. 3.61, the storage capacity factors *C* calculated with only randomized intrinsic permeability or porosity input do not show much variance, compared to the ones calculated with both random permeability and porosity input. This is not the same in the migration process, where the storage capacity factors *C* show almost the same variance according to Fig. 3.62.

Table 3.13. Statistical characteristic for ultimate *C* (time = 10 years) in injection for 200 MCS.

Capacity factor	Stochastic permeability	Mean	Std	COV	5% percentile	Median	95% percentile
Cg	*K* and ϕ	0.0280	0.0070	0.025	0.0269	0.0280	0.0292
	ϕ	0.0280	0.0012	0.004	0.0279	0.0280	0.0282
	K	0.0280	0	0	0.0280	0.0280	0.0280
Cl	*K* and ϕ	0.0046	0.0015	0.034	0.0043	0.0046	0.0048
	ϕ	0.0043	0.0005	0.012	0.0042	0.0043	0.0044
	K	0.0043	0	0	0.0043	0.0043	0.0043
C	*K* and ϕ	0.0326	0.0066	0.020	0.0316	0.0325	0.0337
	ϕ	0.0323	0.0008	0.002	0.0322	0.0323	0.0325
	K	0.0323	0	0	0.0323	0.0323	0.0323

Table 3.14. Statistical characteristic for ultimate *C* (time = 95.13 years) in migration for 200 MCS

Capacity factor	Stochastic permeability	Mean	Std	COV	5% percentile	Median	95% percentile
Cg	*K* and ϕ	0.0258	0.012	0.046	0.0236	0.0259	0.0276
	ϕ	0.0255	0.0077	0.030	0.0242	0.0255	0.0269
	K	0.0258	0.0087	0.034	0.0243	0.0259	0.0272
Cl	*K* and ϕ	0.0244	0.0056	0.023	0.0233	0.0244	0.0252
	ϕ	0.0253	0.0043	0.017	0.0246	0.0254	0.0261
	K	0.0244	0.0036	0.015	0.0237	0.0244	0.0249
C	*K* and ϕ	0.0502	0.015	0.030	0.0475	0.0502	0.0524
	ϕ	0.0508	0.010	0.020	0.0491	0.0509	0.0525
	K	0.0502	0.010	0.021	0.0483	0.0503	0.0519

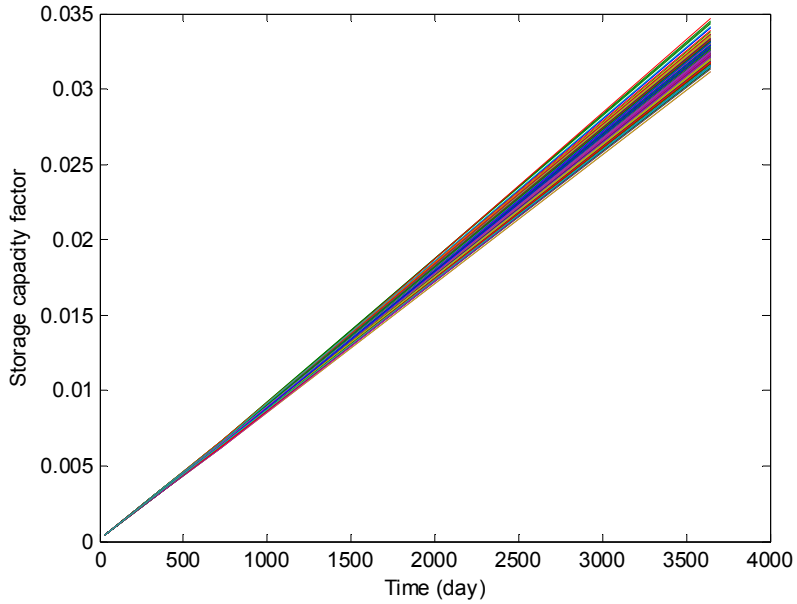

Fig. 3.57. Plots of *C* from injection simulation with stochastic *K* and ϕ input with 200 MCS.

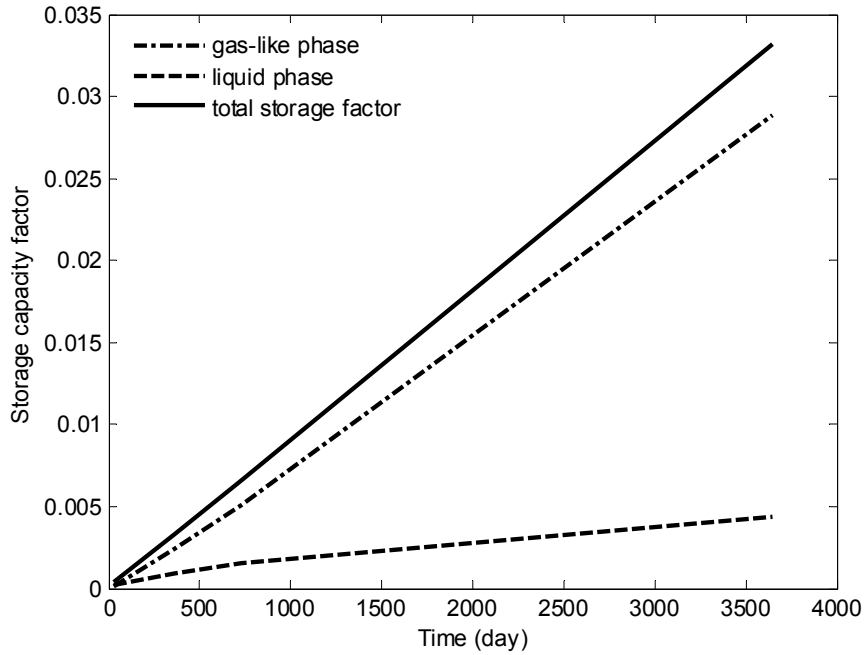

Fig. 3.58. Plots of *Cg*, *Cl* and *C* in a single realization.

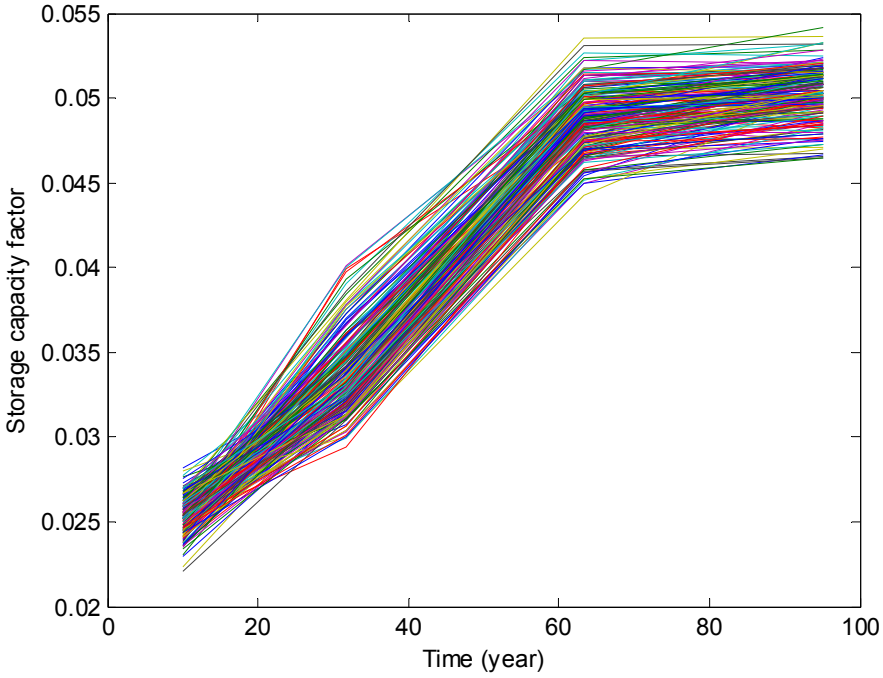

Fig. 3.58 - Plots of *C* from migration simulation with stochastic *K* and ϕ input with 200 MCS.

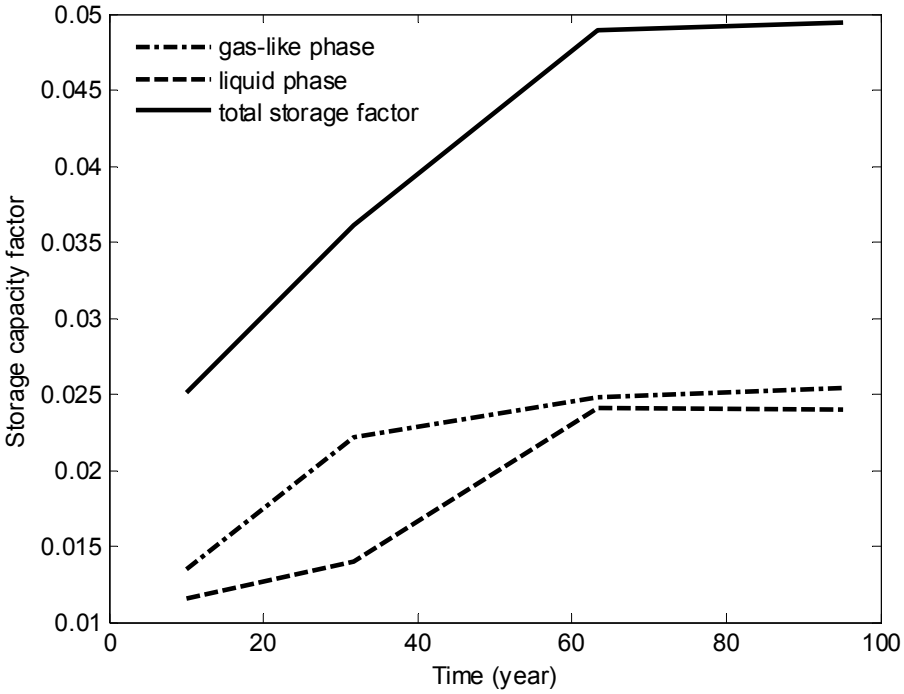

Fig. 3.60 - Plots of *Cg*, *Cl* and *C* in a single realization.

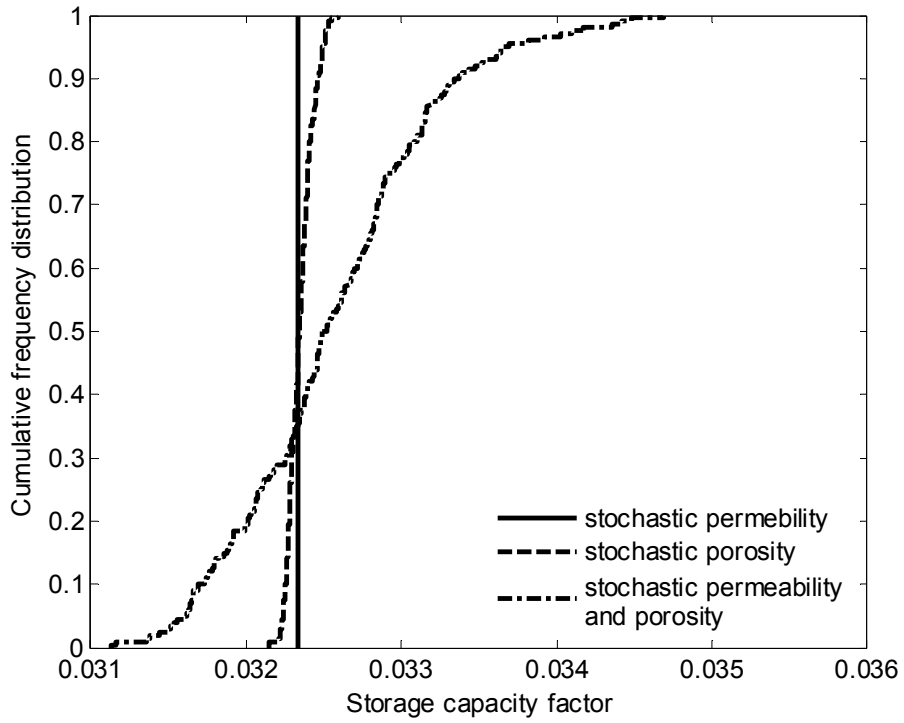

Fig. 3.61 - Cumulative frequency distribution plots of ultimate *Cg*, *Cl* and *C*, in injection simulation with 200 MCS.

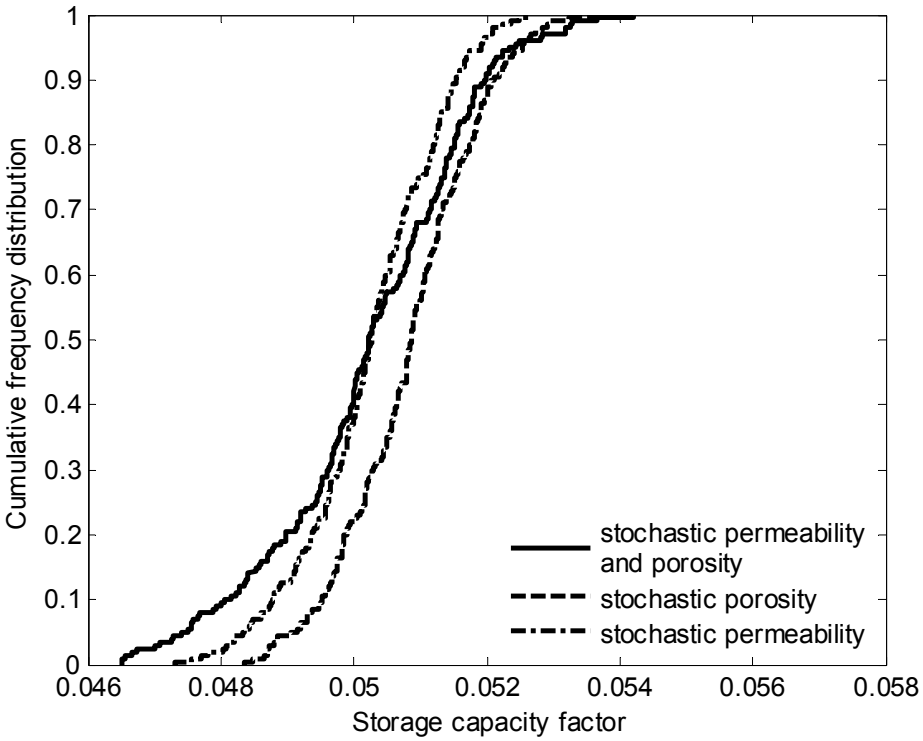

Fig. 3.62 - Cumulative frequency distribution plots of ultimate *Cg, Cl* and *C,* in migration simulation with 200 MCS.

3.5 Test and validation of the models

To show their use, value and validity the models are tested and validated using: 1) theoretical predictions from poroelasticity, 2) a prototype CO_2 field sequestration using and idealized field sequestration reservoir and hydro-mechanical properties, 3) the Sleipner CO_2 sequestration project in the Norwegian North Sea, and 4) the In Salah CO_2 storage project in Algeria. The model prediction for the prototype model, Sleipner and In Salah are compared to previous studies of two-phase flow hydromechanical models. The main motivation for test and validation studies is to demonstrate the performance of the models against previous results and studies. Several aspects of the hydro-mechanical response of CO_2 storage reservoirs, including pore pressure development, fluid movements, deformation of the reservoir and surrounding rocks, ground/seabed uplift are investigated. In addition, the potential for mechanical failure and leakage in the cap rock are investigated. Even though some simplifications have been made, key features of the actual injection sites and/or existing models are captured in the models. These features include: (1) thickness of the overburden, caprock, and reservoir, (2) rock properties, (3) initial porosity and permeability, (4) injection rate, and (5) initial viscosity and density of CO_2.

3.5.1 Validation of the Coupled H-M Model Against Theoretical Predictions

To show its validity, the proposed coupled hydro-mechanical (H-M) modeling procedure should be able to reproduce two important poroelastic effects: (1) The Mande-Cryer effect, and (2) The Norbergum effect. It is shown below that the proposed coupling procedure can faithfully replicate these two effects demonstrating the validity of the proposed procedure.

One of the poroelastic effects was first presented by Mandel (1953) with an analytical solution for the pore pressure response during fluid extraction in a layer of poroelastic mediums sandwiched between two rigid layers. It shows non-monotonic pore pressure behavior which cannot be found from an uncoupled H-M solutions such as Terzaghi's 1D consolidation theory (1943). This non-monotonic fluid flow behavior results pore pressure rise in the porous material during pore pressure dissipation. Later, Cryer (1963) obtained a similar result and it has since been referred to as the Mandel-Cryer effect. Since Mandel introduced one of the first solutions of Biot's theory, it became a popular analytical model to validate fully-coupled numerical codes.

In Mandel's problem, an infinitely long rectangular vertical cross-section of saturated poroelastic material is placed between two rigid frictionless plates (Fig. 3.63). The lateral sides are free from normal and shear stress, and pore pressure. An instant load is applied at the top and bottom of the plates without allowing drainage on the lateral sides. Therefore, a uniform vertical stress across the sample and a uniform excess pore pressure is generated by the Skempton effect (1954) at $t=0^+$. Then drainage is allowed at the lateral sides and the pore pressure is allowed to dissipate as time progresses. As drainage proceeds at the lateral sides, additional pore pressure in the central region higher than initial value is predicted at the beginning due to the non-uniform dissipation of excess prore pressure. After a long time, $t=\infty$, all excess pore pressure in the sample vanishes. Cryer (1963) obtained similar results at the center of a sphere consolidating under hydrostatic pressure and this non-monotonic pore pressure increase above the initial value cannot be observed in a simple diffusion phenomenon such as that modeled by Terzaghi's one dimensional consolidation theory.

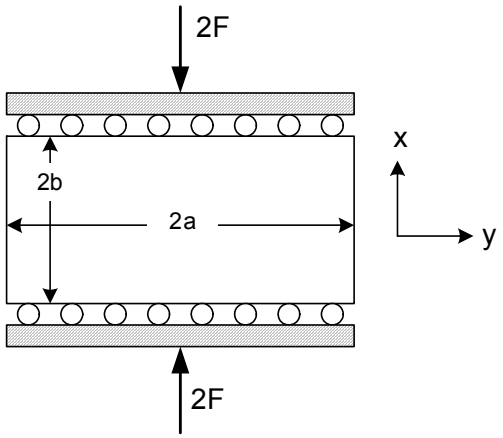

Fig. 3.63 - Mandel's Problem

The coupled procedure outlined above is used in the solution of Mandel's problem outlined in Fig. 3.64 using a linear stress-strain relation with 2D plane strain condition. Incompressible fluid and solid grains are assumed. Mandel's problem is solved 80 elements in FLAC, and only a quarter of the problem geometry is considered in the FE model due to the symmetry. As it can be seen from Fig. 3.64, the mechanical boundary conditions for symmetry correspond to roller boundaries along the bottom and the left side. After load is applied, the pore pressures are reduced to zero at the right side of the model. Rigid body motion is enforced by locating a weightless Euler-beam on the top of the elastic porous material with high rigidity (high EI, where E = Young's modulus and I = moment of inertia of the beam) and uniformly distributed load is applied at the top of the rigid beam.

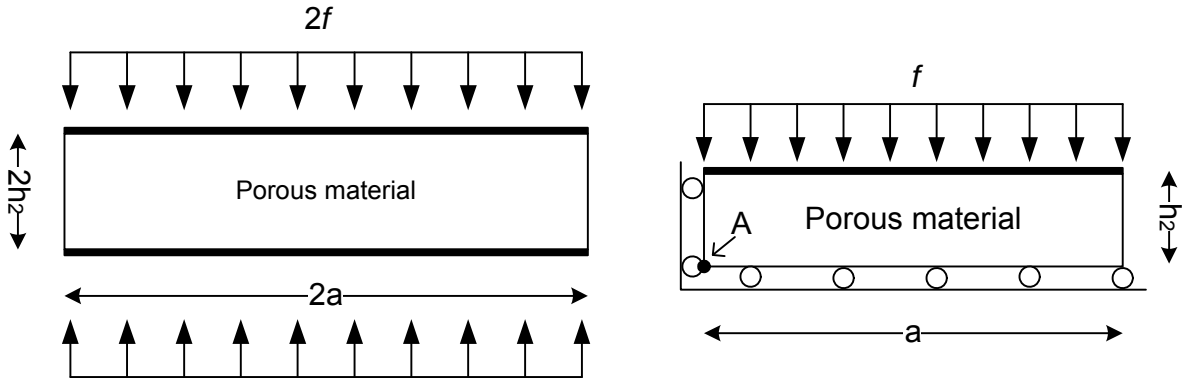

Fig. 3.64 - Mechanical Boundary Conditions for FE Model

Fig. 3.65 shows the pore pressure profile from analytical and coupled FEM solutions at the center of the porous material (point 'A') as a function of time. The load generates a uniform excess pore pressure which is half of the amount of applied load due to the Skempton's effect, that is:

$$\frac{ap(0^+)}{F} = \frac{1}{3}B(1+\nu_u) \tag{3.24}$$

Equation (3.24) gives dimensionless pore pressure value as 0.5 with given undrained Poisson's ration and Skempton's coefficient. As it can be seen from Fig. 3.65, pore pressure rises above the initial value for a small time period because non-uniform dissipation of pore pressure during the short time causes compression near the lateral side where drainage takes place. The resulting stress concentration in the central region then causes an additional rise in excess pore pressure. As can be seen, the numerical solutions agree with the analytical solutions.

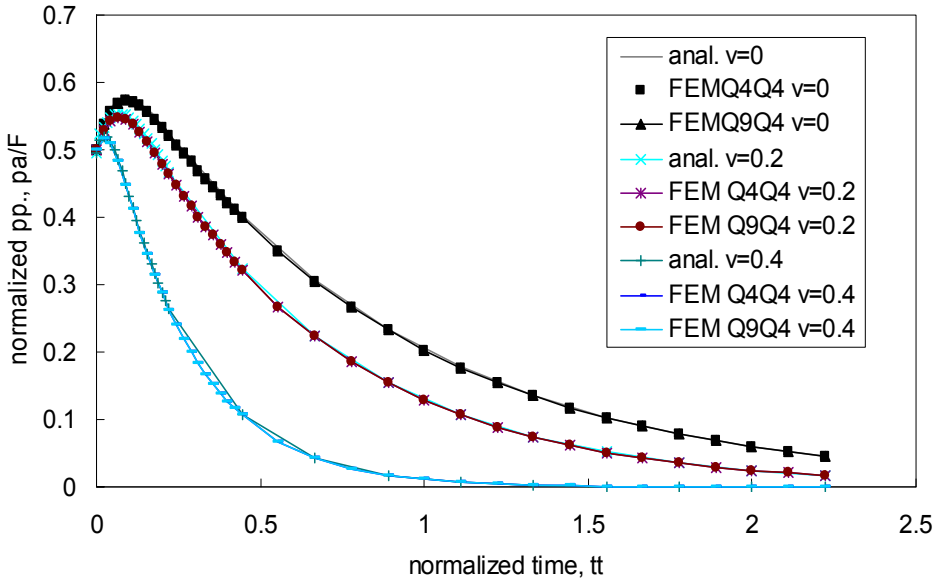

Fig. 3.65 - Pore pressure profile at 'A' vs. time

The Norbergum effect is a second type of poroelastic effect that can only be obtained by proper solution of the coupled HTM problem. The Nordbergum effect, named after the hydrocarbon field in which the effect was observed, is similar but different from the Mandel-Cryer effect and is manifested as an increase in pore pressure due to the deformation of the porous medium, and is referred to as "compaction drive" in hydrocarbon reservoir engineering. In uncoupled simulation, the main mechanism accounting for the compaction drive is the pore compressibility. In coupled simulation, the downward movement of the overburden also contributes the compaction drive. This contribution, particularly the increase of pore pressures above the initial pressure, cannot be accounted for by simply adjusting the pore compressibility in uncoupled flow simulations. The compaction drive will be very pronounced for soft reservoirs but can also be significant for the case of relatively stiff reservoirs. The increase in pore pressure during continued fluid extraction was first explained as a porolastic mechanism in a pumped aquifer by Verruijt (1969). The Noordbergum effect is related to, but is not the same, as the so-called ''Mandel–Cryer effect'' discussed above.

To demonstrate that the proposed coupling procedure can model the Norbergum effect, a two-dimensional plane strain model of fluid extraction from an underground reservoir is modeled using the coupled TOUGH2-FLAC code. The geometry and the boundary conditions of the reservoir are shown in Fig. 3.66. The reservoir consists of a 7-km wide and 0.3 km thick reservoir overlain by a 3 km thick overburden. To model the surrounding non-producing formation around the reservoir, the model extends 27 km wide and 3.66 km deep.

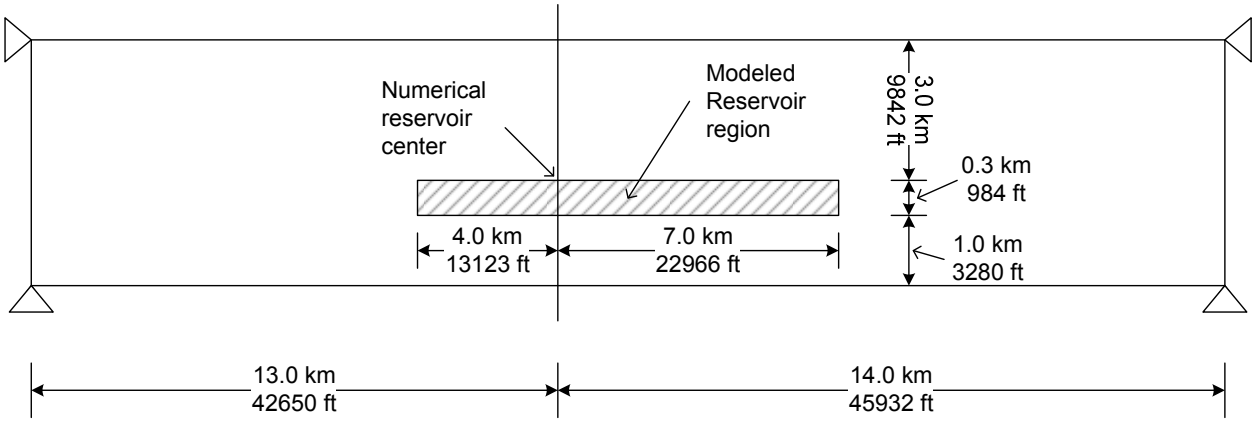

Fig. 3.66 - Model of a reservoir used to simulate the Nordbergum effect using the proposed coupled HTM procedure.

Fig. 3.67 shows the FLAC grid used for the coupled simulation. Fig. 3.68 shows final deformed mesh after 14 years of production and it illustrates the general displacement profiles including surface subsidence and reservoir compaction due to the fluid being pumped out of the producing reservoir. Fig. 3.69 shows the subsidence and compaction profiles along the width of the model. As can be seen, despite the fluid extraction, some heave (negative compaction and subsidence) were observed close to the flanks of the reservoir. To explain this heave that accompanies fluid extraction, the pore pressure profiles along the width of the model the mid depth of the reservoir after the production at different periods of time are plotted in Fig. 3.70. It may be noted that the fluid pressures increased above the initial reservoir of 48 MPa outside of the reservoir despite the fact that fluid is being continuously extracted from the reservoir. This

increase in reservoir pressure is the cause of the heave of the reservoir and the ground surface. The increase in pore pressure is due to the pumping action a result of the downward movement of the overburden at the reservoir center. This downward movement squeezes the fluids from the reservoir center towards the flanks causing the observed increase in reservoir pressure above initial values. Note that this Norbergum effect can only be properly predicted if the coupling between fluid flow and mechanical response is correctly modeled as is the case for the proposed procedure.

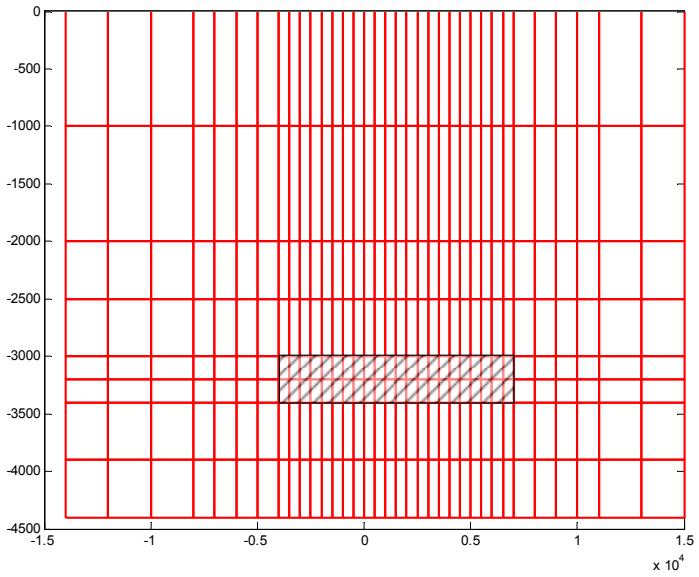

Fig. 3.67 - Initial FE mesh with surrounding area (shaded area represents reservoir field).

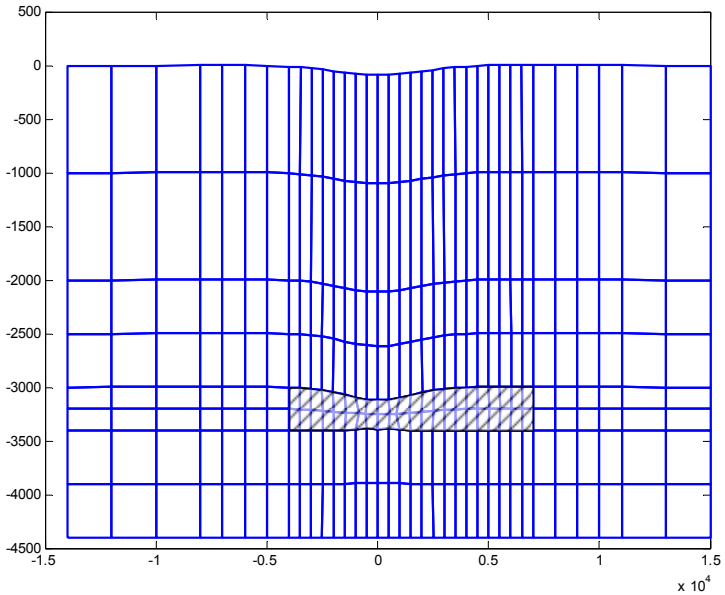

Fig. 3.68 - Final displacements profile after 14 years production with magnified 10 times (shaded area represents reservoir field).

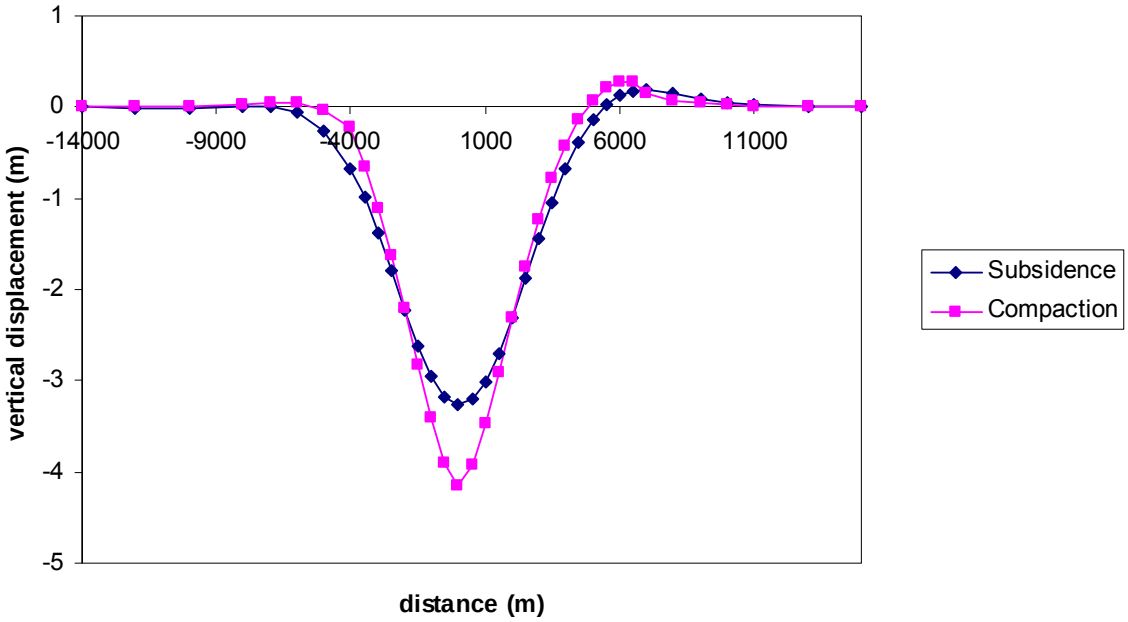

Fig. 3.69 - Final subsidence and compaction profiles along the width of the model.

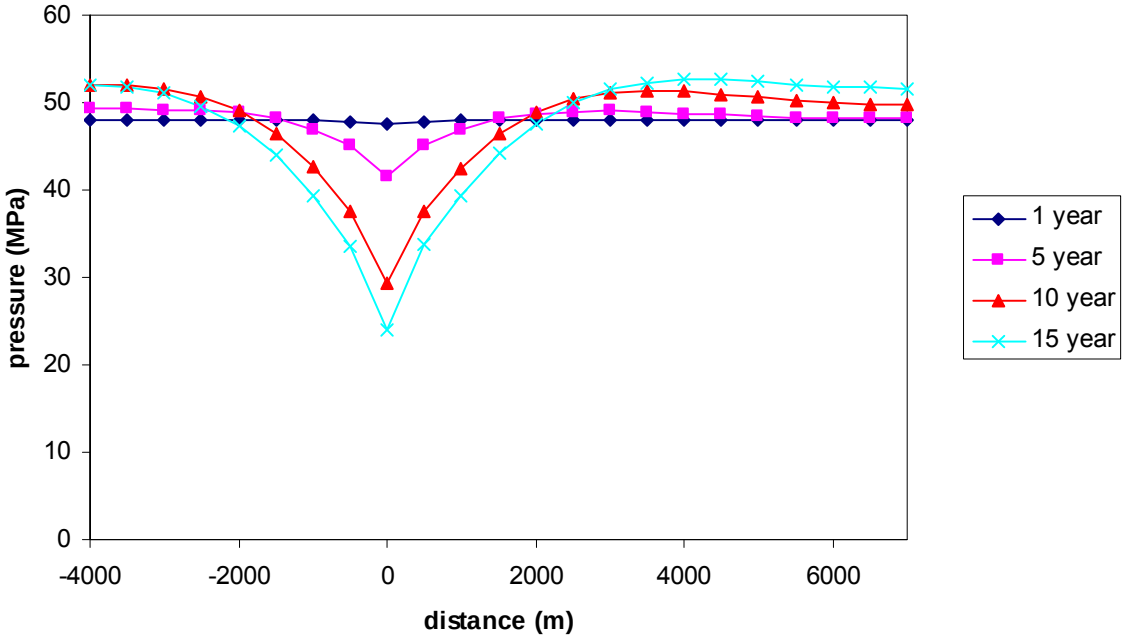

Fig. 3.70 - Reservoir pressure profiles in reservoir region along the mid depth.

3.5.2 Validation of the Coupled H-M Model Against a Prototype CO_2 GS Reservoir

The prototype model follows the model developed by Rutqvist and Tsang (2002), with material properties from those presented by Pan et al. (2013). Pan et al. (2013) used the prototype model from Rutqvist and Tsang (2002) to test their software package, TOUGH2-RDCA, with more complete material properties.

The rock mechanical and hydrogeologic properties for the validation of the coupled H-M model are given in Table 3.15. The cross-section of the reference prototype model is shown in Fig. 3.71 together with the FLAC model that is developed in this study. The hydrostatic water pressure gradient is 10 MPa/km, and the total vertical stress gradient is 22.6 MPa/km. The FLAC model is 3000 m in depth and up to 10 km in length to represent an infinite boundary. It consists of overburden (0-1200 m), caprock (1200 to 1300 m), reservoir (1300 to 1500 m), and basement (1500 to 3000 m). CO_2 is injected at a depth of 1500 m with an injection rate of $0.5 \cdot 10^{-3}$ kg/(m-s) for a total injection period of 10 years. Roller boundary conditions are applied on all boundaries except at the ground surface, which is free to move. The near-lateral boundary (at x = 0) and bottom boundary are impermeable. The far-lateral boundary (at x = 5 km) and ground surface are permeable by fixing its pore pressures. This is done to prevent over-pressuring the formation (Pruess et al., 2002).

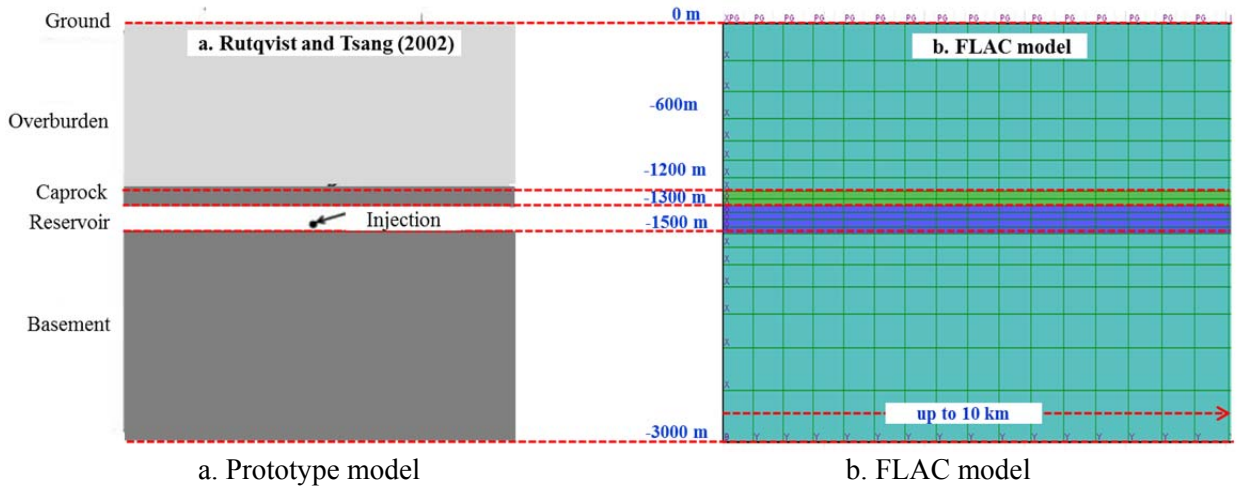

a. Prototype model b. FLAC model

Fig. 3.71 - Reference prototype model (a) and FLAC model (b).

The simulation results in the current study are compared with the more recent results from Winterfeld and Wu (2011), who have updated the study by Rutqvist and Tsang (2002) using TOUGH2-FLAC3D. In addition, the surface uplift in Rutqvist and Tsang (2002) is incorrect as there was a problem with the interpolation of pressure from TOUGH2 to FLAC3D (J. Rutqvist, personal communication, May 8, 2013). Locations of the points for presenting profiles of hydromechanical responses are always taken along the near-lateral boundary (x = 0 m from the injection point) unless otherwise stated. The main three results to be compared are discussed below. Other results for hydromechanical responses are presented afterwards.

Table 3.15 - Rock and hydrogeologic properties for the prototype FLAC model (Pan et al. 2013).

Property	Overburden	Caprock	Reservoir	Basement
Young's modulus, *E* (GPa)	5	5	5	5
Poisson's Ratio, *v*	0.25	0.25	0.25	0.25
Bulk modulus, *K* (GPa)	3.33	3.33	3.33	3.33
Shear modulus, *S* (GPa)	2	2	2	2
Saturated rock density, ρ (kg/m^3)	2,260	2,260	2,260	2,260
Porosity, ϕ	0.10	0.01	0.10	0.01
Permeability, *k* (m^2)	1x10^{-15}	1x10^{-17}	1x10^{-13}	1x10^{-17}
Residual gas saturation	0.05	0.05	0.05	0.05
Residual water saturation	0.30	0.30	0.30	0.30
Air-entry pressure, *Po* (kPa)	196	3,100	19.6	3,100
Van Genuchten's exponent, *m*	0.457	0.457	0.457	0.457
Biot's parameter	1.00	1.00	1.00	1.00

Fig. 3.72 shows the spread of the CO_2 plume at 1, 3, and 10 years of injection period. The spread of CO_2 plumes in the FLAC model (Fig. 3.72a) are laterally longer than those in the reference model. The FLAC model shows that the plume reached the bottom of the caprock as early as 1 year after injection with a lateral spread of 300 m. After 10 years of injection, the CO_2 plume has reached a lateral distance of almost 3 km from the injection point, with 50 m of CO_2 penetration into the caprock. On the other hand, the reference model (Fig. 3.72b) shows the CO_2 plume has not even reached the bottom of the caprock after 1 year of injection. Furthermore, the plume has only stretched up to 2 km away from the injection point after 10 years of injection. This difference indicates that the CO_2 plume spreads faster in the FLAC model than in the reference model. We were not able to match the spread of CO_2 plumes to that in the reference model precisely since our FLAC model assumes constant density and viscosity of CO_2. The reference model uses pressure and temperature dependent density and viscosity which make CO_2 denser and less viscous. Nevertheless, our FLAC model still captures the typical shape of the spread of CO_2 plume at various injection periods.

Fig. 3.73 shows the history of injection pressure during the 10 years of the injection period. Our FLAC model estimates an injection pressure of 3 MPa higher than that in the reference for simulation with rock deformation (hydromechanical). This may be attributed to the extensive spread of the CO_2 plume in the FLAC model as shown in Fig. 3.72. However, both the FLAC model and the reference show that the inclusion of rock deformation (hydromechanical simulation) results in lower pressure build-up than the exclusion of rock deformation (hydraulic simulation). The pressure differences between hydromechanical and hydraulic simulation in the FLAC and the reference model are 3.2 and 3 MPa, respectively. In addition, the pressure build-up in the hydromechanical simulation in the FLAC model after 10 years of injection is still 4.4 MPa lower than the lithostatic pressure. The pressure build-up in the hydromechanical simulation (29.5 MPa) is still < 90% of the lithostatic pressure (33.9 MPa).

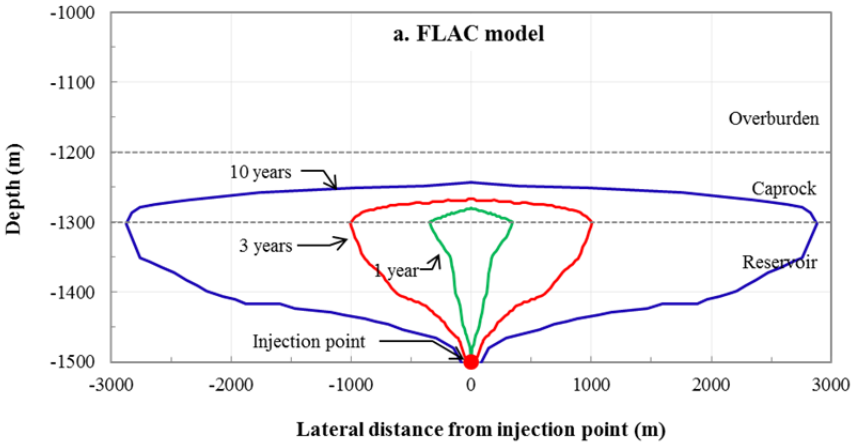

a. FLAC model

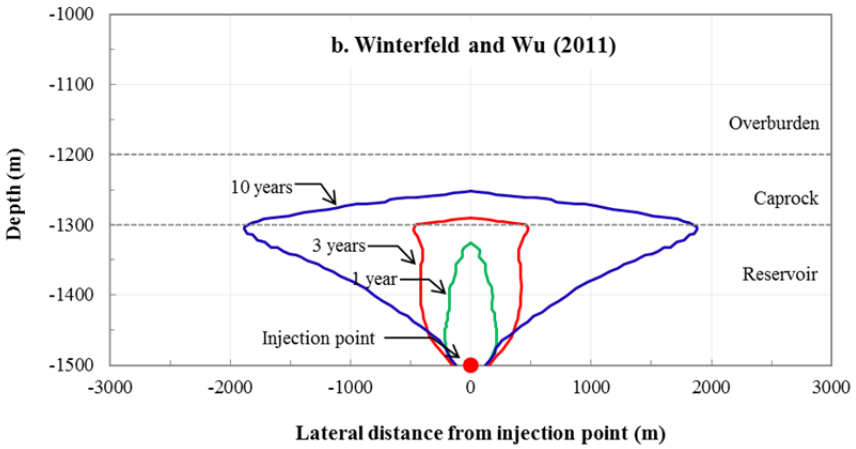

b. Reference model

Fig. 3.72 - Spread of CO_2 plumes at various injection periods.

Fig. 3.74 shows the surface uplift profile at 1, 3, and 10 years of injection for the FLAC model and the reference. The uplifts in the FLAC model agree quite well with the reference even though small discrepancies exist at the lateral distance of 2.5 km. The uplift shapes in the FLAC model flatten somewhat towards the lateral boundary compared to the reference, which dips more. The uplift profile in the FLAC model at 10 years of injection is a little higher (51 cm) than that in the reference (47 cm). In addition to the greater injection pressure as shown in Fig. .73, the higher surface uplift in the FLAC model may come from the exclusion of stress dependent porosity and permeability. These dependencies, as included in the reference model, will make less volumetric change compared to that with constant porosity and permeability with increasing pressure during the injection.

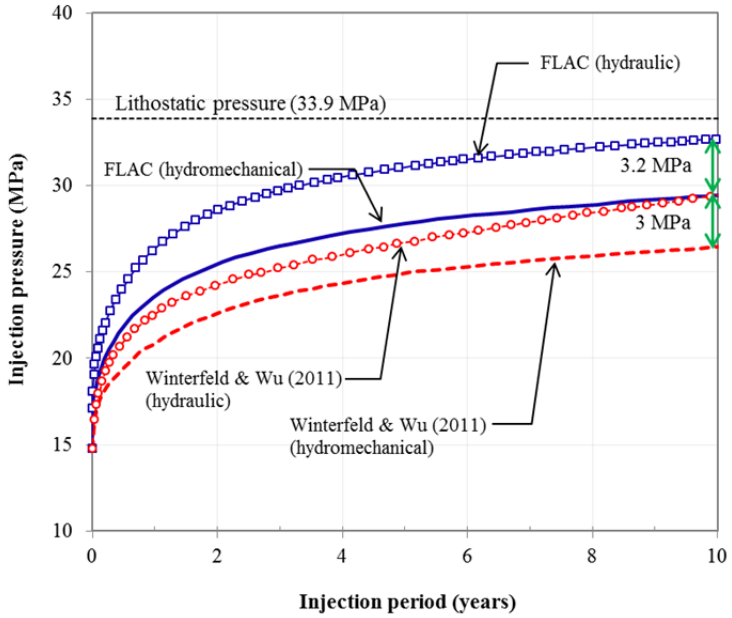

Fig. 3.73 - CO_2 injection pressures from hydromechanical and hydraulic models.

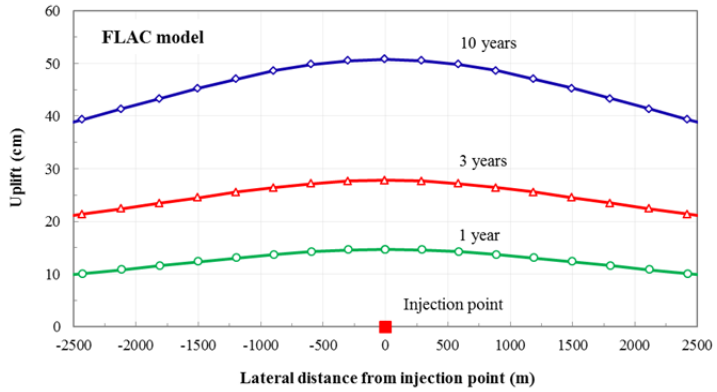

a. FLAC model

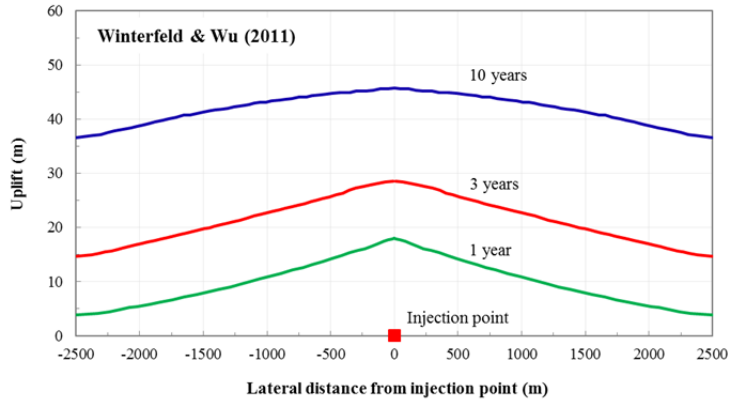

b. Reference model

Fig. 3.74 - Surface uplift at various injection periods.

Fig. 3.75 shows the history of vertical displacements at various depths along the near-lateral boundary during the 10 years of the injection period. It shows that the locations closer to the injection location from the surface (ground surface → mid-upper → top caprock), except at the bottom reservoir, displace more and the degree of displacements attenuates towards the ground surface. This feature results in lower vertical displacement at the ground surface (51 cm) than at the top caprock (57 cm), while the vertical displacement at the middle of the overburden is in between these two values (55 cm). The bottom reservoir, on the other hand, shows negative vertical displacement during the early injection period and goes back up after 1 year of injection. The bottom boundary of the model (-3,000 m) must influence the vertical displacement of the bottom reservoir. This boundary is fixed in the vertical direction.

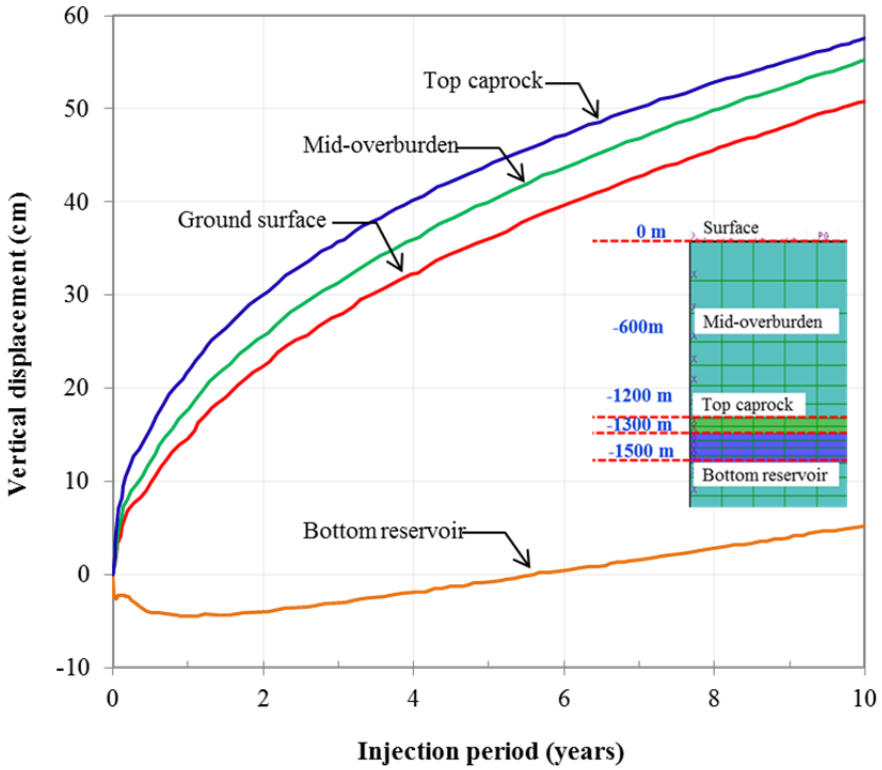

Fig. 3.75 - Vertical displacement histories at various locations in the model.

The horizontal displacements (Fig. 3.76), on the other hand, do not show the same orderly fashion of displacement histories with depth as in the vertical displacements. During the 10 years of the injection period, there is no stable pattern in the displacement histories and the degrees of displacements are lower (0-3.8 cm) than those in the vertical displacements (0 to 58 cm). The horizontal displacement of the top part of the caprock intersects the bottom part of the reservoir after 10 years of injection, while the ground surface still displaces more than the middle overburden layer. However, if the injection period was simulated longer, it seems that the order of horizontal displacement histories (from the largest to the smallest) might become ground surface, mid-overburden, top caprock, and bottom reservoir.

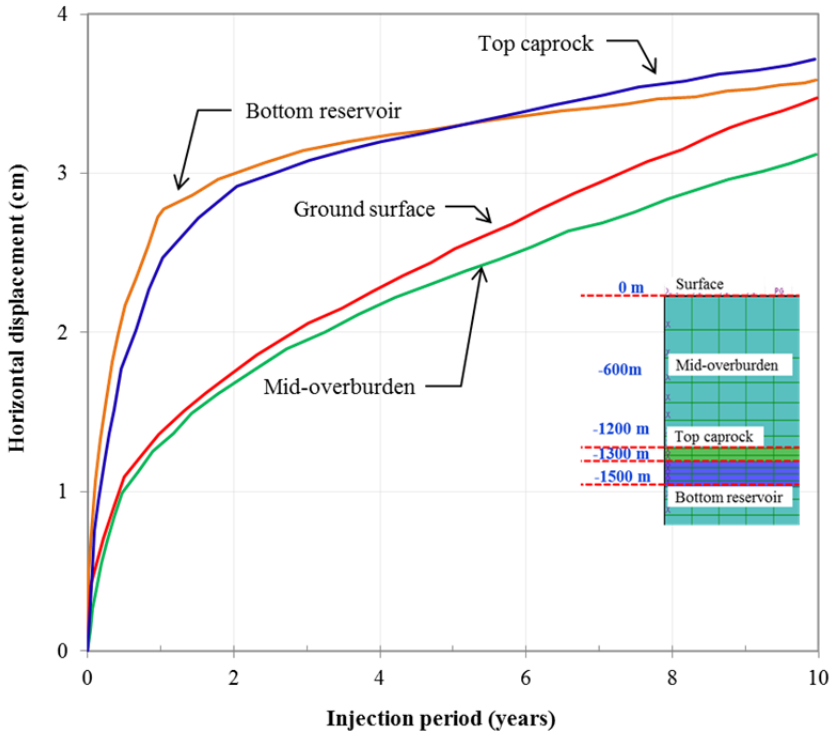

Fig. 3.76 - Horizontal displacement histories at various locations in the model.

The vertical displacement histories in Fig. 3.75 are also supported by the vertical displacement profile from the surface as shown in Fig. 3.78. The profiles show that during any injection periods, the maximum vertical deformation always occurs at the caprock and then attenuates toward the ground surface. Negative vertical displacements occur on the interface between the reservoir and basement layer in early injection periods due to the compression effect from the increase of pore pressure in the reservoir. This pressure change results in the layers above the basement layer being uplifted as the ground surface is free to move, and the basement layer being compressed as the bottom boundary is fixed vertically. The vertical displacements in the basement layer are then heading to zero towards the bottom boundary. A similarly shaped vertical displacement profile has also been found at the In Salah gas field (Rutqvist et al., 2010).

The expansion of the injected reservoir is also shown by the volumetric strain rate histories in Fig. 3.82. The volumetric strain rates for the top and bottom parts of the reservoir are always in positive values (above zero), which indicate a volumetric expansion is occurring along those parts of the reservoir. Therefore, we can conclude that the expansion is mainly happening in the reservoir since the histories at other locations show relatively small strain rates compared to that in the top and bottom parts of the reservoir. Most of the expansion occurs during the early injection and remains stable after 1 year of injection. Nevertheless, both vertical and horizontal displacement histories show significant increases in displacements during the early injection period (e.g., < 1 year). The displacements, then, increase more gradually with increasing injection periods. This feature can also be seen in the velocity histories shown in Fig. 3.77. In both vertical (Fig. 3.77a) and horizontal (Fig. 3.77b) velocity histories, significant displacement velocities occur right after the injection and gradually decrease with time. The velocities are relatively more stable after 1 year until the end of the injection period.

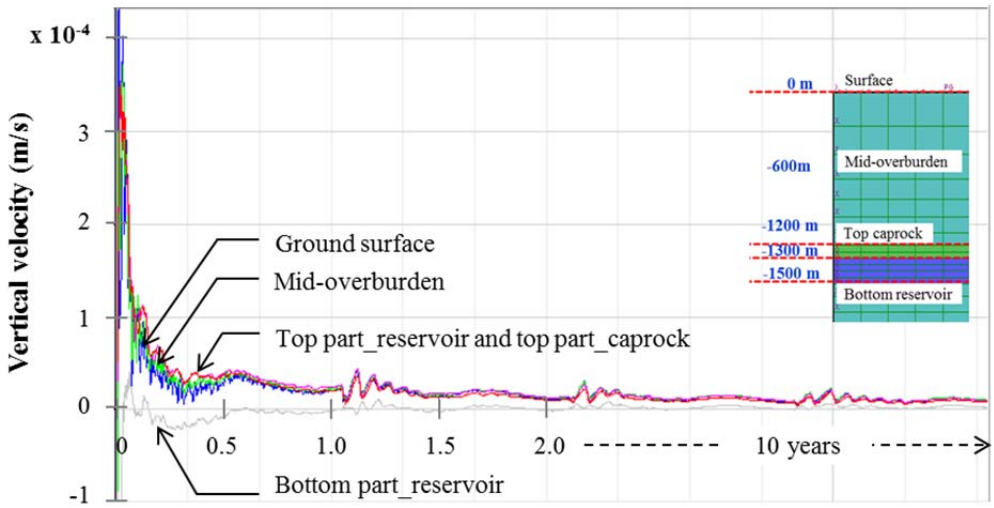

a. Vertical velocity histories

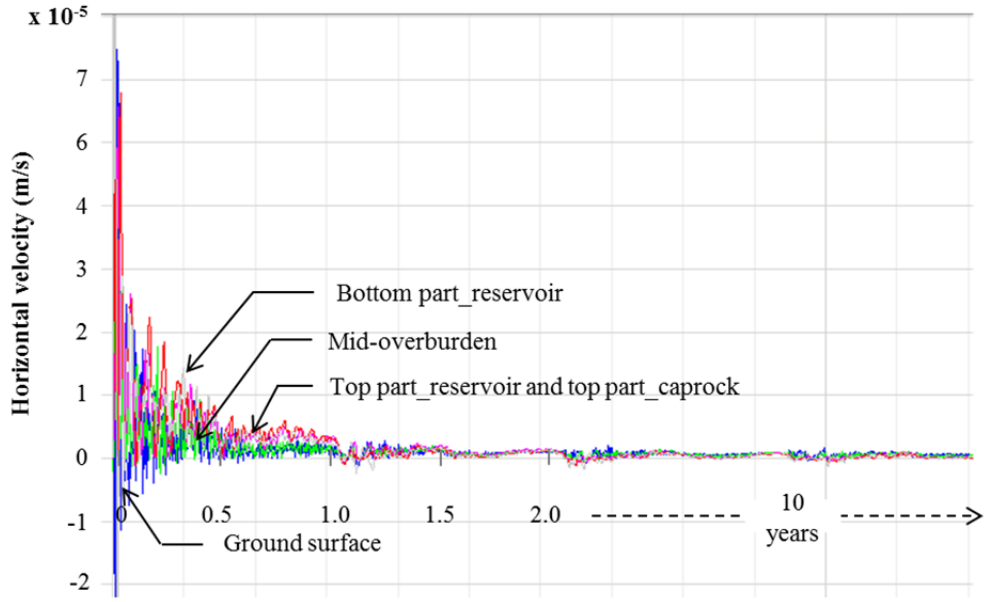

b. Horizontal velocity histories

Fig. 3.77 - Vertical (a) and horizontal (b) velocity histories at various location in the model.

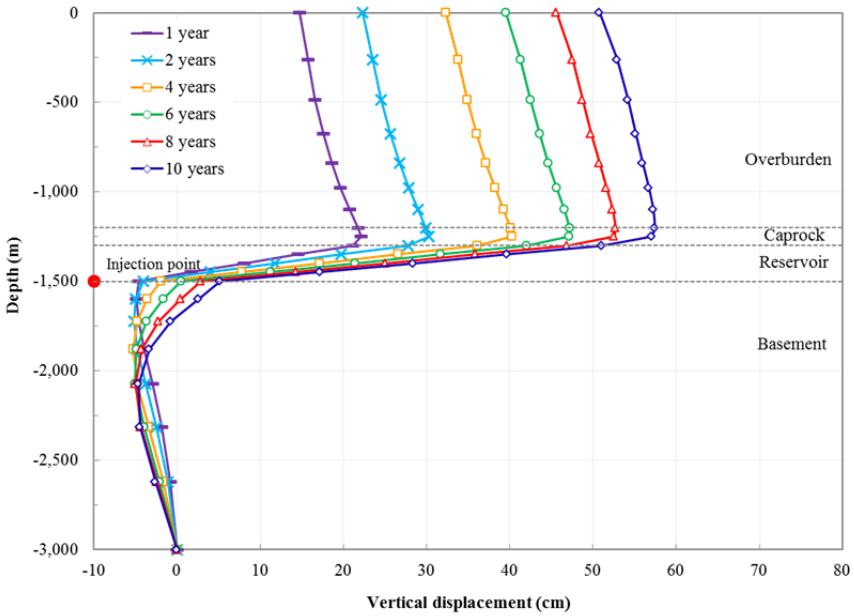

Fig. 3.78 - Vertical displacements profiles with depth.

Horizontal displacements, on the other hand, show maximum deformations in the reservoir layer at any lateral distances from the injection point (Fig. 3.79). These deformations are shown as the horizontal strains profiles after 10 years of injection. The horizontal strain profile at 0 m is not shown because the values are all zero (fixed in the lateral). Fig. 3.79 shows that horizontal strains are at maximum in the location in the vicinity of the injection point (400 m) and in the reservoir layer in which CO_2 gas is laterally injected. In terms of lateral distance, vertical strains are also at maximum in the vicinity of the injection point (0 m), but in terms of depth from surface, the strains are at maximum in the caprock. This difference is due to the CO_2's lighter-than-water density, which naturally makes the CO_2 always dissipate upwards.

Since the ground responds to the injection by deformation, it is interesting to see how the deformed shape of the reservoir after such a long injection period compared to its reference shape before the injection. Fig. 3.80 shows the deformed and the reference shape of the reservoir after 10 years of injection. The deformed shape is the total displacement of the reservoir boundaries. It is exaggerated (not to scale) to better display the effect of injection, with a maximum total deformation of 51 cm in the top reservoir above the injection point and only 21 cm in the bottom reservoir at some lateral distance from the injection point.

To better understand what this deformed shape means, we separate the total displacement into vertical and horizontal displacements. Fig. 3.81 captures the vertical and horizontal displacement profile of the top and bottom part of the reservoir. These profiles indicate that the reservoir is inflated vertically and stretched out laterally due to the injection. In terms of vertical displacements, the reservoir is uplifted along its lateral distance from the injection location. The maximum uplifting occurs to the top part of the reservoir above the injection point, while a relatively small descending occurs in the bottom part of the reservoir. In terms of horizontal displacements, both the top and bottom parts of the reservoir are mostly stretched out at a distance 4 km away from the injection point. The horizontal displacement profiles show similar shapes in both parts. These shapes seem to be affected by the boundary conditions at the near and far-lateral boundaries, which are constrained in a horizontal direction.

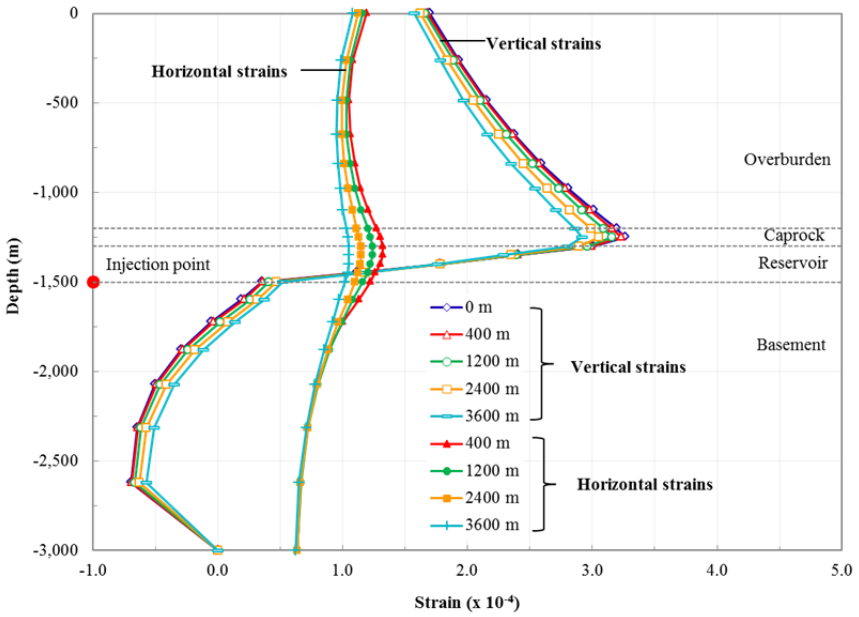

Fig. 3.79 - Horizontal and vertical strain profiles with depth after 10 years of injection period.

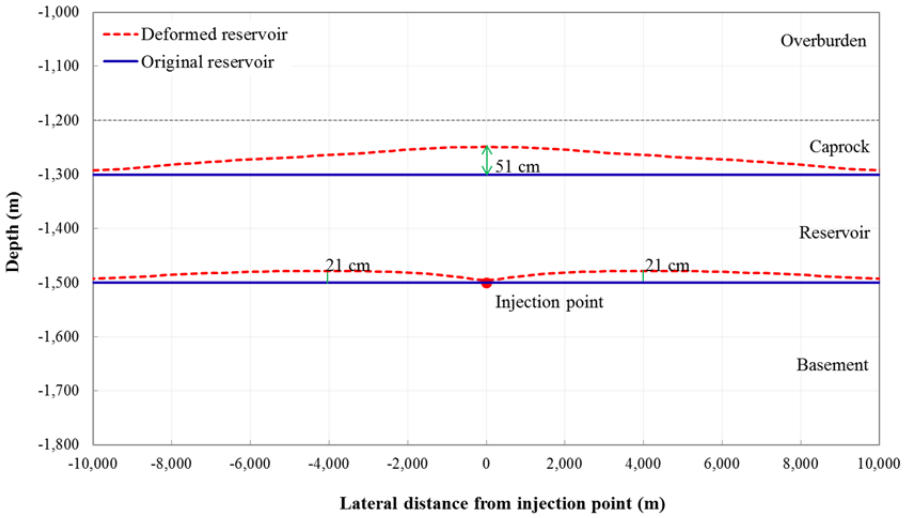

Fig. 3.80 - Deformed and reference shapes of the reservoir after 10 years of injection period.

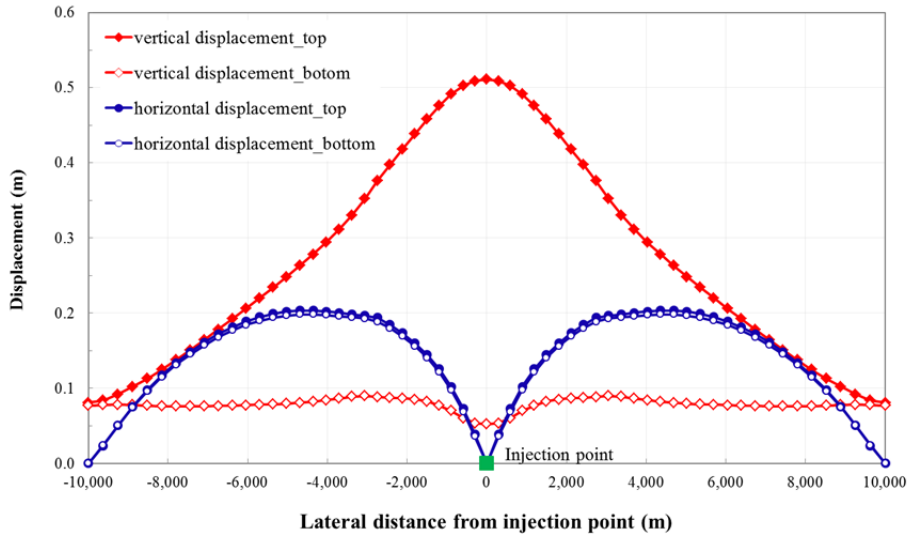

Fig. 3.81 - Vertical and horizontal displacement profiles of the top and bottom reservoir after 10 years of injection period.

The expansion of the injected reservoir is also shown by the volumetric strain rate histories in Fig. 3.82. The volumetric strain rates for the top and bottom parts of the reservoir are always in positive values (above zero), which indicate a volumetric expansion is occurring along those parts of the reservoir. Therefore, we can conclude that the expansion is mainly happening in the reservoir since the histories at other locations show relatively small strain rates compared to that in the top and bottom parts of the reservoir. Most of the expansion occurs during the early injection and remains stable after 1 year of injection.

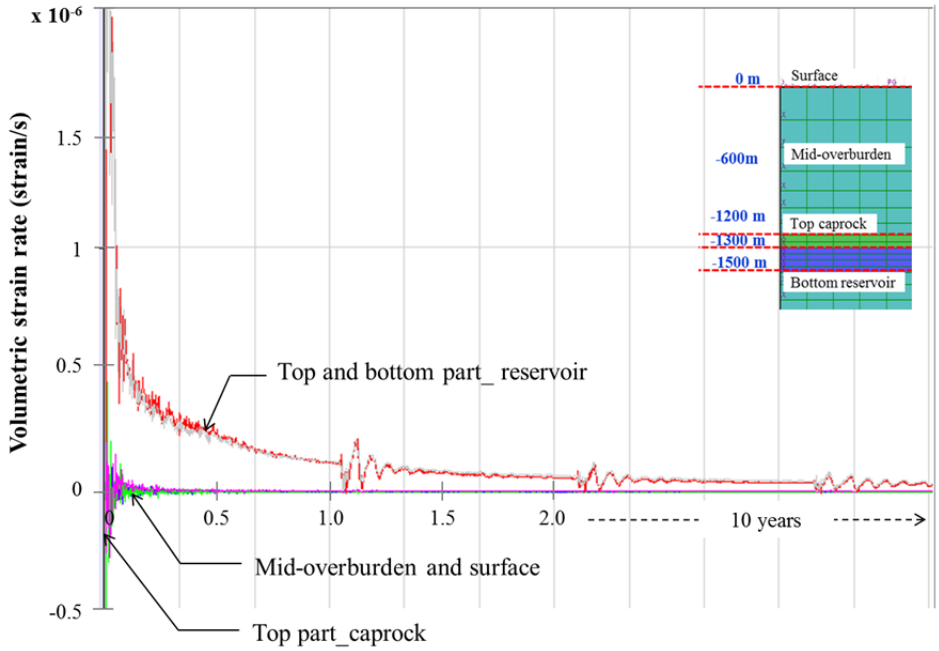

Fig. 3.82 - Volumetric strain rate histories at various locations in the model.

The results show that displacements in the vicinity of the injection point are unique in both the vertical and horizontal directions. The injection has caused expansion of the reservoir due to the increase in pore pressure from the injection. Hence, it is necessary to see how the pore pressures and stresses change at this location after the injection relative to their in situ values before the injection. These features are presented below.

Fig. 3.83 shows profiles of pore pressure and pore pressure changes with depth at various injection periods. Pore pressure increases linearly with depth (Fig. 3.83a) but starts to deviate when the depth reaches the caprock. It is at maximum value in the reservoir layer and goes back to the in situ value in the basement layer starting at several hundred meters below the reservoir. This change in pore pressure can be seen in the profile of pore pressure change with depth shown in Fig. 3.83b. As the injection period increases, the pore pressure change shows relatively very small variation in the overburden layer, but it increases dramatically in the caprock and reservoir and decreases towards zero in the basement layer.

Pore pressures are at maximum in the reservoir layer. This feature corresponds to the maximum pore pressure changes that also occur in that layer. In addition, the values of pore pressures in the reservoir also increase with injection period, which is also shown by the increase of pore pressure change with time. Pore pressure in the reservoir layer has increased by 15 MPa after 10 years of injection. However, the pore pressure does not exceed lithostatic pressure at any time. After 10 years of injection, the closest pore pressure value to the lithostatic pressure line is still 95% (28.3 MPa) of the lithostatic pressure in that location (30 MPa).

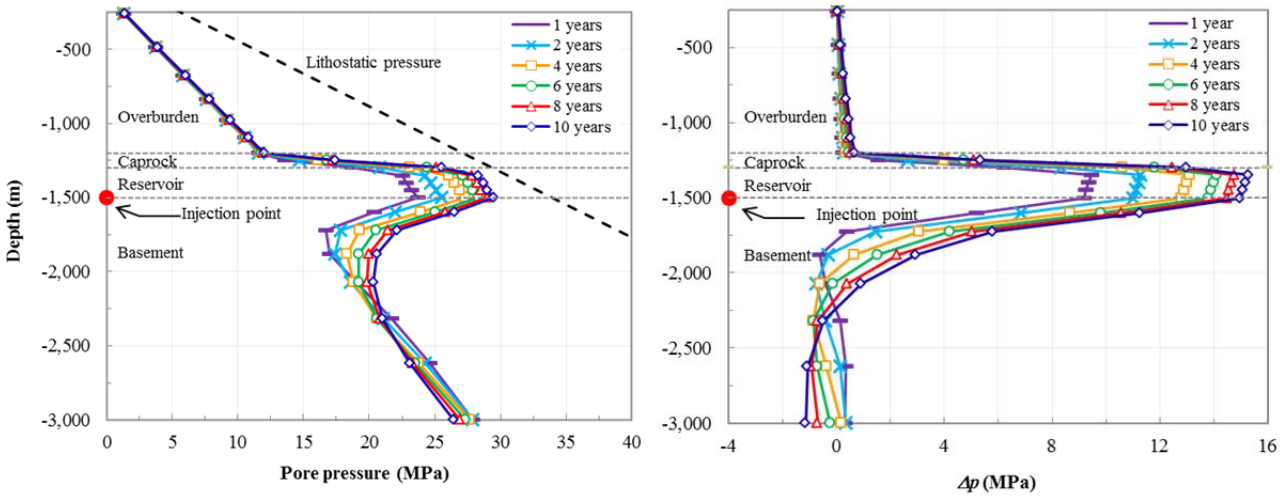

a. Pore pressure profile with depth

b. Pore pressure change with depth

Fig. 3.83 - Profile of pore pressure (a) and pore pressure changes (b) with depth.

In addition to changing with depth, pore pressures also change with distance from the injection point. Fig. 3.84 shows pore pressure profiles and pore pressure changes with time in the lateral distance from the injection point at the depth of injection point. Pore pressure increases at the injection point and decreases towards its in situ value at the lateral boundary. After 10 years of injection, the pore pressure in the injection point is almost 30 MPa and it decreases to 15 MPa at the lateral distance close to 10 km (Fig. 3.84a). This change is also shown in Fig. 3.84b, in which 15 MPa of pore pressure change occurs at the injection point after 10 years of injection and decreases towards zero with lateral distance.

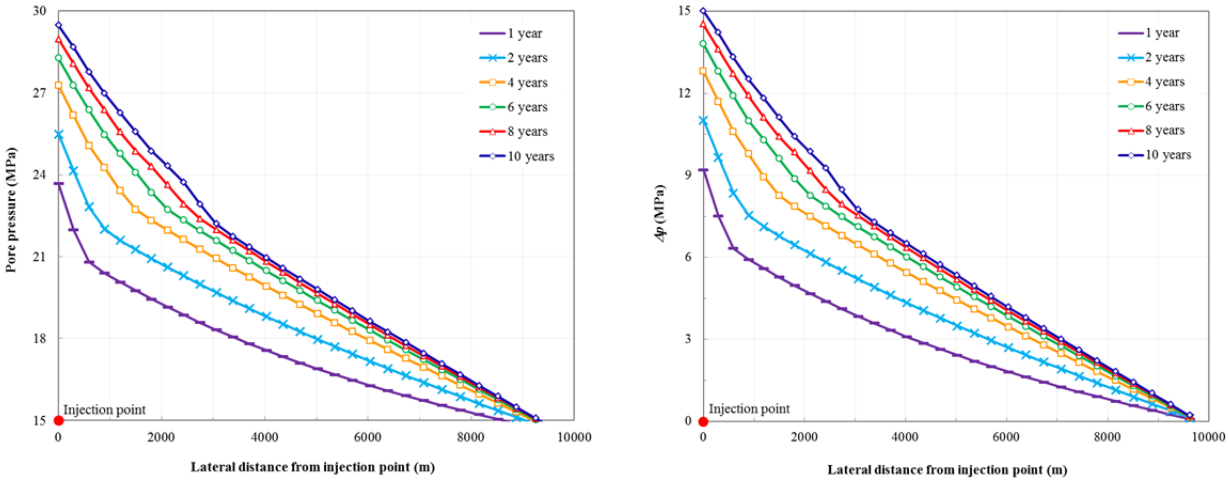

a. Pore pressure

b. Pore pressure changes

Fig. 3.84 - Profiles of pore pressure (a) and pore pressure changes (b) with lateral distance.

Even though deformation is due to change in effective stress, we are more interested in total stress change since change in effective mean stress is calculated as the mean change in total stress minus change in pore pressure (Pruess et al., 2002). Fig. 3.85 shows the profile of total stress changes with depth at various injection periods. For both total vertical and horizontal stress profiles, significant stress changes start from the caprock layer and reach maximum in the reservoir layer before heading back to zero in the basement layer. This type of profile is similar to that of pore pressure change with depth (Fig. 3.84b), strains with depth (Fig. 3.79), and vertical displacement with depth (Fig. 3.78).

Fig. 3.85 also shows that total horizontal stress changes in the reservoir layer are more significant (0-10 MPa) than the total vertical stress changes (0-1 MPa) at any injection periods. This is because no lateral expansions is allowed at the near (close to the injection point) and far lateral boundaries, while vertical deformation is allowed on the ground surface. This obvious difference is also shown in the profile of total stress changes with lateral distance from injection point (Fig. 3.86). At the injection point, the total vertical stresses increase about 0.9-1 MPa (Fig. 3.86a), while a 6-10 MPa stress increase occurs to the total horizontal stresses (Fig. 3.86b). Towards the far-lateral boundary, the change in vertical stress is then relatively constant at 0.7 MPa, while the change in horizontal stresses decreases towards 1 MPa.

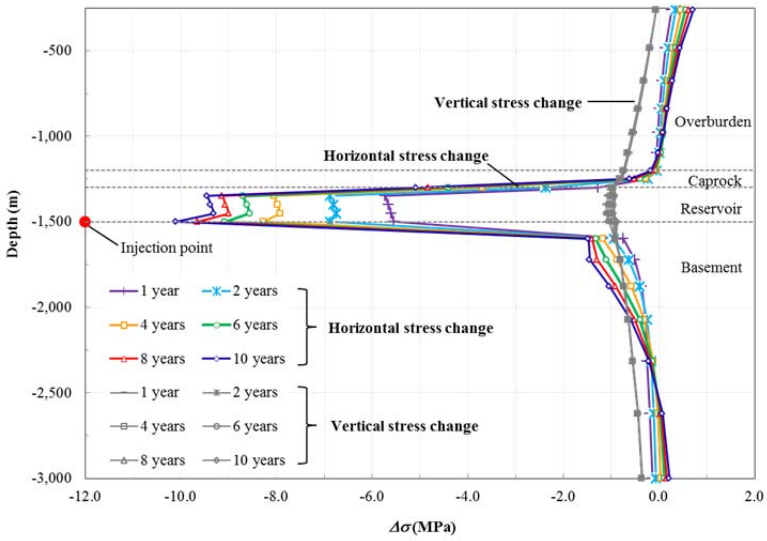

Fig. 3.85 - Profile of total stress changes with depth.

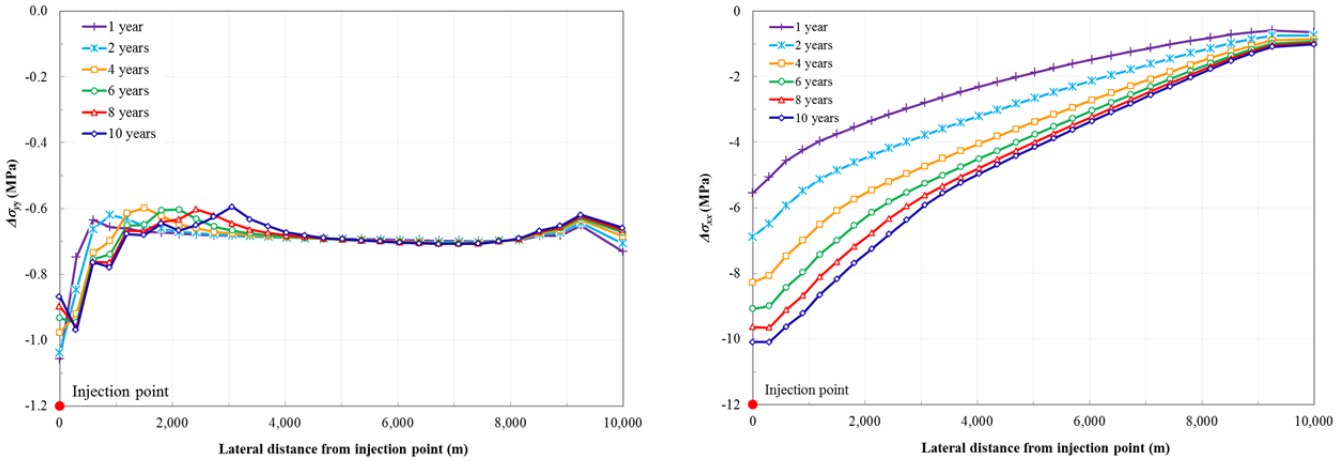

a. Vertical stress changes

b. Horizontal stress changes

Fig. 3.86 - Profile vertical (a) and horizontal (b) stress changes with lateral distance.

Summary of the results from the prototype model. The following differences were observed in the proposed model as compared to the previous modeling work done by Winterfeld and Wu (2011):

1) The CO_2 plume spreads faster in the proposed model because constant CO_2 viscosity and density were.
2) Larger injection pressure appears in the FLAC model which can be attributed to the extensive spread of the CO_2 plume. However, both the FLAC and the reference models show similar behavior of lower pressure build-up with inclusion of rock deformation (hydromechanical simulation) than with exclusion.
3) The surface uplifts in the FLAC model agree quite well with those in the reference model. The uplift shapes in the FLAC model are somewhat flattened towards the lateral boundary compared to the reference, which dips more.

4) Both vertical and horizontal strains are at maximum in the caprock and reservoir layers, respectively. This difference is due to CO_2's lighter-than-water density that naturally makes the CO_2 always dissipate towards the overburdens.
5) Due to the injection, the reservoir is inflated vertically and stretched out laterally. The most inflated location is above the injection point, while the most stretched-out location is in the middle distance between the injection point and far-lateral boundaries.
6) Displacements that occur to the formation are caused by the induced pore pressure from the injection. The change in pore pressures then causes changes in the total stress, both vertically and horizontally.
7) The maximum pore pressure and total stress changes occur in the reservoir layer and decrease towards the far-lateral boundary. The total horizontal stress changes are more significant than the total vertical stress changes. This is because the horizontal lateral boundaries are fixed but the vertical lateral boundary is free to move on the ground surface.
8) The model has reached equilibrium based on the predetermined equilibrium ratio. The histories of unbalanced force and equilibrium ratio show progression towards zero and below the default value with small oscillations as the solution evolves.

3.5.3 Validation of the coupled H-M model CO_2 Injection at the In Salah CO2 Storage Project, Algeria

A photograph of the In Salah gas plant at the Krechba site and its CO_2 injection cycle are shown in Fig. 3.87. The In Salah model follows the model developed by Preisig and Prevost (2011), who used Dynaflow to simulate the two-phase flow hydromechanical coupling process in their model. The cross-section of the reference model is shown in Fig. 3.88 together with the FLAC model developed in this study. The material properties for the FLAC model are given in Table 3.16. The rock and hydrogeologic properties are taken from Rutqvist et al. (2010) as suggested by Preisig and Prevost (2011). The hydrostatic water pressure igradient s 10 MPa/km, and the total vertical stress gradient is 22 MPa/km.

The FLAC model is 3,600 m in depth and up to 5,000 m in length to follow the reference model. It consists of overburden (0-900 m), caprock (900-1,800 m), reservoir (1,800-1,820 m), and basement (1,820-3,600 m). CO_2 is injected at a depth of 1,820 m with the injection rate of 2.2×10^{-3} kg/(s.m) for a total injection period of 3 years. The boundary conditions for the In Salah FLAC model follow those for the prototype model.

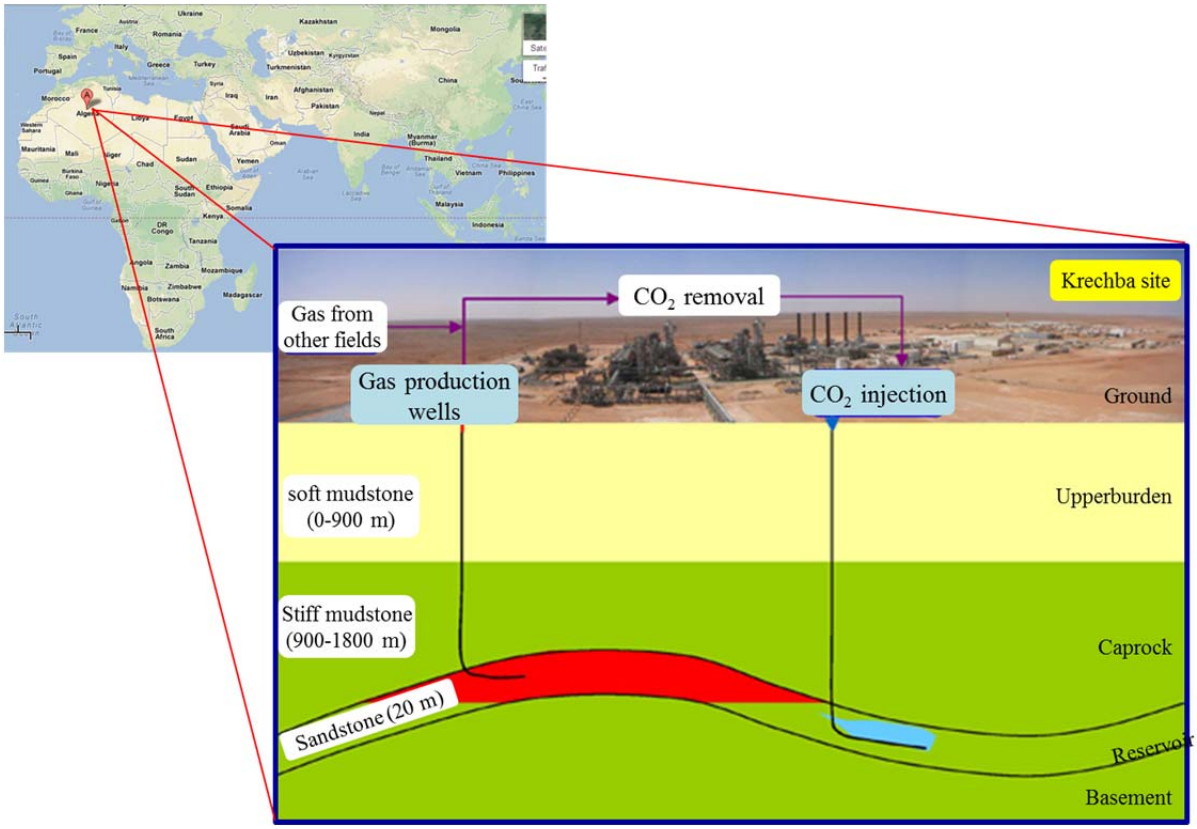

Fig. 3.87 - Photograph of the In Salah natural gas plant and its CO_2 injection cycle (modified from LLNS, 2009).

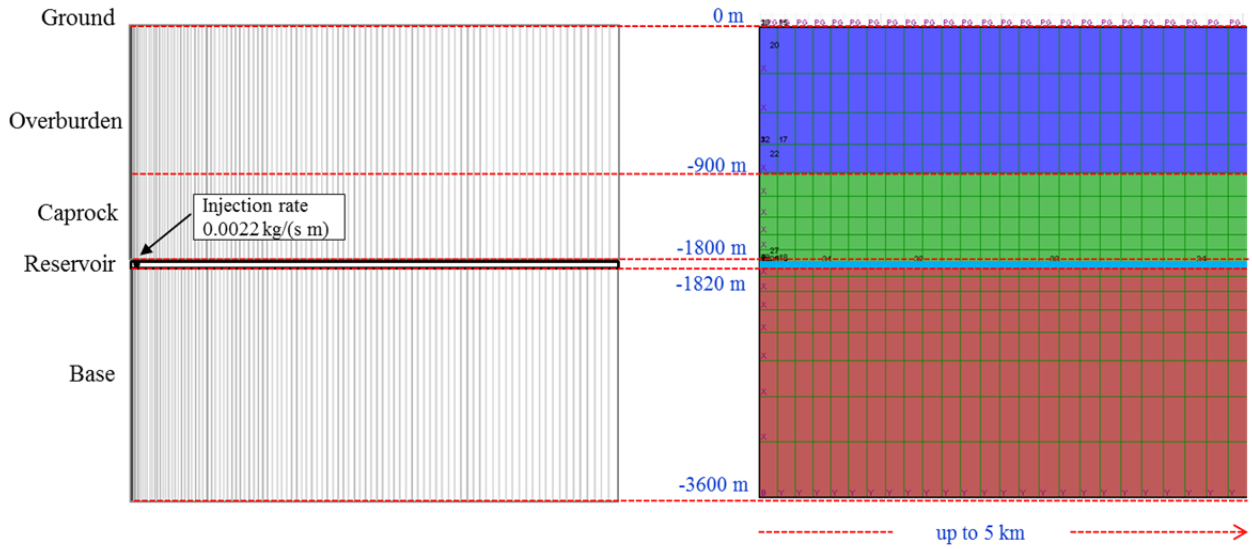

a. Reference model (Preisig & Prevost, 2011) b. FLAC model

Fig. 3.88 - The reference In Salah model (a) and FLAC model (b).

Table 3.16 - Rock and hydrogeologic properties for the In Salah FLAC model (Rutqvist et al. 2010)

Property	Overburden	Caprock	Reservoir	Basement
Young's modulus, *E* (GPa)	1.50	20	6	20
Poisson's Ratio, *v*	0.20	0.15	0.20	0.15
Bulk modulus, *K* (GPa)	0.83	9.52	3.33	9.52
Shear modulus, *S* (GPa)	0.62	8.69	2.50	8.69
Saturated rock density, ρ (kg/m^3)	2,200	2,200	2,200	2,200
Porosity, ϕ	0.10	0.01	0.17	0.01
Permeability, *k* (m^2)	1x10^{-17}	1x10^{-19}	1.3x10^{-14}	1x10^{-19}
Residual gas saturation	0.05	0.05	0.05	0.05
Residual water saturation	0.30	0.30	0.30	0.30
Air-entry pressure, *Po* (kPa)	19.9	621	19.9	621
Van Genuchten's exponent, *m*	0.457	0.457	0.457	0.457
Biot's parameter	1.00	1.00	1.00	1.00

Fig. 3.89 compares lateral profiles of CO_2 saturation as a function of time from the injection point. Compared to the reference model (Fig. 3.3b), the FLAC model (Fig. 3.89a) shows relatively small discrepancies in the lateral extent of CO_2 distribution, but far less saturation value. Again, some of these discrepancies may be due to the constant viscosity and density of CO_2 used in the FLAC model, while a pressure-dependent function is used in the reference model. The use of a pressure dependent function will make the CO_2 phase less viscous but denser. Fig. 3.90Fig. shows the spread of CO_2 plumes from the FLAC model at various injection periods up to 3 years. CO_2 has penetrated towards the basement as early as 6 months of injection and penetrated deeper into basement and caprock after 15 months of injection while continuing to spread laterally. This breakthrough may be due to the low air-entry pressure in the caprock and basement. Hence it only takes 621 kPa higher for the CO_2 gas to penetrate into these two layers. This air-entry pressure is five times lower than that in the prototype model (3.1 MPa).

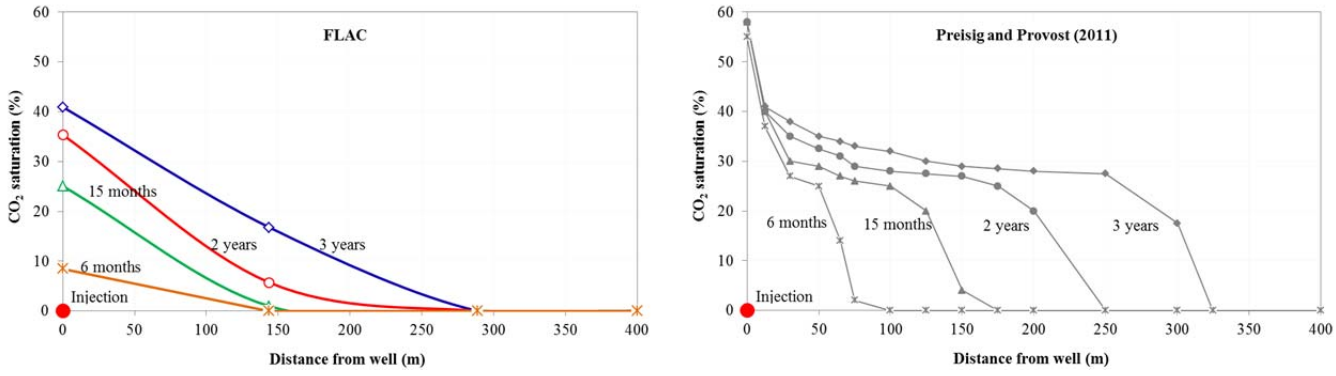

a. FLAC model b. Reference model

Fig. 3.89 - Lateral CO_2 profile from the FLAC (a) and reference model (b).

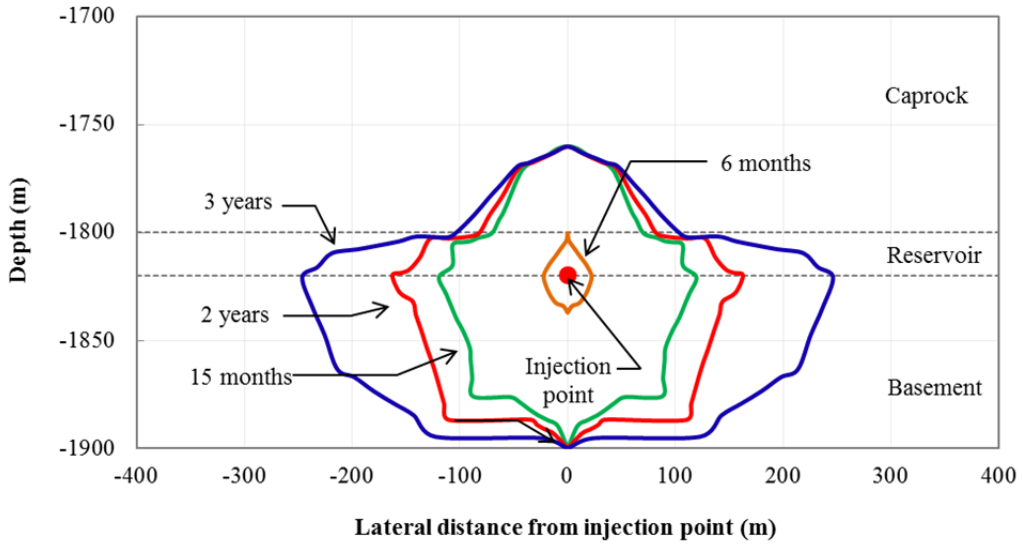

Fig. 3.90 Spread of CO_2 plumes at various injection period.

During the simulation, pore pressure increase in the FLAC model is monitored at several locations from the injection point and the history is compared to the reference model. Fig. 3.91 shows these histories after 3 years of injection.

Overall, the histories of pore pressure increase in the FLAC model agree quite well with the reference model. The history of pore pressure increase is almost perfectly matched at the well (Fig. 3.91a), which shows a pressure increase of 11 MPa after 3 years of injection. This is the maximum pore pressure increase in the model since the increase of pore pressure at other locations decline with lateral distance from the well (Fig.s 3.91b-3.91f). At these locations, the FLAC model shows relatively lower pressure increases compared to those in the reference. However, the differences are no more than 2 MPa.

The maximum increase of pore pressure at the injection point can also be seen in Figs. 3.92 and 3.93. In Fig. 3.92a, significant pore pressure increases occur at the injection point and dissipate to zero towards the far lateral boundary. After 3 years of injection, the pore pressure at the injection point increases to 29 MPa (Fig. 3.92b) and the value decreases towards the lateral boundary at which the pore pressure goes back to its initial value before the injection (18 MPa).

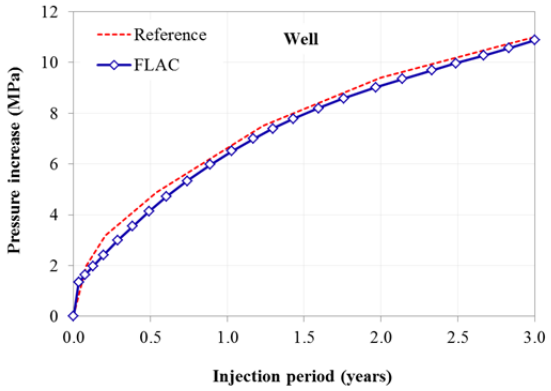

a. Well

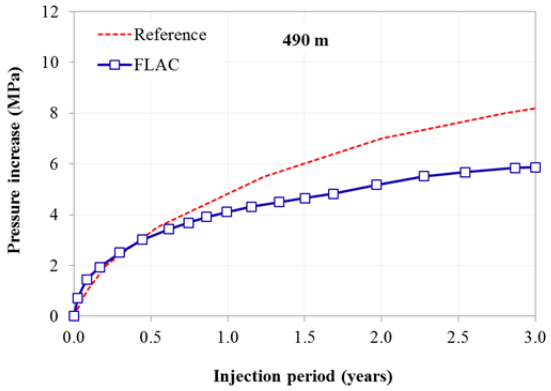

b. 490 m

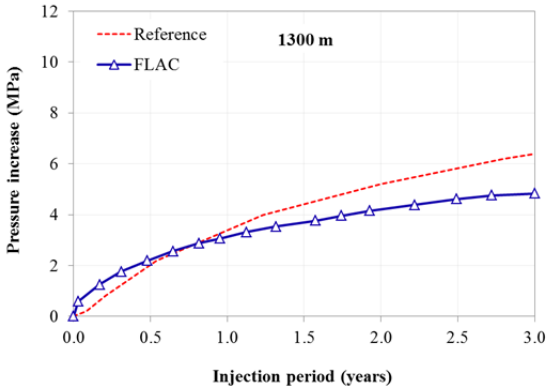

c. 1300 m

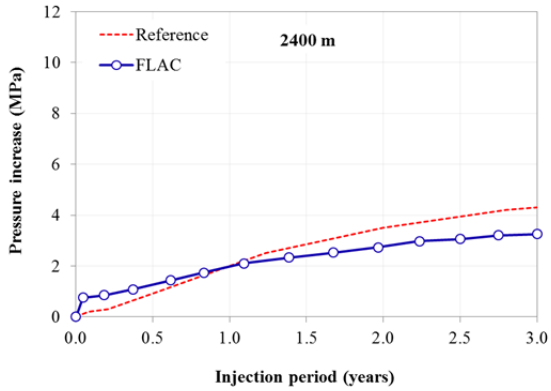

d. 2400 m

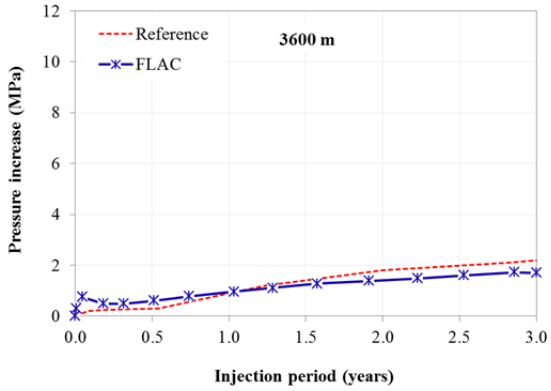

e. 490 m

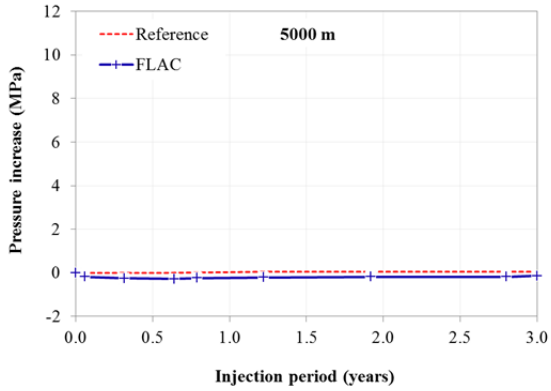

f. 5000 m

Fig. 3.91 - Histories of pore pressure increases at various distances from the injection point.

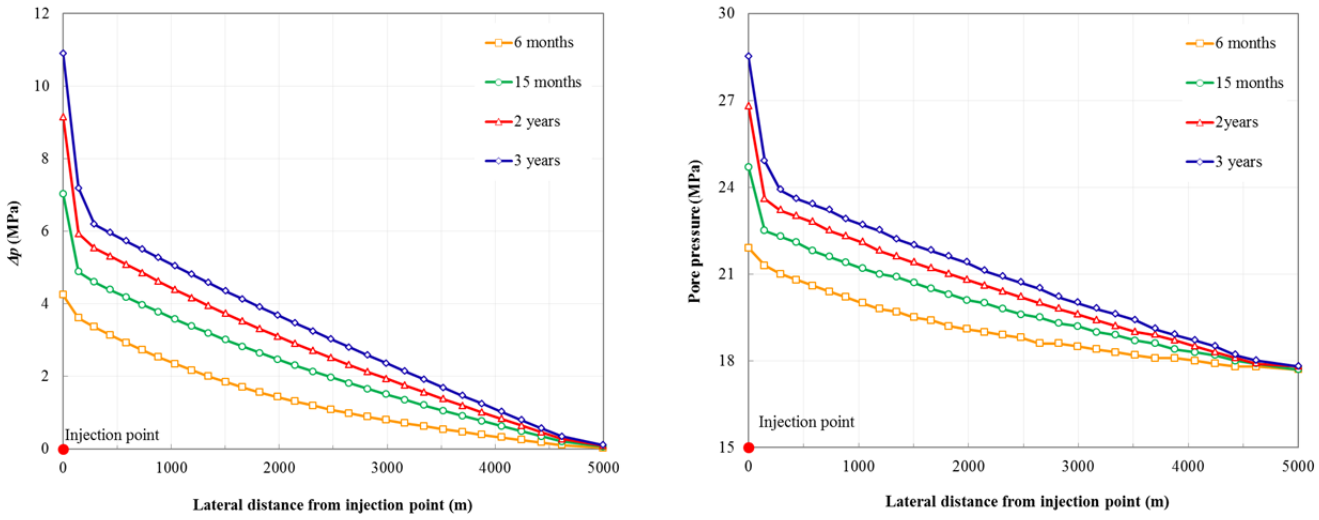

a. Pore pressure change b. Pore pressure

Fig. 3.92 - Profile of pore pressure change (a) and final pore pressure (b) from injection point.

Fig. 3.93 also shows that the maximum pore pressure change with depth is in the reservoir layer (Fig. 3.93a). This increase causes inflated pore pressure in the reservoir as shown in Fig. 3.93b. However, the inflating pressure is still below the lithostatic pressure line. Another interesting feature is the negative pore pressure changes at 100 m above and 200 m below the reservoir in Fig. 3.93a. According to Vilarrasa et al. (2011), these locations would be the extension zones at which the pore pressure decreases while the pore volume increases.

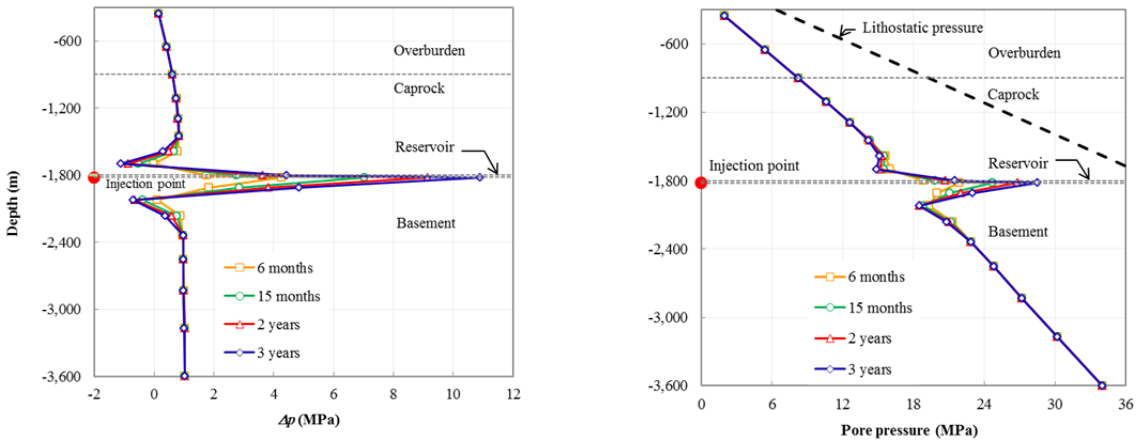

a. Pore pressure change b. Pore pressure

Fig. 3.93 - Profile of pore pressure change (a) and final pore pressure (b) from surface.

Fig. 3.94 compares the history of vertical displacement at the ground surface from the FLAC model, the reference model by Preisig and Prevost (2011), the simulation from Rutqvist et al. (2010), and the field measurements (KB-503 and KB-501). The FLAC model predicts a maximum surface uplift of 1.6 cm after 3 years of injection, while the reference model predicts 3.0 cm and Rutqvist et al. (2010) predict 2.0 cm. However, the field measurements at two

locations at the Krechba site are in fact in agreement with the FLAC model. The maximum surface uplift at KB-503 is approximately 1.5 cm and approximately 1.4 cm at KB-501.

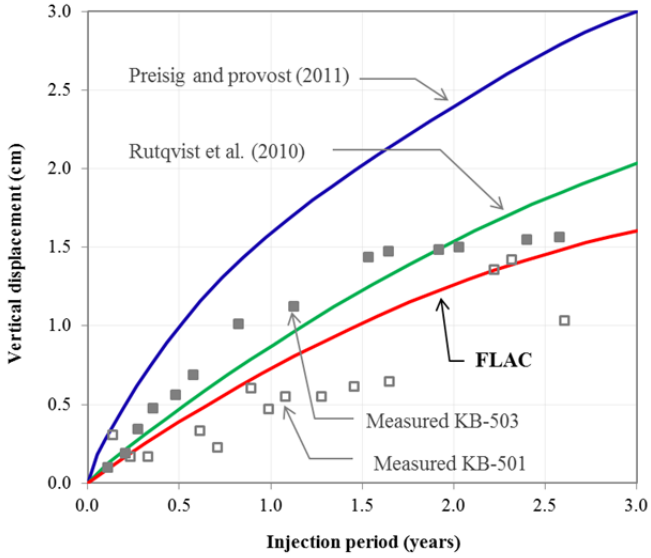

Fig. 3.94 - History of vertical displacement on the surface.

The overestimated prediction from the reference model is also shown in the profile of surface uplift as shown in Fig. 3.95. The FLAC model (Fig. 3.95a) predicts far less surface uplift than the reference model (Fig. 3.95b). In addition, some subsidence occurs near the far-lateral boundaries in the FLAC model at 5 and 15 months after injection. This subsidence indicates the existence of a compression zone towards the lateral boundaries of the model. Vilarrasa et al. (2012) found a similar zone.

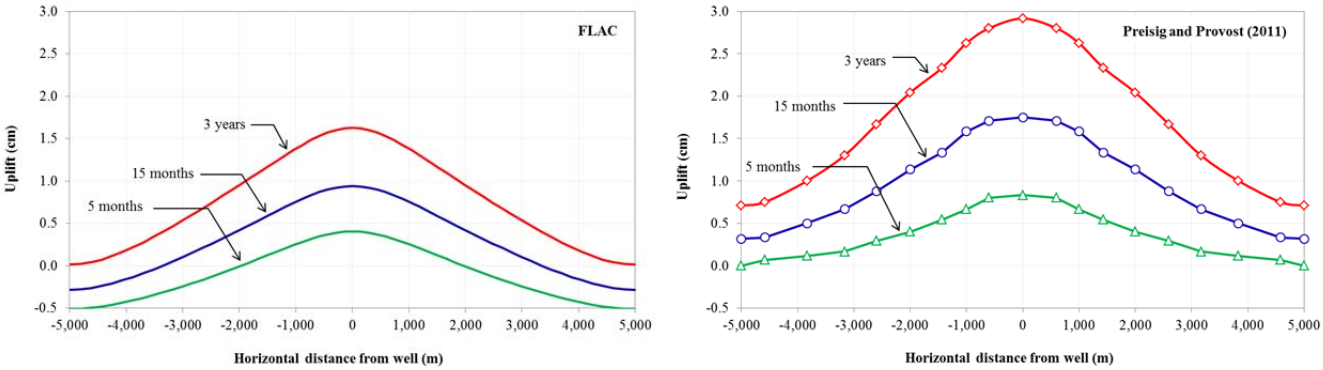

a. FLAC model b. Reference model

Fig. 3.95 - Profile of the surface uplifts from the FLAC (a) and reference model (b).

Fig. 3.96 shows the history of vertical displacement in which the locations closer to the injection point displace more and the displacement attenuates towards the ground surface. An exception is for the bottom part of the reservoir as the bottom boundary is constrained. Similar histories have been observed for the prototype model analyzed above. After 3 years of injection, the surface uplift (1.6 cm) is about 70% of the uplift of the top part of the reservoir (2.25 cm).

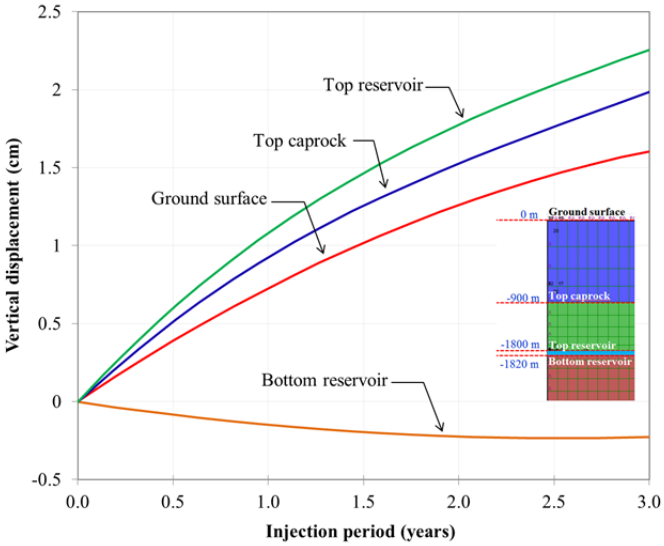

Fig. 3.96 - History of vertical displacement at various locations in the model.

Summary of the results from the In Salah CO_2 Storage Project. The following differences were observed in the proposed model as compared to the previous modeling work done by Preisig and Prevost (2011), and Rutqvist et al. (2010):

1) The predicted surface uplift (1.6 cm) in the FLAC model agrees well with the field observations at the Krechba site (1.4-1.5 cm). However, the predicted surface uplifts in the FLAC model are below those in the reference model (3 cm).
2) The lateral CO_2 distribution from the injection point in the FLAC model is considerably in agreement with the reference model, but the saturation values in the FLAC model are still below those in the reference model.
3) The histories of pore pressure increases from the injection point in both models generally agree well, particularly the pore pressure increase at the well in which a maximum pressure increase of 11 MPa in the reference is perfectly matched by the FLAC model.

3.5.4 Validation of the Coupled H-M Model Against the Sleipner CO_2 Sequestration Project in Norway

The location of the Sleipner gas field is shown in Fig. 3.97. The cut-view of the reference Sleipner model is also shown in Fig. 3.97 together with the FLAC model developed in this study. The FLAC model follows the reference Sleipner model developed by Pruess et al. (2002). Due to the limited number of zones in the current version of FLAC, our Sleipner FLAC model is only 184 m wide and 750 m long. The reference model is 184 m wide and up to 5,000 m long. The injection point is 940 m below the sea floor (1,020 m below sea level). The formation, called the Utsira Formation, consists of a series of four low permeability shale layers of 3 m thickness each. Each shale layer is separated by a 30 m sandstone layer. CO_2 is injected for 2 years at 30 m below the lowest shale layer and 22 m above the bottom part of the reservoir.

The boundary conditions are impermeable on all sides except the far-lateral boundary (at x = 750 m) at which the pore pressure is fixed at its hydrostatic value. We are only interested in evaluating pressure distribution and CO_2 saturations in the reservoir. Hence, only the reservoir layer is modeled in this report.

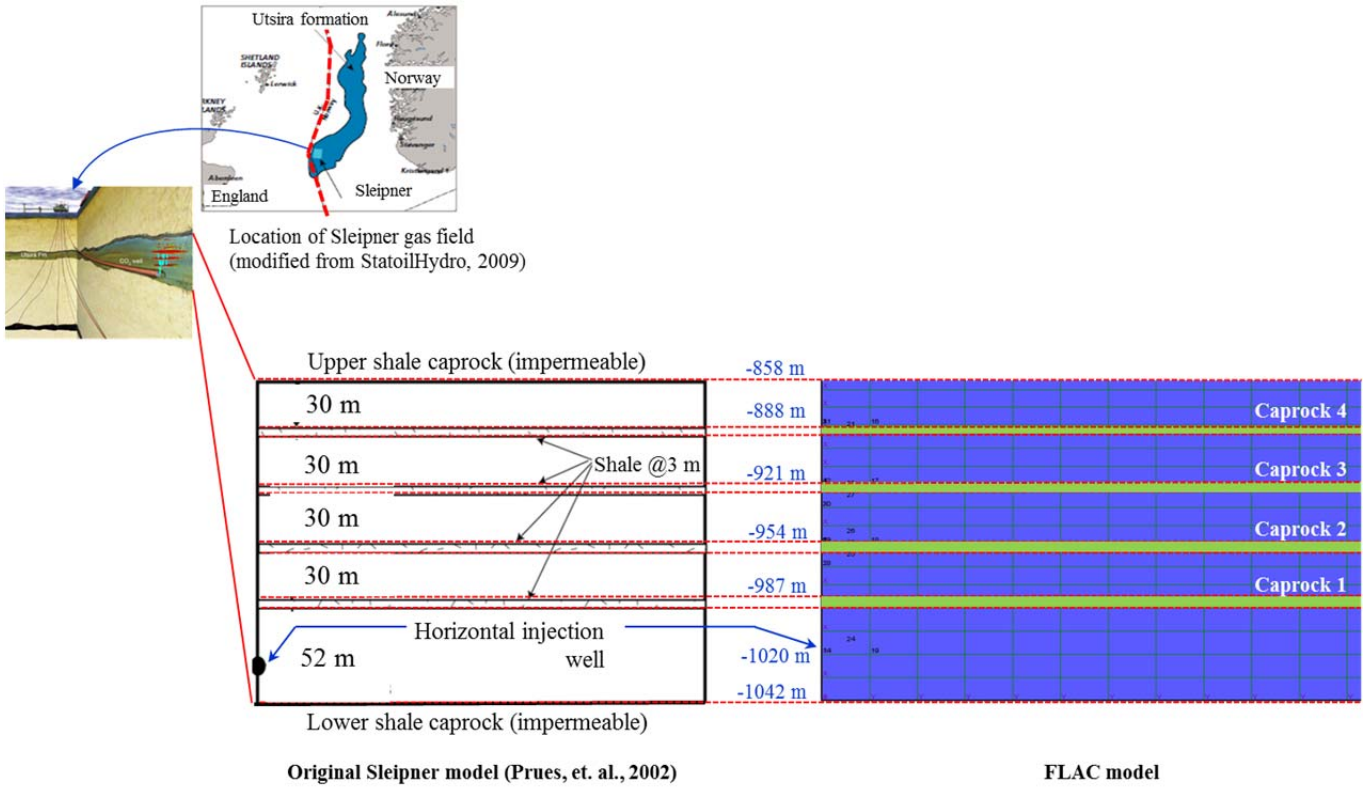

Fig. 3.97 - Location of Sleipner gas field, its reference model (lower left) and FLAC model (lower right).

The rock properties for the FLAC model are given in Table 3.17, while the hydrogeologic properties are given in Table 3.18. Since the rock properties are not shown in Pruess et al. (2002), we follow those in Rutqvist et al. (2007) who developed a similar problem of multilayered reservoir-caprock system.

Table 3.17 - Material properties for Sleipner FLAC model (Rutqvist et al., 2007).

Property	**Caprocks**	**Reservoir**
Young's modulus, E (GPa)	5	5
Poisson's Ratio, v	0.25	0.25
Bulk modulus, K (GPa)	3.33	3.33
Shear modulus, S (GPa)	2.00	2.00
Saturated rock density, ρ (kg/m^3)	2,260	2,260

Table 3.18 - Hydrogrologicl properties for Sleipner FLAC model (Pruess et al., 2002).

Property	**Caprocks**	**Reservoir**
Porosity, ϕ	0.1025	0.35
Permeability, k (m^2)	$1x10^{-14}$	$3x10^{-12}$
Residual gas saturation	0.05	0.05
Residual water saturation	0.20	0.20
Air-entry pressure, Po (kPa)	62.0	3.58
Van Genuchten's exponent, m	0.40	0.40
Biot's parameter	1.00	1.00

The simulation results for the Sleipner FLAC model are compared with the results from Pruess at al. (2002) at various injection periods (30 days, 1 year, and 2 years). Fig. 3.98 shows the vertical profiles of CO_2 saturation in the reservoir at a distance of 10 m away from the injection point at various injection periods. Fig. 3.99 shows the vertical profiles of CO2 saturation in the reservoir after 1 year of injection at various distances from the injection point.

Even though the values and shapes of CO_2 saturation from the FLAC model (Figs. 3.98 to 3.100) do not perfectly match with those from the reference (Figs. 3.100a -3.100b), the FLAC model still captures the capability of caprocks to limit the ascent of CO_2. Some discrepancies are observed, such as that the CO_2 saturations in the upper part of the reservoir in the FLAC model are always larger than those in the reference model. Conversely, the CO_2 saturations at the lower part of the reservoir in the FLAC model are relatively lower than those in the reference model. These profiles indicate that the CO_2 plumes in the FLAC model migrate upward faster than those in the reference model.

Fig. 3.100 shows the vertical profiles of CO_2 saturation in the reservoir after 2 years of injection at various distances from the injection point. Fig. 3.101 shows pore pressure distribution inside the reservoir after 2 years of injection. We only show the distribution up to 750 m from the injection point since the lateral extent of the FLAC model is limited to that distance. Both models show contours of 12.6 MPa at the injection point, indicating pore pressure increases of 1.6 MPa have occurred after 2 years of injection (initial pore pressure at the injection point is 11 MPa). Fig. 3.101 shows relatively similar pore pressure distribution between the two models. It is very difficult (if not impossible) to match the distribution with the reference considering the FLAC model only extends up to 750 m. Hydrostatic boundary conditions may influence the distribution in the FLAC model. Hence, small discrepancies may occur.

Similar pore pressure distributions between the two models also occur in terms of depth from the upper part of the reservoir (Fig. 3.102). The most noticeable pore pressure increase occurs at the lowest sandstone layer below Caprock 1 at which the injection point is located. At this layer, both models show a pore pressure decrease with increasing injection period, while the opposite is observed at the layers above this layer.

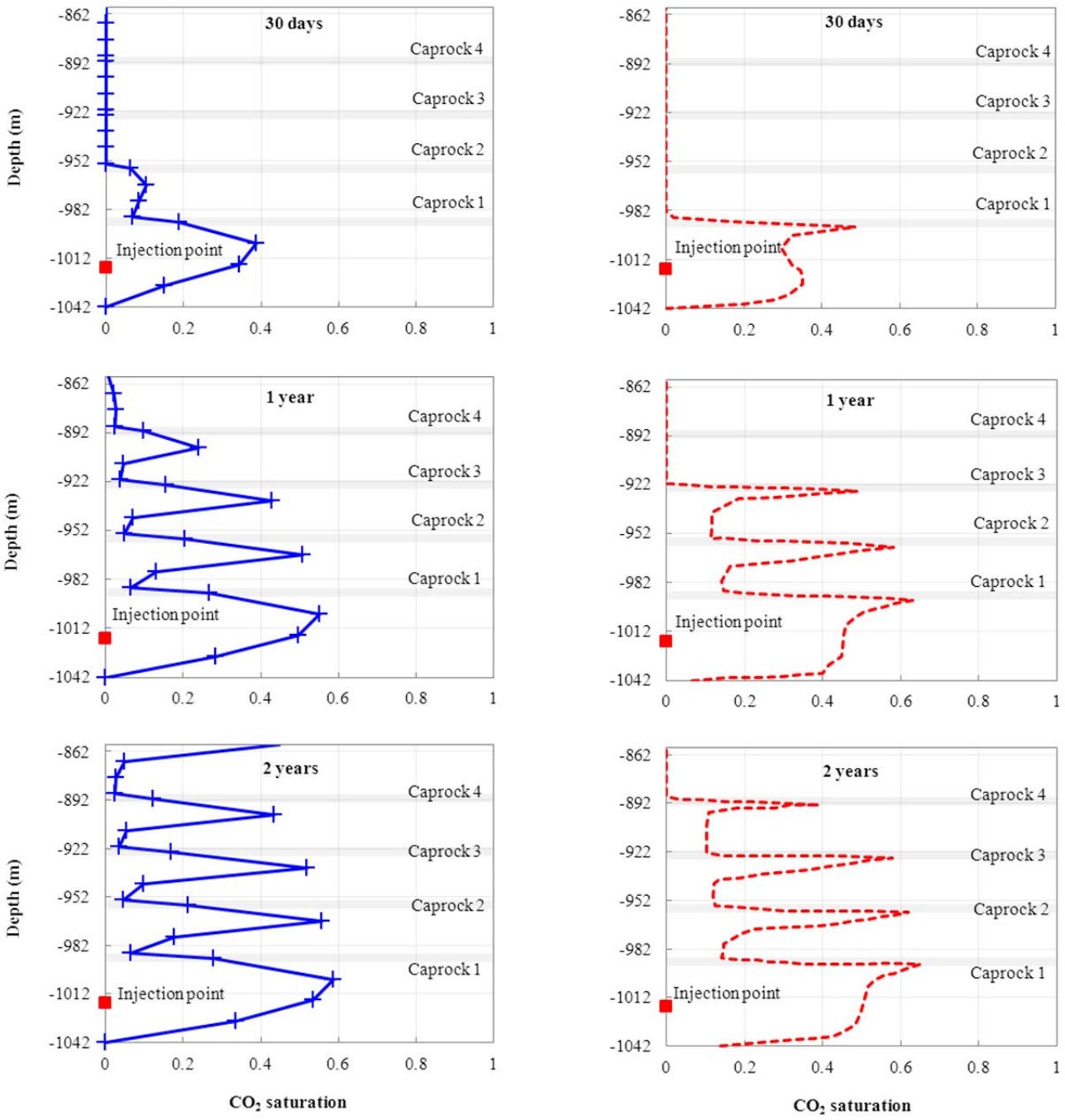

a. FLAC b. Reference (Pruess et al., 2002)

Fig. 3.98 - Vertical profiles of CO_2 saturation in reservoir from the FLAC (a) and reference model (b) at 10 m from the injection point.

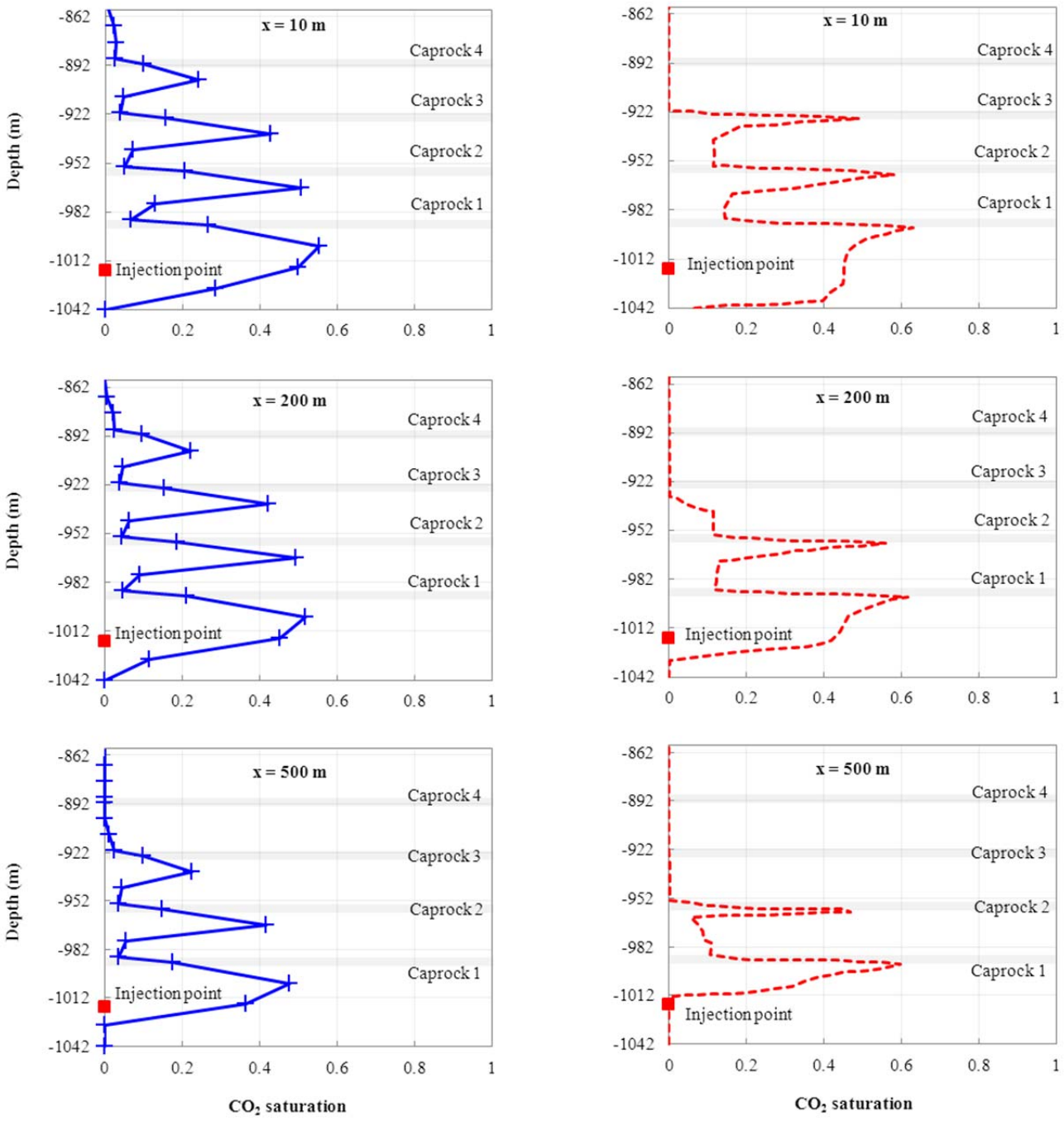

a. FLAC

b. Reference (Pruess et al., 2002)

Fig. 3.99 - Vertical profiles of CO_2 saturation in the reservoir from the FLAC (a) and reference model (b) after 1 year of injection.

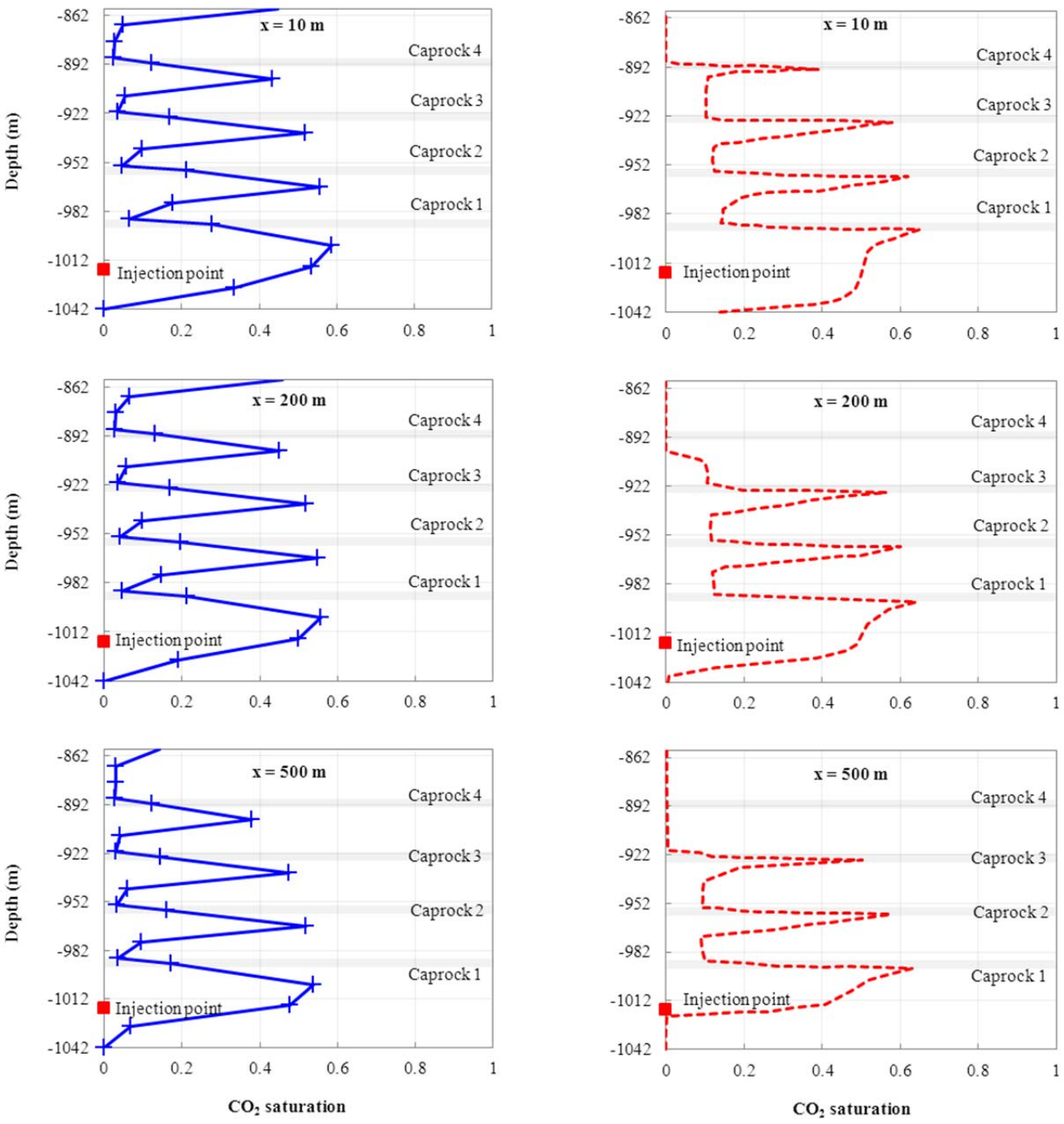

a. FLAC

b. Reference (Pruess et al., 2002)

Fig. 3.100 - Vertical profiles of CO_2 saturation in the reservoir from the FLAC (a) and reference model (b) after 2 years of injection.

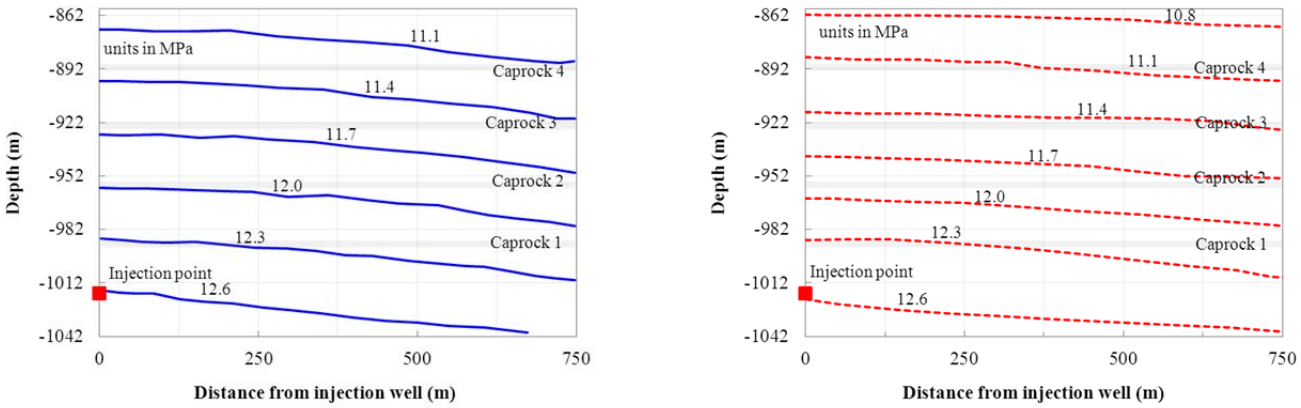

a. FLAC b. Reference (Pruess et al., 2002)

Fig. 3.101- Profiles of pore pressure distribution in the reservoir from the FLAC (a) and reference model (b) after 2 years of injection.

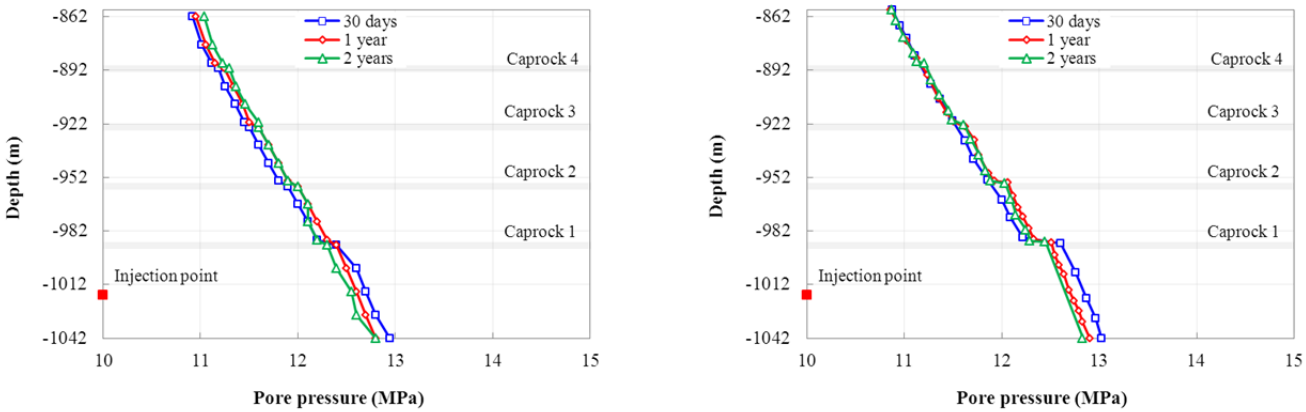

a. FLAC b. Reference (Pruess et al., 2002)

Fig. 3.102 - Profiles of pore pressure distribution with depth from the FLAC (a) and reference model (b) after 2 years of injection.

Summary of the results from the Sleipner CO_2 Sequestration Project. The following differences were observed in the proposed model as compared to the previous modeling work done by Pruess at al. (2002):

1) The FLAC model is able to capture the CO_2 plume movement in the reservoir where CO_2's upward migration is decelerated by the low-permeable shale layers. However, the degree of the saturation of the migrated CO_2 does not perfectly agree. There are some saturation discrepancies in the lower and upper parts of the reservoir in the FLAC model compared to the saturation in the reference model.
2) Pore pressure distributions in the reservoir are relatively similar between the two models. Some pressure difference exists, but it is quite insignificant.

3.5.5 Potential for Failure and Leakage in the Caprock

This section presents the results of the modeling for the potential for mechanical failures and leakage of the caprock due to the injection pressure. By using the critical pressure approach, a failure may occur when the injection pressure exceeds the critical pressure of the failure mode. This approach was firstly introduced by Rutqvist and Tsang (2002) and later used by Rutqvist, et al. (2007) for single and multilayer CO_2 injection models, respectively. The prototype model and its material properties for this failure analysis were used. The caprock was modeling with Mohr-Coulomb failure criterion with cohesion, tension, and friction angle as 2.75 MPa, 2.50 MPa, and 18^o, respectively. These follow those suggested by Josh et al. (2012) for shale gas reservoirs. The model is 3 km deep and 20 km wide.

Two types of mechanical failures are studied, tensile and shear failures, since these two are the most common failures leading to leakage for hydrocarbon migration (Nygard, et al., 2006). We use the term potential since, in reality, we are not truly able to see the process of failures in the formation. For this type of failure, a rather conservative assumption is adopted from Jaeger et al. (2007), that is, the caprock may potentially fail when the injection pressure (P) exceeds the least compressive principal stress (σ_3). Hence, the critical pressure for tensile failure (P_{ct}) is defined as

$$P_{ct} = -\sigma_3 \tag{3.25}$$

Since the fluid pressure is positive for compression, the negative sign is needed to convert the stress into positive magnitude (stress is negative for compression). Therefore, as long as the injection pressure (P) in the caprock is still below the critical pressure for tensile failure (P_{ct}), the caprock is safe. Conversely, when the injection pressure (P) is above the critical pressure for tensile failure (P_{ct}), the caprock may potentially fail in tension. Quantitatively, the previous two statements may be expressed in terms of pressure margin for tensile failure (P_{mt}) as:

$$P_{mt} = P - P_{ct} \quad (3.25) \tag{3.26}$$

where

$P_{mt} < 0$ = no failured
$P_{mt} > 0$ = failure in tension.

Fig. 3.103 shows the close-up view of pressure margin value for tensile failure (Fig. 3.103a) and contour of tensile region (Fig, 3.103b) after 10 years of CO2 injection. Both figures indicate the region near the bottom of caprock until 250 m below the bottom of reservoir is potentially failing in tension.

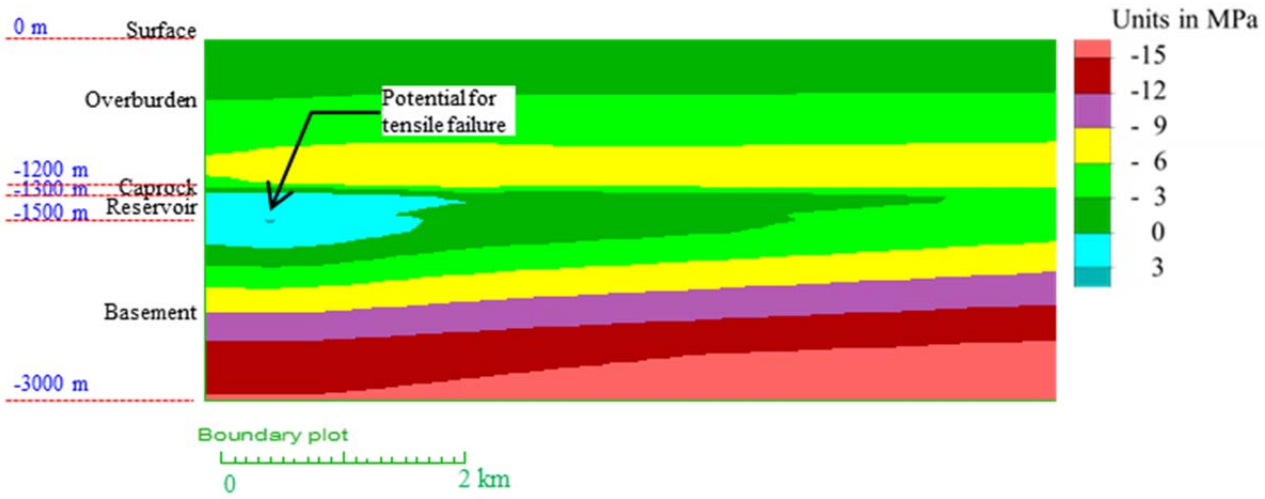

a.Pressure margin showing potential location for tensile failure (P_{mt} > 0 MPa)

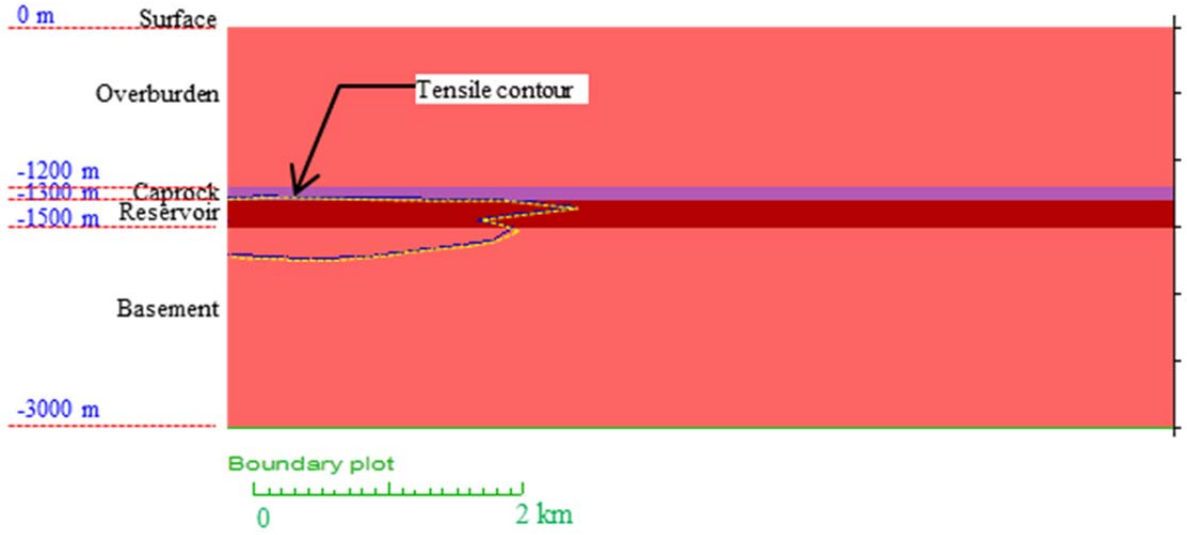

b. Contour of tensile region

Fig. 3.103 - Potential location for tensile failure after 10 years of CO_2 injection.

The vertical profiles of the critical pressure and pressure margin (at x = 0 m) also show clearly the potential location of tensile failure (Fig. 3.104). After 10 years of CO_2 injection (Fig. 3.104a), the injection pressure (solid blue line) exceeds the critical pressure (solid red line) by 0.5-1 MPa near the interface between caprock and reservoir, and more evident until 250 m below the reservoir before it approaches the hydrostatic fluid pressure (fluid pressure at 0 year) which is well below the critical pressure. This profile is also confirmed very well with the vertical profiles of pressure margin (Fig. 3.104b). The pressure margin after 10 years goes beyond the safe margin boundary (0 MPa) near the interface between caprock and reservoir, and more noticeable until 250 m below the reservoir before it goes back far below the safe margin boundary (-15 MPa) towards the bottom of the basement.

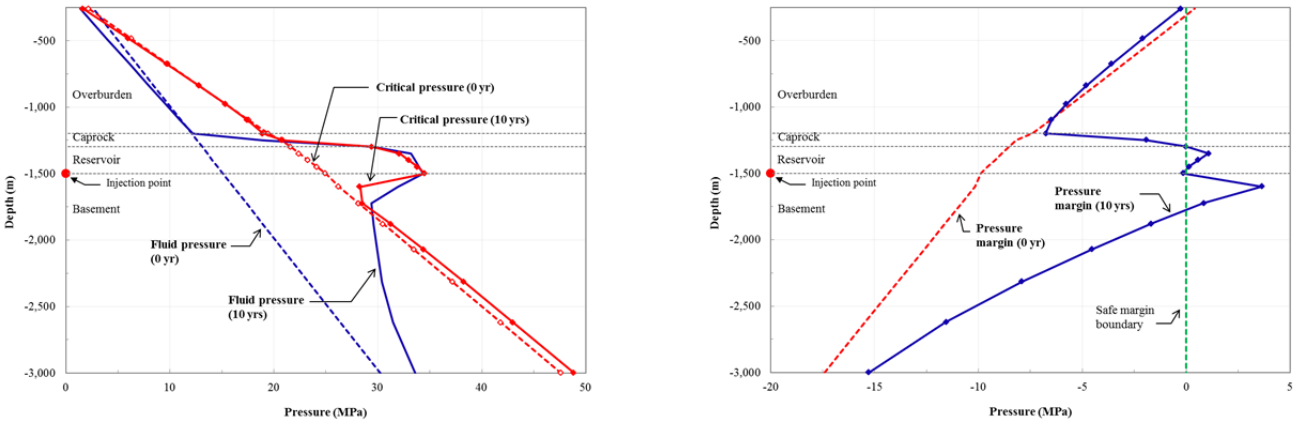

a. Critical pressure

b. Pressure margin

Fig. 3.104 - Vertical profiles of critical pressure and pressure margin for tensile failure (hydraulic fracturing).

In terms of potential for leakage, Figs. 3.103 and 3.104 suggest that it may need a longer injection period or increase in the injection pressure for the tensile failure to reach the top of the caprock which can induce CO_2 leakage to the overburden that is more porous than the caprock. With current injection pressure after 10 years, it is unlikely that the tension failure would propagate towards the top of of the caprock since the presurre margin at that location is about 7 MPa below the safe margin boundary.

Shear failure may be expressed using Mohr-Coulomb failure criterion with the effect of pore pressure (P) (Jaeger, et al., 2007) as:

$$|\tau_m| = (-\sigma_m - P)\sin\phi + S_o \cos\phi \tag{3.27}$$

where $\tau_m = (\sigma_1 - \sigma_3)/2$ is the shear stress, $\sigma_m = (\sigma_1 + \sigma_3)/2$ is the mean stress, S_o = cohesion, and ϕ = friction angle.Again, the negative sign before σ_m is needed to convert the stress into positive magnitude to be compatible with pore pressure (P). The critical pressure for shear failure is then derived from Eq. (3.24 as

$$P_{cs} = \sigma_m - |\tau_m| \sin c\phi + S_o \cot\phi \tag{3.28}$$

Therefore, just like the calculation of potential for tensile failure in the above section, as long as the injection pressure (P) in the caprock is still below the critical pressure for shear failure (P_{cs}), the caprock is safe. Conversely, when the injection pressure (P) is above the critical pressure for shear failure (P_{cs}), the caprock may potentially fail in shear. Quantitatively, the previous two statements may be expressed in terms of pressure margin for shear failure (P_{ms}) as:

$$P_{ms} = P - P_{cs} \tag{3.29}$$

where

$P_{ms} < 0$ = no failure

$P_{ms} > 0$ = failure in shear.

The potential for shear failure may be firstly seen from the distribution of effective principal stress tensors before and after the injection Fig. 3.104. Before the injection (Fig. 3.104a), it can be seen that the major effective principal stress is vertical. This is indicated by the vertical lines that are longer than the horizontal lines. The stresses also increase with depth as expected. After 10 years injection, the effective principal stress tensors rotate in the regions of

caprock and reservoir (Fig. 3.104b). Change in principal stress tensor direction indicates shear stresses are developed due to the injection.

Fig. 3.106 shows the close-up view of pressure margin value for shear failure after 10 years of CO_2 injection. The figure indicates the region in the caprock and reservoir is potentially failing in shear if a longer injection period or increase in the injection pressure is conducted. With the current pressure margin that is still approaching 0 MPa, the shear failure is still unlikely to occur.

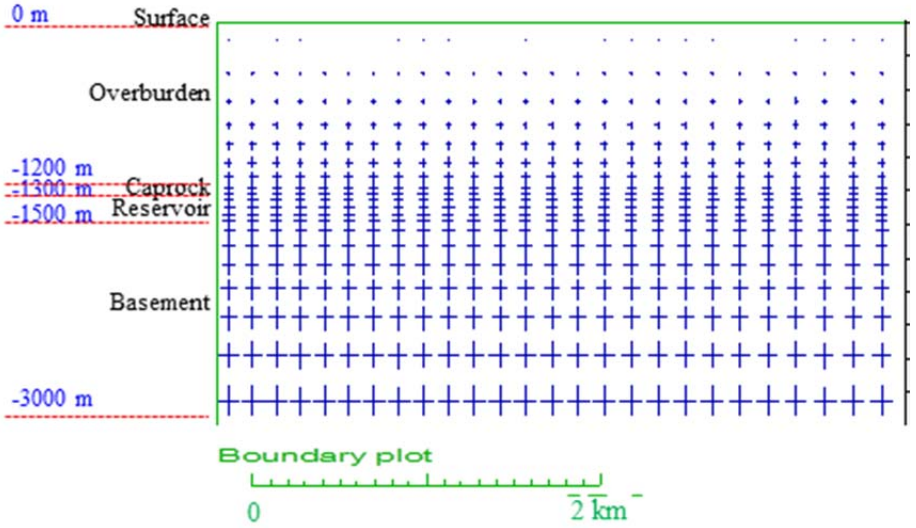

a. Effective principal stress before the injection

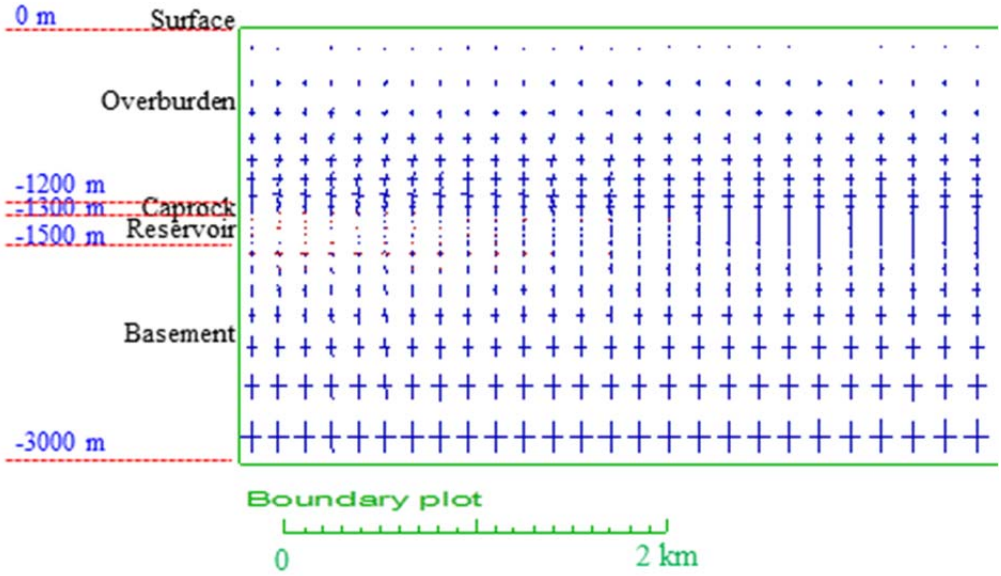

b. .Effective principal stress after 10 years of injection

Fig. 3.105 - Close-up view of effective principal stress tensor distribution before (a) and after (b) CO_2 injection.

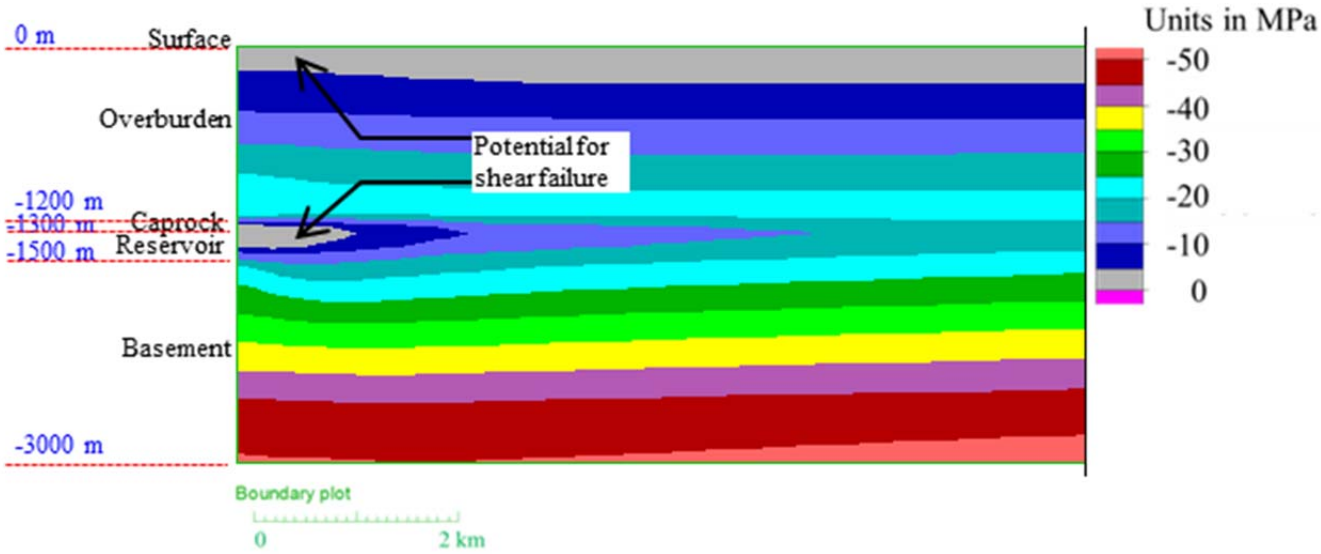

Fig. 3.106 - Pressure margin for shear failure after 10 years of CO_2 injection.

Another interesting result from Fig. 3.106 is the potential of shear failure near the ground surface. There are two possible reasons that might be able to explain this phenomena: 1) The assumption of zero stresses on the ground surface. This assumption will lead pressure margin calculation close to zero near the ground surface, and 2) Displacement induced from the injection point that propagate to the surface as surface uplift which is likely to induce mechanical failure.

The vertical profiles of the critical pressure and pressure margin for shear failure (at $x = 0$ m) also show that the shear failure is not happening yet (Fig. 3.107). After 10 years of CO_2 injection (Fig. 3.107a), the injection pressure (solid blue line) has not exceeded the critical pressure (solid red line) at any depth. However, if the injection is continued, the increase of injection pressure may overlap the critical pressure near the interface between the caprock and reservoir. This can be seen in Fig. 3.107b where only about 1 MPa additional pressure margin to go beyond the safe margin boundary and induce shear failure at that interface. Hence, there is an imminent risk for shear failure.

The potential for leakage due to shear failure may occur when there is an unfavorable oriented fault in the caprock through the thickness of the caprock. However, this possibility will need a significant increase of injection pressure because the pressure margin for shear failure through the thickness of the caprock is still far (> 25 MPa) below the safe margin boundary (Fig. 3.107b). Hence, the potential for shear failure to cause leakage through the caprock is much less prominent than that for tensile failure.

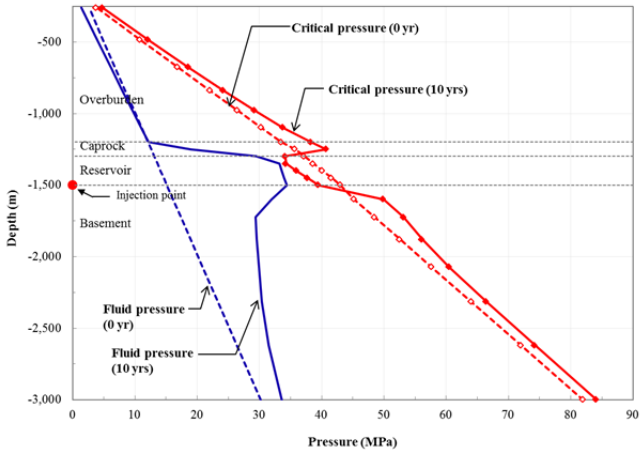

a. Critical pressure

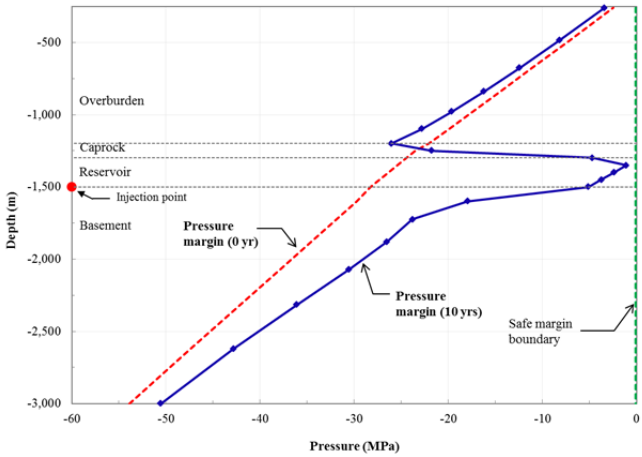

b. Pressure margin

Fig. 3.107- Vertical profiles of critical pressure and pressure margin for shear failure.

4. SUMMARY AND CONCLUSIONS

Research and training were conducted in the development and validation of an advanced CO_2 GS (Geological Sequestration) probabilistic simulation and risk assessment model. The developed models considered the full coupling of multiple physical processes (geomechanical and fluid flow) and describe the effects of stochastic hydro-mechanical (H-M) parameters on the modeling of CO_2 flow and transport in fractured porous rocks. Graduate students were involved in the development and validation of the model that can be used to predict the fate, movement, and storage of CO_2 in subsurface formations, and to evaluate the risk of potential leakage to the atmosphere and underground aquifers. The main major contributions from the project include the development of: 1) an improved procedure to rigorously couple the simulations of hydro-thermo-mechanical (H-M) processes involved in CO_2 GS; 2) models for the hydro-mechanical behavior of fractured porous rocks with random fracture patterns; and 3) probabilistic methods to account for the effects of stochastic fluid flow and geomechanical properties on flow, transport, storage and leakage associated with CO_2 GS. The research project provided the means to educate and train graduate students in the science and technology of CO_2 GS, with a focus on geologic storage. Specifically, the training included the investigation of an advanced CO_2 GS simulation and risk assessment model that can be used to predict the fate, movement, and storage of CO_2 in underground formations, and the evaluation of the risk of potential CO_2 leakage to the atmosphere and underground aquifers.

4.1 Project Accomplishments

The following are the main accomplishments from the project:

1. A technique for full coupling of hydro-mechanical (H-M) modeling consistent with Biot's poroelastic theory was developed and implemented in FLAC and TOUGH2.
2. Hydro-mechanical (H-M) models for fractured porous rocks were developed and implemented in a simulation program.
3. A Monte-Carlo-based risk assessment procedure developed to stochastically predict flow and transport of CO_2 in geological storage reservoirs.
4. Comprehensive studies on the effects of stochastic fracture distribution on the elastic compliance, permeability and REV of fractured rock masses were performed.
5. Comprehensive study on the effects of stochastic hydro-mechanical (H-M) parameters on CO_2 geological sequestration completed.
6. The models were applied to field prototype and actual CO_2 GS case histories.
7. Three Ph.D. students trained through research in stochastic coupled hydro-mechanical (H-M) modeling of CO_2 geological sequestration (GS) in fracture porous rocks.

4.2 Conclusions from the Research

4.2.1 Equivalent Continuum Modeling of the Permeability of Fractured Rock Masses

This project critically evaluated the sensitivities of the permeability values calculated from Equivalent Continuum Models, particularly Oda's permeability tensor, to variability in fracture distribution and the length scale. An extensive parametric study was conducted to evaluate the dependence of rock mass permeability to fracture geometrical parameters and the sampling

volume. A large number of fracture geometry realizations were generated using Monte Carlo Simulation (MCS) based on different Probability Distributions Functions (PDFs) to represent the variability of fracture geometry. Fracture geometrical parameters were based on field data obtained from different sources on studies of fracturing from varied geological sites. The results were used to establish relationships between variations in fracture geometry, length scale and rock mass permeability. The following are the main conclusions from the study:

1. Discretizing the PDFs of the input variables into 2,000 discrete data and performing a corresponding number of Monte Carlo Simulations yielded permeability values that deviated only about 5% from the values obtained from 10,000 discretized data. Thus, performing 2,000 MCS was deemed to be sufficient for the study.
2. A high fractal dimension in the power law distribution of fracture length, which produces more long fractures than shorter ones, provided higher permeabilities compared to a low fractal dimension.
3. A high exponent in the correlation between fracture aperture and fracture length produced higher permeability than a low exponent. Aperture distribution had more significant effects to the permeability than the length distribution. These results are simply due to the cubic law which states that permeability is function of the cubic power of the exponent.
4. Increasing the number of fracture sets resulted in a more isotropic permeability. The k_1/k_3 ratio decreases exponentially when the number of fracture sets is relatively small, but as the number of fracture sets becomes large, the ratio tended towards a value of 1.0.
5. Using the Side Length Ratio *SLR*, which is equal to the length of the side of the square sampling area divided by the length of the square region of interest, it was found that the mean values of the major and minor principal permeability values are independent of *SLR* above a certain threshold *SLR* value and oscillate below this threshold.
6. Using the Fracture Intensity *FIT*, defined as the sum of all the fracture lengths over the total volume of the region of interest, to quantify the degree of fracturing in a rock mass, it was found that *FIT*, like the mean principal permeability values, is also relatively constant above a certain threshold *SLR* value and oscillate below this threshold. The threshold *SLR* values for both *FIT* and mean principal permeability values were the same.
7. REV was formally defined as the *SLR* below which both the mean permeability and *FIT* values start to oscillate. Above this *SLR* value, the mean permeability and *FIT* remain relatively constant and independent of the size of the sampling volume.
8. A linear relationship was obtained between the logarithmic values of the *SLR* and the REV, which is valid for both the major and principal permeability values, and for a wide range of *FIT* values ranging from 10^{-5} to 10^{2} m^{-1}, and REVs from 10^{-7} to 10^{6} m. The REV determined from *FIT* can be employed to decide on the size of elements relative to the degree of fracturing that can be used in numerical simulations of fluid flow in fractured rock masses.

4.2.2 Equivalent Continuum Modeling of the Elasto-Plastic Behavior of Fractured Rock Masses

This project extensively evaluated the sensitivities of the elastic parameters calculated from equivalent continuum models, in particular, Oda's compliance tensor, of fractured rock masses. Also evaluated is the use of the smeared crack formulation for the elasto-plastic stress-strain behavior of fractured rock masses. A parametric study covering a wide spectrum of field data was conducted to evaluate the dependence of rock mass stiffness on fracture geometrical parameters and sampling volume. A large number of fracture geometry realizations were generated using Monte Carlo simulation based on different probability distributions functions to

reflect the variability of fracture geometry. Fracture geometrical parameters were based on field data obtained from different sources in studies of fracturing from varied geological sites. The results were used to establish relationships between variations in fracture geometry, length scale, and rock mass stiffness. The following are the main conclusions from the investigation:

1) A high fractal dimension in the power law fracture length distribution resulted in higher Young's modulus and smaller Poisson's ratio distributions, which indicates higher equivalent continuum stiffness. The deviation of the elastic parameters is linearly related to the magnitude of fractal dimension.
2) A high fracture normal stress produced higher fracture stiffness parameters, and ultimately results in a larger Young's modulus and smaller Poisson's ratio. Owing to directional sensitivities for both Young's modulus and Poisson's ratio, a lower normal stress yields strong directional variations and produces clear anisotropy of the elastic parameter distributions. When the normal stress is extremely high, the mechanical effect of the fracture system may be ignored because of the low fracture stiffness ratio (R = 1) and high fracture stiffnesses (not exceeding intact rock stiffness) corresponding to the intact rock mass' mechanical behavior.
3) Increasing the number of fracture sets resulted in increasingly isotropic elastic parameter distributions. The convergence rate decreases exponentially when the number of fracture sets is relatively large.
4) Using the side length ratio SLR, which is equal to the length of the side of the square sampling area divided by the length of the square region of interest, it was found that the mean values of the equivalent Young's modulus and Poisson's ratio are independent of SLR above a certain threshold SLR value and oscillate below this threshold.
5) REV was defined by the SLR below which both the mean Young's modulus and Poisson's ratio values start to oscillate. Above this SLR value, the mean elastic stiffness parameters remain relatively constant and independent of the size of the sampling volume. In order to suggest a quantified oscillation value in a general manner, a relative error calculation was applied.
6) A linear relationship was obtained between the logarithmic values of MOV, which is the maximum length of fracture over the total sampling volume, and the REV. The relationship of REV and MOV can be used as a guideline to determine the REV and the size of elements that can be applied in numerical simulations of mechanical behavior of fractured rock masses based on the degree of fracturing.
7) The smeared crack formulation provides a convenient and realistic model for the elasto-plastic behavior of fractured rock masses. Model predictions were found to agree with analytic and experimental predictions of the deformation and shear strength of fractured rock masses.

4.2.3 Stochastic Modeling of CO_2 Injection and Migration

The study performed stochastic analysis on both injection process and migration process that occur during CO2 sequestration project. By using randomized input and performing Monte Carlo simulation on TOUGH2, the uncertainty of the results from injection and migration processes was studied. Most of the observation quantities are very likely to follow normal distribution, except for the CO2 saturation above the gas plume in the migration case. Results indicate that:

1) Both the injection and migration stages provided uncertain output with random input.

2) In the migration stage, CO_2 saturation profiles are more determinate compared to other quantities such as block-to-block flow rate, well flow rate and CO_2 mass fraction.
3) During the injection, the uncertainty in CO_2 saturation profiles is more significant compared to other quantities
4) Intrinsic permeability has strong influence in the flow path during the injection process
5) Intrinsic permeability has stronger influence on the uncertainty of the simulation than porosity, in such a way that the uncertainty of permeability will result in uncertainty of most of the flow properties. Porosity uncertainty cannot be neglected, especially when one evaluates the storage capacity factor in injection process.

4.2.4 Coupled H-M Modeling and Validation of Models

The research studied the validity and performance of the procedure developed for full coupling two-phase fluid flow and geomechanical modeling using TOUGH2 and FLAC. The models were validated against theoretical predictions from poroelasticity, prototype reservoir and two real CO_2 injection operations at the In Salah gas field in Algeria and the Sleipner gas field in North Sea, Norway. The summaries of results for each models analyzed are provided above. However, the following concluding remarks can be made on the coupled H-M modeling procedure and validation of models.

1) Rigorous coupling between geomechanics and two-phase fluid flow that follows Biot's poroelasic theory is possible using a staggered solution technique allowing for use of two existing computer programs (TOUGH2 and FLAC).
2) Coupled geomechanics and fluid flow simulation technique produces poroelastic effects predicted by Mandel-Cryer, and Nordbergum.
3) The proposed coupled H-M procedure is able to capture the three main components of hydromechanical response with respect to the reference CO_2 reservoir model: spread of CO_2 plumes, pore pressure distribution, and surface uplift.
4) The agreement between results from the procedure model and the reference CO_2 reservoir model ranges from moderate to well agreed. It is very difficult (if not impossible) to match the simulation results between the two models perfectly.
5) Some discrepancies occur may be attributed to the difference in the applied fluid and rock properties between the two models. The constant fluid and rock properties adopted in FLAC result in different hydromechanical responses from those in the reference models in which stress and pressure-dependent properties were adopted. Future modeling studies should include more accurate fluid and rock properties and their dependent functions with stress and pressure. In FLAC, these functions can be written in FISH.
6) The potential for mechanical failures are calculated using critical pressure approach. With the current injection pressure, our analysis shows that the caprock is more prominent to tensile failure than the shear failure. However, there is a need for greater injection period or increase in injection pressure for the failures to propagate through the thickness of the caprock that may induce leakage towards the overburden.

REFERENCES

Ackermann RV, Schlische RW (1997). Anticlustering of small normal faults around larger faults. Geol 25 (12):1127-1130

Altunin, V.V. (1975). Thermophysical Properties of Carbon Dioxide (in Russian). Standartov, Moscow.

Baecher G, Lanney N (1978). Trace Length biases in joint surveys. In: Proceedings of the 19th US Rock Mechanics Symposium, Mackay School of Mines 56-65

Baecher G, Lanney N, Einstein H (1977). Statistical description of rock properties and sampling. In: Proceedings of the 18th US Rock Mechanics Symposium, Colorado School of Mines, 5c1.1-8

Bahat D (1987). Jointing and fracture interactions in middle Eocene chalks near Beer-Sheva, Israel, Techtonophysics 136(3-4):299-321

Bandis S, Lumsden AC, Barton NR (1981). Experimental studies of scale effects on the shear behavior of rock joints. Int J Rock Mech Min Sci 18(1):1-21

Barton C, Zoback M (1990). Self-similar distribution of macroscopic fractures at depth in crystalline rock in the Cajon Pass scientific drillhole. C.A. Barton, O. Stephansson (eds.) Rock Joints. Rotterdam, Balkema, 163-170

Barton NR, Choubey V (1977) The shear strength of rock joint in theory and practice. Rock Mech 10(1):1-54

Battistelli, A., Calore, C., Pruess, K. (1997). The simulator TOUGH2/EWASG for modelling geothermal reservoirs with brines and non-condensible gas. Geothermics 26, 437-464.

Bellin, A., Rubin, Y. (1996). HYDRO_GEN: A spatially distributed random field generator for correlated properties. Stochastic Hydrology and Hydraulics 10, 253-278.

Biot, M.A. (1941a). General theory of three-dimensional consolidation. J. Appl. Phys. vol. 12, pp. 155-164

Biot, M.A. (1941b). Theory of elasticity and consolidation for a porous anisotropic solid. J. Appl. Phys., vol. 26, pp. 182-185

Blackstone DLR (1988). Traveler's Guide to the Geology of Wyoming. Bull Geol Surv Wyo, Laramie, WY, 130 p

Bonnet E, Bour O, Odling NE, Davy P, Main I, Cowie P, Berkowitz B (2001). Scaling of fracture systems in geological media. Rev Geophys 39 (3):347-383

Borst RD, Remmers JJC, Needleman A, Abellan M (2004). Discrete vs smeared crack models for concrete fracture: bridging the gap. Int J Num Anal Meth Geomech; 28(7-8):583-607

Bras, R., Rodriguez-Iturbe, I. (1985). Random Functions and Hydrology. Addison-Wesely. Reading, MA.

Brown SR, Bruhn RL (1998). Fluid permeability of deformable fracture networks. J Geophys Res 103 (B2):2489-2500

Cacas M, Ledoux E, De Marsily G, Barbreau A, Calmels P, Margritta R (1990). Modeling fracture flow with a stochastic discrete fracture network: calibration and validation: 2. The Transport model. Water Resour Res 26(3):491-500

Cai M, Horii H (1992). A constitutive model of highly jointed rock masses. Mech Mater 13 (3):217-246

Call R, Savely J, Nicholas D, Call PD (1976). Estimation of joint set characteristics from surface mapping data. In: Proceedings of the 17th US Symposium on Rock Mechanics, Snow Bird, UT, 2B2-1-9

Chen, T., Gutierrez, M. (2011). 1-D stochastic analysis of CO_2 sequestration in geologic formations. Drafted for International Journal of Greenhouse Gas Control.

Chin, L.Y., Thomas, L.K., Sylte J.E. and Pierson, R.G. (2002). Iterative coupled analysis of geomechanics and fluid flow for rock compaction in reservoir simulation. Oil and Gas Sci. Tech., vol. 57, pp. 485-497.

Cladouhos TT, Marrett R (1996). Are fault growth and linkage models consistent with power-law distributions of fault lengths? J Struct Geol 18 (2-3):281-293

Clark R, Cox S, Laslett G (1999). Generalizations of power law distributions applicable to sampled fault trace lengths: model choice, parameter estimation and caveats. Geophys J Int 136 (2):357-372

Clark R, Cox S, Laslett G (1999). Generalizations of power law distributions applicable to sampled fault trace lengths: model choice, parameter estimation and caveats. Geophys J Int 136(2):357-72

Corey, A.T. (1954). The interrelation between gas and oil relative permeabilities. Producers Monthly 19, 38-41.

Dagan, G. (1989). Flow and transport in porous formations. Springer-Verlag New York.

De Dreuzy J, Davy P, Bour O (2002). Hydraulic properties of two-dimensional random fracture networks following power law distributions of length and aperture. Water Resour Res 38 (12):1276

De Dreuzy J, Davy P, Bour O (2002). Hydraulic properties of two-dimensional random fracture networks following power law distributions of length and aperture. Water Resour Res 38(12):1276

Dershowitz B, LaPointe P, Eiben T, Wei L (2000). Integration of discrete feature network methods with conventional simulator approaches. SPE Res Eval Eng. 3 (2):165-170

Dershowitz W, Einstein H (1988). Characterizing rock joint geometry with joint system models. Rock Mech and Rock Eng 21 (1):21-51

Doughty, C., Pruess, K. (2004). Modeling supercritical carbon dioxide injection in heterogeneous porous media. Vadose Zone Journal 3, 837.

Doughty, C., Pruess, K., Benson, S.M., Hovorka, S.D., Knox, P.R., Green, C.T. (2001). Capacity investigation of brine-bearing sands of the Frio Formation for geologic sequestration of CO2.

Edwards, A.L. (1966). TRUMP: a computer program for transient and steady-state temperature distributions in multidimensional systems. Lawrence Radiation Lab., Univ. of California, Livermore.

Eshelby JD (1957). The determination of the elastic field of an ellipsoidal inclusion, and related problems. Proc Roy Soc London. Ser A, Meth Phys Sci 241(1226):376-396

Fisher R (1953). Dispersion on a sphere. In: Proc. Roy Soc London Ser A Math Phys Sci 217 (1130):295-305

Flett, M., Gurton, R., Weir, G. (2007) Heterogeneous saline formations for carbon dioxide disposal: Impact of varying heterogeneity on containment and trapping. Journal of Petroleum Science and Engineering 57, 106-118.

Fossen H, Hesthammer J (1997) .Geometric analysis and scaling relations of deformation bands in porous sandstone. J Struct Geol 19 (12):1479-1493

Gale J (1982). Assessing the permeability characteristics of fractured rock. Spl Pub Geol Soc Am, University of Waterloo, Ontario 189 (CONF-790284):163-181

Gale J (2004). Self-organization of natural mode-1 fracture apertures into power law distributions. In: Proc. North Am Rock Mech Symp, ARMA/NARMS, Houston, TX, June 5-9, 2004, ARMA/NARMS 04-563

Gauthier B, Lake S (1993). Probabilistic modeling of faults below the limit of seismic resolution in Pelican Field, North Sea, offshore United Kingdom. AAPG Bull 77 (5):761-777

Gelhar, L. (1993). Stochastic subsurface hydrogeology. Prentice Hall, Englewood Cliffs, New Jersery.

Gudmundsson A (1987). Geometry, formation, and development of tectonics fractures on the Reykjanes Peninsula, southwest Iceland, Tectonophysics 139(3-4):295-308

Gudmundsson A (1987). Tectonics of the Thingvellir fissure swarm, SW Iceland, J Struct Geol 9(1):61-69

Gutierrez, M. and Lee, I. (2009). Fully-Coupled Partitioned Solution of Fluid Flow in Porous Media Based on the Biot's Theory. Proc. 4th Biot Conf. Poromechanics, pp. 923-928

Gutierrez, M. and Lewis, R.W. (2002). Coupling of Fluid Flow and Deformation in Underground Formations. J. Eng. Mech., ASCE, vol. 128, no. 7, pp. 779-787

Guvanasen V, Chan T (2000). A three-dimensional numerical model for thermohydromechanical deformation with hysteresis in a fractured rock mass. Int J Rock Mech Min Sci 37(1):89-106

Heffer K, Bevan T (1990). Scaling relationships in natural fractures: data, theory, and application. In: Proceedings of the 2nd European Petroleum Conference, Society of Petroleum Engineers, Richardson, TX, 367-376

Hovorka, S.D., Doughty, C., Holtz, M. (2004). Testing efficiency of storage in the subsurface: Frio Brine Pilot experiment.

IFC (1967). A formulation of the thermodynamic properties of ordinary water substance. IFC Secretariat, Düsseldorf, Germany.

Itasca (2005). FLAC- Fast Langrangian Analysis of Contiua. 5th ed. Minneapolis, MN: Itasca Consulting Group.

Jaeger, J. C., Cook, N. G. W. and Zimmerman, R. W. (2007). Fundamentals of Rock Mechanics. 4th ed. Oxford, UK: Blackwell Publishing.

Josh, M. et al. (2012). Laboratory characterisation of shale properties. Journal of Petroleum Science and Engineering, Volume 88-89, pp. 107-124.

Journel, A., Alabert, F. (1989). Non-Gaussian data expansion in the earth sciences. Terra Nova 1, 123-134.

Kakimi T (1980). Magnitude-frequency relation for displacement of minor faults and its significance in crustal deformation. Bull Geol Surv Japan 31:467-487

Kazemi H (1969). Pressure transient analysis of naturally fractured reservoirs with uniform fracture distribution. Soc Pet Eng J 9 (4):451-462

Knott SD, Beach A, Brockbank PJ, Lawson Brown J, McCallum JE (1996) .Welbon AI. Spatial and mechanical controls on normal fault populations. J Struct Geol 18(2-3):359-72

Krantz RW (1988). Multiple fault sets and three-dimensional strain: theory and application. J Struct Geol 10 (3):225-237

Kulatilake P, Chen J, Teng J, Shufang X, Pan G (1996). Discontinuity geometry characterization in a tunnel close to the proposed permanent shiplock area of the three gorges dam site in China. Int J Rock Mech and Min Sci 33 (3):255-277

Lee CH, Deng BW, Chang J (1995). A continuum approach for estimating permeability in naturally fractured rocks. Eng Geol 39(1-2):71-85

Lengler, U., De Lucia, M., Kühn, M. (2010). The impact of heterogeneity on the distribution of CO2: Numerical simulation of CO2 storage at Ketzin. International Journal of Greenhouse Gas Control 4, 1016-1025.

LLNS (2009). LLNL Community News: https://newsline.llnl.gov/_rev02/ articles/2009/may/ 05.22.09-sequestration.php,

Long JCS, Remer J, Wilson C, Witherspoon P (1982). Porous media equivalents for networks of discontinuous fractures. Water Resour Res 18(3):645-58

McMahon BK (1971). A statistical method for the design of rock slopes. In: Proceedings of the 1st Australia-New Zealand Conference on Geomechanics, Melbourne 314-21

Min KB, Rutqvist J, Tsang CF, Jing L (2004). Stress-dependent permeability of fractured rock masses: a numerical study. Int J Rock Mech and Min Sci 41 (7):1191-1210

Mood, A.M., Graybill, F., Boes, D. (1963). Introduction into the theory of statistics. McGraw-Hill International Bok Company.

Morris, J., Hao, Y., Foxall, W. and McNab, W. (2011). A study of injection-induced mechanical deformation at the In Salah CO2 storage project. International Journal of Greenhouse Gas Control, 5(2), pp. 270-280.

Narasimhan T, Pruess K (1988). MINC: an approach for analyzing transport in strongly heterogeneous systems. E. Custodio, A. Gurgui and J,P, Lobo Ferreira (eds.) Groundwater Flow and Quality Modelling, Lisbon, June 2-6, D Reidel Publishing Co, Boston, pp 375-391

Narasimhan, T., Witherspoon, P. (1976). An integrated finite difference method for analyzing fluid flow in porous media. Water Resources Research 12, 57-64.

Neuman SP (1988). Stochastic continuum representation of fractured rock permeability as an alternative to the REV and fracture network concepts. In: Proc. 28th US Rock Mech Symp, Tucson, AZ, pp 533-561

Nygard, R., Gutierrez, M., Bratli, R. K. and Hoeg, K. (2006). Brittle-ductile transition, shear failure and leakage in shales and mudrocks. Marine and Petroleum Geology, 23(22), pp. 201-212.

Oda M (1982). Fabric tensor for discontinuous geological mataerials. Soils Found 22 (4):96-108

Oda M (1985) .Permeability tensor for discontinuous rock masses. Geotechnique 35 (4):483-495

Oda M (1988). An experimental study of the elasticity of Mylonite rock with random cracks. Int J Rock Mech Min Sci Geomech Abstr 25(2):59-69

Oda M, Yamabe T, Ishizuka Y, Kumasaka H, Tada H, Kimura K (1993). Elastic stress and strain in jointed rock masses by means of crack tensor analysis. Rock Mechanics and Rock Engineering 26 (2):89-112

Odling N, Gillespie P, Bourgine B, Castaing C, Chiles J, Christensen N, Fillion E, Genter A, Olsen C, Thrane L (1999). Variations in fracture system geometry and their implications for fluid flow in fractures hydrocarbon reservoirs. Petr Geosci 5 (4):373-384

Ouenes A, Hartley LJ (2000). Integrated fractured reservoir modeling using both discrete and continuum approaches. In: Proc. SPE Ann Tech Conf and Exh, Dallas TX, October 1-4, 2000, SPE 62939

Ouillon G, Casting C, Sornette D. (1996). Hierarchical geometry of faulting. J Geophys Res 101(B3):5477-87

Pan, P.-Z., Rutqvist, J., Feng, X.-T. and Yan, F. (2013). An approach for modeling rock discontinuous mechanical behavior under multiphase fluid flow conditions. Rock Mechanics and Rock Engineering, pp. 1-15.

Park YJ, De Dreuzy JR, Lee KK, Berkowitz B (2001). Transport and intersection mixing in random fracture networks with power law length distributions. Water Resour Res 37 (10):2493-2501

Pickering G, Peacock DCP, Sanderson DJ, Bull JM (1997). Modeling tip zones to predict the

Post RM, Kemeny JM, Murphy R (2001). Image processing for automatic extraction of rock joint orientation data from digital images. In: Proceedings of the 38th US Rock Mech Symposium, Washington, DC, 877-84

Preisig, M. and Prevost, J. H. (2011). Coupled multi-phase thermo-poromechanical effects. Case study: CO2 injection at In Salah, Algeria. International Journal of Greenhouse Gas Control, 5(4), pp. 1055-1064.

Priest S (1993). Discontinuity analysis for rock engineering. Chapman and Hall, London and New York, 473 p

Pruess, K. (2005). ECO2N: A TOUGH2 Fluid Property Module for Mixtures of Water, NaCl, and CO2, s.l.: Earth Sciences Division, Lawrence Berkeley National Laboratory, University of California, Berkeley, CA.

Pruess, K. and Garcia, J. (2003). Solutions of test problems for disposal of CO2 in saline aquifers, Berkeley: Lawrence Berkeley National Laboratory.

Pruess, K. et al. (2002). Intercomparison of numerical simulation codes for geologic disposal of CO2, Berkeley, CA: Lawrence Berkeley National Laboratory.

Pruess, K., Benson, S.M., Hovorka, S.D. (2005). ECO2N: A TOUGH2 fluid property module for mixtures of water, NaCl, and CO2. Lawrence Berkeley National Laboratory.

Pruess, K., Moridis, G., Oldenburg, C., Laboratory, L.B.N. (1999). TOUGH2 user's guide, version 2.0. Lawrence Berkeley National Laboratory.

Rashid YR (1968) Analysis of reinforced concrete pressure vessels. Nuclear Eng Des 7:334-344

Reches Z (1986). Network of shear faults in the field and in experiment. In: Englman R, Jaeger Z, editors. Fragmentation, form and flow in fractured media. Annals of the Israel Physical Society, 42-51

Robertson A (1970). The interpretation of geological factors for use in slope theory. In: Proceedings of Symposium on the theoretical background to the planning of open pit mines with special reference to slope stability, 55-71

Rots JG (1991). Smeared and discrete representations of localized fracture. Int J Fract 51(1):45-59

Rutqvist, J. and Tsang, C. -F. (2002). A study of caprock hydromechanical changes associated with CO2-injection into a brine formation. Environmental Geology , 42(2-3), pp. 296-305.

Rutqvist, J., Birkholzer, J. and Chin-Fu, T. (2007). Couple Reservoir-Geomechanical Analysis of the Potential for Tensile and Shear Failure Associated with CO2 Injection in Multilayered Reservoir-Caprocks Systems. Int J Rock Mech Mining Sci, 45(2), pp. 132-143.

Rutqvist, J., Vasco, D. and Myer, L. (2010). Coupled reservoir-geomechanical analysis of CO2 injection and ground deformations at In Salah, Algeria. International Journal of Greenhouse Ground Control, 4(2), pp. 225-230.

Rutqvist, J., Wu, Y. -S., Tsang, C. -F. and Bodvarsson, G. (2002). A modeling approach for analysis of coupled multiphase fluid flow, heat transfer, and deformation in fractured porous rock. International Journal of Rock Mechanics and Mining Sciences, 39(4), pp. 429-442.

Schlische RW, Young SS, Ackermann RV, Gupta A (1996). Geometry and scaling relations of a population of very small rift-related normal faults. Geol 24 (8):683-686

Scholz CH, Dawers NH, Yu JZ, Anders MH, Cowie PA (1993). Fault growth and fault scaling laws: Preliminary results. J Geophys Res 98(B12):21951-61

Scott RB, Castellanos M (1984). Stratigraphic and structural relations of volcanic rocks in drill holes USW GU-3 and USW G-3, Yucca Mountain, Nye County, Nevada. US Geol Surv, Denver, CO; Fenix and Scisson, Inc., Mercury, NV (United States), Technical Report, 136 p

Segall P, Polland DD (1983). Joint formation in granitic rock of the Sierra Nevada. Geol Soc Am Bull 94(5):563-75

Silvester, L.F., Pitzer, K.S. (1976). Thermodynamics of geothermal brines. I. Thermodynamic properties of vapor-saturated NaCl (aq) solutions from 0-300oC. California Univ., Berkeley (USA). Lawrence Berkeley Lab.

Snow DT (1969) .Anisotropic permeability of fractured media. Water Resour Res 5 (6):1273-1289

Span, R. and Wagner, W. (1996). A new equation of state for Carbon Dioxide covering the fluid region from the triple-point temperature to 100 K at pressures up to 800 MPa. Journal of Physical and Chemical Reference Data, 25(6), pp. 1509-1596.

Spycher, N., Pruess, K. (2005). CO2-H2O mixtures in the geological sequestration of CO2. II. Partitioning in chloride brines at 12-100oC and up to 600 bar. Geochimica et Cosmochimica Acta 69, 3309-3320.

Spycher, N.F., Reed, M.H. (1988). Fugacity coefficients of H2, CO2, CH4, H2O and of H2O-CO2-CH4 mixtures: A virial equation treatment for moderate pressures and temperatures applicable to calculations of hydrothermal boiling. Geochimica et Cosmochimica Acta 52, 739-749.

StatoilHydro (2009). Carbon Dioxide capture, transport and storage, Stavanger, Norway: StatoilHydro.

Stewart JH (1980). Geology of Nevada. vol 4, Special Publication of Nevada Bureau of Mines and Geology, 136 p

Terzaghi, K. (1943). Theoretical Soil Mechanics. New York: Wiley

Van Genuchten, M. (1980). A closed-form equation for predicting the hydraulic conductivity of unsaturated soils. Soil Sci. Soc. Am. J 44, 892-898.

Vanmarcke, E.H. (1983). Random fields: analysis and synthesis. MIT-Press, Cambridge, Massachusetts.

Vilarrasa, V., Carrera, J. and Olivella, S. (2012). Hydromechanical charaterization of CO2 injection sites. International Journal of Greenhouse Gas Control, Volume In Press (Corrected Proof).

Villemin T (1987). Distribution logarithmique self-similaire des rejets et longueurs de failles: exemple du Bassin Houiller Lorrain. Comp RendsAcad Sci. Série 2, Gauthier-Villars 305 (16):1309-1312

Warren J, Root PJ (1963). The behavior of naturally fractured reservoirs. Soc Pet Eng J 3 (3):245-255

Watterson J, Walsh J, Gillespie P, Easton S (1996). Scaling systematics of fault sizes on a large-scale range fault map. J Struct Geol 18 (2-3):199-214

Winterfeld, P. H. and Wu, Y. S., 2011. Numerical simulation of CO2 sequestration in saline aquifers with geomechanical effects. Pittsburgh, PA, s.n.

Yielding G, Needham T, Jones H (1996). Sampling of fault populations using sub-surface data: a review. J Struct Geol 18 (2-3):135-146

Yoshida H, Horii H (1998). Micro-mechanics based continuum analysis for the excavation of large-scale underground cavern. In: Proceedings of SPE/ISRM Rock Mechanics in Petroleum Engineering, Trondheim, Norway, 209-218

Yoshinaka R, Yamabe T (1986). Joint stiffness and the deformation behaviour of discontinuous rock. In, 1986. Elsevier, pp 19-28

Zienkiewicz OC, Pande GN (1997). Time dependent multi-laminate model of rocks - A numerical study of deformation and failure of rock masses. Int J Num Anal Meth Geomech 1(3):219-247

COST STATUS

Final Quarterly Spending and Project Cost

	Year 1 Start: 1/1/10 End: 12/31/10				Year 2 Start: 1/1/11 End: 12/31/11				Year 3 Start: 1/1/12 End: 12/31/12				End: 5/31/13	
Reporting Quarter	Q1	Q2	Q3	Q4	Q1	Q2	Q3	Q4	Q1	Q2	Q3	Q4	Q1	Q2
Baseline Cost Plan (from Sf-424)														
Federal Share	23646	23646	23646	23646	23646	23647	23647	23648	23647	23648	23649	23649	23649	
Non-federal Share	0	0	0	0	0	0	0	0	0	0	0	0	0	
Total Planned (federal and Non-federal	23646	23646	23646	23646	23646	23647	23647	23648	23647	23648	23649	23649	23649	
Cumulative Baseline cost	23646	47292	70938	94584	104226.2	127873	151520	175168	198815	222463	246112	269761	293410	
Actrual Incurred Cost														
Federal Share	0	13075	32985	27691	31475	21348	24237	15660	24412	16553	14274	9335	24985	37050
Non-federal Share	0	0	0	0	0	0	0	0	0	0	0	0	0	0
Total Planned (federal and Non-federal	0	13075	32985	27691	31475	21348.4	24237	15660	24412	16553	14274	9334.64	24985	37050
Cumulative Baseline cost	0	13075	46060	73751	105226	126574	150812	166472	190884	207437	221711	231045	256031	293080
Variance														
Federal Share	23646	10571	-9339	-4045	-7829	2299	-590	7988	-765	7095	9375	14314	-1336	-37050
Non-federal Share	0	0	0	0	0	0	0	0	0	0	0	0	0	0
Total Planned (federal and Non-federal	23646	10571	-9339	-4045	-7829	2299	-590	7988	-765	7095	9375	14314	-1336	-37050
Cumulative Baseline cost	23646	34217	24878	20833	13004	15303	14712	22700	21935	29030	38405	52720	51383	14334

PRODUCTS PRODUCED AND TECHNOLOGY TRANSFER ACTIVITIES

The following papers were completed as part of the project:

Youn, D.J. and Gutierrez, M. (2011), "Effect of Fractured Distribution on the Permeability of Fractured Rock Masses," Rock Mechanics and Rock Engineering, in review.

Gutierrez, M. and Youn, D.-J. (2012), "Scale Effects on the Elastic Behavior of Fractured Rock Masses," Acta Geotechnica, in review.

Chen, T., Gutierrez, M. (2011). 1-D stochastic analysis of CO2 sequestration in geologic formations. Drafted for International Journal of Greenhouse Gas Control.

Chin, L.Y., Thomas, L.K., Sylte J.E. and Pierson, R.G. (2002). Iterative coupled analysis of geomechanics and fluid flow for rock compaction in reservoir simulation. Oil and Gas Sci. Tech., vol. 57, pp. 485-497.

Gutierrez, M. and Youn, D. (2012), "Fracture Geometry and Scale Effects on the Equivalent Continuum Permeability of Fractured Rock Masses," Proc. IXth Conference on

Geostatistics for Environmental Applications (geoENV 2012), Valencia, Spain, September 19-21, 2012, Electronic Proceedings.

Chen, T., Katsuki, D. and Gutierrez, M. (2012), "Forward and Inverse Modeling of Laboratory Tests on CO2 Injection in Porous Rocks," Proc. 46th US Rock Mechanics and Geomechanics Symposium, Chicago, IL, June 24-27, 2012, Electronic Proceedings.

Youn, D. and Gutierrez, M. (2012), "Scale Effects on the Elastic Behavior of Fractured Rock Masses," Proc. 46th US Rock Mechanics and Geomechanics Symposium, Chicago, IL, June 24-27, 2012, Electronic Proceedings.

Chen, T. and Gutierrez, M. (2011), "Stochastic Analysis of Carbon Sequestration in Geologic Formation," Proc. 45th U.S. Rock Mechanics and Geomechanics Symposium, San Francisco, CA, June 26-29, 2011, Electronic Proceedings.